STAR
178

NASA Conference Publication 2239

Earth Radiation Science Seminars

Lectures from a series of seminars
held at Langley Research Center
Hampton, Virginia
June 1980 to October 1981

NASA

NASA Conference Publication 2239

Earth Radiation Science Seminars

John B. Hall, Jr., *Compiler*
Langley Research Center
Hampton, Virginia

Lectures from a series of seminars
held at Langley Research Center
Hampton, Virginia
June 1980 to October 1981

National Aeronautics
and Space Administration

**Scientific and Technical
Information Branch**

1982

PREFACE

The importance of monitoring the solar flux and the components of the Earth radiation budget to understand their roles in influencing and predicting climate change is well documented in the National Climate Program 5 Year Plan published in September 1980. These components consist of the incoming radiation from the Sun and the outgoing radiation reflected and emitted from the Earth's surface and atmosphere. The components are significantly affected by clouds, trace gases, aerosols, surface reflectivity, and processes that occur on the Sun.

In recognition of the fundamental importance of understanding the Earth radiation budget over varying time and space scales, NASA has been designated as the lead agency responsible for solar and Earth radiation as a principal thrust in the National Climate Program. Accordingly, the NASA Langley Research Center (LaRC) has implemented a viable research activity in this discipline that is focused on understanding the Earth radiation budget components as measured from satellite systems. Included in this activity is the Radiation Science Seminar Series, which is structured to provide an interchange of information between LaRC researchers and other scientists working in the radiation science field. These seminars have been formulated to enhance this interchange through presentations on the following topics:

Earth radiation budget fundamentals
Earth radiation budget climate system role
Historical background
Radiative transfer theory
Radiation instruments and measurements
Measurement analysis
Radiation budget data use

The eight papers presented in this publication are the results of the initial seminar series held at Langley Research Center, Hampton, Virginia, from June 1980 to October 1981. Those who lectured at the seminars and their associated Langley Research Center contacts responsible for arranging the seminars are listed as follows:

Lecturer	NASA LaRC Contact
Dr. J. M. Davis	E. F. Harrison
Dr. R. D. Cess	D. S. Graves
Dr. D. A. Crommelynck	J. B. Hall, Jr.
Dr. E. Raschke	J. B. Hall, Jr.
Dr. F. L. Bartman	Dr. G. L. Smith
Dr. R. W. Saunders	E. F. Harrison
Mr. W. R. Bandeen	J. L. Raper

It is desired to acknowledge the active participation of those who made these seminars possible. Special acknowledgement is due to James L. Raper, who formulated the idea behind these seminars and under whose guidance the seminars were organized and implemented. Special thanks are due to the lecturers and the NASA LaRC contacts for conducting the seminars.

John B. Hall, Jr., Compiler
Langley Research Center

CONTENTS

ORBITAL MEASUREMENTS OF THE EARTH'S RADIATION BUDGET DURING THE FIRST DECADE OF THE SPACE PROGRAM

William R. Bandeen
NASA Goddard Space Flight Center
Greenbelt, Maryland

INTRODUCTION

A knowledge of the radiation budget of the Earth-atmosphere system and its components (i.e., the total solar irradiance, its partition into absorbed and reflected shortwave radiation, and the infrared radiation emitted to space) is fundamental to an understanding of weather, climate, and possible climate change. During the period from 1959 to 1969, radiation budget studies were carried out using data from the Explorer 7, TIROS 2, 3, 4, and 7, and Nimbus 2 and 3 experimental satellites. Many difficulties were encountered in analyzing data from these early satellites, including the following:

The value of the solar "constant" was not accurately known

There was marked degradation of the sensors in orbit

The total reflected and emitted radiation had to be inferred from "filtered" measurements

Corrections for the anisotropy of the reflected and emitted radiances had to be developed to determine the outgoing flux densities at the moment of measurement

Corrections to account for diurnal variability had to be developed to estimate the daily average of outgoing flux densities (because of the "undersampled" nature of the data)

In spite of these sources of error, the early measurements indicated that the planetary albedo was lower (i.e., approximately 29 percent as opposed to 35 percent), the emitted radiation was higher, and the equator-to-pole gradient of net radiation was greater than had been previously supposed.

Lessons learned from these early satellites have been applied to later missions, and increasingly accurate determinations of the radiation budget are expected from the Earth Radiation Budget (ERB) sensors flown on Nimbus 6 and 7 and from the Earth Radiation Budget Satellite (ERBS) and NOAA F and G satellites scheduled for launch in 1984 and 1985.

EARTH-ATMOSPHERE HEAT ENGINE

Figure 1 illustrates the fact that the Earth-atmosphere heat engine is driven by the Sun. The incoming solar radiation, which amounts to about 173 000 TW, is either reflected or absorbed by the Earth-atmosphere system. The absorbed radiation is distributed either by surface heating or by latent heat transfer through water vapor condensation, with precipitation falling back to the surface of the Earth. A smaller amount is transferred to sensible heat. The potential energy available from differential heating of the atmosphere drives the winds, which in turn drive the ocean currents. Emitted longwave radiation is lost to space.

The albedo shown in figure 1, about 29 percent, is a value derived from measurements made during the first 10 years of space exploration. As an aside, it occurs to me that we have no energy problem on the planet Earth because all of mankind uses about 15 TW of energy, so that using only about 0.01 percent of the incoming solar radiation would enable us to meet our needs. Of course, the problem is learning how to tap that available energy.

EXPLORER 7 HEMISPHERICAL SENSORS

Explorer 7 was launched on October 13, 1959, about 21 years ago, and carried the wide-field-of-view hemispherical sensors developed by Verner Suomi. These sensors were mounted on aluminum mirrors, so they did not "see" the spacecraft. They merely saw a reflection of the scene in the mirror, and thus acted virtually as spheres, radiatively isolated in space. The arrangement of the sensors on the spin-stabilized spacecraft is shown schematically in figure 2.

Equation (1) represents the radiation equation at night, when only infrared radiation is involved:

$$\alpha\beta W_L = 4\pi\varepsilon\sigma T^4 + 2H\frac{\partial T}{\partial t} + 2k(T - T_m) \tag{1}$$

where

$\alpha=\varepsilon$	infrared absorptivity, emissivity
β	solid angle to Earth
σ	Stefan-Boltzmann constant
T	temperature of sensor
H	heat capacity of sensor
t	time

k conductivity between sensor and mount (i.e., mirror temperature, T_m)

W_L infrared radiant emittance of Earth

As shown on the right-hand side of the equation, the absorbed incoming longwave radiation can produce three effects. First, it can be radiated back to space, as expressed in the first term. Second, it can be stored in the mass of the sensor by causing the sensor to heat at the rate shown. Third, it can cause heat conduction from the sensor to the satellite or, in this case, to the mirror. If the temperature of the mirror is less than the temperature of the sensor, heat can be conducted to the mirror.

Results of analyzing the Explorer 7 radiation budget data are shown in figure 3. Isolines of nighttime radiation loss to space are shown superimposed on surface positions of several weather fronts. It can be seen that the low of outgoing radiation is associated with what must be cloud cover associated with a low-pressure system. Measurements of surface fronts are synoptic, taken every 12 hours, while the satellite measurements are asynoptic, so it is difficult to correlate the positions of the fronts with the radiation analysis when the measurements are not necessarily taken at the same time. Moreover, wide-field measurements like this will receive radiation from the entire disk of the Earth, so when we say that a low occurs in a certain place it is really an integration of measurements from the entire disk.

At its perigee of about 550 km, Explorer 7 saw out to a great circle arc of about 25°. However, the majority of the measurements came from a rather restricted area underneath the satellite. Despite the problems of rigorous interpretation, this experiment showed the close relationship between outgoing radiation and tropospheric weather patterns.

THE TIROS SERIES SCANNING RADIOMETERS

Vonder Haar (1968) analyzed many of the subsequent wide-field-of-view measurements from experiments designed at the University of Wisconsin and conducted with both hemispherical and flat-plate sensors flown on many of the early TIROS satellites. A new radiation-sensing instrument, the five-channel scanning radiometer, was flown on TIROS 2 (launched in November 1960), TIROS 3 (launched in July 1961), and TIROS 4 (launched in February 1962). Each of the channels had a rather narrow instantaneous field of view of about 5°; hence, the measurements could be interpreted as being measurements of radiances rather than of fluxes.

An attempt was made to analyze the radiation budget from these three instruments on TIROS 2, 3, and 4, but there were difficulties. First, the satellite had an inclination of only 48°, and therefore saw only a "quasi-globe," not the entire Earth. By quasi-globe we mean the region from 55°N to 55°S latitude as viewed by the scanning radiometers. Shown in figure 4 is an example of measurements of the quasi-global power interpreted in terms of the equivalent albedo. The albedos interpreted from the early TIROS measurements were disturbingly low, on the order of 15 to 17 percent. These values were about half of what had been expected, even taking into account the following possible sources of error:

Original calibration

Sensor degradation

Solar constant

Unfiltered radiation from filtered measurements

Angular dependence

Sampling problem

Calibration in the days of the TIROS satellites was a rather primitive procedure, done without the benefit of specialized calibration facilities. The calibration equation for the visible sensors was:

$$\bar{w}^* = \frac{\Omega}{\pi} \int_0^\infty w_\lambda \, \phi_\lambda \, d\lambda \tag{2}$$

where

$\bar{w}^*$	effective radiant emittance measured by sensor if it viewed a perfectly diffuse, perfectly reflecting target (albedo = 1) normal to incident solar radiation, W m^{-2}
Ω	solid angle of Sun as seen from Earth
w_λ	spectral radiant emittance of a 6000-K blackbody, W m^{-2} λ^{-1}
ϕ_λ	spectral response function for channel

Solar spectral information available in those days led us to assume a solar blackbody temperature of about 6000 K to fit the incident solar energy over the bandwidth of the shortwave sensor, from about 0.2 to 5 μm.

In addition to such problems as possible calibration errors and a lack of knowledge of the true solar constant and its spectral distribution, it was clear that sensor degradation was a major problem on these early instruments. Another form of wide-field low-resolution sensor, flown on TIROS 2 by Dr. Hanel of Goddard Space Flight Center, degraded so quickly in just a few days of exposure to space vacuum and solar ultraviolet and particle radiation that it was no longer useable after a week of flight.

Apparent problems with sensors are indicated by the large difference between the absorbed solar radiation (interpreted from quasi-global albedo) and emitted terrestrial radiation obtained from the 8- to 12-μm and 8- to 30-μm channels on TIROS 2, 3, and 4, as shown in figure 4. Obviously, if we are to remain comfortable on the Earth, the emitted radiation in terms of quasi-global power should approximately equal the absorbed solar radiation. If the differences indicated in figure 4 were real, the Earth should have been heating up so fast that we should have been boiling after a few months.

Note that in every case the longwave value observed at launch decreased with time. We already had a qualitative idea of how longwave and reflected radiation should behave, based on the earlier work of Dr. London and others (London, 1957). The observed behavior was so persistent and regular, and so consistently out of agreement with what we expected, that it was interpreted as being due to sensor degradation in space rather than to a real phenomenon. Since the science of materials in the space environment was not very far advanced at the time of the TIROS satellites, a likely cause of sensor degradation was the use of unsuitable materials for coating the sensor surfaces. It is reasonable to assume that the black paints used on the chopper of the sensor boiled off of one side and coated the other, mirrored, side.

TIROS 7 MEASUREMENTS

The first satellite to provide a continuous record for 1 year was TIROS 7, launched in June 1963. It used the same instrument as was flown on TIROS 2, 3, and 4. In figure 5, effective radiant emittance as measured from TIROS 7 is plotted versus time for 1 year from June 1963 to June 1964. We looked first at measurements over the equatorial Pacific Ocean, where we expected the seasonal variations to be small between about 30°N and 30°S latitude. However, the measurements again showed clear evidence of degradation of the instrument with time. We also looked at the so-called quasi-global map averages and again found evidence of degradation.

The sinusoidal curve at the top of each part of figure 5 is an attempt to take into account the changing geometry between the Sun and the satellite orbit plane. The inclination of TIROS 7 was 58°, and the precession of this orbit plane relative to the Sun has a period of about 76 days. Looking from the Sun, one would see the descending node on the longitude of the subsolar point shortly after launch. The orbit regresses to the west, and after about 20 days the orbital plane as viewed from the Sun would shift as shown in figure 6. The different orbital geometries noted in figure 6 correspond to the numbered points on the orbit-Sun-phase sinusoidal curve at the top of figures 5(a) and (b).

Because of the changing orientation of the orbit plane relative to the Sun, we expected substantial differences when analyzing the quasi-globe if we were looking, say, at the Northern Hemisphere in summer in the sunlight and the Southern Hemisphere in winter at night. We grouped these orbit plane configurations into regimes, took approximately 2-week averages in each regime, and averaged them to try to smooth out the diurnal variations that we suspected in a given latitude band. However, we still found a marked degradation of the infrared channel and, similarly, an apparent degradation in the reflectances through the visible channel. Therefore, in analyzing these data we had to develop an empirical time correction factor which simply extrapolated each point back to the time of launch.

TIROS 7 had two other channels which would have been better for radiation budget analyses. One was a broad infrared channel covering wavelengths from 5 to 30 μm, but this channel exhibited greater degradation than the narrower 8- to 12-μm channel. We had to develop a regression equation to try to convert the severely filtered 8- to 12-μm radiance to an equivalent total outgoing unfiltered radiance. Similarly, there was a 0.2- to 5-μm channel that would have been much better for making reflectance measurements, but it degraded much more severely than the 0.55- to 0.75-μm channel. Therefore, we had to infer albedo from the narrower, severely filtered channels even though we would have preferred to use the broader channels.

After making some rather simplistic corrections for obvious degradation, we obtained curves of longwave radiation zonally averaged from 90°S to 90°N, which we compared to London's (1957) Northern Hemisphere results. This comparison is shown in figure 7(a). We could not attach much significance to the fact that our outgoing longwave radiation was a little greater than London's, because our data had been subject to so many corrections.

In figure 7(b) we have plotted our inferred albedo compared to London's (1957) data. Here we could be even less confident of our values, because even after making our so-called corrections for degradation from launch we found that we had to multiply the resultant albedos by a factor of 1.6 in order to create radiative equilibrium over the quasi-globe. (Even our requirement that the quasi-globe must be in equilibrium is an assumption.) We finally determined that the quasi-global albedo was 32.2 percent. We had some indication that the outgoing longwave radiation might have been a little greater than London's analysis and the albedo might have been a little lower. In fact, the indications were that the albedo was quite a bit lower in the tropics and somewhat higher in the high latitudes. This would indicate that the "firebox" in the atmospheric engine was hotter than was previously supposed, which in turn would demand that the equatorial transport of heat to higher latitudes was greater than had been supposed.

THE NIMBUS SATELLITE SERIES

The Medium-Resolution Infrared Radiometer (MRIR) was a five-channel instrument flown on the Nimbus satellites. MRIR is actually a misnomer since one of the channels was a visible channel which monitored radiation from the Sun between 0.2 and 5.0 μm. The other four channels, however, did respond to various parts of the infrared spectrum. The IFOV of each channel was a little less (about 2.8°) than those on the TIROS instrument.

A four-step sequence was devised to analyze the MRIR data from Nimbus 2 and 3, the two satellites on which the MRIR was flown. First, the total shortwave and longwave unfiltered radiances had to be computed from filtered radiances. (This computation is one of the possible sources of error mentioned previously.) Next we had to correct for the anisotropy, or angular dependence, of the radiances for the limb darkening in the case of infrared radiances, and the anisotropy of backscattered solar radiation through clouds, oceans, land, etc. Statistical models had to be used, since the satellite flew over at 7 km/sec and a given spot on the Earth was therefore viewed at only one angle.

We had to infer the radiances at all angles over the upper hemisphere from that spot, even though only one measurement was made at a given set of zenith and azimuth angles.

The third step involved an integration over all angles to obtain the outgoing flux density at the moment of measurement. Here one could use only a finite number of practical situations in the ranges of solar zenith angle in order to make this a tractable problem. Finally, we had to compute the daily averages of outgoing flux, both reflected solar radiation and infrared emitted radiation, having made a determination of this flux only at the instant the satellite flew over. This brings forward the familiar sampling problem. Nimbus was in a noon-midnight Sun-synchronous orbit, so that measurements were made only at noon and midnight, local time, at low latitudes. The angular convention used in the analyses of infrared data from Nimbus 2 and 3 is shown in figure 8.

Nimbus 2 and 3

Nimbus 2 was launched on May 15, 1966, and Nimbus 3 on April 14, 1969. Nimbus 2 had a broad infrared channel, from about 5 to 30 μm, which would have been better than a number of narrow channels in the infrared part of the spectrum for radiation budget measurements. Unfortunately, the Nimbus 2 MRIR lasted only 2-1/2 months. It was launched in May and it became inoperative at the end of July. We did, however, carry out analyses of the data and publish results (Raschke and Bandeen, 1970).

Nimbus 3 provided measurements over an entire year, and we consider those measurements to be more significant than those of Nimbus 2, which were made over only 10 weeks. Unfortunately for radiative budget purposes, the MRIR on Nimbus 3 was modified to have four rather narrow spectral channels in the infrared: one around the water vapor absorption band at 6.7 μm, one around the window at between 10 and 12 μm, one around the CO_2 absorption band at 15 μm, and one at the rotation water vapor absorption region around 20 μm. (See fig. 9.)

To calculate values for longwave outgoing radiation in the infrared, we first had to develop a regression equation to compute the total radiance in the direction of the satellite using filtered measurements made in four different channels, as described previously:

$$N_t = a_0 + a_1N_2 + a_2N_2^2 + a_3N_2^3 + a_4N_4 + a_5N_1 + a_6N_3 \qquad (3)$$

where

a regression coefficients

N radiances measured at channels shown in figure 9

We calculated three coefficients for channel 2 (the window channel) and only one for the other three channels. The 10- to 12-μm channel (the window channel) had a much more significant effect than the other channels, and this is reflected in the equation by including a set of higher order terms for this channel. Since the other three channels had a much smaller effect on the total radiation, only first-order terms were used.

To develop the coefficients here we used the early work of Wark et al. (1962), which used 105 model atmospheres in a computer program that served many purposes in the first 10 years and beyond in the space program. Having used that program to develop the regression coefficients, we now had a means of developing the total radiance across the entire spectrum in the direction of the satellite.

Correction for Longwave Anisotropy

The next step is to correct for the anisotropy of the longwave radiation by integrating over all angles to obtain the total outgoing longwave flux density at the moment of measurement. The total longwave radiant emittance is the integral of the total radiance in the direction θ over all data from the zenith down to the horizon, over all azimuth angles:

$$W_L = \int_0^{2\pi} \int_0^{\pi/2} N_t(\theta) \sin\theta \cos\theta \, d\theta \, d\psi \tag{4}$$

where

N_t	total radiance in direction θ
W_L	total longwave radiant emittance
θ	zenith angle of radiance
ψ	azimuth angle of radiance

Since the radiance is assumed not to be a function of azimuth, the 2π can be taken out of the integral. Further, we can develop a limb-darkening model which relates the radiance that would be observed at nadir to a radiance measurement in an arbitrary direction. Then we are left only with an integral over a limb-darkening function $f(\theta)$:

$$W_L = 2\pi N_t(\theta = 0^\circ) \int_0^{\pi/2} f(\theta) \sin\theta \cos\theta \, d\theta \tag{5}$$

This limb-darkening function would be the radiance over the total spectrum in the direction θ divided by the radiance in the zenith direction. We approximated this ratio by using measurements from the Nimbus 2 broadband instrument (5 to 30 μm). Even though Nimbus 2 only lasted 10 weeks, we had a good sample of data from which to take the ratio of the radiance in the broad infrared channel at various angles θ to the radiance in the zenith direction. This enabled us to develop an expression for the limb-darkening corrections:

$$f(\theta) = \frac{N_t(\theta)}{N_t(\theta=0^\circ)} \approx \frac{N_{5-30\ \mu m}(\theta)}{N_{5-30\ \mu m}(\theta=0^\circ)} = 1 + b_1\theta + b_2\theta^2 + b_3\theta^3 \qquad (6)$$

where

b regression coefficients

Having developed the limb-darkening models, we could integrate and determine the total outgoing longwave radiation in the upper hemisphere at the instant of measurement.

The limb-darkening functions were developed for five cases; two extremes are shown in figure 10. The function varies from less than 0.8 to 1.0 for the entire range of zenith angles between 0° and 90°. The function is, by definition, equal to 1 at a zenith angle of 0°. The arctic function was the least severe, and the desert curve was the most severe. An antarctic curve falls just under the arctic curve. Midlatitude and tropical curves are nearly identical, and fall between these two extremes.

This still left the problem of computing daily averages. Since we could not know what happened to the outgoing radiation between the instant the satellite passed over at noon and the instant around midnight when it happened to pass over the same place, we simply averaged the noon and night measurements with equal weighting and assumed that this was somehow representative of the diurnal variability.

Correction for Shortwave Anisotropy

The total unfiltered radiances are computed by assuming that the bidirectional reflectance behavior over the total spectrum is the same as the behavior inferred in the 0.2- to 4-μm band. This is a rather broad band and contains virtually all of the solar radiation. The bidirectional reflectance function ρ is defined as the ratio of measured radiance reaching the satellite at a zenith angle θ and azimuth angle ψ with a solar zenith angle ζ, at a time t', to the incoming filtered distance-corrected solar constant S_f at the same solar zenith angle and time:

$$\rho(\theta,\psi,\zeta;t') = \frac{N_f(\theta,\psi,\zeta;t')}{S_f L \cos\zeta(t')} \qquad (7)$$

where

N_f filtered radiance

t' measurement time

L ratio squared of mean to true Earth-Sun distance

Now we can integrate over all angles to obtain the outgoing flux density at the time of measurement. We want to determine the directional reflectance r, i.e., the radiation reflected over the entire upper hemisphere divided by the solar radiation incident on the target at that same time. This would be the integral of the bidirectional reflectance over the upper hemisphere:

$$r(\zeta;t') = \int_0^{2\pi} \int_0^{\pi/2} \rho(\theta,\psi,\zeta;t') \sin\theta \cos\theta \, d\theta \, d\psi \tag{8}$$

However, the bidirectional reflectance was measured at only one satellite and solar zenith angle at one instant in time before the satellite moved on to another place. Since the satellite could not hover and look at all angles over the upper hemisphere, we had to develop a model to infer the total reflectance at all angles in the upper hemisphere based on measurements from one particular direction. We developed a function χ which was multiplied by the measured bidirectional reflectance at a given angle θ and ψ, solar zenith angle ζ, and time of measurement t', and then multiplied this by π. The departure from anisotropy is reflected in this function χ:

$$r(\zeta;t') = \chi(\theta\psi\zeta) \, \pi\rho(\theta,\psi,\zeta;t') \tag{9}$$

where

r directional reflectance

χ directional reflectance function

and

$$\chi(\theta,\psi,\zeta=\text{const.}) = \frac{r(\zeta=\text{const.})}{\pi\rho(\theta,\psi,\zeta=\text{const.})} \tag{10}$$

Figure 11 is an example of the kind of bidirectional reflectance functions we developed. We used only three ranges of solar zenith angles to keep the problem tractable. The figure shows the models for solar zenith angles between 35° and 60° and between 60° and 80°. We developed another model for the range between 0° and 35°. Models like this were developed for three different surface types: (1) an ocean clear-sky model, defined as a situation in which the directional reflectances were 0.1 or less and the observed surface temperature was greater than or equal to 273 K so that the surface was not frozen; (2) a snow model for use whenever the directional reflectance was greater than 0.5 and the latitude was greater than 65°; and (3) a "land" model for all other cases. In summary, we produced a total of nine different models similar to those shown in figure 11.

The left side of figure 11 illustrates a situation in which the Sun is at a large zenith angle, around 70°. If the satellite looks back to see the radiation in the direction from which the Sun is shining, we would expect to see a strong forward scattering. If we assumed a Lambertian surface to infer the total flux from a beam measurement made in a region of strong forward scattering, then we would overestimate the total scattering. We would consequently expect the χ function to be less than 1 in other directions, so that when the bidirectional reflectance in a region of strong forward scattering is multiplied by the χ function this would give the proper directional reflectance over the whole upper hemisphere. Indeed, it can be seen that χ is 0.9 at a satellite zenith angle of 50°. If more data were available, we would find χ values even as low as 0.5 at larger θ angles.

The data for developing the χ functions came from several different sources. Shown in figure 12 are bidirectional reflectance models developed from a series of measurements made from the NASA Convair 990 aircraft stationed at Ames Research Center. An engineering model of the MRIR was mounted in the tail of this aircraft and flown over a variety of targets using several flight patterns to try to obtain a representative number of viewing zenith and azimuth angles for measuring scattered radiation. Flights were made at different times of the day to make measurements over a range of solar zenith angles. Figures 12(a) and (b) show the resulting bidirectional models obtained from flights over the Pacific Ocean at an altitude of 40,000 ft and an azimuth angle of 0° (looking back at the Sun), and are illustrative of the rather strong forward scattering that occurs over the uniform stratocumulus clouds encountered there. The bidirectional reflectances vary from about 7 percent at nadir to about 45 percent near the horizon. The derived directional models are shown in figure 12(c). Models like these are representative of those made using data from the Convair 990 and other sources in this country and Europe, as well as from analyses of the early TIROS data (Arking, 1965; Arking and Levine, 1967).

Having determined directional reflectance at the instant of measurement, we still have to infer the reflectance over the entire day from sunrise to sunset in order to compute daily averages of reflected and absorbed solar radiation. The total outgoing radiation for a solar day (1440 minutes) integrated from sunrise to sunset is:

$$R = \frac{1}{1440} \int_{t_r}^{t_s} SL \cos \zeta(t)\ r[\zeta(t)]\ dt \qquad (11)$$

where

S solar spectral radiance

t_s, t_r times of sunset and sunrise, respectively

R total outgoing radiation for 1 day

To evaluate this integral we developed a function E which was defined as the directional reflectance (a function only of solar zenith angle for any given target) divided by the directional reflectance for that target at a solar zenith angle of 0°. The three directional reflectance models used on Nimbus 3 are shown in figure 13. The ocean model shows strong forward scattering as the Sun approaches either sunset or sunrise, the snow model (Kondratiev et al., 1968) shows little dependence on zenith angle, and the cloud-land model lies in between. For comparison, the single Nimbus 2 model is also shown; this was applied to all surface types (Raschke and Bandeen, 1970; Raschke et al., 1973a, b). The flatness of the snow model is due to the fact that the strong forward scattering is balanced by very weak backscattering, so that an integration over the hemisphere yields a very flat curve for the directional (as opposed to the bidirectional) model. Now equation (11) becomes:

$$R = \frac{1}{1440} \int_{t_r}^{t_s} SL \cos \zeta(t) \frac{r(\zeta;t')}{E(t')} E(t)\, dt \tag{12}$$

where

E the function $r[\zeta(t)]/r(\zeta=0^{\circ})$

Analysis of Nimbus 3 data yields results such as those shown in figure 14. The albedo was found to be about 28.4 percent and the longwave emission was about 0.345 cal cm^{-2} min^{-1}. Some areas exhibit radiation surpluses, defined as more absorbed solar radiation than outgoing longwave radiation, and others exhibit deficits, defined as more outgoing longwave radiation than absorbed solar. This lack of balance is what drives the atmospheric heat engine.

A significant feature is the deficit found over the Sahara Desert. This deficit has been interpreted as an annual feature based on our measurements from May 1969 to February 1970. The results surprised many people because it was assumed that there should be a surplus of radiative energy, as defined, over that hot low-latitude desert. At about the same time Jule Charney was developing some theoretical models which, surprisingly, predicted the same sort of radiation deficit over hot deserts at low latitude. The satellite data shown in figure 14 confirmed his predictions, which can be explained qualitatively by noting that the high desert albedo prevents absorption of enough radiation to produce a surplus.

The Nimbus satellites were in a Sun-synchronous orbit (fig. 15), as are the NOAA operational satellites today. The inclination of the orbit plane is 98.6°. The oblateness of the Earth makes the orbital plane regress at a rate of 0.9856° per day, the same rate as the average apparent motion of the Sun around the celestial sphere. Hence, the Nimbus satellites always cross the equator at the same local time. In the case of Nimbus, it is noon (local time) when the satellite crosses the equator from south to north, and midnight on the other side of the Earth when the satellite crosses the equator from north to south. This caused severe problems for our method of determining the outgoing radiation over all hours of the day; we had no way of knowing the diurnal variability for Nimbus. Therefore we just assumed that the target conditions viewed at noon persisted from sunrise to sunset. The meteorology was actually hardly ever constant in this way, but we simply did not know what else to do.

The early TIROS spacecraft had non-Sun-synchronous orbits, as does one of the proposed ERBE satellites. In this case the orbit plane precesses relative to the Sun such that all available latitudes can eventually be sampled at all local times, typically over about a 2-month period. Vonder Haar (1968) made a study of diurnal variability from the early TIROS satellites. He demonstrated that the minimum albedo occurred at around 9:00 or 10:00 a.m. and the maximum at around 2:00 or 3:00 p.m. These positions are reversed for infrared radiation. His results are shown in figure 16. At the times of minimum albedo there is maximum infrared radiation loss. When the albedo is high, as in cloudy scenes, there is a minimum of infrared radiation loss to space. We found that the Nimbus results fell somewhere in between these peaks and gave an overall balance. Results from the ERBE measurements will tell in a few years how good or bad the Nimbus results were.

HISTORICAL DETERMINATIONS OF SOLAR CONSTANT AND ALBEDO

The solar "constant" is a source of error in all these radiation calculations. Values for the solar constant which have been determined over the last 57 years are given in table I, beginning with Abbott's early measurements made at the Smithsonian Institution over a 30-year period (Abbott, 1922). His value was 1352 W m^{-2}, or 1.94 ly min^{-1}. Johnson (1954) obtained a slightly higher value of 1395 W m^{-2}, or 2.0 ly min^{-1}; this was the solar constant used in the TIROS and Nimbus 2 analyses. Verner Suomi and his colleagues at the University of Wisconsin made a determination of the solar constant from analyses of wide-field-of-view satellite measurements (Vonder Haar, 1968). These early experiments were useful because they were extremely simple. Using the complete form of equation (1), which includes solar radiation terms, the variation of sensor heating with time could be used to determine several things, such as the solar constant.

In 1966 Drummond and coworkers determined the value of the solar constant at 1360 W m^{-2} (Drummond et al., 1967). Willson and coworkers determined the value at 1368 W m^{-2} in June 1976 and 1373 W m^{-2} in November 1978 (Willson et al., 1980). The 1978 value represents about a 0.4-percent increase over their first value. Willson et al. state that this might be the true indication of the variability of the solar constant.

A rocket flown in May 1980, at the peak of the solar cycle, gave the same value as that determined in November 1978. Hickey et al. (1980) recently published a result of the Nimbus 7 ERB cavity radiometer (1376 W m^{-2}), and

Willson's latest value, taken from the Solar Maximum Mission launched on February 14, 1980, is 1368 W m^{-2} (Willson et al., 1981). Many researchers are concluding that these changing values reflect the fact that there is actually some variability in the solar constant.

The Solar Maximum Mission value of 1368 W m^{-2} has shown a variation of a few tenths of a percent over short time intervals. Instrument calibration and degradation are two possible sources of error mentioned earlier which are of concern in this mission when trying to make very precise measurements. For instance, Willson compared measurements made with two instruments both on the ground and in rocket flights and found unexplained variations which make the small percentage changes found in data from the Solar Maximum Mission more suspect (Willson et al., 1980; R. C. Willson, private communication).

Values of the Earth albedo determined by various researchers over the past 63 years are given in table II. There is an amazing, almost monotonic, decrease in these measurements over the years, again reflecting the introduction of more sophisticated instruments and improved methods of data analysis.

REFERENCES

Abbott, C. G. 1922: Application of Solar Radiation Measurements. Annals of the Astrophysical Laboratory of the Smithsonian Institution - IV, Chapter 6, The Smithsonian Institution, Washington, D.C.

Aldrich, L. B. 1919: The Reflecting Power of Clouds. Smithsonian Misc. Coll., vol. 69, no. 10, pp. 1-9.

Angstrom, Anders 1962: Atmospheric Turbidity, Global Illumination, and Planetary Albedo of the Earth. Tellus, vol. 14, no. 4, pp. 435-450.

Arking, A. 1965: The Angular Distribution of Scattered Solar Radiation and the Earth Albedo as Observed From TIROS. Annual Research Report, Goddard AFC, July 1964-June 1965, pp. 47-67.

Arking, A.; and Levine, J. S. 1967: Earth Albedo Measurements: July 1963 to June 1964. J. Atmos. Sci., vol. 24, no. 6, pp. 721-724.

Bandeen, W. R.; Halev, M.; and Strange, I. 1965: A Radiation Climatology in the Visible and Infrared From the TIROS Meteorological Satellites. NASA TN D-2534.

Baur, F.; and Phillipps, H. 1934: Der Warmehaushalt der Lufthulle der Nordhalbkugel in Januar and Juli und zur Zeit der Aquinoktien und Solstitien. Part 1. Die Einstrahlung bei normaler Solarkonstante. Gerlands Beitr. Geophys., vol. 42, pp. 160-207.

Dines, W. H. 1917: The Heat Balance of the Atmosphere. Quart. J. Roy. Meteorol. Soc., vol. 43, no. 182, pp. 151-158.

Drummond, A. J.; Hickey, J. R.; Scholes, W. J.; and Love, E. G. 1967: Multichannel Radiometer Measurement of Solar Irradiance. J. Spacecr. & Rockets, vol. 4, no. 9, pp. 1200-1206.

Fritz, S. 1949: The Albedo of the Planet Earth and of Clouds. J. Meteorol., vol. 6, no. 4, pp. 277-282.

Hickey, J. R.; Stowe, L. L.; Jacobowitz, H.; Pellogrino, P.; Maschhoff, R. H.; House, F.; and Vonder Haar, T. H. 1980: Initial Solar Irradiance Determinations From Nimbus 7 Cavity Radiometer Measurements. Science, vol. 208, no. 4441, pp. 281-283.

Houghton, H. G. 1954: On the Annual Heat Balance of the Northern Hemisphere. J. Meteorol., vol. 11, no. 1, pp. 3-9.

House, Fred B. 1965: The Radiation Balance of the Earth From a Satellite. Ph. D. Thesis, Univ. of Wisconsin, Madison. (Available as NASA CR-76422.)

Johnson, F. S. 1954: The Solar Constant. J. Meteorol., vol. 11, no. 4, pp. 431-439.

Kondratiev, K. Ya.; Dyachenko, L. N.; and Vinnikov, K. Ya. 1968: The Climatology of the Net Radiation of the Earth. Paper presented at Symposium on Radiation, Including Satellite Techniques (Bergen, Norway), August 22-28.

Lettau, H. 1954: A Study of the Mass, Momentum, and Energy Budget of the Atmosphere. Archiv. Meteorol. Geophys. Bioklim. A, vol. 7, no. 1, pp. 133-157.

London, Julius 1957: A Study of the Atmospheric Heat Balance. AFCRC-TR-57-287, ASTIA no. 117227, Coll. Eng., New York Univ., July.

National Aeronautics and Space Administration 1961: Juno II Summary Project Report. Vol. I, Explorer VII Satellite. NASA TN D-608.

National Aeronautics and Space Administration 1963: TIROS 4 Radiation Data Catalog and Users' Manual. NASA TM X-72526.

Raschke, E.; and Bandeen, W. R. 1970: The Radiation Balance of the Planet Earth From Radiation Measurements of the Satellite Nimbus II. J. Appl. Meteorol., vol. 9, no. 2, pp. 215-238.

Raschke, E.; and Pasternak, M. 1968: The Global Radiation Balance of the Earth Atmosphere System Obtained From Radiation Data of the Meteorological Satellite Nimbus II. Space Research, VIII, North Holland Publ. Co., Amsterdam.

Raschke, Ehrhard; Vonder Haar, Thomas H.; Bandeen, William R.; and Pasternak, Musa 1973a: The Annual Radiation Balance of the Earth-Atmosphere System During 1969-70 From Nimbus 3 Measurements. J. Atmos. Sci., vol. 30, no. 3, pp. 341-364.

Raschke, Ehrhard; Vonder Haar, Thomas H.; Pasternak, Musa; and Bandeen, William R. 1973b: The Radiation Balance of the Earth-Atmosphere System From Nimbus 3 Radiation Measurements. NASA TN D-7249.

Simpson, G. C. 1928: Further Studies in Terrestrial Radiation. Mem. Roy. Meteorol. Soc., vol. 3, no. 21, pp. 1-26.

Vonder Haar, Thomas H. 1968: Variations of the Earth's Radiation Budget. Ph. D. Thesis, Univ. of Wisconsin, Madison.

Wark, D. Q.; Yamamoto, G.; and Leinesch, J. H. 1962: Methods of Estimating Infrared Flux and Surface Temperatures From Meteorological Satellites. J. Atmos. Sci., vol. 19, no. 5, pp. 369-384.

Willson, R. C.; Duncan, C. H.; and Geist, J. 1980: Direct Measurement of Solar Luminosity Variation. Science, vol. 207, no. 11, pp. 177-179.

Willson, R. C.; Gulkis, S.; Janssen, M.; Hudson, H. S.; and Chapman, G. A. 1981: Observations of Solar Irradiance Variability. Science, vol. 211, no. 4483, pp. 701-702.

TABLE I.- MEASUREMENTS OF SOLAR CONSTANT

Reference	W m^{-2}	ly min^{-1}
Abbott (1922)	1352	1.94
Johnson (1954)	1395	2.00
Vonder Haar (1968) (wide-field satellite sensors)	1388	1.99
Drummond et al. (1967) (aircraft)	1360	1.95
Willson et al. (1980)		
June 1976	1368	1.96
November 1978	1373	1.97
Hickey et al. (1980) (Nimbus 7 ERB)	1376	1.97
Willson et al. (1981) (Solar Maximum Mission)	1368	1.96

TABLE II.- EVOLUTION OF PLANETARY ALBEDO

Reference	Albedo, percent
Dines (1917)	50
Aldrich (1919)	43
Simpson (1928)	43
Baur and Phillipps (1934)	41.5
Fritz (1949)	34.7
Houghton (1954)	34
Lettau (1954)	34
London (1957)	35
Angstrom (1962)	33-38
House (1965)	35
Bandeen et al. (1965) (TIROS 7)	32
Raschke and Pasternak (1968) (Nimbus 2)	30
Vonder Haar (1968)	29
Raschke et al. (1973a, b) (Nimbus 3)	28.4

ORIGINAL PAGE IS
OF POOR QUALITY

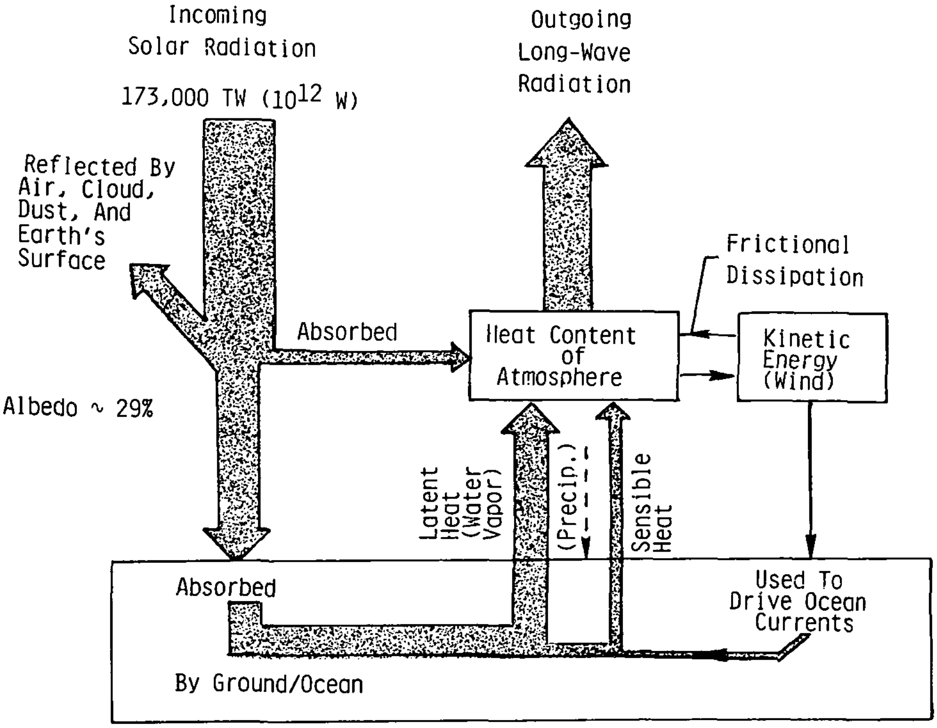

Figure 1.- Earth-atmosphere heat engine.

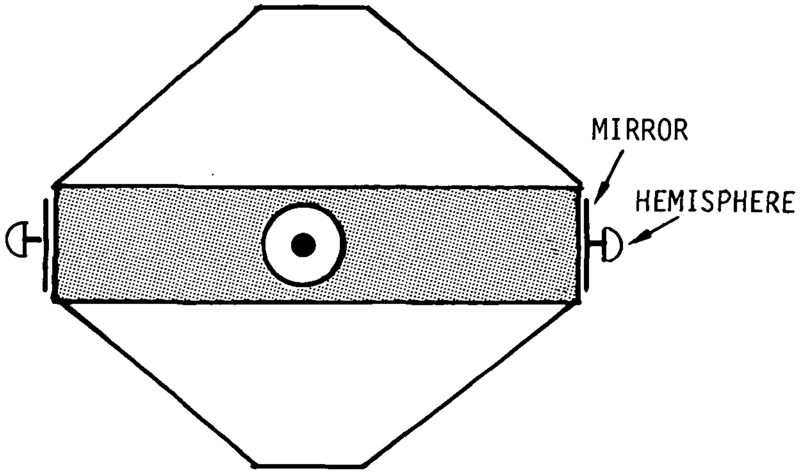

Figure 2.- Explorer 7 satellite hemispherical sensors.

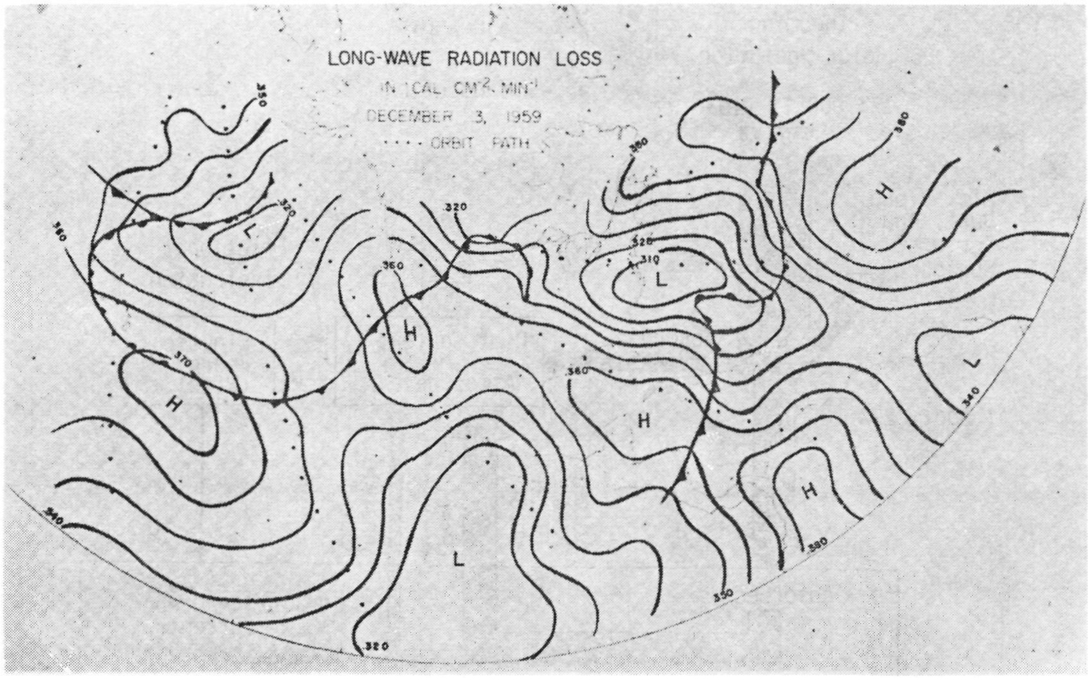

Figure 3.- Explorer 7 thermal radiation balance experiment. (From National Aeronautics and Space Administration, 1961.)

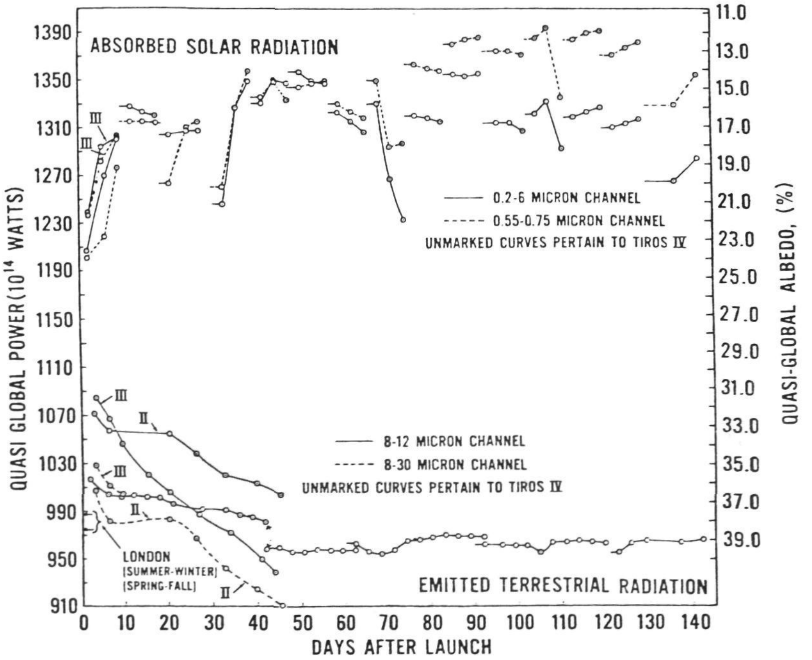

Figure 4.- Quasi-global ($55^{o}N$ to $55^{o}S$) radiative energy budget as inferred from TIROS 2, 3, and 4 measurements. (From National Aeronautics and Space Administration, 1963.)

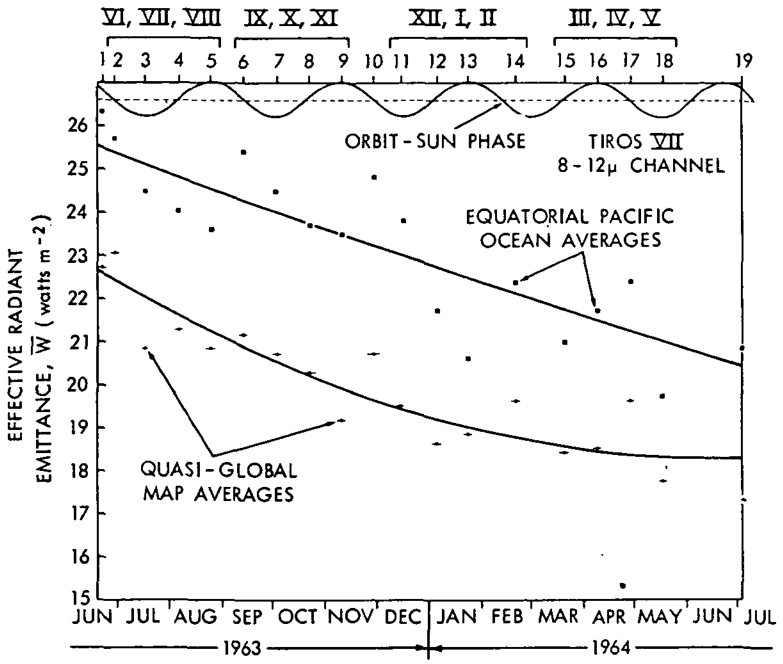

(a) Emitted radiation.

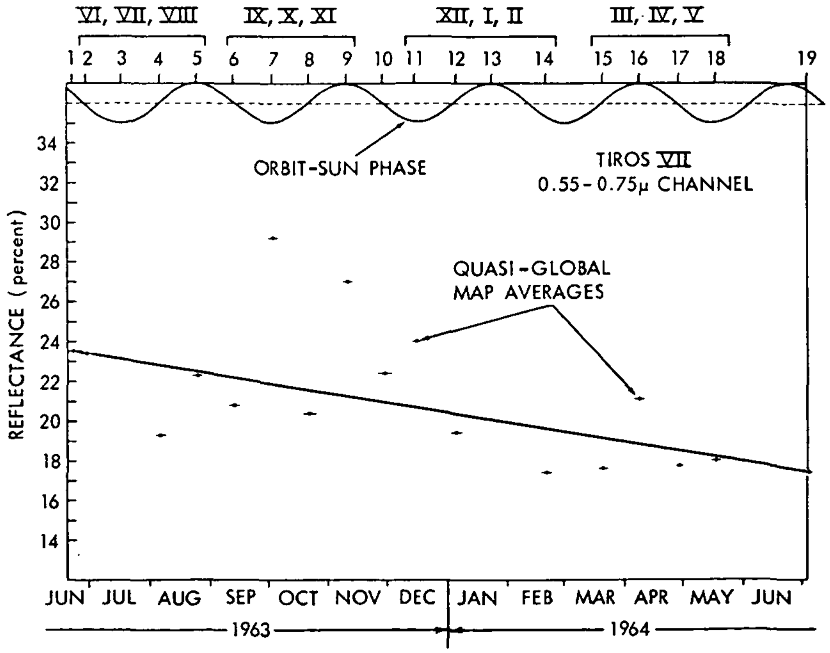

(b) Reflected radiation.

Figure 5.- Radiation measurements from TIROS 7. (From Bandeen et al., 1965.)

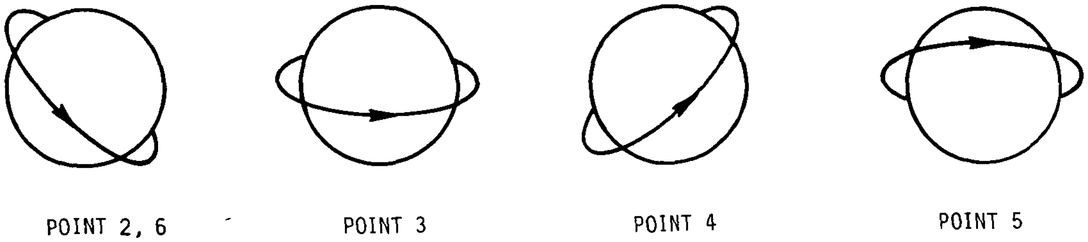

Figure 6.- Satellite orbit geometries correlated with numbered points on sinusoidal curve at top of figures 5(a) and (b). Synodic period is 76 days.

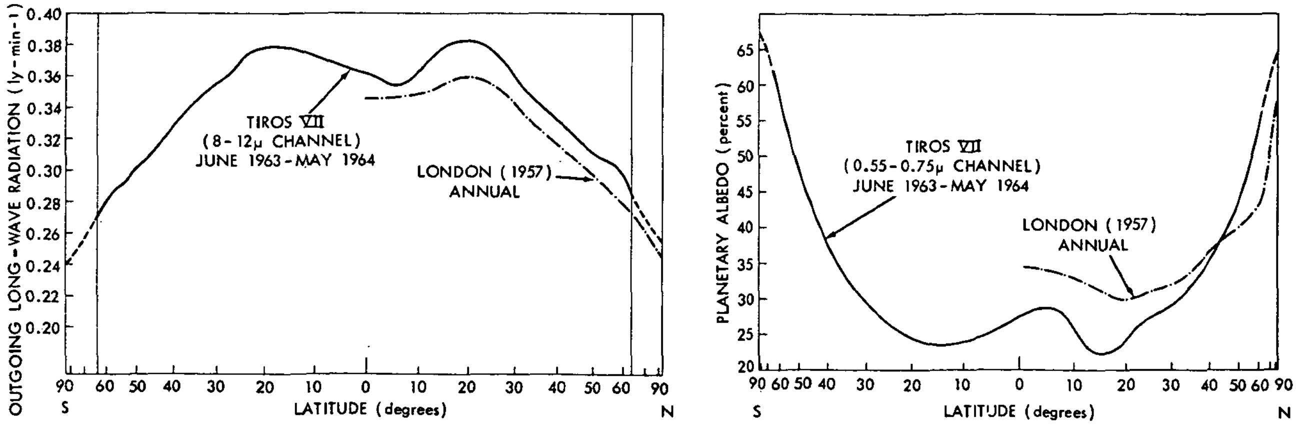

(a) Longwave radiation.

(b) Albedo.

Figure 7.- Annual mean albedo and outgoing longwave radiation. (Note: albedo above 55 percent was extrapolated using the slope obtained from London's (1957) Northern Hemisphere analysis.) (From Bandeen et al., 1965.)

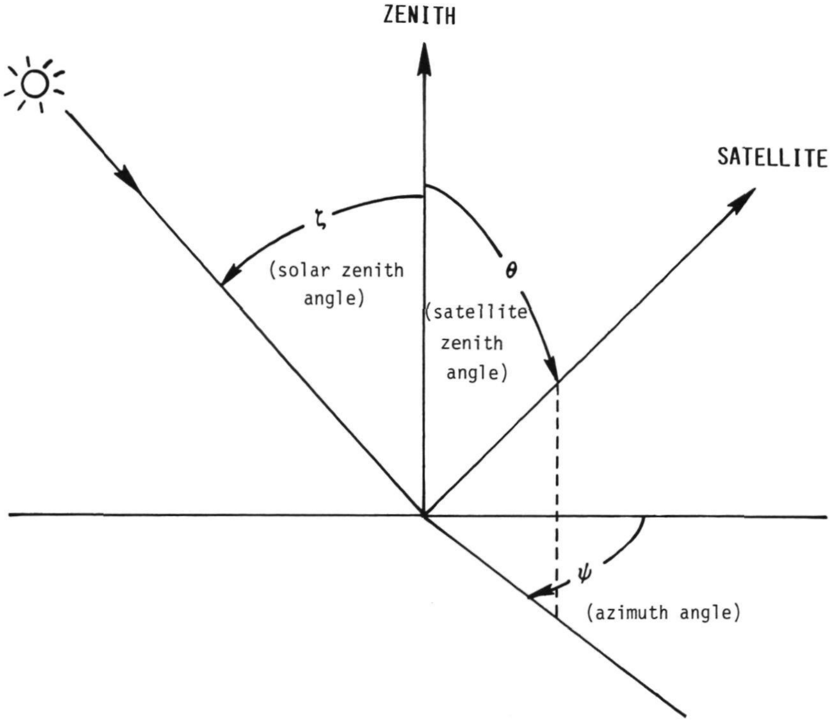

Figure 8.- Angular convention used in analyzing MRIR data from Nimbus 2 (launched May 15, 1966) and Nimbus 3 (launched April 14, 1969).

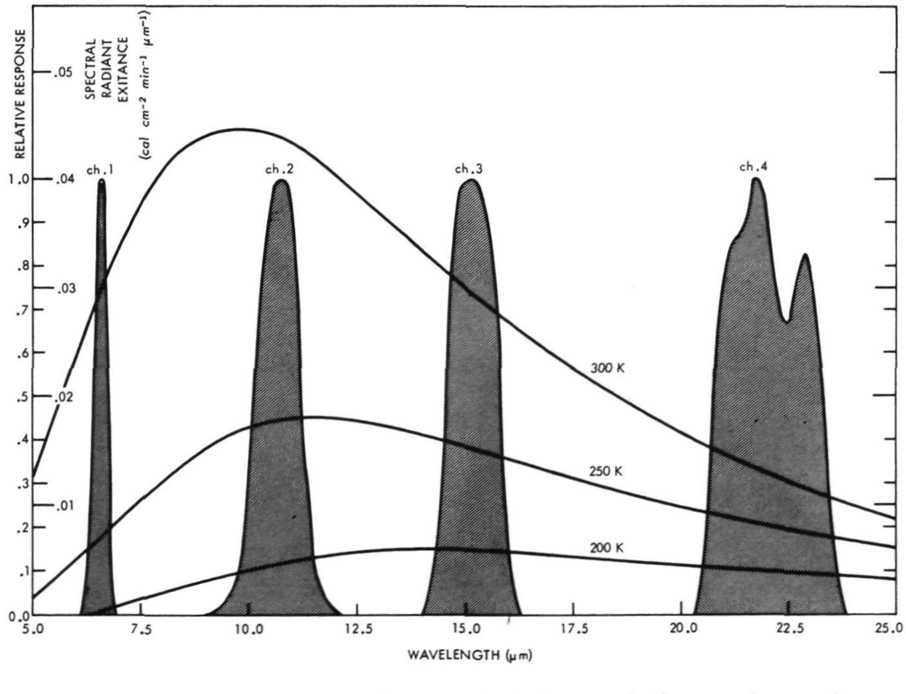

Figure 9.- Approximate spectral sensitivity of four channels on modified MRIR and spectral radiant exitance of a blackbody at temperatures of 200, 250, and 300 K. (From Raschke et al., 1973.)

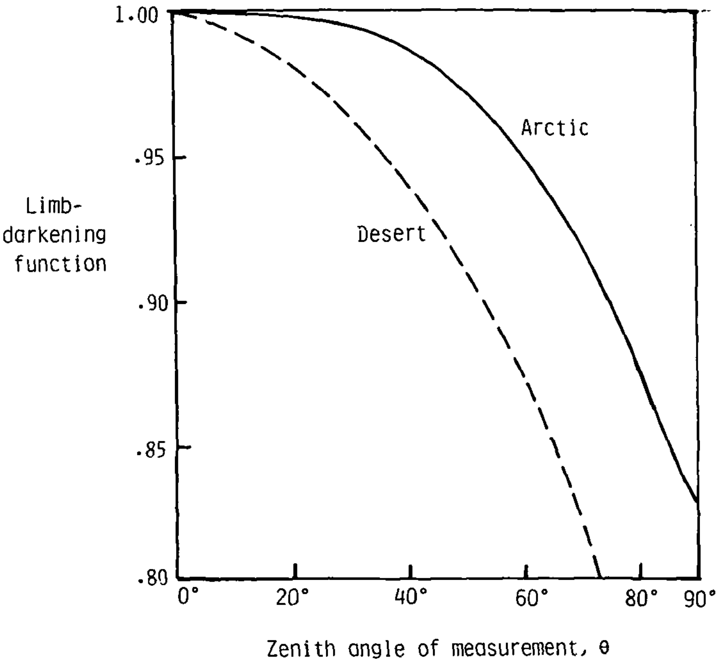

Figure 10.- Longwave radiation limb-darkening function.

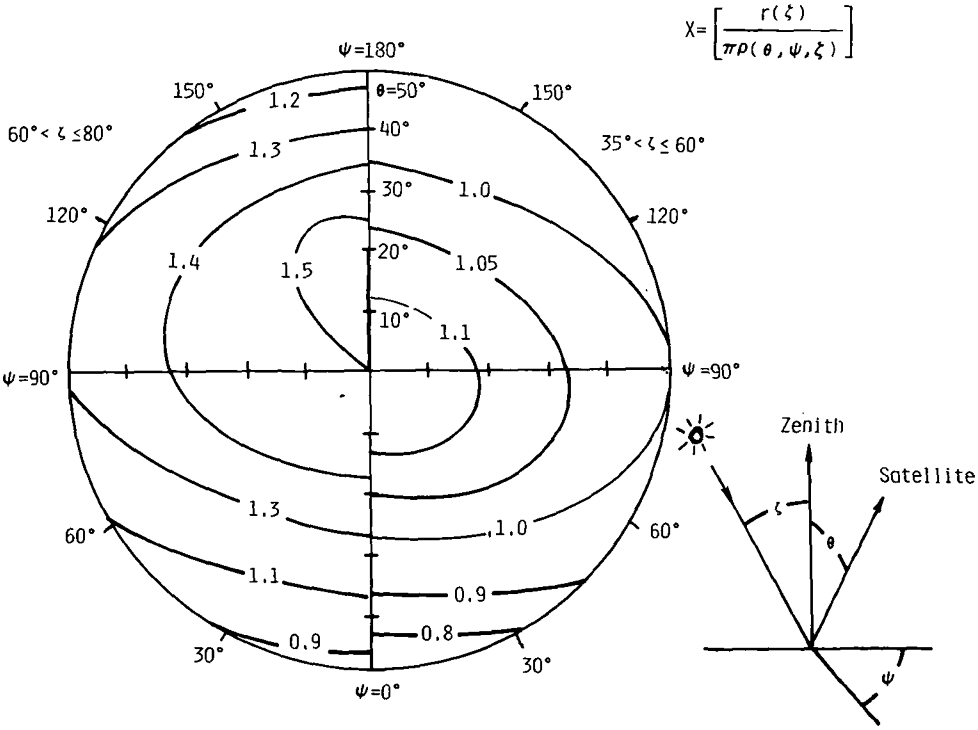

Figure 11.- Shortwave radiation model.

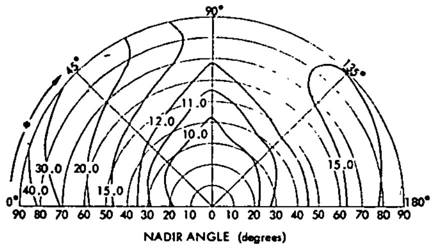

(a) Visible (0.55 to 0.85 μm).

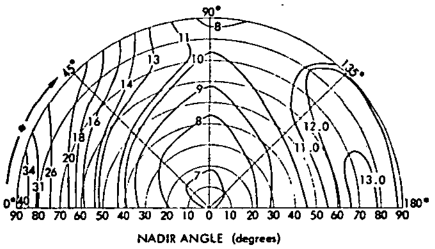

(b) Near-infrared (0.2 to 4.0 μm).

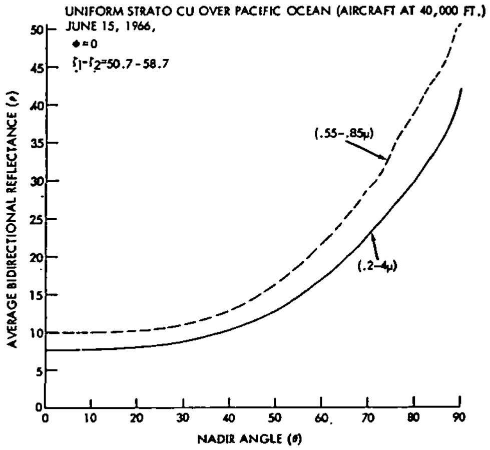

(c) Influence of nadir angle on bidirectional reflectance.

Figure 12.- Bidirectional reflectances measured by MRIR on NASA Convair 990 (altitude = 40 000 ft).

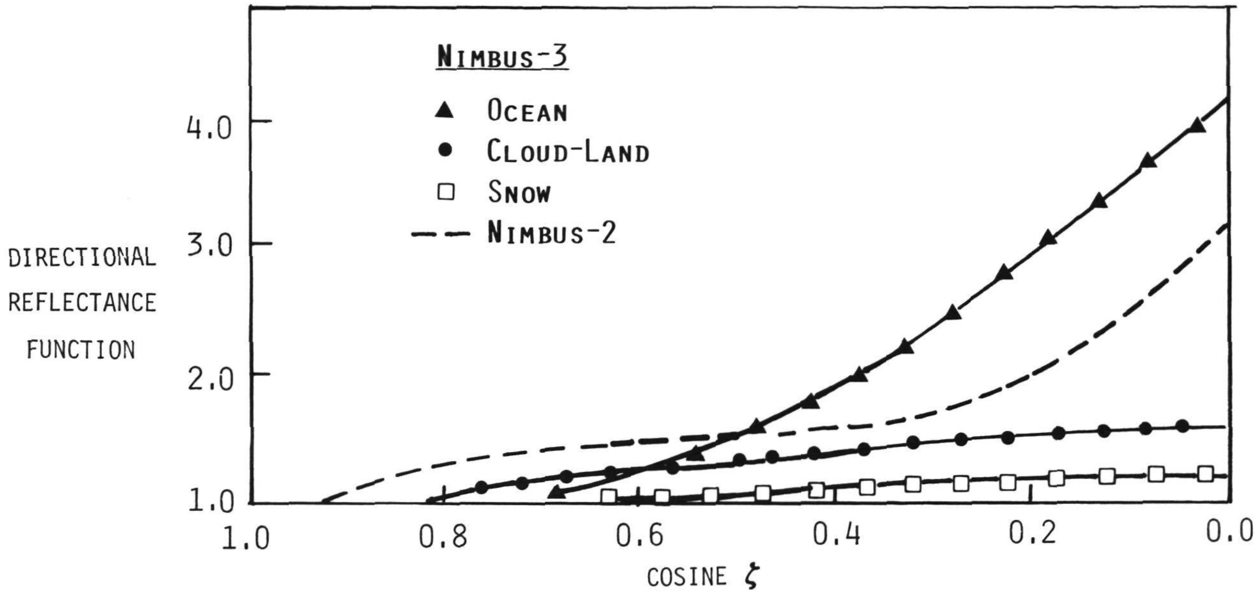

Figure 13.- Directional reflectance models used in Nimbus 3 data analysis.

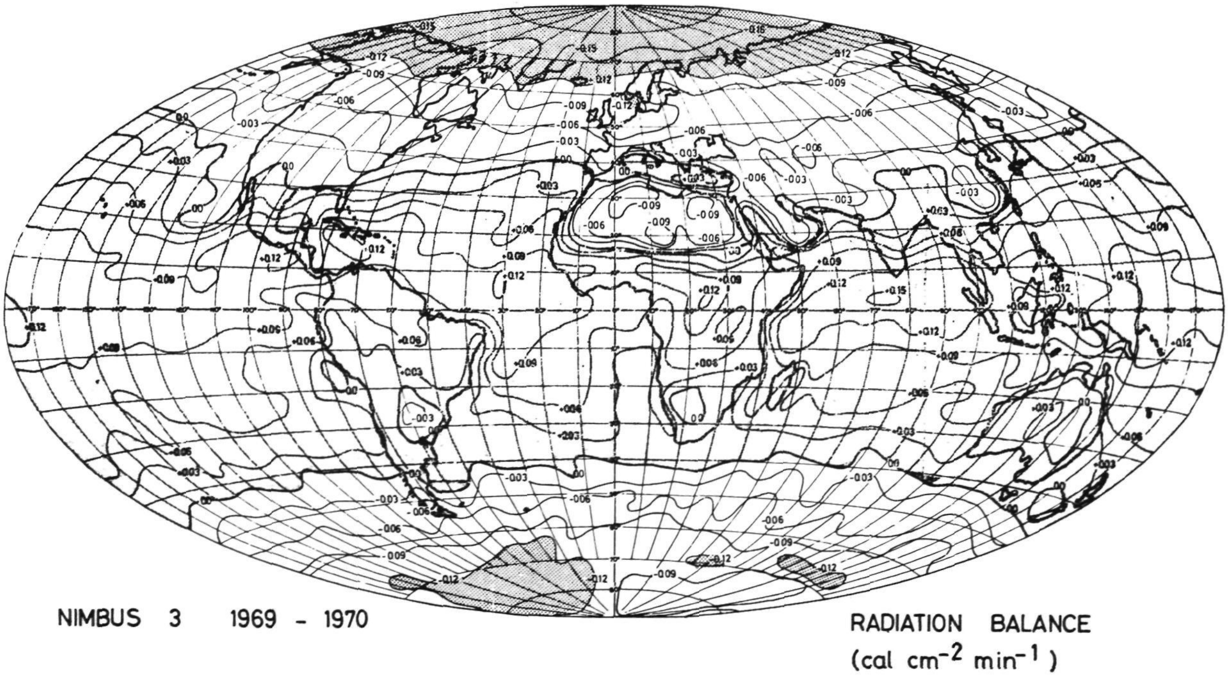

Figure 14.- Global radiation balance as derived from Nimbus 3 measurements. (From Raschke et al., 1973.)

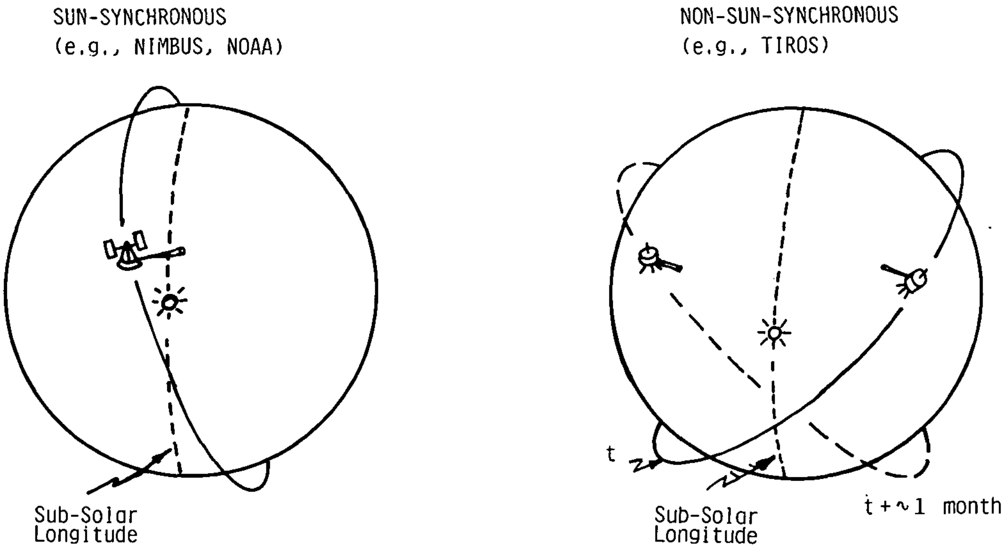

Always passes at Same Local Time

Passes At Different Local Times From Day-To-Day

Figure 15.- Typical meteorological satellite orbits.

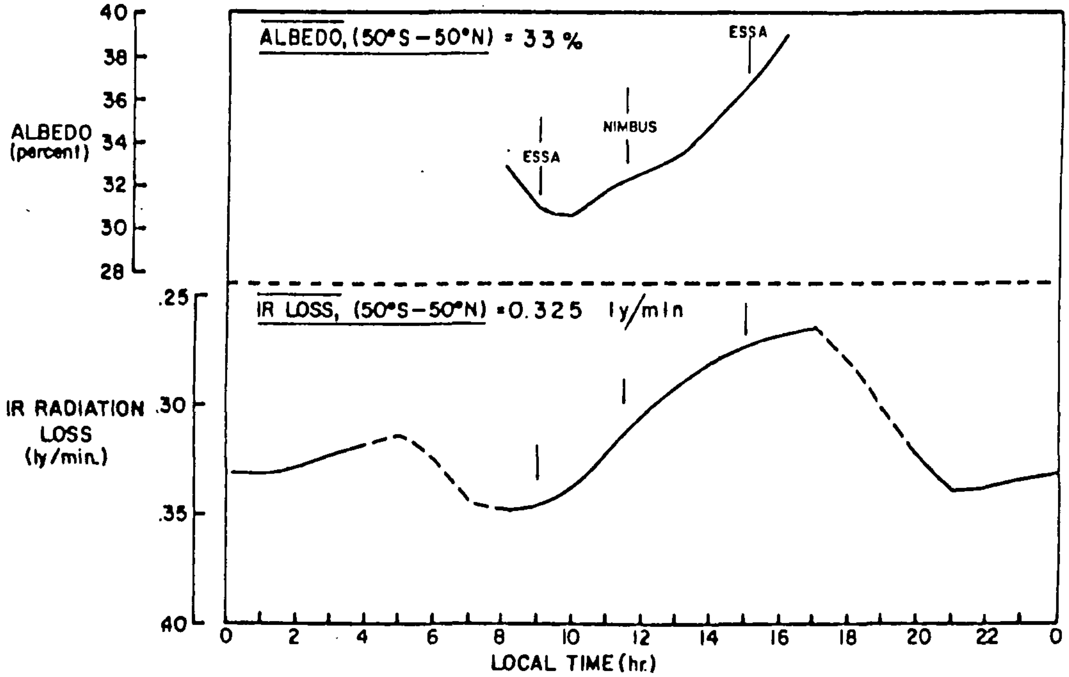

Figure 16.- Diurnal variation of planetary albedo and outgoing longwave radiation based on TIROS 4 measurements. (From Vonder Haar, 1968.)

N82 33322

D2

INCREASED ATMOSPHERIC CARBON DIOXIDE AND CLIMATE FEEDBACK MECHANISMS

Robert D. Cess
Laboratory for Planetary Atmospheres Research
State University of New York
Stony Brook, New York

INTRODUCTION

As a consequence of fossil fuel burning, the atmospheric concentration of carbon dioxide has increased from 314 ppm in 1958, when detailed measurements of this quantity began, to a present value of 335 ppm; and it is estimated that during the next century, the CO_2 concentration will double relative to its assumed preindustrial value of 290 ppm. Since CO_2 is an infrared-active gas, increases in its atmospheric concentration would lead to a larger infrared opacity for the atmosphere which, by normal logic, would result in a warmer Earth. A number of modeling endeavors suggest a 2° to $4^\circ C$ increase in global mean surface temperature with doubling of the CO_2 concentration.

But such estimates of CO_2-induced warming are highly uncertain because of a lack of knowledge of climate feedback mechanisms. Interactive influences upon the solar and infrared opacities of the Earth-atmosphere system can either amplify or damp a climate-forcing mechanism such as increasing CO_2. This paper discusses a number of such climate feedback mechanisms.

CLIMATE SENSITIVITY

A convenient measure of the sensitivity of the global climate, for the purpose of feedback comparisons, is the sensitivity parameter $\beta = S_o(dT_S/dS)$ as originally introduced by Schneider and Mass (1975), where T_S is the global mean surface temperature and S the solar constant, with S_o denoting the current solar constant. Thus β is a measure of the sensitivity of global climate to a change in solar constant. From a global energy balance,

$$\frac{S}{4}(1 - \alpha_p) = F \tag{1}$$

where α_p and F denote the global albedo and outgoing infrared flux, respectively. It thus follows from equation (1) that

$$\beta = S_o \frac{dT_S}{dS} = \frac{F}{dF/dT_S + (S_o/4)(d\alpha_p/dT_S)} \tag{2}$$

The absence of climate-induced changes in either infrared opacity or albedo of the Earth-atmosphere system, which comprise the feedback coupling mechanisms of present concern, results in $d\alpha_p/dT_S = 0$, while dF/dT_S is evaluated as follows. Let $F = \varepsilon\sigma T_S{}^4$, where σ is the Stefan-Boltzmann constant; then for $F = 233\ \mathrm{W/m^2}$ and $T_S = 288\ \mathrm{K}$, $\varepsilon = 0.6$ is the emissivity of the Earth-atmosphere system. Thus $dF/dT_S = 3.3$, and from equation (2),

$$\beta = 70^{\circ}\mathrm{C} \tag{3}$$

so that a 1-percent change in S would produce a 0.7°C change in T_S. The above constitutes a reference value for the sensitivity parameter, in that it contains the basic temperature-radiation negative feedback but none of the possible feedback associated with variable optical properties of the Earth-atmosphere system.

Change in water vapor amount is a positive atmospheric feedback mechanism since an increase in surface temperature increases the water vapor content of the atmosphere, which increases the atmospheric infrared opacity with a subsequent further increase in surface temperature. Most studies are in agreement that this feedback roughly doubles climate sensitivity. For example, Cess (1976) has empirically suggested that $dF/dT_S = 1.6$ for which $\beta = 145^{\circ}\mathrm{C}$, essentially twice that of equation (3).

An additional positive mechanism is ice-albedo feedback. A warmer planet results in less snow and ice cover and thus in a lower albedo and in turn a yet warmer planet. Annual models (Lian and Cess, 1977; Manabe and Wetherald, 1975) suggest that this mechanism increases β from 145°C to 185°C, although a recent seasonal model (Wetherald and Manabe, 1981) indicates that an annually averaged seasonal model is more stable than the analogous annual model; this subject is discussed further in a later section.

In addition to water vapor and ice-albedo feedbacks, there are numerous other possible feedback mechanisms, perhaps the most controversial being cloudiness-radiation feedback. In the following section, some aspects of this mechanism are discussed.

CLOUDINESS-RADIATION FEEDBACK

Cloudiness-radiation feedback contains two uncertain aspects. The first is the question of whether or not cloud amounts, heights, optical properties, and structure will significantly change in response to CO_2-induced warming. If such changes are not significant, then obviously there will be no cloudiness-radiation feedback. But if cloud amounts and heights are influenced by climatic change, then both the solar and the infrared components of the radiation budget will be altered; it is the relative role of these radiation changes that constitutes the second uncertain aspect of the problem.

For example, if cloud amounts decrease, then since clouds are generally brighter than clear-sky regions, the Earth-atmosphere system albedo would be reduced, resulting in increased solar heating of the system. But decreased cloudiness would also reduce the infrared opacity of the atmosphere, resulting in increased infrared cooling of the Earth-atmosphere system. Thus the separate solar and infrared modifications act in opposite directions. A corresponding change in effective cloud height would further modify the outgoing infrared radiation: a reduction in effective cloud height, for example, would enhance infrared cooling since the lower (and hence warmer) clouds would radiate more energy to space.

Employing a general circulation model which predicts both cloud amount and cloud height, Manabe and Wetherald (1980) have suggested that equatorward of 50° latitude, doubling and quadrupling atmospheric CO_2 would reduce net cloud amount and effective cloud height because of CO_2-induced warming; both effects increase the outgoing infrared radiation. But this increase is nearly compensated in the model by the corresponding increase in absorbed solar radiation due to reduced cloud amount. Poleward of 50°, they found an increase in net cloud amount without any substantial change in effective cloud height. But the absence of the latter, which contributed to the near solar-infrared compensation at lower altitudes, is in effect offset by reduced insolation at higher latitudes, so that again the model predicts near compensation between absorbed solar and outgoing infrared radiation.

Manabe and Wetherald (1980) emphasize, "In view of the uncertainty in the values of the optical cloud parameters and the crudeness of the cloud prediction scheme incorporated into the model, it is premature to conclude that the change of cloud cover has little effect on the sensitivity of climate." There have, in fact, been suggestions (Petukhov et al., 1976; Hunt, 1981; Wang et al., 1981; Charlock, 1981) that changes in cloud optical properties associated with climatic change might be important in modeling cloudiness-radiation feedback.

Alternate approaches to estimating the relative solar-infrared components of cloudiness-radiation feedback involve empirical studies using Earth radiation budget data. In one such approach, Cess (1976) has suggested solar-infrared compensation, whereas Ohring and Clapp (1980) and Hartmann and Short (1980) have suggested that the solar component dominates the infrared component by roughly a factor of 2. Cess employed the satellite data compilation of Ellis and Vonder Haar (1976), while the other two studies utilized radiation budget data derived from scanning radiometer measurements by the National Oceanic and Atmospheric Administration (NOAA). Recently Cess et al. (1982) have reviewed these studies and illustrate that such empirical conclusions depend substantially upon the satellite data set which is employed. They further suggest that the conclusions of solar dominance (Ohring and Clapp, 1980; Hartmann and Short, 1980) might be attributable to the NOAA albedo values at 0900 local time together with the NOAA data being derived from narrow spectral measurements.

Clearly the empirical approaches comprise an important means of studying the cloudiness-radiation feedback problem. The approach by Ohring and Clapp (1980) is particularly attractive. They have employed interannual variability in regional monthly mean radiation data, from which they estimate the relative solar-infrared cloudiness feedback components by attributing this variability to interannual variability in cloudiness. It would seem most worthwhile to reexamine their conclusions by employing radiation budget data which do not suffer the possible deficiencies noted above.

CLIMATE CHANGE PREDICTIONS

An obvious test of a climate model is its ability to reproduce seasonal climatic change. Recently Ramanathan et al. (1979) have formulated a seasonal energy balance climate model; the seasonal change in surface air temperature predicted by this model is compared with observations in figure 1. The extremely good agreement between predicted and observed surface air temperatures is due in part to tuning of the model, since the latitudinal heat capacity of the Earth-atmosphere system was tuned to the observed surface air temperature. Nevertheless, tuning a single parameter results in both phase and amplitude being correct.

Reproducing the observed seasonal cycle does not, however, ensure that the model can correctly predict a perturbed climate. For example, the energy balance model does not account for changes in the heat capacity of the Earth-atmosphere system due to changes in the thickness and extent of sea ice. But Wetherald and Manabe (1981) have indicated that such changes can significantly influence the high-latitude seasonal response of surface temperature to enhanced atmospheric CO_2. Furthermore, Wetherald and Manabe find that their seasonal model predicts significantly less sensitivity to increased atmospheric CO_2 than does the corresponding annual model, and this also appears to be related to changes in sea ice thickness and extent.

To illustrate the dependence of climate sensitivity upon high-latitude Earth-atmosphere heat capacity changes associated with sea ice changes, we have changed arbitrarily high-latitude heat capacity within the seasonal energy balance model described by Ramanathan et al. (1979). This change is summarized in table I for a doubling of atmospheric CO_2. Here R is the latitudinal heat capacity of the Earth-atmosphere system, with the values for present CO_2 being those obtained by tuning to the present climate. For doubled CO_2, we have arbitrarily increased R at the high latitudes to crudely mimic the fact that a warmer planet would result in a reduction in both thickness and extent of sea ice, and thus allow more efficient interaction between atmosphere and ocean with a corresponding increase in the heat capacity of the Earth-atmosphere system at these latitudes.

Figure 2 illustrates the seasonal increase in surface air temperature in several high-latitude regions for doubled CO_2 concentrations, both with and without the change in R listed in table I. Clearly our arbitrary change in R is not realistic, since at 85° N, it reduced annual mean surface air temperature. But the point of figure 2 is obvious: the perturbed seasonal cycle at high latitudes is highly sensitive to climate-induced changes in R. Moreover, the qualitative features shown in figure 2 are consistent with the model results of Wetherald and Manabe (1981), in that maximum high-latitude warming occurs during the winter. This is also consistent with an interesting empirical study by Vinnikov and Groysman (1979). Employing observed climatic change over roughly the past century, they have evaluated $\Delta T_S/\Delta \bar{T}_S$ as a function of season and latitude, where ΔT_S is the change in seasonal surface temperature at a given latitude and $\Delta \bar{T}_S$ is the corresponding change in global mean surface temperature. Their results are summarized in figure 3, from which it is again shown that maximum sensitivity occurs during the winter.

Aside from zonal seasonal sensitivity, recall that Wetherald and Manabe (1981) additionally found that global warming due to increased atmospheric CO_2 was reduced when they employed a seasonal rather than an annual climate model. The present energy balance model suggests that this reduction is associated with the influence of the change in R upon the seasonal cycle. Employing the energy balance model in both annual and seasonal modes, we obtain the following increases in global mean surface temperature for a doubling of atmospheric CO_2 concentration:

$$\Delta\bar{T}_S = 3.3^{\circ}C \quad \text{for annual model}$$

$$\Delta\bar{T}_S = 3.3^{\circ}C \quad \text{for seasonal model with fixed } R$$

$$\Delta\bar{T}_S = 2.7^{\circ}C \quad \text{for seasonal model with variable } R$$

The point here, of course, is that the seasonal model produces reduced global warming only if the heat capacity is allowed to vary.

In addition to warming as a consequence of CO_2 additions to the atmosphere, fossil fuel burning can alter chemical composition in other ways through interactive atmospheric chemistry; this is discussed in the following section.

INTERACTIVE ATMOSPHERIC CHEMISTRY

Recent atmospheric chemical models indicate that as a consequence of increasing emissions of CO, NO_x, and CH_4 due to fossil fuel burning, tropospheric ozone and methane concentrations might significantly increase in the near future (Logan et al., 1978; Hameed et al., 1979). This increase in tropospheric O_3 and CH_4 is a consequence of interactive chemical processes involving species derived from CH_4, H_2O, NO_x, and O_2. Although only about 10 percent of atmospheric ozone is located within the troposphere, this ozone contributes roughly half of the total ozone greenhouse effect because of pressure broadening of the 9.6-µm band (Ramanathan and Dickinson, 1979). Thus an increase in tropospheric ozone, in conjunction with a corresponding increase in tropospheric methane, could possibly produce a significant climatic effect, augmenting the global warming due to increasing atmospheric CO_2, which is also a consequence of fossil fuel burning.

An additional interactive effect is that a warmer climate would, by itself, influence atmospheric chemical composition, since increased atmospheric water vapor, resulting from a warmer climate, would produce increased OH, an important constituent in chemical reactions which govern the amounts of tropospheric ozone and methane. Thus, not only can changes in atmospheric composition alter the climate, but also climatic change can alter atmospheric composition through interactive chemistry. This then constitutes a climate feedback mechanism.

To crudely appraise whether or not increased emissions of CO, NO_x, and CH_4, resulting from increased fossil fuel consumption, could significantly augment the related CO_2 warming, we have constructed a coupled climate-chemical model for the purpose of investigating the sensitivity of the global climate to changes in CO, NO_x, and CH_4 emissions. This model is described as follows.

The climate-chemical model is a combination of the energy balance climate model described by Ramanathan et al. (1979) and an extended version of the tropospheric chemical model of Hameed et al. (1979). Both models employ latitude as the sole dimension. The climate model incorporates separately calculated changes in surface-troposphere radiative heating due to changes in atmospheric CO_2 and tropospheric O_3 and CH_4. The chemical model employs vertically averaged conditions, so that it predicts changes in the total tropospheric column abundance of O_3 and CH_4 as a function of latitude.

Figure 4 illustrates, in schematic form, the most important chemical processes resulting from changes in CO, CH_4, and NO_x emissions. An increase in CO emission will, for example, lead to a conversion of OH to HO_2. Since OH is the only known tropospheric sink for CH_4, this reduction in OH thus leads to an increase in tropospheric CH_4. In addition, the increased HO_2 converts NO to NO_2, with photodissociation of the latter producing odd oxygen which then combines with O_2 to increase the level of tropospheric O_3. Thus, increasing the emission of CO leads to increases in both CH_4 and O_3.

An increase in CH_4 emission does, of course, directly increase the concentration of CH_4. Moreover, the oxidation of CH_4 produces CO which, by the process just discussed, increases the concentration of O_3.

Increasing the emission of NO_x also leads to an increase in O_3 as a consequence of the NO_2 to O to O_3 process just discussed. In addition, photodissociation of O_3 produces $O(^1D)$ which reacts with H_2O to form OH; then the increased OH subsequently leads to a reduction in CH_4. So, although enhanced NO_x emission leads to increased tropospheric O_3, increased O_3 reduces the amount of tropospheric CH_4. Of course, the dependence of OH upon O_3 also modifies the increase in CH_4 due to increasing either CH_4 or CO emissions.

Changes in tropospheric O_3 and CH_4, through altering the infrared opacity of the troposphere, lead to climatic change, and this in turn influences the atmospheric composition through a secondary feedback loop as illustrated in figure 4. For example, an increase in both tropospheric CH_4 and O_3 would lead to warming of the Earth-tropospheric system, which in turn would increase tropospheric H_2O and, through the reaction with $O(^1D)$, lead to enhanced OH. This in turn would decrease the CH_4 concentration, as well as the concentration of CO, and subsequently of O_3. Thus the climate-chemical interaction results in a negative feedback mechanism, partially, but not totally, reducing the increased CH_4 and O_3 which produced climate change in the first place. Obviously there are numerous interactive processes at work concerning the influence of chemical composition change upon climate.

To model the coupled climatic change, the CO_2-climate model of Ramanathan et al. (1979) is employed. In that model, climatic change was induced by reducing the outgoing latitudinal infrared flux by the amount $\Delta F(CO_2)$ corresponding to a specified increase in atmospheric CO_2. The quantity $\Delta F(CO_2)$ was determined from a separate radiation calculation. We use the same procedure in this study, with $\Delta F(CO_2)$ replaced by

$$\Delta F = \Delta F(CO_2) + \Delta F(O_3) + \Delta F(CH_4) \tag{4}$$

The calculations of $\Delta F(O_3)$ and $\Delta F(CH_4)$ account for the increase in infrared opacity of the troposphere due to the fundamental vibration-rotation bands of O_3(9.6 µm) and CH_4(7.8 µm). Ultraviolet (UV) absorption by O_3 within the troposphere has been neglected, since most of the UV is absorbed within the stratosphere. As in the comparable CO_2 calculation, overlap by water vapor absorption is included as well as the influence of clouds. Illustrative results for $\Delta F(O_3)$ and $\Delta F(CH_4)$, corresponding to a doubling of the present atmospheric concentrations of both species, are shown in figure 5.

It should be emphasized that the present climate-chemical model does not include an interactive stratosphere. Since the stratosphere acts as the primary source of tropospheric O_3, we would not anticipate changes in tropospheric O_3 to significantly influence the stratosphere. But just the reverse is the case for CH_4: tropospheric methane is transported into the stratosphere, so that changes in tropospheric CH_4 should induce stratospheric change.

Although carbon-cycle models exist for the purpose of estimating future atmospheric CO_2 concentrations, it is a far more hazardous endeavor to attempt to predict future CO, NO_x, and CH_4 emissions. Table II lists estimated anthropogenic and natural emissions of these quantities for the entire globe in 1976. Except for major depressions and wars, the annual increase in fossil fuel consumption has been 4.3 percent over the past century (Rotty, 1978). If this growth rate continues, fossil fuel consumption will increase by a factor of 8 in 2025 relative to 1976. But this by no means implies that anthropogenic emissions of CO, NO_x, and CH_4 will increase by the same factor.

Roughly 60 percent of the present anthropogenic CO emission stems from automobiles, and it is not likely that future petroleum consumption by automobiles will increase at the same rate as total fossil fuel consumption. On the other hand, conventional coal-fired power plants produce twice the amount of CO per unit of energy as do oil-fired plants, because of the combined effects of coal's lower heating value and its less complete combustion. Thus, in this context, conversion from oil to coal would by itself lead to increased anthropogenic CO emission. But technological improvements in the utilization of coal, such as coal gasification and the use of fluidized bed reactors in the burning of pulverized coal, could reduce future CO emission per unit of energy. In principle, of course, it is technologically possible to significantly reduce emissions of CO, NO_x, and CH_4; however, the global extent to which this might be done will surely be influenced by economic factors.

Future changes in natural emissions of CO, NO_x, and CH_4 are just as difficult to predict. Vegetation is the primary source of natural CO, while a substantial production of natural CH_4 stems from swamps and rice fields. Deforestation and the draining of swamps might decrease such emissions, although it has been suggested that deforestation may be leveling off as the result of more efficient use of existing agricultural land (Rotty, 1979). There is, in fact, some evidence for reforestation on the North American Continent, with forests replacing abandoned agricultural land which has proven to be only marginally productive. On the other hand, future CO_2 warming of the biosphere, coupled possibly with increased global precipitation and CO_2 fertilization, might tend to significantly increase natural CO and CH_4 emissions. In particular, the natural production of CH_4 is strongly temperature dependent.

Obviously the above discussion precludes any sort of quantitative estimate of future CO, NO_x, and CH_4 emissions. For the present purpose of illustrating nothing more than the sensitivity of global climate to changes in these emissions, we choose arbitrarily the following scenario:

1. The CO_2 content of the atmosphere increases by a factor of 1.7, consistent with Keeling and Bacastow's (1977) carbon-cycle model for 2025 relative to 1976.

2. Natural emissions of CO, NO_x, and CH_4 remain the same.

3. Anthropogenic emissions of these constituents increase by factors of 4 and 8.

4. Latitudinal emission distributions remain the same.

Results of the coupled climate-chemical model, for this hypothetical 1976 to 2025 scenario for the change in emissions, are listed in tables III and IV. In table III, no account has been taken of the previously discussed negative climate-chemical feedback resulting from the climate-induced change in atmospheric H_2O. Without changing the anthropogenic emissions of CO, NO_x, and CH_4, global temperature is increased by 2.63°C because of the increase in CO_2 concentrations by a factor of 1.7. Significantly greater warming occurs when CO, NO_x, and CH_4 emissions are increased.

The results of table IV incorporate the negative climate-chemical feedback. For no change in anthropogenic CO, NO_x, and CH_4 emissions, increasing OH resulting from global warming due to the CO_2 increase reduces tropospheric O_3 and CH_4 by factors of 0.9 and 0.85, respectively. The resulting climatic effect is rather minor, reducing the prior 2.63°C warming to 2.45°C. Although reduced somewhat from the corresponding values in table III, the increase in hemispheric warming due to increased emissions of CO, NO_x, and CH_4 is still significant. Relative to the global temperature increase of 2.63°C, which corresponds to no interactive chemistry, global warming is increased by 0.7°C and 1.4°C for increases in anthropogenic emissions by factors of 4 and 8, respectively.

We again emphasize that we chose the assumed 1976 to 2025 scenario regarding the increase in CO, NO_x, and CH_4 emissions solely for the purpose of illustrating how the climate responds to a change in such emissions. A realistic appraisal of future emissions of these constituents requires knowledge not only of future power-production technology on a global scale, but also of the manner in which the biosphere responds to future climatic change. It might well be that the latter is more significant than the former. The conclusion of this study is simply that the climate can respond to changes in the total emissions of CO, NO_x, and CH_4, as the result of the ensuing changes in tropospheric O_3 and CH_4.

REFERENCES

Cess, R. D.; Briegleb, B. P.; and Lian, M. S. 1982: Low-Latitude Cloudiness and Climate Feedback: Comparative Estimates From Satellite Data. J. Atmos. Sci., vol. 31, no. 1, pp. 53-59.

Cess, Robert D. 1976: Climate Change: An Appraisal of Atmospheric Feedback Mechanisms Employing Zonal Climatology. J. Atmos. Sci., vol. 33, no. 10, pp. 1831-1843.

Charlock, Thomas P. 1981: Cloud Optics as a Possible Stabilizing Factor in Climate Change. J. Atmos. Sci., vol. 38, no. 3, pp. 661-663.

Ellis, James S.; and Vonder Haar, Thomas H. 1976: Zonal Average Earth Radiation Budget Measurements From Satellites for Climate Studies. Atmospheric Science Paper 240 (NGR 06-002-102), Colorado State Univ. (Available as NASA CR-149319.)

Hameed, Sultan; Pinto, Joseph P.; and Stewart, Richard W. 1979: Sensitivity of the Predicted CO-OH-CH_4 Perturbation to Tropospheric NO_x Concentrations. J. Geophys. Res., vol. 84, no. C2, pp. 763-768.

Hartmann, Dennis L.; and Short, David A. 1980: On the Use of Earth Radiation Budget Statistics for Studies of Clouds and Climate. J. Atmos. Sci., vol. 37, no. 6, pp. 1233-1250.

Hunt, B. G. 1981: An Examination of Some Feedback Mechanisms in the Carbon Dioxide Climate Problem. Tellus, vol. 33, no. 1, pp. 78-88.

Keeling, Charles D.; and Bacastow, Robert B. 1977: Impact of Industrial Gases on Climate. Energy and Climate, Natl. Acad. Sci.-Natl. Res. Counc., pp. 72-95.

Lian, M. S.; and Cess, R. D. 1977: Energy Balance Climate Models: A Reappraisal of Ice-Albedo Feedback. J. Atmos. Sci., vol. 34, no. 7, pp. 1058-1062.

Logan, Jennifer A.; Prather, M. J.; Wofsy, S. C.; and McElroy, M. B. 1978: Atmospheric Chemistry: Response to Human Influence. Philos. Trans. R. Soc. London, ser. A, vol. 290, no. 1367, pp. 187-234.

Manabe, Syukuro; and Wetherald, Richard T. 1975: The Effects of Doubling the CO_2 Concentration on the Climate of a General Circulation Model. J. Atmos. Sci., vol. 32, no. 1, pp. 3-15.

Manabe, Syukuro; and Wetherald, Richard T. 1980: On the Distribution of Climate Change Resulting From an Increase in CO_2 Content of the Atmosphere. J. Atmos. Sci., vol. 37, no. 1, pp. 99-118.

Ohring, George; and Clapp, Philip 1980: The Effect of Changes in Cloud Amount on the Net Radiation at the Top of the Atmosphere. J. Atmos. Sci., vol. 37, no. 2, pp. 447-454.

Petukhov, V. K.; Feygelson, Ye. M.; and Manuylova, N. I. 1976: The Regulating Role of Clouds in the Heat Effects of Anthropogenic Aerosols and Carbon Dioxide. Atmos. & Oceanic Phys., vol. 11, no. 8, pp. 505-508.

Ramanathan, V.; and Dickinson, Robert E. 1979: The Role of Stratospheric Ozone in the Zonal and Seasonal Radiative Energy Balance of the Earth-Troposphere System. J. Atmos. Sci., vol. 36, no. 6, pp. 1084-1104.

Ramanathan, V.; Lian, M. S.; and Cess, R. D. 1979: Increased Atmospheric CO_2: Zonal and Seasonal Estimates of the Effect on the Radiation Energy Balance and Surface Temperature. J. Geophys. Res., vol. 84, no. C8, pp. 4949-4958.

Rotty, Ralph M. 1978: Atmospheric Carbon Dioxide - Possible Consequences of Future Fossil Fuel Use. Resour. & Energy, vol. 1, pp. 231-249.

Rotty, Ralph M. 1979: Uncertainties Associated With Global Effects of Atmospheric Carbon Dioxide. ORAU/IEA-79-6(0), Oak Ridge Assoc. Univ.

Schneider, Stephen M.; and Mass, Clifford 1975: Volcanic Dust, Sunspots, and Temperature Trends. Science, vol. 190, no. 4216, pp. 741-746.

Vinnikov, K. Ya.; and Groysman, P. Ya. 1979: Empiricheskaya Model' Sovpemennykh Izmeneniy Klimata (An Empirical Model of the Present-Day Climatic Changes). Meteorol. Gidrol., no. 3, pp. 25-36.

Wang, Wei-Chyung; Rossow, William B.; Yao, Mao-Sung; and Wolfson, Marilyn 1981: Climate Sensitivity of a One-Dimensional Radiative-Convective Model With Cloud Feedback. J. Atmos. Sci., vol. 38, no. 6, pp. 1167-1178.

Wetherald, Richard T.; and Manabe, Syukuro 1981: Influence of Seasonal Variation Upon the Sensitivity of a Model Climate. J. Geophy. Res., vol. 86, no. C2, pp. 1194-1204.

TABLE I.- VALUES OF HEAT CAPACITY AT HIGH LATITUDES FOR PRESENT AND DOUBLED ATMOSPHERIC CO_2 CONCENTRATIONS

CO_2 concentration	Heat capacity R, J/m^2-°C, at latitudes of -				
	45° N	55° N	65° N	75° N	85° N
Present[a]	33	30	18	22	15
Doubled	33	30	30	30	30

[a] R values in model tuned to present climate.

TABLE II.- ESTIMATED 1976 EMISSIONS OF CO, NO_x, AND CH_4

Constituent	Anthropogenic emission, metric tons/year	Natural emission, metric tons/year
CO	700×10^6	2730×10^6
NO_x	20	16
CH_4	95	380

TABLE III.- HYPOTHETICAL 1976 TO 2025 CLIMATE CHANGE SCENARIO WITHOUT CLIMATE-CHEMICAL FEEDBACK

Anthropogenic emissions of CO, NO_x, and CH_4 increased by factors of -	Resulting factor increases in -		ΔT_S, °C
	O_3	CH_4	
0	1.00	1.00	2.63
4	1.68	1.92	3.57
8	2.29	3.62	4.42

TABLE IV.- HYPOTHETICAL 1976 TO 2025 CLIMATE CHANGE SCENARIO WITH CLIMATE-CHEMICAL FEEDBACK

Anthropogenic emissions of CO, NO_x, and CH_4 increased by factors of -	Resulting factor increases in -		ΔT_S, °C
	O_3	CH_4	
0	0.90	0.85	2.45
4	1.50	1.53	3.28
8	2.00	2.68	4.00

ORIGINAL PAGE IS
OF POOR QUALITY

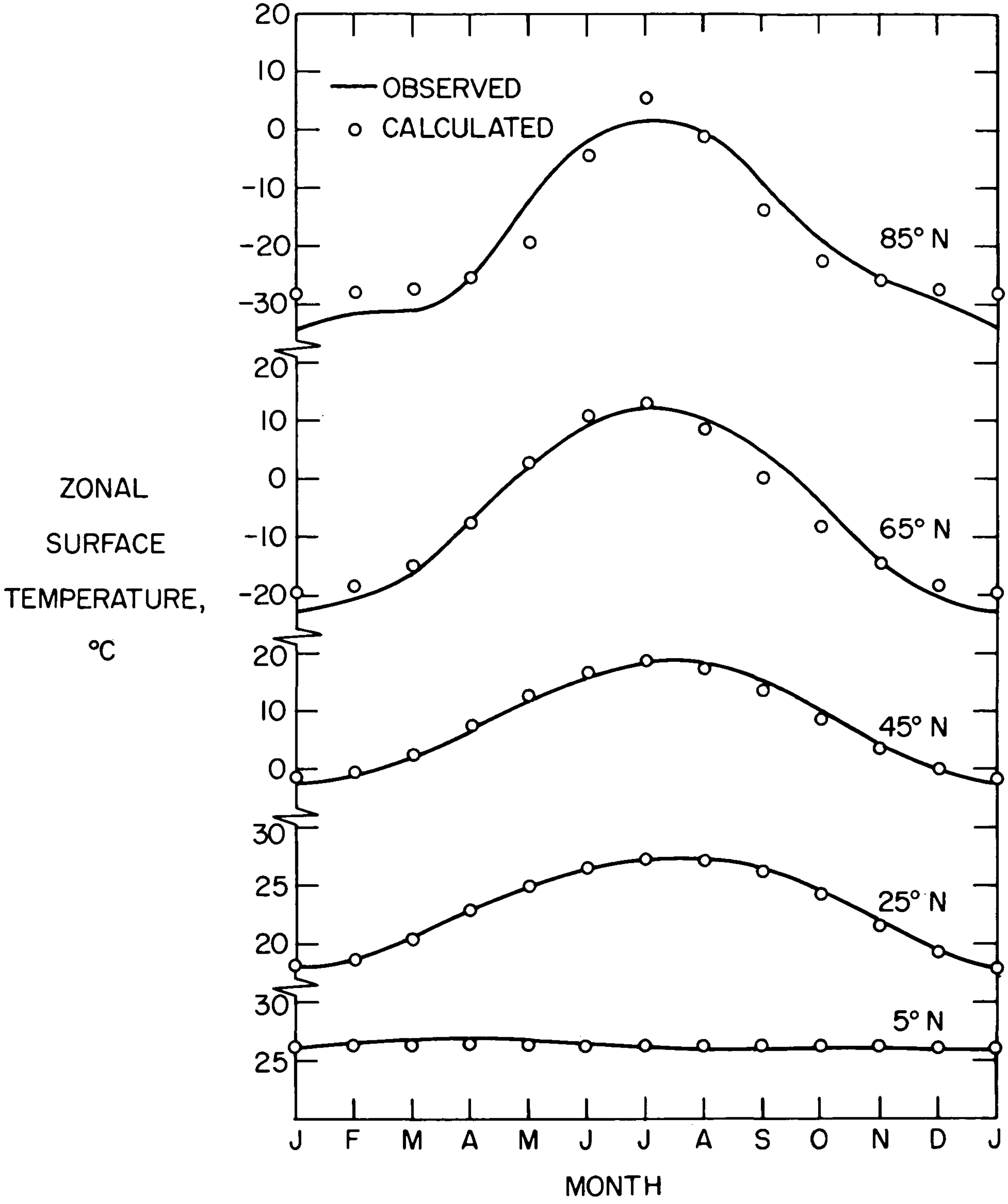

Figure 1.- Comparison between observed and calculated seasonal zonal surface temperatures.

ORIGINAL PAGE IS
OF POOR QUALITY

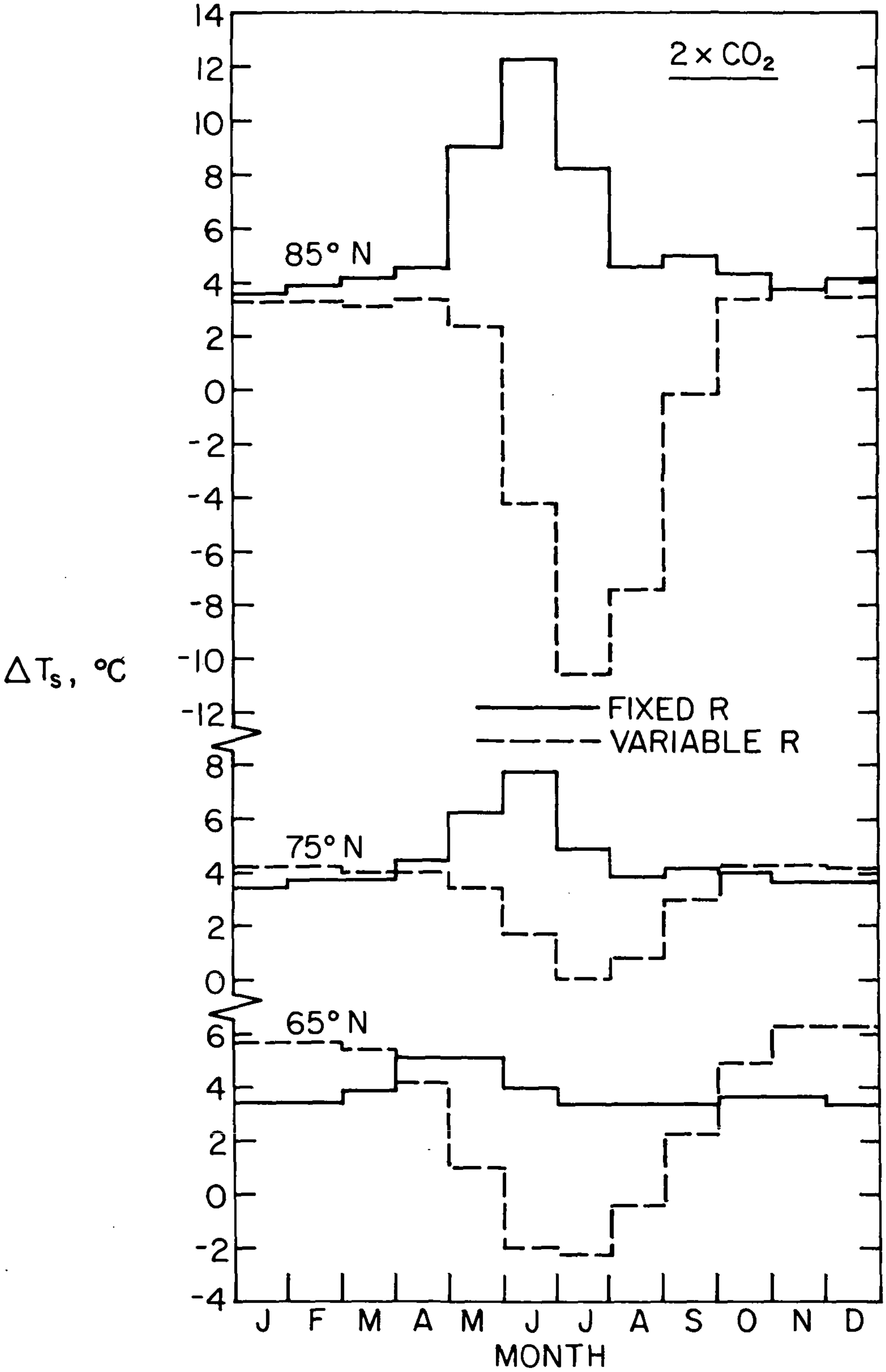

Figure 2.- Calculated change in zonal seasonal surface temperature ΔT_S for doubling of CO_2 concentration, with and without change in heat capacity R.

ORIGINAL PAGE IS
OF POOR QUALITY

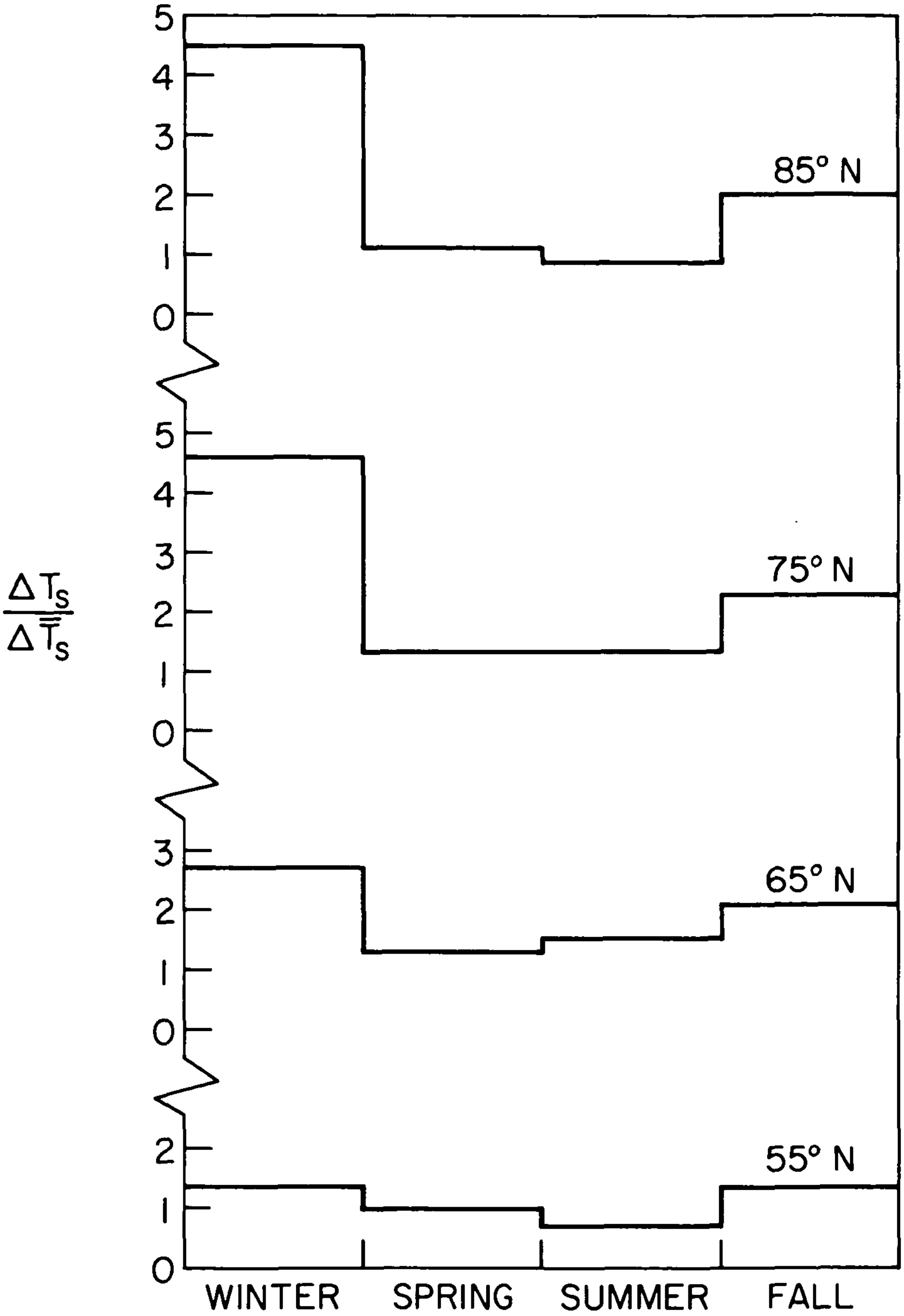

Figure 3.- Empirically determined zonal seasonal climate sensitivity $\Delta T_S/\Delta \bar{T}_S$ from Vinnikov and Groysman (1979).

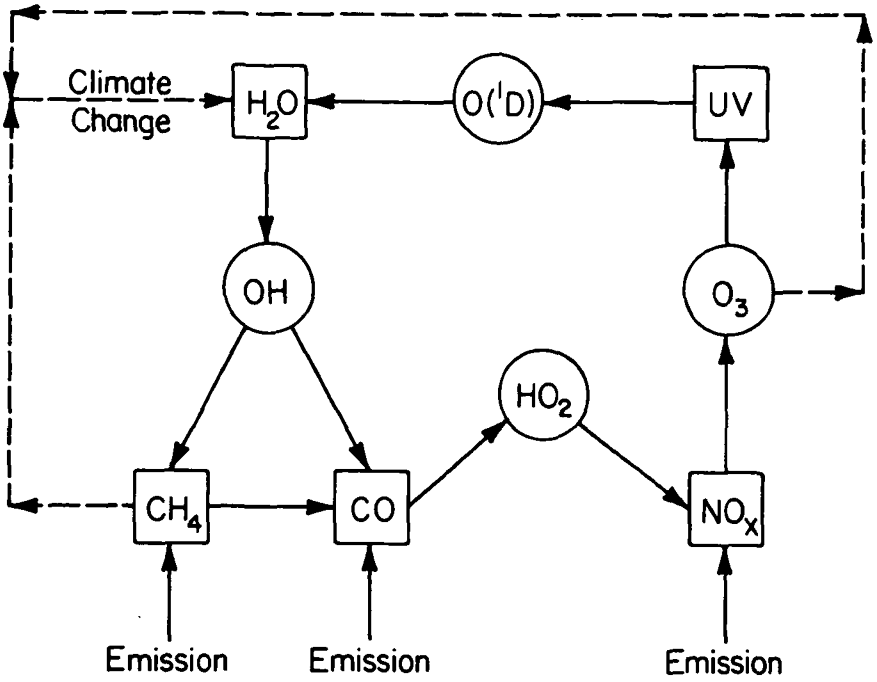

Figure 4.- Schematic illustration of the major chemical reactions affecting tropospheric O_3 and CH_4.

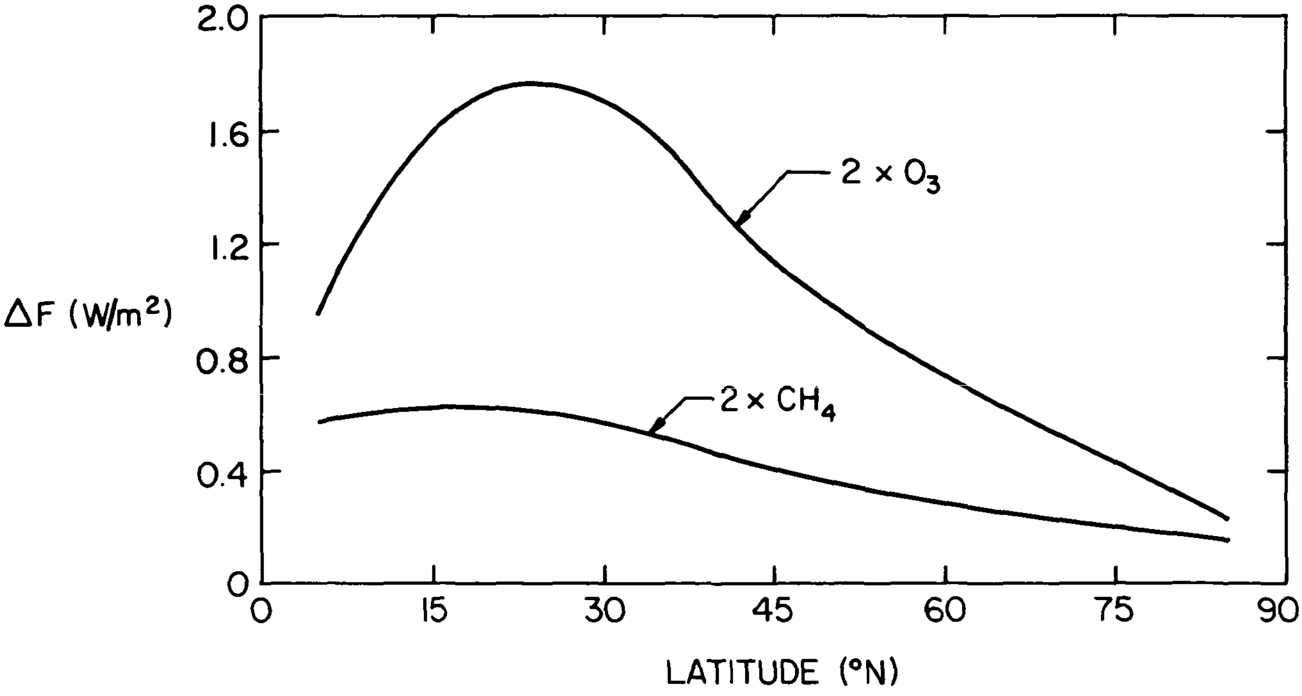

Figure 5.- The surface-troposphere heating for doubling O_3 and CH_4 relative to their present concentrations.

REGIONALLY APPLICABLE ANGULAR REFLECTANCE MODELS

J. M. Davis
Colorado State University
Fort Collins, Colorado

INTRODUCTION

The inference of the reflected component of the Earth's radiation budget from medium- or narrow-field-of-view radiometer measurements requires knowledge of the angular variation of the reflected radiance field. Arking (1965), Ruff et al. (1968), Salomonson and Marlatt (1968), Salomonson (1968), Griggs and Margraff (1967), Bartman (1968), and Brennan and Bandeen (1970) have investigated the angular variation of upwelling radiance fields, and in general they have found a significant degree of anisotropy in almost every type of reflecting surface with the possible exception of desert sand. One of the major tasks of the Earth Radiation Budget Experiment (ERBE) is to compile a data base which could be used to produce adequate angular reflectance models. Updates on this effort may be found in Stowe et al. (1980) and Stowe and Taylor (1981). Minnis and Harrison (1980) have used bidirectional reflectance models in developing a methodology for estimating cloud parameters from geostationary satellite data.

MODEL DESCRIPTION

The present research is similar to the works cited above in that one of the major goals is to establish the nature of the angular variation of reflected radiance fields. However, the present research attempts to define the average angular model over a spatial scale pertinent to regional climate modeling or monitoring, i.e., from 250 to 1000 km. Important information is also provided regarding the nature of the convergence of the radiance patterns to the regional means. This research is based on data collected during Summer Monex 1979 using a multidetector instrument described by Davis et al. (1982). (See fig. 1.) The instrument was flown on NASA's Convair 990 research aircraft at altitudes above 30 000 feet over a variety of surfaces, from the broken ice fields of Hudson Bay to the desert sands of the Saudi Arabian Peninsula. The radiances measured over the scenes were averaged and then normalized by multiplying by π and dividing by the scene-averaged reflected flux density. This cast the models into the inverse of the bidirectional reflectance normalization coefficient, which has a value of unity for an isotropic surface.

When this quantity was compared with the same quantity derived from many of the works cited previously, agreement was generally good ($\approx$10 percent rms) except in two cases, the 70° to 80° solar zenith angle desert case (compared to a model based on Salomonson's (1968) data) and a 40° to 50° ocean model (compared to a model generated from the data of Brennan and Bandeen (1970)). Comparison of these cases with the data of Salomonson and Brennan and Bandeen resulted in an rms difference of 0.43 and 0.21, respectively, between normalized radiances evaluated at 105 points in a nadir-relative azimuth angle coordinate system.

(See figs. 2 and 3.) In the first case the discrepancies were most likely the result of the forward scattering of the dust-laden atmosphere prevalent during Summer Monex. Salomonson's data were collected at relatively low altitudes (approximately 300 m), limiting the atmospheric contribution. In the second case the differences result primarily from the lack of a Sun glint feature in the data of Brennan and Bandeen, which may have resulted from a rough sea state. Nevertheless, it is obvious that significantly different values of reflected flux density would be inferred depending upon which data are utilized in these cases.

The multidetector design of the data collection instrument allowed for the sampling of the upwelling radiance field from 12 directions simultaneously. These data may be analyzed to reveal the nature of the spatial convergence of the radiances to the regional models. If bidirectional reflectance models are used to infer the reflected flux density of a region, it is important to insure that the model is representative of the region. Spatial variations in the radiance fields should be considered as carefully as angular variations in this regard.

For example, consider the following numerical experiment. Let us assume that the reflected flux density E_i at a point i is given by

$$E_i = k \sum_{j=1}^{12} n_{ij} \cos \theta_j \, \Delta\omega_j$$

where

n_{ij}	radiance measurement at the ith point from the jth sensor
θ_j	nadir angle of the jth sensor
$\Delta\omega_j$	solid angle subtended by the field of view of the jth detector
k	factor which scales E, the scene average of reflected flux density E_i, to E', the scene average of the reflected flux density E_i' as measured by an Eppley pyranometer. (Actually, E_i and E_i' differ by about 10 percent rms over a particular scene.)

If, for a particular scene, we use the set of measurements n_{ij} and the scene average of E_i to form a bidirectional reflectance model, we may then examine the convergence of the inferred to the actual value of E as a function of averaging distance and the number of measurements or satellites. Table 1 shows the results of such an analysis for the 10° to 20° clear ocean data. The entries in the table represent the percentage difference between the average of E_i over the given distance and the average of the inferences of the same quantity using the appropriate bidirectional reflectance model. Also, the results represent averages with respect to which sensor or combination of sensors was used to make the inference. For example, if n sensors were used to make an inference, the table entry is an average over all of the possible $C\binom{12}{n}$ sensor combinations.

The results in table 1 may be interpreted as follows. An inference of the flux density reflected from the ocean for solar zenith angles between 10° and 20° may be made to within 6 percent accuracy along a 50-km path if the averages from 12 angular positions are taken, or to about the same accuracy if the scene is viewed from two angular coordinates for a distance of 200 km. Similar analyses of other atmospheric scene types indicate that the so-called "clear" ocean scene with its attendant fair-weather cumulus distributions requires the greatest effort from both the angular and the spatial sampling standpoints in order to obtain a meaningful flux density inference.

CONCLUSION

The results of this study support the premise that the reflected component of the Earth's radiative budget may be inferred to an accuracy of about 2.5 percent with medium- or narrow-field-of-view radiometers if (1) the appropriate regionally averaged bidirectional reflectance models are used, (2) adequate spatial sampling is maintained (generally greater than 200 km and less than 1000 km), and (3) the inference is derived from adequate angular sampling (from one to four angular viewing coordinates).

REFERENCES

Arking, A. 1965: The Angular Distribution of Scattered Radiation and the Earth Albedo as Observed From TIROS. Goddard Institute for Space Studies, Annual Res. Rept., June, pp. 47-67.

Bartman, F. L. 1968: Earth Reflectance Patterns Measured by Radiometer on High Altitude Balloon Flights. Tech. Rept. 05863-13-T, Univ. of Michigan (Contract NASr-54(03)), 15 pp.

Brennan, B.; and Bandeen, W. R. 1970: Anisotropic Reflectance Characteristics of Natural Earth Surfaces. Appl. Opt., vol. 9, no. 2, pp. 405-412.

Davis, J. M.; and Cox, S. K. 1980: Radiance Patterns Over Extended Regions. Proceedings of the International Radiation Symposium, American Meteorological Society, Boston, pp. 370-327.

Griggs, M.; and Margraff, W. A. 1967: Measurement of Cloud Reflectance Properties and the Atmospheric Attenuation of Solar and Infrared Energy. Report prepared by the General Dynamics Corporation, Convair Division, San Diego, Ca. (Contract AF19(628)-5517), 153 pp.

Minnis, P.; and Harrison, E. F. 1980: A Methodology for Estimating Cloud Parameters From Geostationary Satellite Infrared and Visible Data. Proceedings of the International Radiation Symposium, American Meteorological Society, Boston, pp. 340-342.

Ruff, I.; Koffler, R.; Fritz, S.; Winston, J. S.; and Rao, P. K. 1968: Angular Distribution of Solar Radiation Reflected From Clouds as Determined From TIROS IV Radiometer Measurements. J. Atmos. Sci., vol. 25, no. 2, pp. 323-332.

Salomonson, V. V.; and Marlatt, W. E. 1968: Anisotropic Solar Reflectance Over White Sand, Snow, and Stratus Clouds. Atmos. Sci. Paper No. 120, Colorado State Univ., Ft. Collins, 41 pp.

Salomonson, V. V. 1968: Anisotropy in Reflected Solar Radiation. Atmos. Sci. Paper No. 128, Colorado State Univ., Ft. Collins, 142 pp.

Stowe, L. L.; Jacobwitz, H.; and Taylor, V. R. 1980: Reflectance Characteristics of Earth and Cloud Surfaces as Measured by the ERB Scanning Channels on the Nimbus 7 Satellite. Proceedings of the International Radiation Symposium, American Meteorological Society, Boston, pp. 430-432.

Stowe, L. L.; and Taylor, V. P. 1981: Emission Characteristics of Earth and Cloud Surfaces as Measured by the ERB Scanning Channels on the Nimbus 7 Satellite. Proc. Fourth Conference on Atmospheric Radiation, American Meteorological Society, Boston, pp. 124-127.

TABLE 1.- PERCENTAGE ERROR IN INFERENCE OF REFLECTED FLUX DENSITY AS A FUNCTION OF AVERAGING DISTANCE AND NUMBER OF ANGULAR SAMPLING COORDINATES

[10° to 20° clear ocean scene]

Averaging distance, km	Error, percent, when number of measurements (satellites) is -											
	1	2	3	4	5	6	7	8	9	10	11	12
1	32.9	23.5	19.3	16.9	15.2	14.0	13.1	12.3	11.7	11.2	10.7	10.4
2	32.3	23.0	19.0	16.6	14.9	13.7	12.8	12.1	11.5	11.0	10.5	10.2
10	26.5	19.0	15.8	13.9	12.6	11.7	11.0	10.5	10.0	9.6	9.3	9.0
20	22.1	15.8	13.1	11.5	10.4	9.6	9.0	8.5	8.1	7.8	7.5	7.3
50	16.6	12.0	10.1	9.0	8.2	7.7	7.2	6.9	6.7	6.4	6.3	6.1
100	12.0	8.7	7.4	6.6	6.0	5.7	5.4	5.2	5.0	4.8	4.7	4.6
200	8.4	6.3	5.4	4.9	4.6	4.4	4.2	4.1	4.0	3.9	3.9	3.8

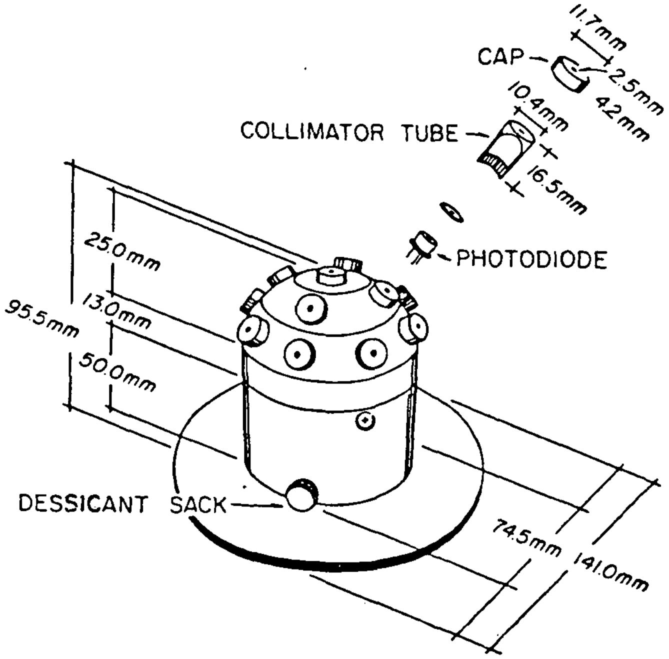

Figure 1.- Schematic of the multidetector instrument used for measuring reflected radiances.

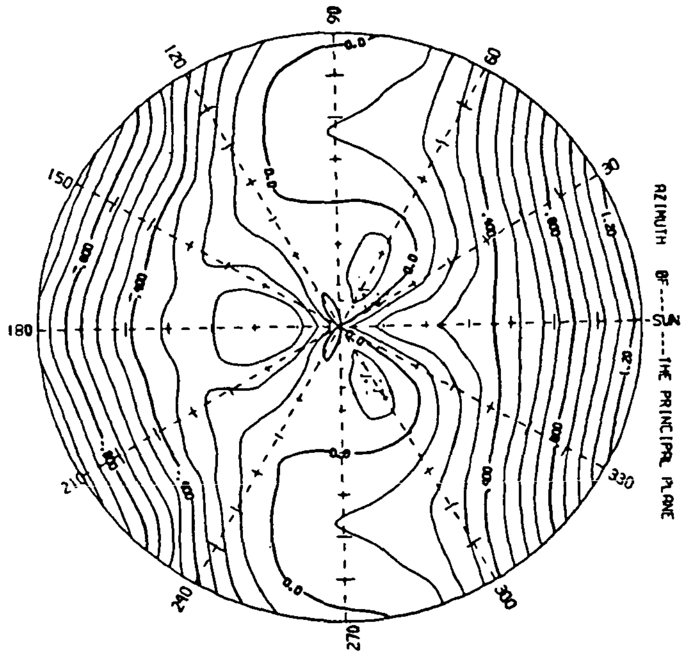

Figure 2.- Contours of differences between normalized reflected radiances from the present study and the same quantity from data of Salomonson (1968) for a 70° to 80° solar zenith angle desert scene. Positive values indicate that brighter features were measured in the present study. Contours are plotted as a function of observation nadir (increasing from 0° at the center to 70° at the rim) and azimuth measured relative to the solar azimuth.

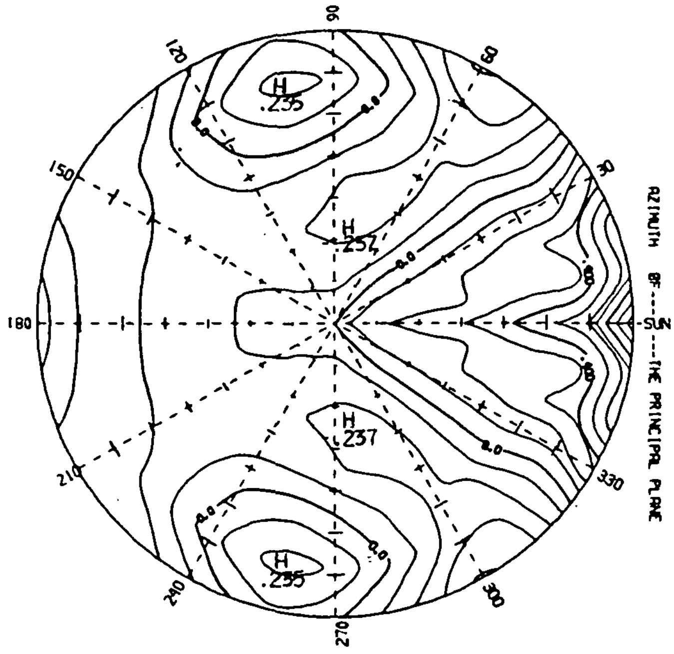

Figure 3.- Contours of differences between normalized reflected radiances from the present study and the same quantity from data of Brennan and Bandeen (1970) for a 40° to 50° solar zenith angle ocean scene. Positive values indicate that brighter features were measured in the present study. Contours are plotted as a function of observation nadir (increasing from 0° at the center to 70° at the rim) and azimuth measured relative to the solar azimuth.

N82 33324

FUNDAMENTALS OF ABSOLUTE PYRHELIOMETRY

AND OBJECTIVE CHARACTERIZATION

D. A. Crommelynck
Royal Meteorological Institute
Brussels, Belgium

INTRODUCTION: ABSOLUTE INSTRUMENTS FOR IRRADIANCE MEASUREMENTS

The accurate measurement of the irradiance on a given surface is not trivial. It is the purpose of this contribution to describe the radiometric methodology in use at the Royal Meteorological Institute (RMI) and to show the importance of radiometer characterizations.

As an example, we will consider the narrow-field-of-view radiometer developed at the RMI for the observation of the solar constant. The metrology of radiation is a difficult subject which is strongly dependent on the radiation source behavior. The radiation field will seldom be distributed uniformly. Generally the space-time variability of natural radiation fields is large. For our purpose, to simplify the problem, we will consider the Sun's radiation output to be constant. The solar source can be monitored by a single instrument accurately pointed at the Sun, to measure its output as a function of time. In this simplest case, we will show how it is possible to perform absolute measurements with relatively high accuracy.

An instrument can be considered to be absolute if its measurements expressed in SI units are based only on the independent knowledge of the different coefficients appearing in the equation defining the output signal in terms of basic physical characteristics. An absolute radiometer may thus in no case be calibrated by comparison to another radiometer. The purpose of radiometric comparisons of absolute radiometers is only to measure the differences found between different and independent technologies. These differences, if sufficiently small, are an indication of the state of the art.

ANGULAR RESPONSE OF RADIOMETER

Absolute radiometer detectors are usually built without any optical accessories such as lenses or mirrors, because these would introduce nonuniformities in spectral sensitivity. The sensors are generally designed to have the highest effective efficiency for radiation sensing, and their sensitive area is determined by the area of a hole placed in front of the cavity of the detector at the sensor plane (fig. 1). (See the section on cavity sensor efficiency.) If the hole is circular, an ideal behavior is a cosine response to the displacement of a point source s in a plane passing at n with a constant Ss distance and a variable incident angle Z_i, as long as s is in the full light zone. The sensor responds to all sources in the CDsAB hemisphere (shown in fig. 1), which includes the field-of-view (FOV) limiting device. However, the FOV limiter is

52

meant to provide a shadow zone where the source s cannot be seen by the sensor. When the source is in the penumbra zone the response is proportional to the part of the sensitive area which is irradiated.

The geometric characteristics of the radiometer are thus essentially fixed by the limit angle Z_l and the slope angle Z_p, which are functions of the distance l between the front aperture plane and the sensor plane. The front aperture (radius R) is centered on the sensitive area of the sensor (radius r). Thus

$$Z_l = \arctan (R + r)/l \tag{1a}$$

$$Z_p = \arctan (R - r)/l \tag{1b}$$

A general analysis and computation of the radiometric angular response is given by Kendall (1978).

ABSOLUTE DETECTOR

The absolute measurement of radiative energy is done ideally by comparison with electrical energy; both energy forms induce thermal fields which can be compared if their initial and boundary conditions are identical. The measurement of the temperature at well-defined points of the fields is not easily done with identical heat losses. It is more appropriate to compare the heat transfer of the fields to a common heat sink, since the sensitivity of the measurement is then higher and the physical definition of the heat loss path is better.

The comparison is essentially based on the ability either to transform the two different energies completely into heat, or, if this is not possible, to know accurately the effective absorption coefficient of the surface exposed to the radiation. In fact, the absolute detector will thus have an absorbing sensitive surface on which an electric heater is built. The heat flux is conducted through a well-defined path towards a thermal heat sink and is then measured.

An absolute radiometer sensor can be assembled in a certain number of ways, depending on the type of absorbing surface. This in turn dictates the use of a certain heater and heat flux sensor. The sensitive surface can simply be painted black and can be provided with an optical feedback mirror to enhance the effective absorption of the surface (A in fig. 2). Alternatively, the interior of the cavity can be coated with a diffuse black paint, or it can have a specular surface. The selection of the surface depends on the shape of the cavity, which can be cylindrical with a flat bottom or upwards or downwards conical. The heating element will similarly be flat, cylindrical, or conical. The heat flux detector can be based on a thermoelectric or a thermoresistive method. These detectors can be in the shape of a star or a full or hollow disk.

Several possible combinations of cavities, sensors, and heaters are shown in figure 2; working examples include the Crom radiometer (B-II-b), the active cavity radiometer (C-IV-d), and the PMO (Physical Meteorological Observatory) radiometer with thermoresistive sensors and an inverted cone (D-III-d). The combinations C-III-d and A-II-b were tested at the Royal Meteorological Institute, B-I-c and B-I-b were tested at the National Bureau of Standards, and I-b was tested at the National Physical Laboratory.

A good knowledge of the characteristics of these elements is required. One such characteristic is the sensitivity of the heat flux sensor, which is a function of temperature, output resistance, and thermal conductivity. For the cavity, the absorption of the paint and the resulting effective absorption of the cavity, the emissivity of the outer wall, and the thermal conductivity of its material must be known. It is necessary to be able to monitor the heating part of the resistance heater; this means that it should be fed by a four-wire setup.

Since thermal detectors present a response time, and since the temperature of the heat sink is not fixed at a preset value, thermal compensation must be built into the sensor. This is accomplished by using a differential technique consisting of two sensors, either or both of which are irradiable. The second sensor should be as identical as possible to the first and should also be provided with a heating resistor. If the sensors are placed side by side and either one can be irradiated, the detector is described as being dual compensated; if the second sensor cannot be irradiated then the detector is described as being compensated.

PRINCIPLES FOR ABSOLUTE RADIOMETRIC MEASUREMENTS

Compensated or dual-compensated absolute detectors can generally be used either passively, by directly measuring the output of the thermal detector in response to radiative input, or with the support of an active electronic feedback system. (Refer to the section on active modes of operation.) In both cases the radiometer must be calibrated electrically with a calibration source that duplicates the radiation fields to be measured. In the first case this is done manually, usually before and after a period of 20 minutes of radiation measurements. In the second case, channel open and closed states follow each other every 90 seconds, and the irradiance is given by a relation of the form

$$\Phi = K(P_C - P_O) \tag{2}$$

where P_C is the electrical power sent to the detector when the detector is closed and P_O is the electrical power sent to the detector when the detector is exposed to the radiation. The value of K depends on the sensitive area of the detector and its efficiency. The active mode of operation gives a faster time response from the radiometric system than is possible without feedback electronics. (See the section on frequency response of heat flux detector and absolute radiometer system.)

The dual-channel active-cavity radiometers developed by the author at the Royal Meteorological Institute can be operated as described. (See equations (35) through (39).) However, since the second compensating channel is exactly the same as the measuring channel, and since they are fixed next to each other with their axes parallel and pointing in the same direction, it is also possible to operate this radiometer in the Angström mode, by directly and simultaneously comparing the radiative energy and the electrical energy. This is done by measuring the thermoelectric signal difference between the detectors. This very versatile mode of operation of the dual-channel active-cavity absolute radiometer makes it possible to perform consistency tests between channels and measuring methods.

ACTIVE MODES OF OPERATION

An absolute radiometer used in an active measurement mode can be set up in several ways, depending on whether the feedback electrical power is reinjected at the irradiated heat flux detector or at the nonirradiated compensation side. The type of setup also depends on whether the signal coming from the detector is compared to a reference voltage or to the signal obtained at the output of the compensation detector excited by a reference electrical source. In principle, the same feedback electronics are used in each case. These consist of an error amplifier followed by an ad hoc PDI (proportional differential integrator) system and then an inverter, the whole of which is represented by the block transfer function $H_a(f)$. This is followed by a square root function to linearize the system and an output amplifier of transfer function $H_c(f)$ (fig. 3).

The measurement depends in each case on the knowledge of the compensation current I_c, which is measured by the voltage induced in the reference resistance R_M. The error signal ΔV is the difference between the output signal of the operating channel of the radiometer and the reference channel V_{12P} (figs. 3(a) and 3(d)), F (fig. 3(b)), or $V_{12P} + F$ (fig. 3(c)). The heating resistors are represented by R_1 and R_2, respectively, for the first and second detector, α_1 is the optical efficiency of detector D_1, and G_1 and G_2 are the ratios of the output signal of the first or second detector, respectively, to the electrical excitation P_1 or P_2. Each case is considered separately; thus it is easy to calculate I_c as a function of the incident flux Φ_1 at steady state.

For a double-compensated radiometer (fig. 3(a)), the irradiated sensor is not in the servo loop, and as a result the ratio G_2/G_1 needs to be accurately known, as do R_2 and α_1, as shown by the relation

$$\Phi_1 = \frac{G_2}{G_1}\frac{I_c^2 R_2}{\alpha_1}\left[\frac{(R_2 + R_M)^2}{R_2 G_2 H_a H_c^2} + 1\right] \tag{3}$$

where for an accurate servo system the bracketed expression tends to be equal to 1. With this setup appropriately and successively inverted from the first to the second detector it is possible to operate in the Angström mode, as described previously. The calculated flux will be either the arithmetic or the geometric mean of two successive observations. This allows the elimination of the ratio G_2/G_1 from equation (3) at steady state.

In the case of a thermally uncompensated single radiometer (fig. 3(b)), some parasitic thermal effects are not removed from the measurements. As shown by the relation

$$\Phi_1 = \frac{R_1 I_c^2}{\alpha_1}\left[\frac{(R_1 + R_M)^2}{R_1 G_1 H_a H_c^2} - 1\right] + \frac{F}{\alpha_1 G_1} - \frac{V_{110}}{\alpha_1 G_1} \tag{4}$$

some residual thermoelectric offset (V_{110}) can perturb the instrument when not irradiated. The measurement of the incident flux should be obtained by successive open and closed measurements, the latter being zero checks.

The setup shown in figure 3(c) is an improvement compared to that in figure 3(b); however, the compensation detector does not work at the same excitation level as the irradiated detector. The corresponding radiometric equation

$$\Phi_1 = \frac{R_1 I_c^2}{\alpha_1}\left[\frac{(R_1 + R_M)^2}{R_1 G_1 H_a H_c^2} - 1\right] + \frac{F}{\alpha_1 G_1} + (V_{120} - V_{110}) \frac{1}{\alpha_1 G_1} \tag{5}$$

shows that the parasitic thermoelectric effect will be decreased.

The most commonly used system works with the irradiated and compensated detectors at the same power level (fig. 3(d)). As in the setups shown in figures 3(b) and 3(c), the irradiated detector is included in the servo loop and the system thus has a relatively fast time response. As shown by the corresponding radiometric equation

$$\Phi_1 = \frac{I_c^2 R_1}{\alpha_1}\left[\frac{(R_1 + R_M)^2}{R_1 G_1 H_a H_c^2} - 1\right] + I_2^2 \frac{R_2 G_2}{\alpha_1 G_1} \tag{6}$$

the offset power $I_2^2 R_2 (G_2/\alpha_1 G_1)$ must be removed from the final equation by the execution of successive open and closed measurements, during which the offset is to be held constant. The difference between two successive open and closed states:

$$\text{Closed:} \quad \Phi_\rho' = \frac{P_c}{\alpha_1}\left[\frac{(R_1 + R_M)^2}{R_1 G_1 H_a H_c^2} - 1\right] + I_2^2 \frac{R_2 G_2}{\alpha_1 G_1} \tag{7a}$$

$$\text{Open:} \quad \Phi_1 + \Phi_\rho = \frac{P_o}{\alpha_1}\left[\frac{(R_1 + R_M)^2}{R_1 G_1 H_a H_c^2} - 1\right] + I_2^2 \frac{R_2 G_2}{\alpha_1 G_1} \tag{7b}$$

gives the incident radiation flux Φ:

$$\Phi_1 = \frac{P_o - P_c}{\alpha_1}\left[\frac{(R_1 + R_M)^2}{R_1 G_1 H_a H_c^2} - 1\right] \tag{8}$$

assuming the difference $(\Phi_\rho - \Phi_\rho')$ is negligible.

INSTRUMENTAL PERTURBATIONS AND SENSOR EFFICIENCY

If the radiometer responded only to the radiation incident on the sensitive area of the sensor and coming only from the observed source, then the accuracy of the measurement would depend only on the knowledge of the sensor's efficiency. This is, in fact, not the case, due to a series of parasitic effects which must be taken into account in the radiometric equation (fig. 4).

In a dual-channel absolute radiometer measuring in the successive mode operation, account must be taken of the residual dissymmetry between the two channels during the open state. This dissymmetry is due to

The effect of radiation arriving from outside and incident on the separation plane of the sensor but not on the sensitive area; this induces direct thermal effects Φ_τ between the separation plane and the sensor due to conductive and convective exchanges, with $\tau = \Phi_\tau/\Phi$

Parasitic scattered radiation Φ_Σ on the sensor area coming from the inside of the front field limiter through (a) reflection on the separation plane or (b) incidence from a source outside the limit angle, where $\Sigma = \Phi_\Sigma/\Phi$

Unwanted radiation scattered and diffracted on the front aperture $(\Phi_{\Sigma'}, \Phi_\delta)$ with $\Sigma' = \Phi_{\Sigma'}/\Phi$ and $\delta = \Phi_\delta/\Phi$

The effect of front aperture heating Φ_ψ with $\psi = \Phi_\psi/\Phi$

The difference in infrared energy radiated by the front aperture system to the two channels

These effects are conveniently expressed as a function of the flux Φ incident on the sensitive area. The sensor's efficiency depends on the geometry of the cavity and its coating as well as on the way the heat current is conducted to the heat flux detector.

In the particular case of the absolute instrument developed at the Royal Meteorological Institute the cavity is cylindrical, with a flat bottom covered on the inside with a diffusing black paint. The outside of the cavity's silver wall is polished and gold-plated. The bottom is in direct thermal contact with the heat flux detector. In this way the radiation which falls directly on the bottom is absorbed and measured according to the absorption coefficient a_p of the paint. The reflected radiation $(1 - a_p)$ falling on the cylindrical wall is a function of the diffusion pattern of the paint, which is considered by the paint manufacturer to be Lambertian. To calculate the total efficiency of the detector, the relative sensitivity distribution of the cylindrical cavity must be known.

Finally, thermal expansion of the sensor's sensitive area must also be taken into account. Some of the resulting effects can be calculated on the basis of fairly acceptable assumptions; however, for most of the effects an actual physical characterization is necessary because modeling is not always sufficiently representative of reality. These characterization experiments should be feasible on every absolute radiometer.

HEATING WIRE EFFECT

The accuracy of the absolute radiometric measurements depends on the precise physical definition of the elements whose values appear in the radiometric equation. One of these elements is the value of the compensating heating resistance. This value R_i, as well as the power P_i which is dissipated, is obtained by direct and simultaneous measurement of the heater current I_i and the applied voltage U_i. This can be done with a high degree of electrical accuracy; however, it is possible that the heating wires cd and c'd' contribute to some parasitic electrical power dissipation detected by the heat flux detectors, which in turn could give rise to some systematic error (fig. 5).

Let us assume that the measured parasitic powers P_{p1} and P_{p2} are due to the equivalent parasitic heaters r_c, r_d, $r_{c'}$, and $r_{d'}$. Electrical heating can therefore be expressed by

$$V_{11P} = G_1(r_c + R_1 + r_d)I_1^2 = G_1R_1I_1^2 + G_1P_{p1} \tag{9a}$$

and

$$V_{12P} = G_2(r_{c'} + R_2 + r_{d'})I_2^2 = G_2R_2I_2^2 + G_2P_{p2} \tag{9b}$$

where G_1 and G_2 are trimmed by p1 and p2 such that when $R_1I_1^2 = R_2I_2^2$ with $R_1 = U_1/I_1$ and $R_2 = U_2/I_2$ we have

$$\Delta V = V_{11P} - V_{11P} = 0 \tag{10}$$

At this point we can define $G_1' = V_{11P}/R_1 I_2^2$ and $G_2' = V_{12P}/R_2 I_2^2$ where $G_1' \rightarrow G_1$ and $G_2' \rightarrow G_2$ when the parasitic heating effects tend to zero. The easiest way to determine the parasitic effect is to inject successively the currents $I_{1c} = I_{1d} = I_1$ and $I_{1c'} = I_{1d'} = I_2$ in the respective wires (cAa, dBb) and (c'A'a', d'B'b') and detect the corresponding V_{11P} and V_{12P} deviations. Here the hypothesis is made, based on symmetry, that $r_a = r_c$, $r_d = r_b$, $r_{a'} = r_{c'}$, and $r_{d'} = r_{b'}$. Therefore we find that

$$r_c = \frac{V_{11Pc}}{2G_1' I_{1c}^2} \tag{11a}$$

$$r_d = \frac{V_{11Pd}}{2G_1' I_{1d}^2} \tag{11b}$$

$$r_{c'} = \frac{V_{12Pc'}}{2G_2' I_{2c'}^2} \tag{11c}$$

$$r_{d'} = \frac{V_{12Pd'}}{2G_2' I_{2d'}^2} \tag{11d}$$

where G_1 and G_2 are approximated by G_1' and G_2'. The effective heating is thus equal to the measured heating $R_1 I_1^2$ or $R_2 I_2^2$ plus the parasitic effects $(r_c + r_d) I_1^2$ or $(r_{c'} + r_{d'}) I_2^2$.

If this is applied to absolute radiometric measurements based on successive open and closed states of the irradiated channel 1 of a dual-channel active absolute radiometer, we find, if the excitation of the reference channel is kept constant, that

$$\begin{aligned} \Phi = K(P_c - P_o) &= K\left[R_1 I_{1c}^2 + (r_c + r_d) I_{1c}^2 - R_1 I_{10}^2 - (r_c + r_d) I_{10}^2\right] \\ &= K\left[R_1\left(I_{1c}^2 - I_{10}^2\right) + (r_c + r_d)\left(I_{1c}^2 - I_{10}^2\right)\right] \qquad (12) \end{aligned}$$

where $K(r_c + r_d)\left(I_{1c}^2 - I_{10}^2\right)$ is the error due to the parasitic heating effect.

CAVITY SENSOR EFFICIENCY

Due to the thermal configuration of the cavity sensor as well as the reflection pattern of its inner coating, this sensor is not of uniform sensitivity. The heat flux meter output is proportional to

$$\int_{\lambda}\int_{\text{Cavity}} a(\lambda,r)\Phi(\lambda,r)\ dr\ d\lambda = K_1V_{1\Phi} \tag{13}$$

In fact, $\Phi(\lambda,r) = \Phi(\lambda)$ is uniform over the direct irradiated sensor cavity bottom; elsewhere, for instance on the wall of the cylinder, the distribution depends on the reflected radiation. (See fig. 6.) Since we desire to measure the value of the irradiance E incident on the sensor, and since the heat flux meter deviates proportionally to the input, we need to know $a(\lambda,r)$. We first assume separability at the first order; thus, $a(\lambda,r) = a'(\lambda)a'(r)$. Let us also assume that $\Phi(\lambda,r)$ contains the different parasitic effects considered in the discussion on instrument perturbations. Thus

$$\Phi = \int_{\lambda}\int_{S} \Phi(\lambda)\ dr\ d\lambda = ES + \Phi_{\psi} + \Phi_{\Sigma'} + \Phi_{\Sigma} + \Phi_{\delta} + \Phi_{\tau} - \Phi_{R} + \Phi_{\rho} \tag{14}$$

The energy budget of the sensor can then be written for radiative input:

$$ES\left[1 + \psi + \Sigma' + \Sigma + \delta + \tau - (1 - a_R) + \rho\right]$$

$$= K_2\int_{\lambda}\int_{\text{Cavity}} a(\lambda,r)\Phi(\lambda,r)\ d\lambda\ dr + L + \Phi_E \tag{15}$$

where L represents all thermal losses except those coming from the sensor area itself. For the latter, we consider Φ_R to be the radiation reflected by the cavity, and Φ_E to be the energy emitted by the cavity. In fact, $\Phi_R = (1 - a_R)ES$ where a_R is the effective absorption coefficient of the cavity. (See the section on cavity sensor effective absorption coefficient.) In a similar way, we have for electrical energy input:

$$P = IU = \int_{\text{Cavity}} P(r)\ dr + L' + \Phi_E' = K_3V_{1P} \tag{16}$$

where L' represents all the thermal losses in the cavity when the sensor is electrically excited, and Φ_E' is the energy emitted by the cavity in the same circumstances. In fact, when

$$\int_{\lambda}\int_{\text{Cavity}} a(\lambda,r)\Phi(\lambda,r)\ dr\ d\lambda = P \tag{17}$$

we have $K_1V_{1\Phi} = K_3V_{1P}$ and thus also $\Phi = K_2P + L + \Phi_E$. With this formula it is necessary to know K_2, L, and Φ_E. However, equation (17) can be decomposed into

$$\int_{\lambda}\int_{\text{Bottom}} a(\lambda,r)\Phi(\lambda)\ dr\ d\lambda + \int_{\text{Wall}} a(\lambda,z)\Phi(\lambda,z)\ dz\ d\lambda = P \tag{18}$$

where z is the height above the bottom of the cylinder.

If $a'(\lambda) = a_{514}$ (see the section on spectral sensitivity of the absolute sensor), and if we assume $a'(r) = 1$ (this assumes uniform sensitivity of the bottom of the cavity), we have

$$a_{514}\int_{\lambda}\int_{S} \Phi(\lambda)\ dr\ d\lambda + a_{514}\int_{\lambda}\int_{z} \alpha(z)\Phi(\lambda,z)\ dz\ d\lambda = P \tag{19}$$

Since

$$\Phi(\lambda,z) = (1 - a_{514})\ d(z)\int_{\lambda}\int_{S} \Phi(\lambda)\ dr\ d\lambda \tag{20}$$

we find that

$$a_{514}\Phi + a_{514}\left(1 - a_{514}\right)\Phi\int_{z} \alpha(z)\ d(z)\ dz = P \tag{21}$$

With $m(z) = \alpha(z)\ d(z)$ we have finally

$$\Phi a_{514}\left[1 + (1 - a_{514})\int_{z} m(z)\ dz\right] = P \tag{22}$$

The factor

$$a_{514}\left[1 + (1 - a_{514})\int_{z} m(z)\ dz\right] = \alpha_{eff} = P/\Phi \tag{23}$$

is the efficiency factor of the sensor where

$d(z)$	relative radiation distribution function of the radiative energy reflected from the bottom of the cavity towards the wall of the cylinder band
$\alpha(z)$	relative efficiency function along the wall surface of the cylinder, i.e., the electrical power needed to balance the effect of an incident laser beam kept at constant amplitude and scanning the wall of the cylinder
$m(z)$	relative efficiency function of the tube

As a first good approximation, a_{514} is the value of the absorption factor of the black paint at $\lambda = 514$ nm; however, this value should be very slightly increased due to the fact that the wall of the tube does not totally absorb the incident radiation and reflects part of it back to the bottom (fig. 7). When an error calculation is made to determine the effect of the uncertainty of the absorption coefficient of the paint and the effect of the tube, it will be seen that accuracy can be improved by approximately an order of magnitude by using a cavity element.

Cavity Sensor Relative Efficiency Distribution

The experimental determination of the relative surface efficiency distribution of the cavity sensor $\alpha(z)$ is done with a laser beam (figs. 8 and 9). The measurements are made in air and in a vacuum. In the first phase the laser beam is normally incident on the bottom of the cavity and is moved stepwise from left to right and back. The response of the radiometer is measured with its own electronics.

In air the sensitivity variation over one diameter is at maximum 7×10^{-4} with a signal variability of the same value. In a vacuum, the highest observed relative difference is 2.8×10^{-4} with a variability of 2×10^{-4}. Therefore, we can only say that the sensitivity uniformity is certainly better than 2.8×10^{-4} and that convection effects introduce noise into the experiment in air.

In the second phase the cavity is tilted 6°, and the laser beam is now moved to scan first a part of the bottom and then the vertical wall of the cylindrical cavity. Although the shape of the projection of the beam is not ideal, the resulting observations (fig. 7) show clearly that the efficiency of the cylindrical cavity is better in a vacuum than in air. This is due to the removal of the convection losses. The residual losses should be attributed mainly to losses through the sensor-sensitive area, with some second-order radiative losses between the outer side of the cylinder and the surroundings.

Cavity Sensor Effective Absorption Coefficient

The cavity sensor effective absorption coefficient a_R can be evaluated according to the geometry of the cylindrical cavity and the absorption coefficient a of its inner coating. Since the length to reduced radius ratio is 15 and since $a = 0.97 \pm 0.01$, we have $a_R = 0.99986$. (Without the sensor entrance field stop this length is 8, and then $a_R = 0.99898$.)

It is useful to measure a_R directly to be able to cross-check the theory, and also to try to ascertain the accuracy to which a_R can be determined. We made this determination by using a conical reflectometer developed at the World Radiation Center in Davos. The experimental setup is shown in figure 10. A laser beam is chopped, and a synchronous amplifier is used to detect the output signal of the reflectometer proportional to the back-reflected radiation of the cavity. When sufficient care is taken to avoid mechanical and background noise picked up by the conical pyroelectrical detector, it is possible to observe a reflectivity of 0.00025 with a repetition dispersion of ±0.00003. The value of a_R is given by the ratio

$$a_R = \frac{(S_c - S_{cl}) - (S_{RC} - S_{cl})}{\left[(S_w - S_{cl}) - (S_{RC} - S_{cl})\right] W} = 0.99975 \pm 0.00025 \qquad (24)$$

where

S_c	signal measured from cavity
S_{RC}	signal measured on reference (perfect) cavity
S_{cl}	signal measured with laser beam off
S_w	signal measured on white reference
W	reflectivity of white surface

The uncertainty is determined by the difference in the repeated measurements.

Since the tip of the cone must be withdrawn to be able to send the laser beam into the cavity, it could be that a retroreflection effect would induce some systematic error at the conclusion of the experiment. Therefore we also measured this effect by putting a semitransparent mirror in the way of the laser beam to observe an eventual retroreflection with a monitor silicon cell detector.

THERMAL EFFECTS ON SURFACE OF SENSITIVE AREA

Sensitive Area

The physical definition of the sensitive area of the absolute radiometer is very important because its value is one of the factors in the radiometric equation. This area is circular and separates the radiative incident flux to be measured (Φ) from the flux which is to be rejected from the measurement (Φ_p).

The area given by its diameter should be perfectly circular; however, since this is not strictly possible, the profile as well as the departure from roundness should be known. It is a good practice to cross-check the number obtained by one metrological laboratory with that obtained independently by another. Of course this area is temperature dependent; we apply the formula

$$S_T = S_{To}\left[1 + K(T - T_o)^2\right] \tag{25}$$

which is valid for the linear expansion of stainless steel ($K = 11 \times 10^{-6}/^{\circ}C$). Stainless steel was chosen because it is corrosion resistant and can easily be polished. Indeed it was proven to be necessary to attenuate Φ_p by rejecting it back through the front aperture. The surface of the sensitive area is therefore a slightly spherical mirror.

Thermally Induced Perturbations

Although a mirror is used, it may be that part of the absorbed Φ_p induces a radiometric deviation; an experiment has thus been designed to measure this effect in air or vacuum conditions. The setup is identical to that for the determination of the efficiency distribution except that the mirror at the surface of the sensitive area has been replaced by one without a hole. As the effect is small the power of the laser beam used was increased to 200 mW. The laser scans the diameter of the mirror and the detector output is measured. The results, shown in figure 11, indicate a remarkable difference between air and vacuum conditions, indicating that some energy transfer occurs through convection effects.

The effect on the radiation measurement of the function $f(\rho)$ assumed to be cylindrically symmetrical is obtained as follows: let $\Phi = ES$ be the flux through the sensitive area S, where E is the uniform irradiance. Irradiating the whole front aperture gives rise to the thermal effects Φ_T, whose ratio to Φ is given by τ such that $\tau_i = \Phi_{Ti}/\Phi$, where the subscript i = a (air) or v (vacuum) indicates the experimental condition. The value of τ_i is obtained from

$$\tau_i = \frac{\displaystyle\int_r^R 2\pi f(\rho)\rho \, d\rho}{\displaystyle\int_0^r 2\pi f'(\rho)\rho \, d\rho} \tag{26}$$

where $f(\rho)$ is the distribution of the thermal effect as a function of the location of the constant perturbation. In air this is given by

$$f(\rho) = -2.94 \times 10^{-4}\rho^2 - 2.192 \times 10^{-4}\rho + 0.11239 \qquad (27)$$

where

$f'(\rho)$ is constant and equal to 200 mW

r radius of the sensitive aperture

R radius of the front aperture

In air, with $R = 11.15$ mm and $r = 4$ mm, we find that $\tau_a = 3.045 \times 10^{-3}$. Since $f(\rho) = 3.02 \times 10^{-3}$ mW in a vacuum, we find for the same conditions that $\tau_v \leqslant 0.1022 \times 10^{-3}$. If the front aperture diameter is changed to a lower value, then τ_a and τ_v are decreased accordingly (fig. 12).

Sensor Emission Effects

When both channels of the absolute radiometer are closed, both sensors emit the same amount of radiation towards the closed FOV limiting device, and they also receive the same amount of energy from this assumed isothermal enclosure Φ_ρ. However, when one of the channels is open there is a small dissymmetry in the system because the view factor towards the opened front aperture is different for the two sensors. This difference has not been taken into account because its effect is negligible.

EFFECT OF THE FIELD-OF-VIEW LIMITING SYSTEM

In front of the sensor, whose field of view is quite large, we have installed a removable field-of-view limiting system. Its inner surface is covered with grooves coated with black diffusing paint. The geometry of the instrument is defined by the sensitive surface and the circular front aperture diaphragm, which is centered on the sensor axis. (See the section on the angular response of the instrument.)

Among the different effects which can influence the absolute irradiance measurements are the following:

Part of the light falling on the front aperture can be scattered into the sensor's aperture. If $\Phi_{\Sigma'}$ is the perturbation for a given incident irradiance E, this effect is characterized by the ratio $\Sigma' = \Phi_{\Sigma'}/ES$ where s is the area of the sensitive surface.

Part of the light falling on the entrance aperture is dispersed on the inner part of the view-limiting device, and is absorbed. However, a certain amount, Φ_Σ, can be reflected back into the sensor. The ratio $\Sigma = \Phi_\Sigma/ES$ takes this effect into account.

Some radiation issued from the umbra zone can reach the inner wall of the view limiter, and part of it can be reflected into the sensor (fig. 13). This effect has not yet been measured. It may be very difficult to correct for this objectively because it depends specifically on the external parasitic source distribution.

Diffraction can occur on the front diaphragm as well as on the sensitive area itself; however, these effects, which are expressed by $\delta = \Phi_\delta/ES$, are negligible.

The experimental determination of these different errors is difficult because the effects are relatively small and because the laser beam has a spatial radiation distribution which is quasi-Gaussian. Therefore, the experiments had to be designed on a differential basis, using a silicon cell instead of the cavity detector to enable effective separation of the thermal effects already measured. (Refer to the section on thermal effects.)

In the first configuration (A in fig. 13) the incident beam is measured while scanning a diameter of the sensor, the front surface is coated black to avoid backscattered light, and the FOV limiter is removed. In the second configuration (B in fig. 13) the laser beam is again moved over the same diameter from one side of the front aperture to the other. The general experimental setup is shown in figure 14. The signals are subtracted from each other and the levels β and γ (fig. 15) are compared to the input signal. The results are shown in figure 15.

An analysis of the differential output function (fig. 15) suggests that the zones between WA and IJ indicate the noise level of the experiment ($\sim 7 \times 10^{-6}$ V compared to 11.58 V). The peaks B and H indicate the objective effect of the diffraction combined with scattering on the front aperture ($\Phi_{\Sigma'} + \Phi_\delta$), the distance between B and H being exactly the front aperture diameter. The shape of the signals ABC and GHI is an image of the shape of the laser beam of about 3 mm diameter. The signal DEF suggests that the sensitivity of the silicon cell associated with the repeatability of the positioning of the laser beam is very difficult to achieve to better than 0.5 percent, due to the slope of the beam shape. Therefore, the information between C and G will not be used. The levels C and G are interpreted to be the effect due to Φ_Σ. Therefore we have

$$\Sigma = \frac{\Phi_\Sigma}{ES} = \frac{\int_r^R 2\pi f(\rho)\rho \, d\rho}{\int_0^r 2\pi f'(\rho)\rho \, d\rho} \tag{28}$$

When $r = 4$ mm, $R = 11.15$ mm, $f'(\rho) = 11.56$, and $f(\rho) = 1.28 \times 10^{-5}$, we find that

$$\Sigma = \frac{1.28 \times 10^{-5}(11.15^2 - 4^2)}{11.56 \times 4^2} = 0.749 \times 10^{-5} \tag{29}$$

Since the effect of diffraction and dispersion is due to the edge of the front aperture, $\Sigma' + \delta = (\Phi_{\Sigma'} + \Phi_\delta)/ES$ should be calculated in a different way than for Σ. In fact, we have $\Phi_{\Sigma'} + \Phi_\delta = f(R)2\pi R/\Delta$ when Δ is the width of a rectangular laser beam of equivalent power to the actual beam. It is estimated that $\Delta = 4.76$ mm. Thus we have for the dispersion and diffraction δ

$$(\Sigma' + \delta) = \frac{f(R)2\pi R}{\Delta \int_0^r 2\pi f'(\rho)\rho \, d\rho} = \frac{3.1416 \times 2 \times 11.15 \times 1.8 \times 10^{-3}}{3.1416 \times 11.156 \times 4^2 \times 1.18 \times 2} = 9.19 \times 10^{-5} \tag{30}$$

For $R \geqslant r$, this factor is a linear function of the diameter of the front aperture such that $\Sigma' + \delta = 8.24 \times 10^{-6} R$ (R in mm).

LINEARITY OF THE ABSOLUTE RADIOMETER SYSTEM

It can be shown that the active radiometer servo system will work linearly when a square root function is used in its loop. If this is so, then the precision of the measurement is constant over the working range. Even if the detectors used were nonlinear, which is not the case, the measuring method based on simultaneous or successive balance measurements always gives a linear result.

SPECTRAL SENSITIVITY OF THE ABSOLUTE SENSOR

The measured radiative energy is given by

$$\int_\lambda \alpha_{eff(\lambda)} E_\lambda \, d\lambda = \frac{K}{S}(P_c - P_o) \tag{31}$$

where $\alpha_{eff(\lambda)}$ is the sensor efficiency at wavelength λ. This energy is dependent on the geometry of the cavity and or its inner coating. It has been determined for one wavelength and should be extended to the whole range of wavelengths over which the observed radiation source emits energy. In fact, the solar source peaks at 460 nm, and as the black paint's absorptivity is quite constant over the solar radiation range it is reasonable to take the efficiency determined for 514 nm and use it over the whole range without appreciable error; thus

$$\int_\lambda E_\lambda \, d\lambda = \frac{K}{\alpha_{eff(514)} S}(P_c - P_o) \tag{32}$$

FREQUENCY RESPONSE OF HEAT FLUX DETECTOR AND ABSOLUTE RADIOMETER SYSTEM

When the input flux to the radiometric system changes with time, it is necessary to know its frequency response in order to be able to reconstruct from the measurements the real-time behavior of the incident radiation. This characteristic has been determined for the heat flux detector itself as well as for the complete radiometric system (detector and feedback circuitry) to illustrate the improvement of the detector's otherwise relatively poor frequency response.

The experimental setup is shown in figure 16. It enables the determination of the transfer function in either case and is based on the equation

$$H(f) = \overline{G_{YX}(f)} \Big/ \overline{G_{XX}(f)} \tag{33}$$

where $\overline{G_{YX}(f)}$ is the mean cross spectrum of input and output signals and $\overline{G_{XX}(f)}$ is the mean autospectrum of the input signal. Along with the calculation of $H(f)$, the coherence function γ^2 is also determined to guarantee the value found for $H(f)$:

$$\gamma^2 = \left[\overline{G_{YX}(f)}\right]^2 \Big/ \overline{G_{XX}(f)}\left[\overline{G_{YY}(f)}\right] \tag{34}$$

The radiometric excitation signal is a laser beam chopped in a pseudo-random way. It is measured by an optocoupler, and along with the radiometric output signal (with or without radiometer electronics) is filtered and sent to a Fourier analyzer.

The radiometer itself is operated in air and in a vacuum. The results show that there is no appreciable difference in behavior between air or vacuum response. This means that the thermal contacts are well settled due to the repeated and long vacuum-air cycling.

The compared responses of the detector alone (fig. 17) and the complete radiometric system with feedback (fig. 18) show, as anticipated, a remarkable improvement in the frequency response of the detector used in the system.

RADIOMETRIC EQUATION

The radiometric equation describes the significance of the measurement. At steady state, with the Sun perfectly aligned with the radiometer axis, we have:

$$\alpha_{eff}(ES_T + \Phi_\tau + \Phi_\Sigma + \Phi_{\Sigma'} + \Phi_\delta + \Phi_\rho - \Phi_R - \Phi_{\rho'}) = (P_o - P_c)\left[\frac{(R_1 + R_M)^2}{R_1 G_1 H_a H_c^2} - 1\right] \tag{35}$$

where

E	irradiance (W/m^2)
S_T	sensitive area at temperature T
Φ_τ	thermal effect on sensor surface
Φ_Σ	scattering due to FOV limiter
$\Phi_{\Sigma'}$	scattering on front aperture
Φ_δ	diffraction effect on aperture
Φ_ρ	energy from FOV limiter when channel is open
$\Phi_{\rho'}$	energy from FOV limiter when channel is closed
α_{eff}	efficiency of sensor
P_c	electrical compensation power in closed state
P_o	electrical compensation power in open state

with

$$(P_c - P_o) = R_1\left(I_{1c}^2 - I_{10}^2\right) + (r_c + r_d)\left(I_{1c}^2 - I_{10}^2\right) \tag{36}$$

and

$$S_T = S_{To}\left[1 + K(T - T_o)^2\right] \tag{37}$$

Since

$$ES_T + \Phi_\tau + \Phi_\Sigma + \Phi_{\Sigma'} + \Phi_\delta - \Phi_R = ES_T\left[1 + \tau + \Sigma + \Sigma' + \delta - (1 - a_R)\right] \tag{38}$$

with $ES = \Phi$ and $\tau = \Phi_\tau/\Phi$, $\Sigma = \Phi_\Sigma/\Phi$, $\Sigma' = \Phi_{\Sigma'}/\Phi$, $\delta = \Phi_\delta/\delta$. Since at this measurement $R_1 I_{1c}^2 = I_c V_c$ and $R_1 I_{10}^2 = I_o V_o$, we find that

$$E = \frac{\left[(I_c V_c - I_o V_o) + (r_c + r_d)\left(I_{1c}^2 - I_{10}^2\right)\right]\left[\frac{(R_1 + R_M)^2}{R_1 G_1 H_a H_c^2} - 1\right] - \alpha_{eff}(\Phi_\rho - \Phi_{\rho'})}{S_{To}\left[1 + K(T - T_o)^2\right]\left[1 + \tau + \Sigma + \Sigma' + \delta - (1 - a_R)\right]\alpha_{eff}} \tag{39}$$

REFERENCE

Kendall, J. M., Jr. 1978: Analysis and Tests of a Wide Angle Radiometer View Limiter. JPL Publication No. 78-63, Jet Propulsion Laboratory, California Institute of Technology.

SYMBOLS

a	absorption coefficient
a_R	absorption coefficient of cavity
a_P	absorption coefficient of paint
D_i	detector
$d(z)$	relative radiation distribution function of radiative energy reflected from bottom of cavity towards wall of cylinder band
E	irradiance incident on sensor
ES	flux through sensitive area of sensor
F	reference voltage
f	frequency
$f(\rho)$	distribution of thermal effect as a function of location of perturbation
G_i	ratio of output signal of detector to electrical power P_i
$G_{XX}(f)$	mean autospectrum of input signal
$G_{YX}(f)$	mean cross spectrum of input and output signals
H	transfer function amplitude
$H_a(f), H_c(f)$	block transfer functions
I_i	heater current
I_c	compensation current
K_i	proportionality coefficient
L	all thermal losses except those from the sensor area itself
L'	all thermal losses in cavity when sensor is electrically excited
l	distance between front aperture plane and sensor plane
$m(z)$	relative efficiency function of tube
P_c	electrical compensation power (detector closed)
P_i	electrical power

P_o	electrical compensation power (detector open)
P_{pi}	parasitic measured power
p1,p2	indices for parasitic heating effects
R	radius of front aperture
R_M	reference resistance
R_i	value of compensating heating resistance for detector
r	radius of sensor aperture
r_i	parasitic heaters
S	sensitive area of sensor
S_{RC}	signal measured on reference (perfect) cavity
S_T	sensitive area at temperature T
S_{To}	sensitive area at reference temperature T_o
S_c	signal measured from cavity
S_{cl}	signal measured with laser beam off
S_w	signal measured on white reference
s	point source
T	temperature
U_i	applied voltage
V_{1iO}	residual thermoelectric offset
V_{1iP}	voltage given by detector i when electrically powered
W	reflectivity of white surface
Z_l	limit angle
Z_p	slope angle
z	height above bottom of cylinder
$\alpha(z)$	relative efficiency function along wall surface of cylinder
α_{eff}	efficiency factor of sensor

$\alpha_{eff(\lambda)}$	sensor efficiency at wavelength λ
α_i	optical efficiency of detector D_i
Δ	width of rectangular laser beam
ΔV	error signal
δ	Φ_δ/Φ
λ	wavelength
ρ	Φ_ρ/Φ
Σ	Φ_Σ/Φ
Σ'	$\Phi_{\Sigma'}/\Phi$
Φ	incident radiation flux
Φ_E	energy emitted by cavity
Φ_R	radiation reflected by cavity
Φ_l	incident radiation flux at steady state
Φ_p	radiative incident flux to be rejected from measurement
Φ_δ	diffraction effect on aperture
Φ_ρ	energy from FOV limiter with channel open
$\Phi_{\rho'}$	energy from FOV limiter with channel closed
Φ_Σ	scattering due to FOV limiter
$\Phi_{\Sigma'}$	scattering on front aperture of FOV limiter
Φ_τ	thermal flux incident on separation plane of sensor but not on sensitive area
Φ_ψ	front aperture heating
Φ'_E	energy emitted by cavity when sensor is electrically excited
ψ	Φ_ψ/Φ

Subscripts:

a	air
v	vacuum

ORIGINAL PAGE IS
OF POOR QUALITY

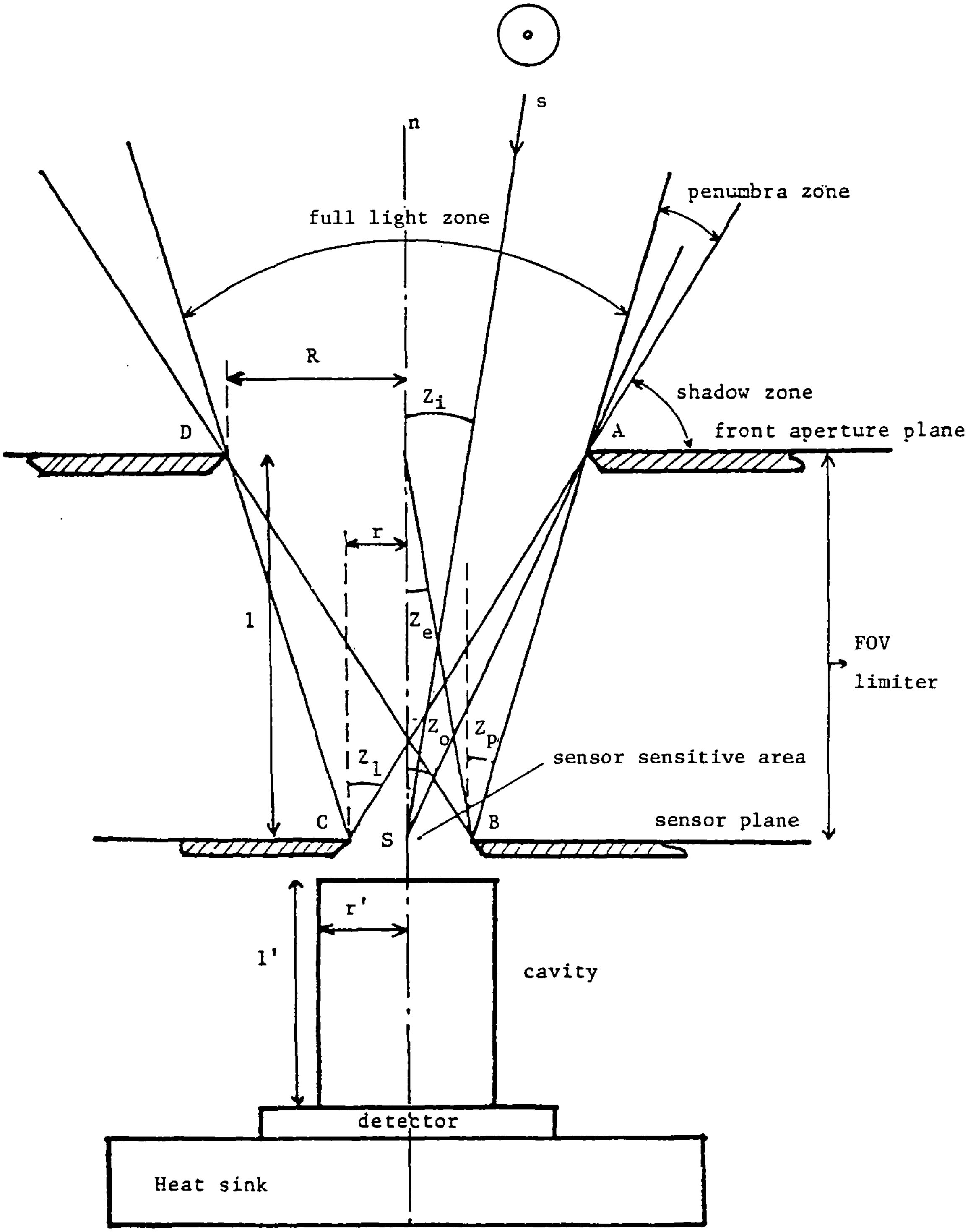

Figure 1.- Geometric characteristics.

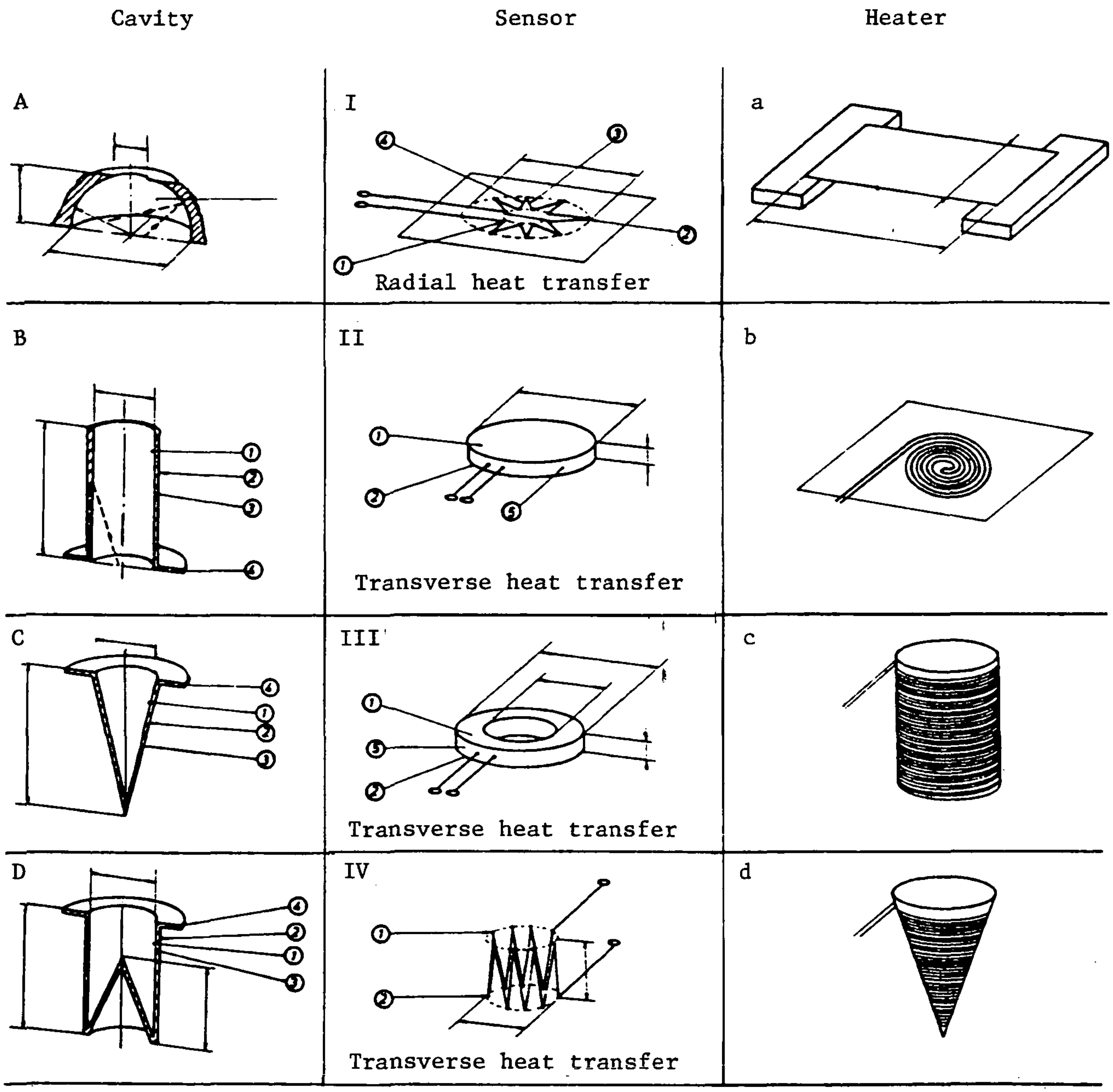

1. Absorbing surface ($\alpha \rightarrow 1$)
2. Reflecting surface
3. High thermal conductivity
4. Fixation ring

1. Hot junction
2. Cold junction
3. Type A element
4. Type B element
5. High thermal conductivity

Figure 2.- Absolute detector elements.

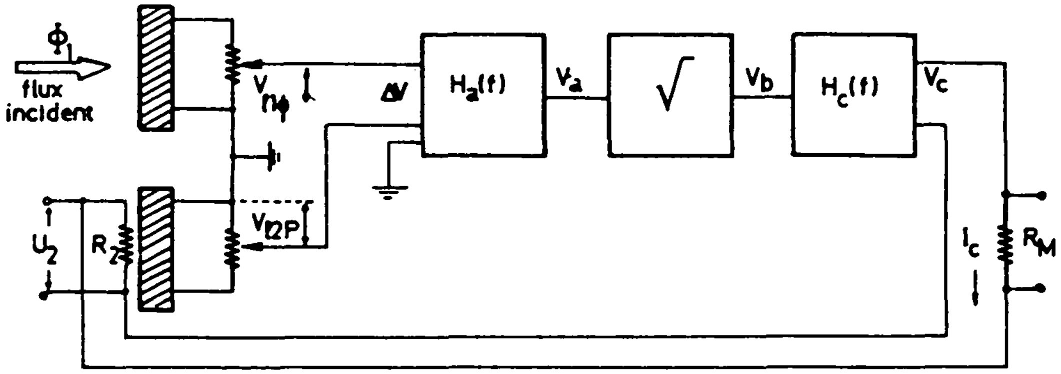

(a) Servo system for a double-compensated radiometer.

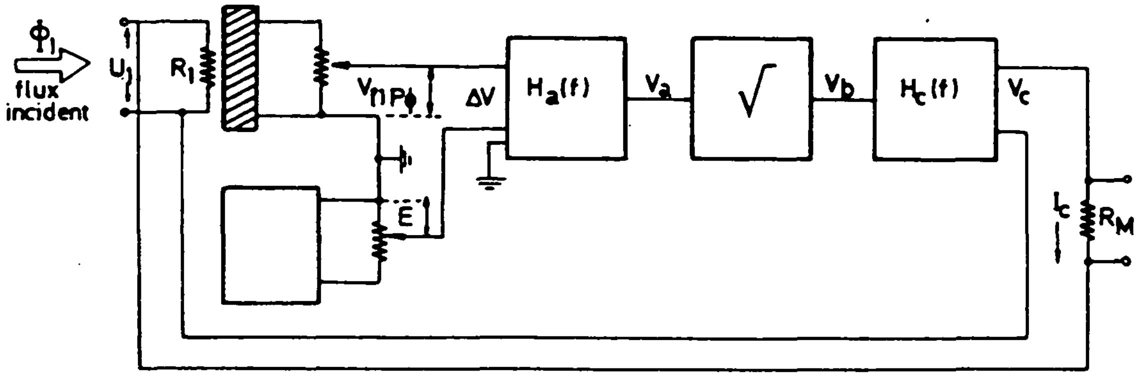

(b) Servo system for a thermally uncompensated single radiometer.

Figure 3.- Examples of radiometer servo systems.

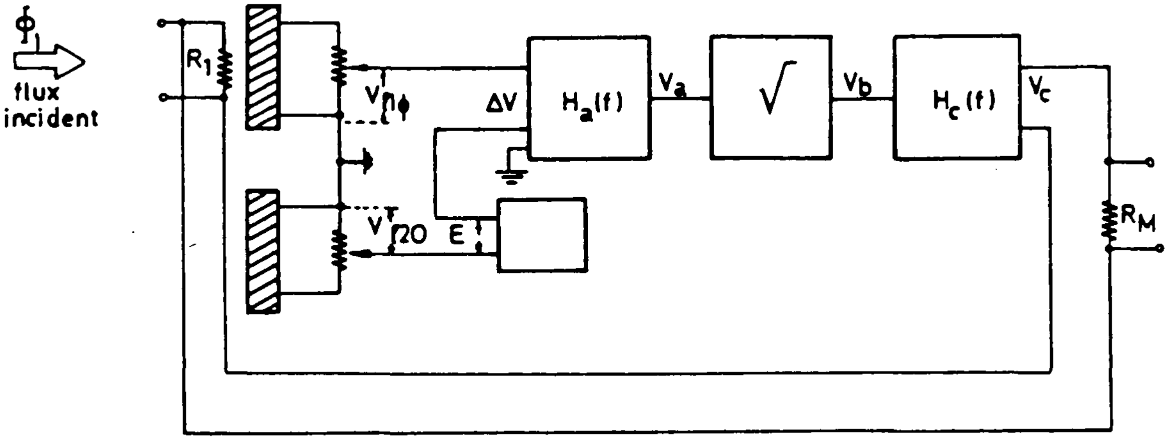

(c) Servo system for a thermally compensated radiometer.

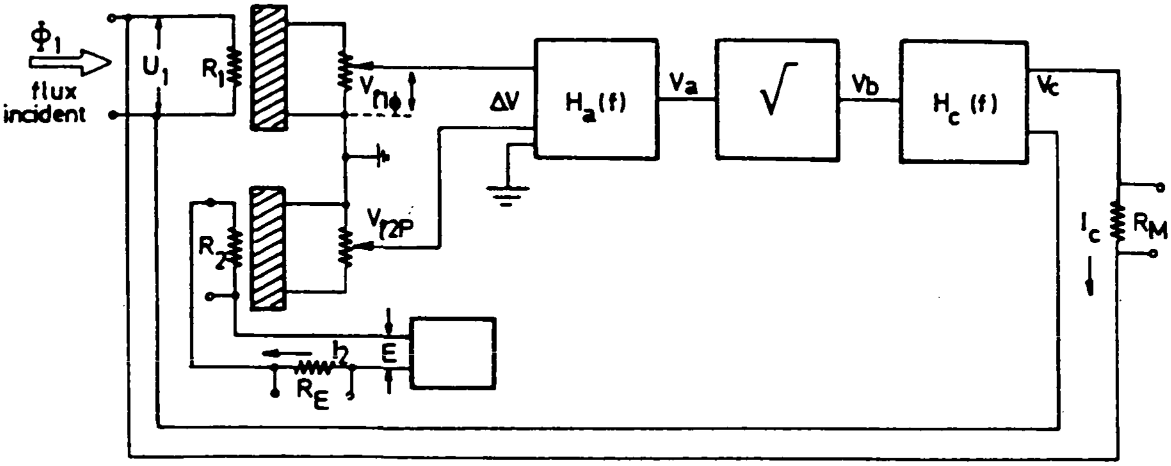

(d) Servo system for a symmetrically working compensated radiometer.

Figure 3.- Concluded.

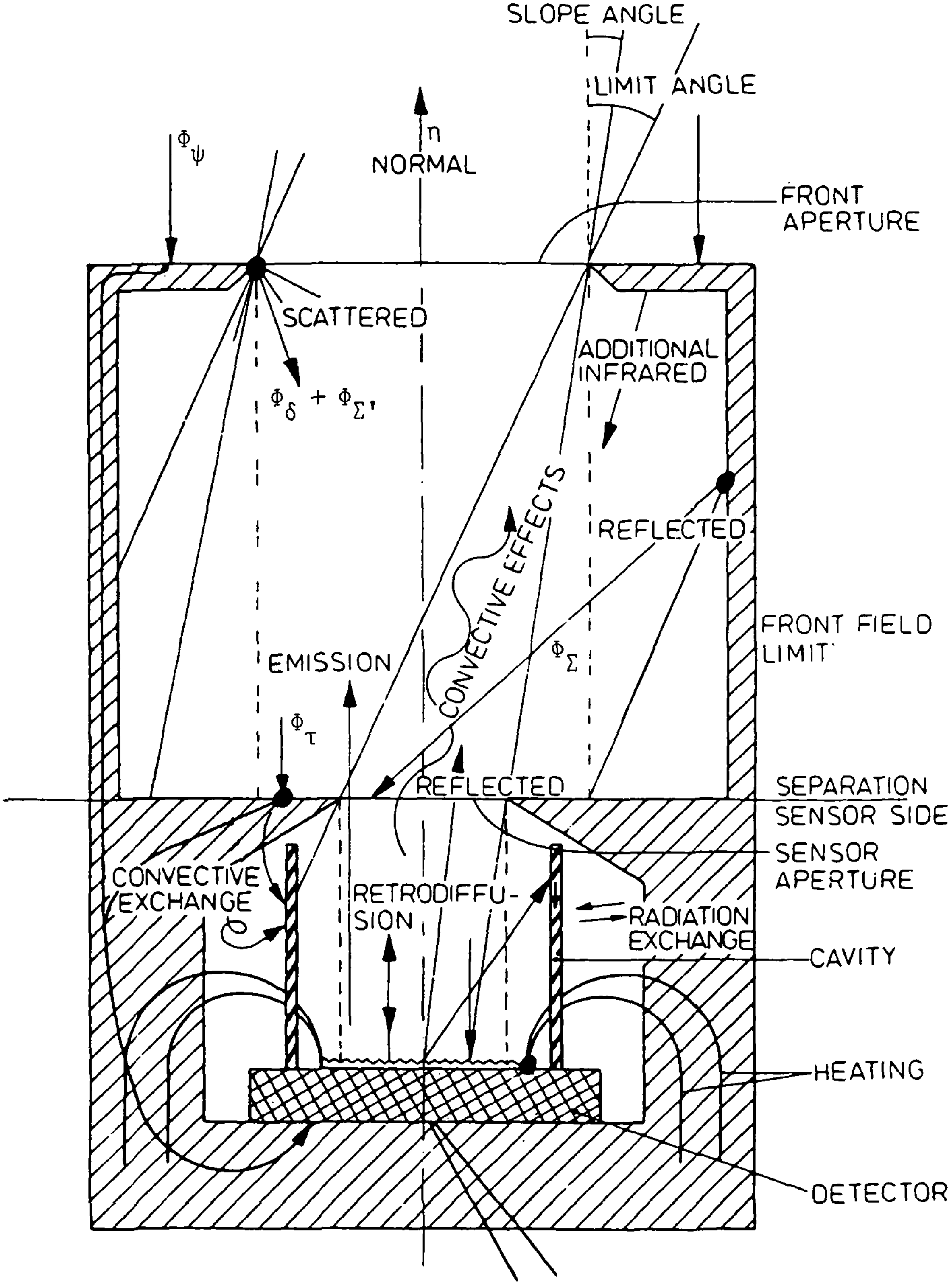

Figure 4.- Effects inducing errors on absolute radiometric measurements.

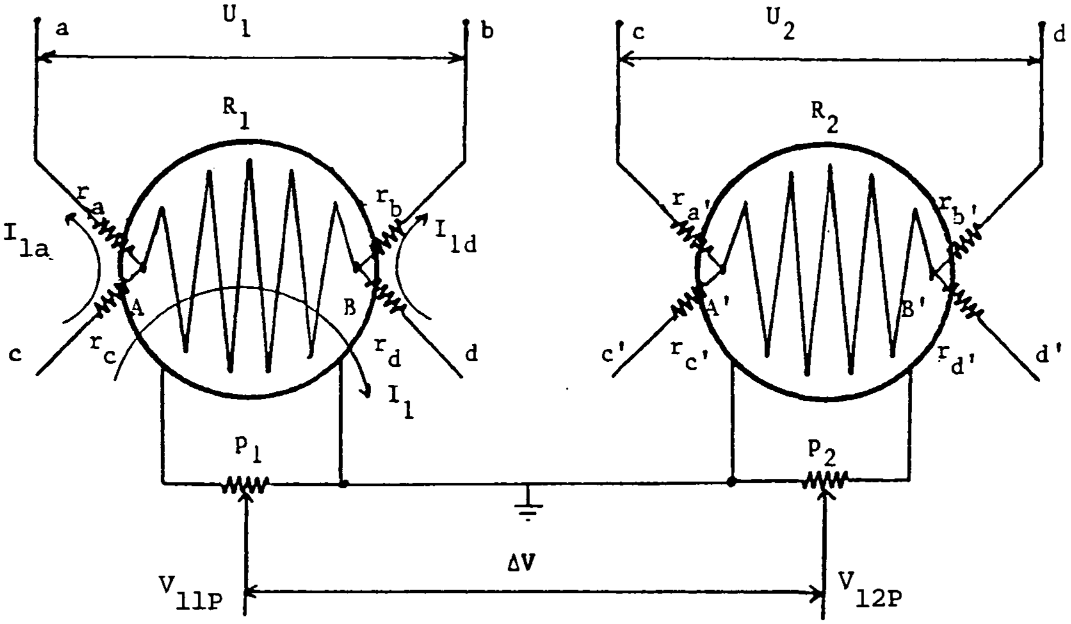

Figure 5.- Heat flux detectors and parasitic heating effect.

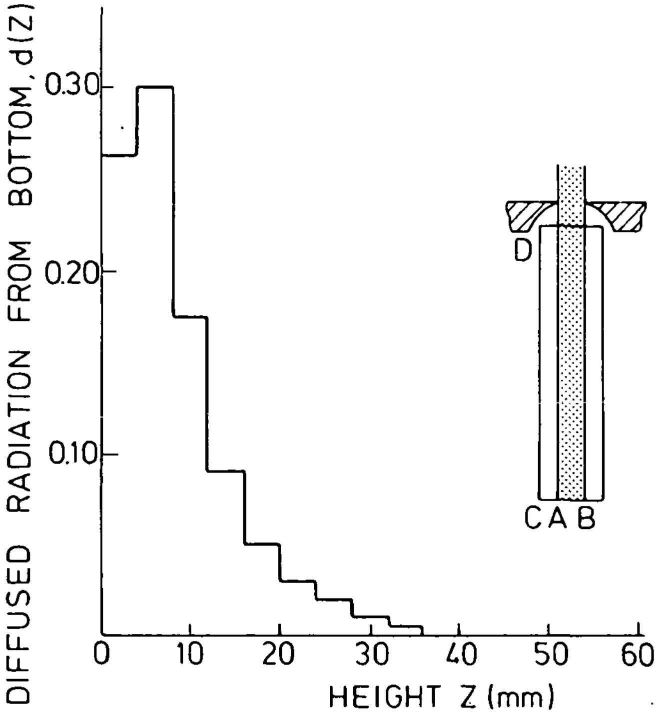

Figure 6.- Relative radiation distribution on inner wall of cavity cylinder.

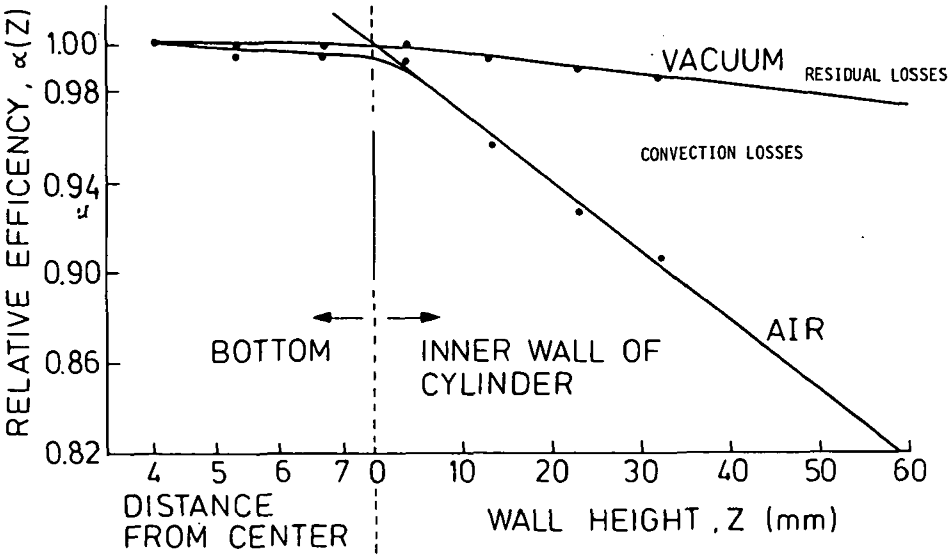

Figure 7.- Relative efficiency of cylindrical cavity (material: Ag, 0.5 mm thick).

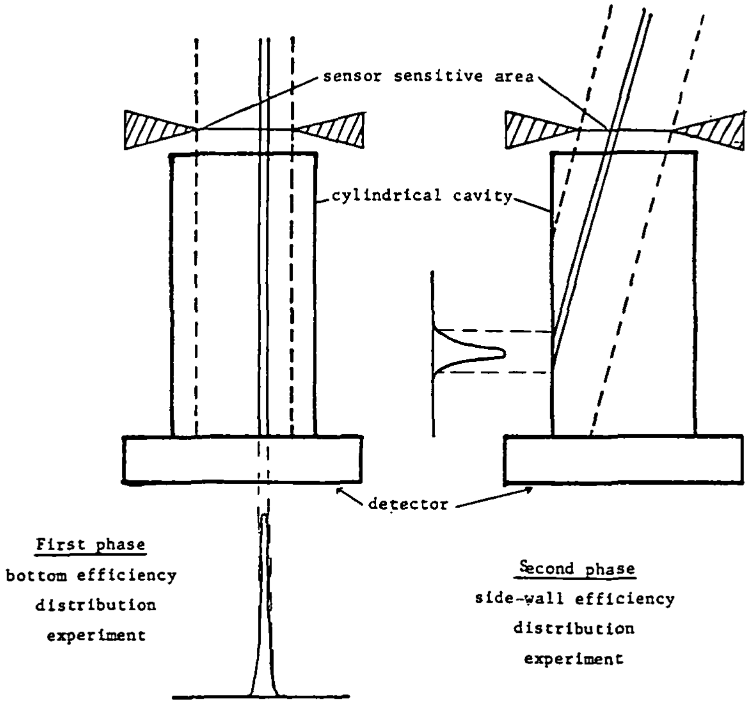

Figure 8.- Close-up of laser beam in cylindrical cavity.

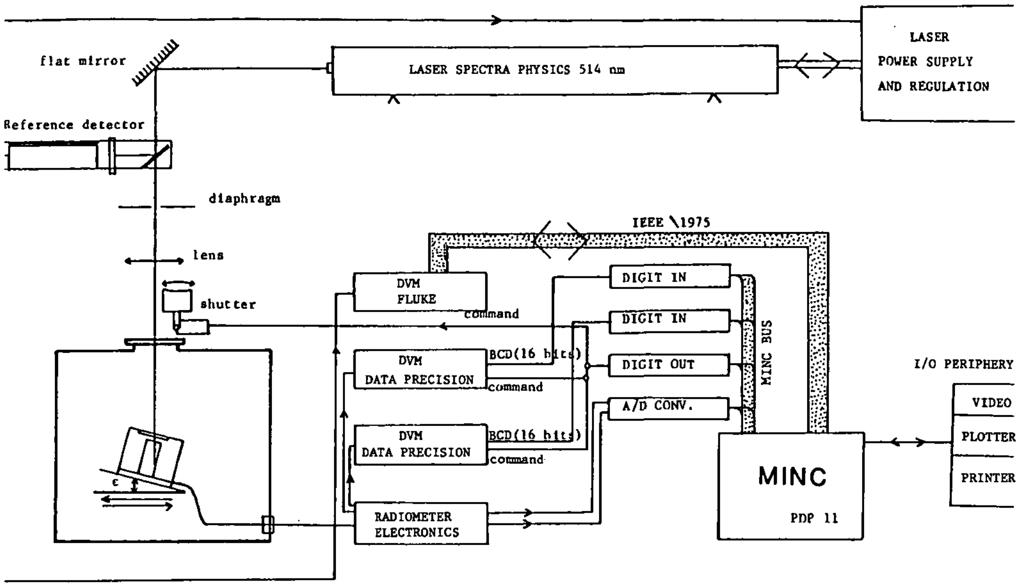

Figure 9.- Experimental setup for determination of relative efficiency distribution in radiometric cavity.

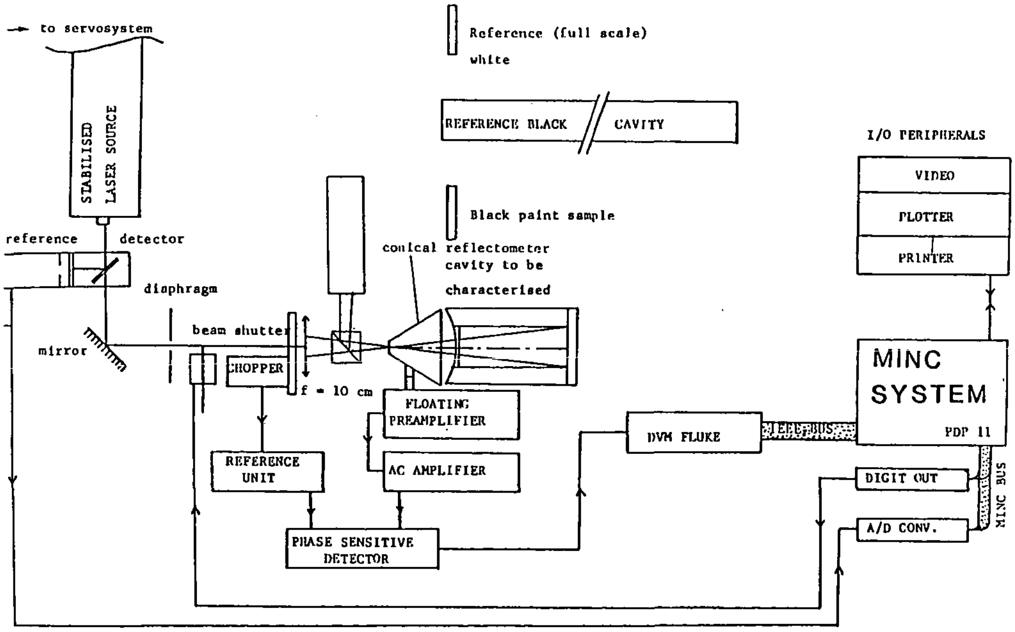

Figure 10.- Experimental setup for measurement of effective absorption coefficient and retroreflection of a cavity.

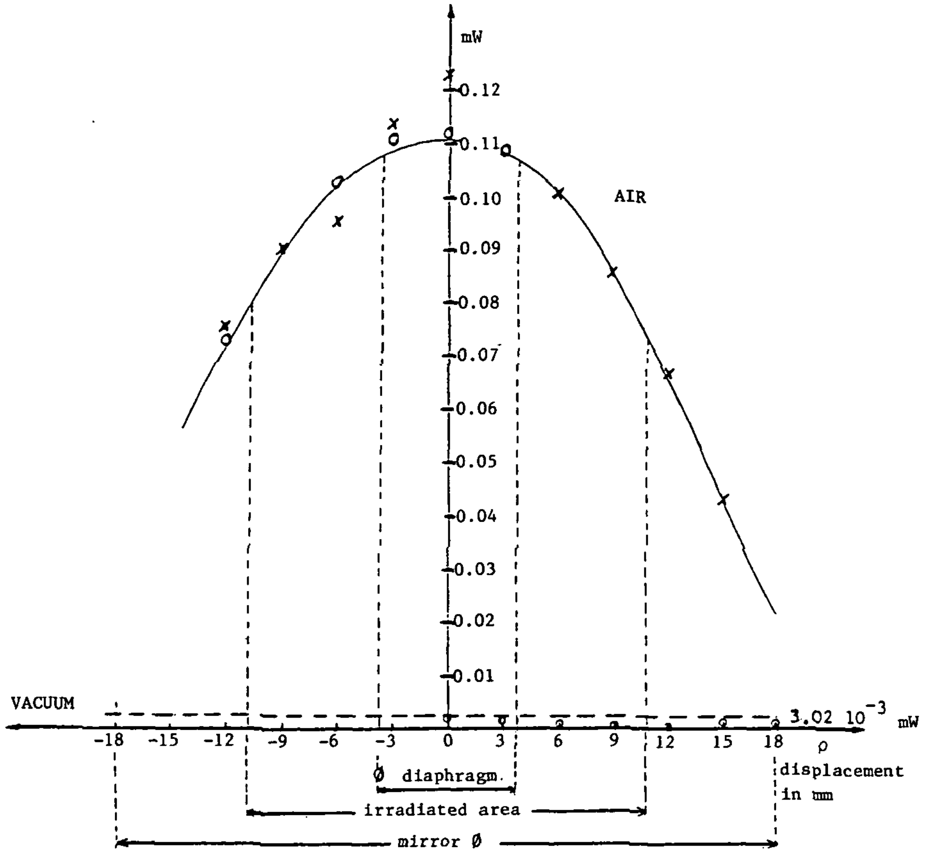

Figure 11.- Function *f*(ρ) measured for incident power of 200-mW laser beam. The experiment shows that $f(\rho) = -2.94 \times 10^{-4}\ \rho^2 - 2.192 \times 10^{-4}\ \rho + 0.11239$.

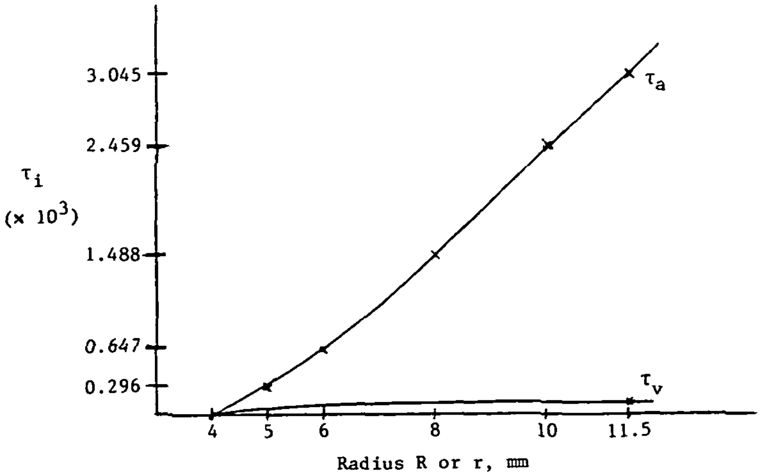

Figure 12.- Parameters τ_a and τ_v as a function of front aperture diameter.

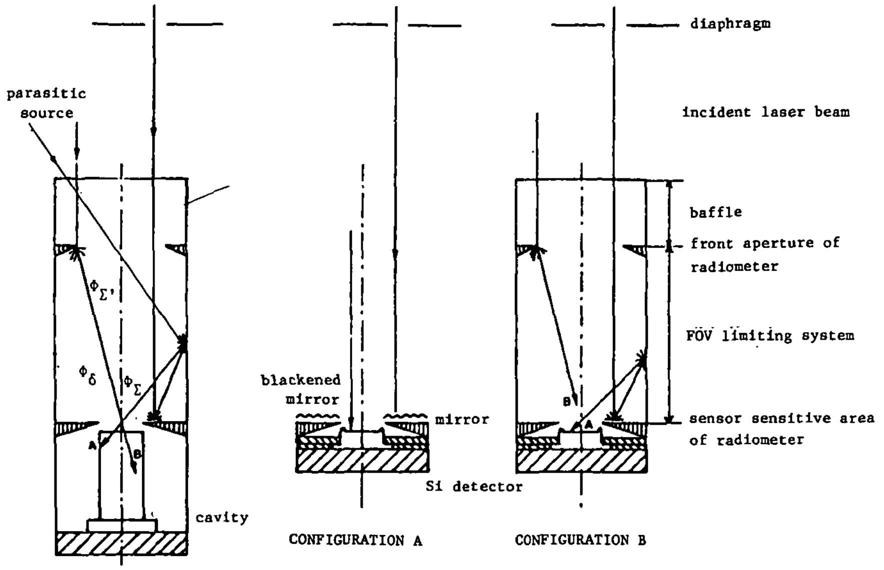

Figure 13.- Illustration of effects due to FOV limiting system. Two configurations are shown for the experiment.

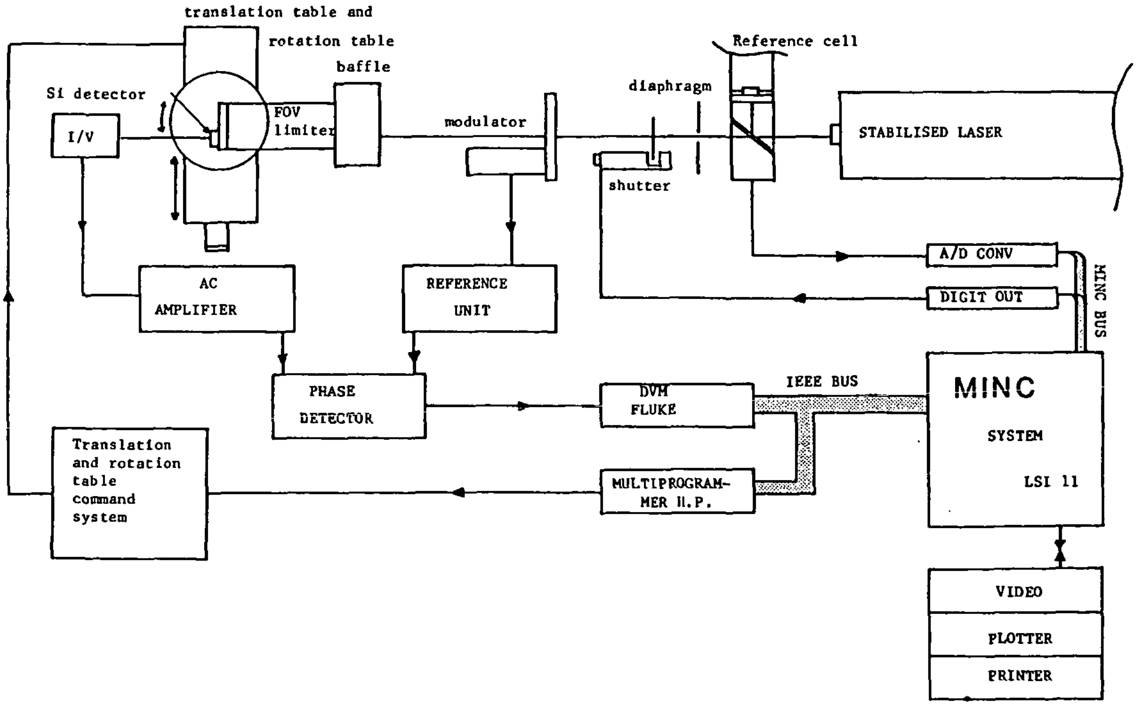

Figure 14.- Experimental setup for determination of FOV limiting system effects.

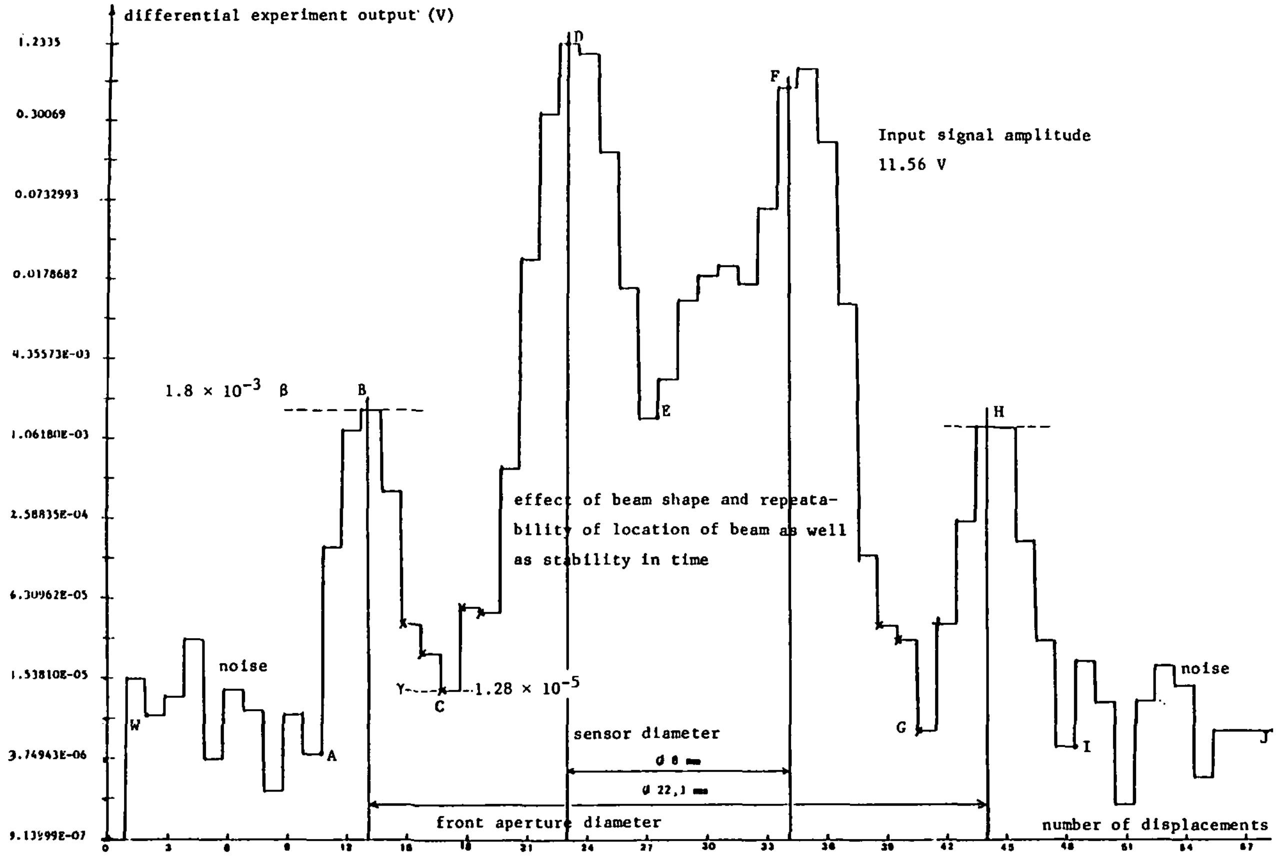

Figure 15.- Experimental result of setup shown in figure 14.

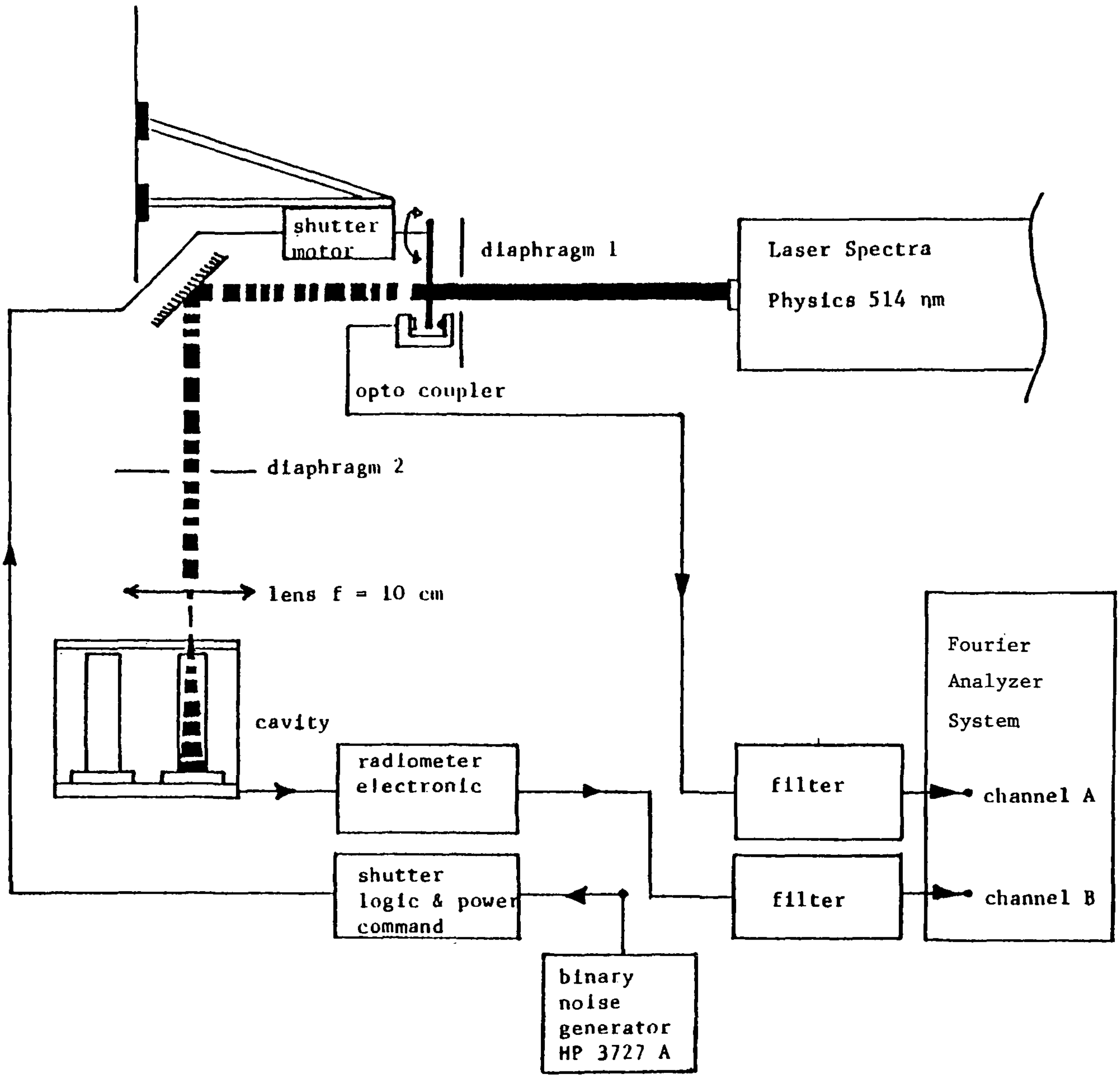

Figure 16.- Determination of transfer function of radiometer.

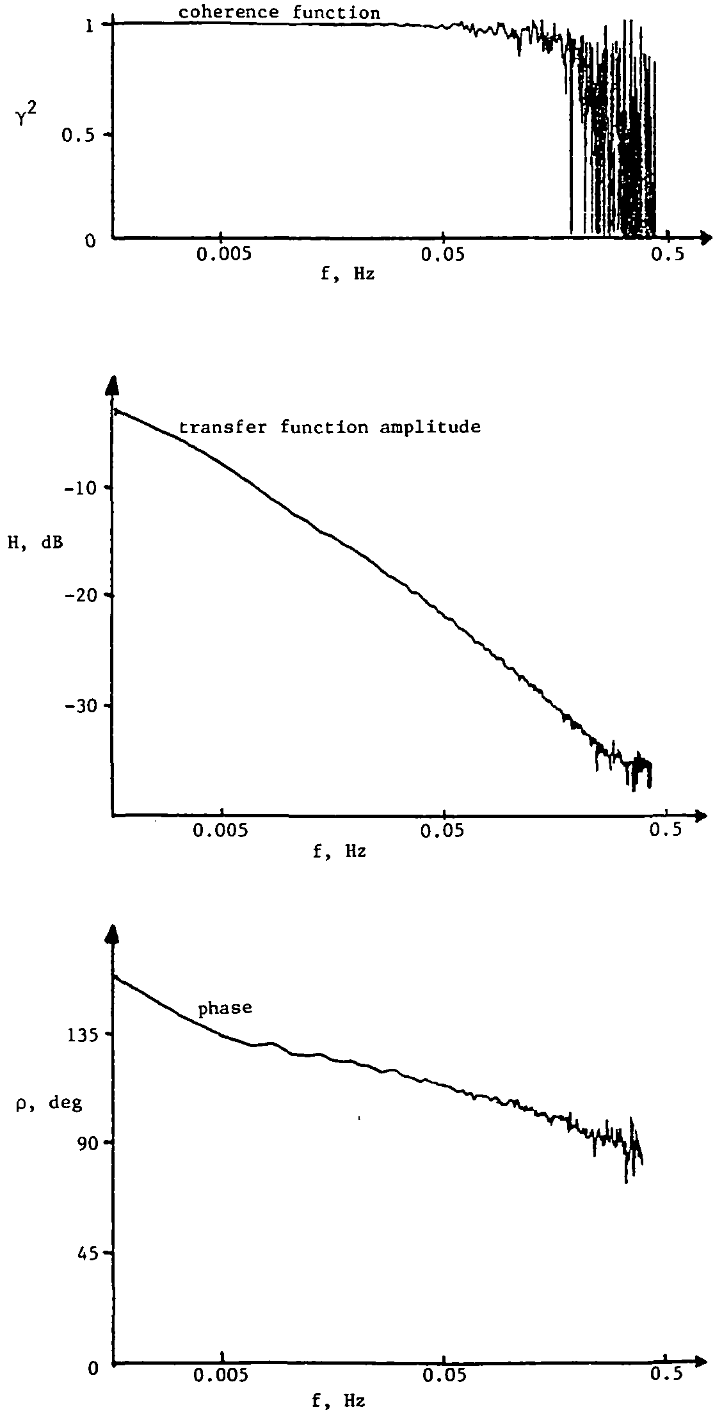

Figure 17.- Coherence and transfer functions of radiometer detector without servo system.

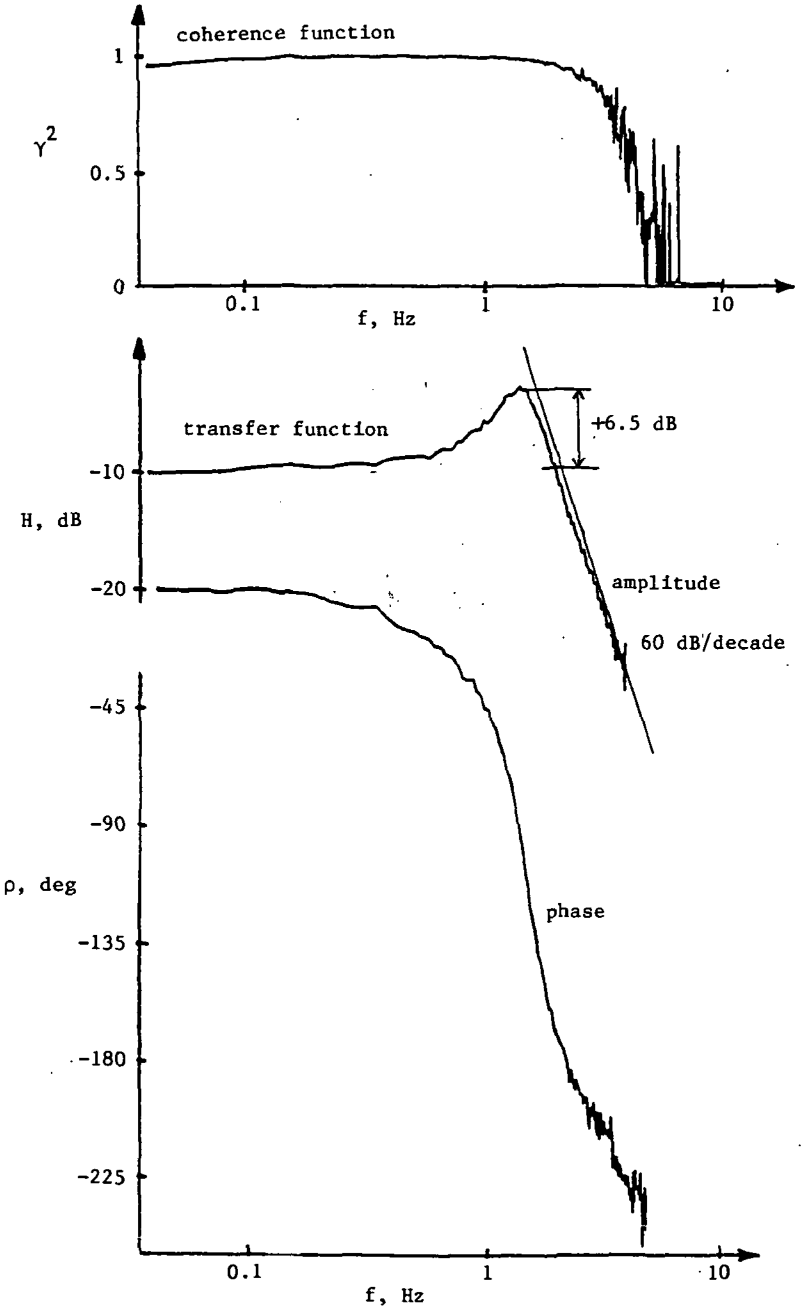

Figure 18.- Coherence and transfer functions of radiometric detector with servo system.

N82 33325

DERIVATION OF THE RADIATION BUDGET AT GROUND LEVEL FROM SATELLITE MEASUREMENTS

Ehrhard Raschke
University of Cologne
Cologne, Germany

INTRODUCTION

The radiation budget at the ground, consisting of two components, plays an important role in atmospheric and climatic energetics. Knowledge of the Earth radiation budget over spatial and temporal scales can be used for several purposes and applications, e.g.,

Radiation budget of the atmosphere

Heat input to the ocean

Convective activity over the ground

Energy budget at the surface

Climatological investigations and modeling

Use of solar energy

Agriculture and forestry

Ocean biology

Sufficiently dense and well-organized networks of measurement ground stations exist only in a few countries. These measurements are affected by the local environment. The data from many such stations have limited availability for scientific research. Therefore, methods must be developed and tested to determine the radiation budget at ground level from satellite measurements. Now and later, the basic data sets will be measurements of the planetary radiation budget components and/or the imaging multi-optical data of operational satellites. Future work at the University of Cologne will be directed toward solving individual problems inherent to this subject.

THE PROBLEM

Keep in mind that radiation budget values will be determined for areas approximately 100 km × 100 km. The two components of the radiation budget at the ground consist of upward and downward fluxes of solar and thermal radiation. They are discussed here separately.

Solar Radiation

The net radiation at the ground $M_{N,S}$ can be expressed as

$$M_{N,S} = G(1 - \alpha)$$

where

G	downward global radiation consisting of a diffuse and a direct component
α	surface albedo or reflectance

Although α, due to angular and spectral dependences, changes slightly with respect to cloud cover, humidity, and solar incidence, it can be estimated and mapped over most land surfaces rather accurately with satellite measurements. Atmospheric effects on measurements can be corrected with models. Its values over oceans are well known.

The global radiation G may also be determined with empirical relations. Some authors use simple regressions between satellite (e.g., GOES data) and ground-based network measurements, while we, along with others, consider clouds as perturbations in the field of clear sky radiation. We either parameterize the cloudiness in fractional units of optically dense clouds or assign specific radiative transfer characteristics to clouds such as those detected in sky photographs or from operational observers.

Thermal Radiation[1]

The net heat radiation at the ground $M_{N,t}$ can be expressed as

$$M_{N,t} = A\downarrow - \varepsilon\sigma T_S^4$$

where

$A\downarrow$	downward atmospheric radiation which is a function of the ambient temperature and moisture profile and of the cloudiness and cloud ceiling heights
ε	emissivity ($\approx$0.98 for most surfaces)
σ	Stefan-Boltzmann constant
T_S	surface temperature, itself a complex dependent of the heat (radiation and other heat fluxes) budget at the ground

---

[1] The symbols used here do not always correspond to those recommended for publication in the official literature.

C-2

No attempt has yet been made to parameterize this quantity. The cloud ceiling height, possibly the most critical quantity, can only be estimated from stereo techniques and/or condensation level calculations. Future laser techniques may improve the accuracy for thin cloud layers, e.g., cirrus.

SOME RESULTS OF OUR RESEARCH AT THE UNIVERSITY OF COLOGNE

Calculations of the Radiation Budget in a Circulation Model

We have developed an economic delta-two stream approximation; clouds had previously been treated with a random distribution in each layer. Therefore, we overestimated the albedo as seen from space and the global radiation at the ground.

Figure 1 shows a comparison of preliminary results of the global radiation calculated for the period February 15-25, 1976, using three methods: (1) the long-range forecasting model of the European Center of Medium Range Weather Forecast (ECMWF), (2) University of Cologne method, and (3) daily planetary radiation budget calculated from data from the National Oceanographic and Atmospheric Administration (NOAA) archives. These satellite data may contain systematic errors due to their method of calculation.

In table I, global averages of radiation budget components are compared. Table II shows a comparison with concurrent pyranometer measurements available from the rather crude World Meteorological Organization (WMO) network. Such comparisons require more careful design and maintenance of ground-Earth networks. As of March 31, 1980, our routine has been improved, and with the improved routine, further tests with the ECMWF will include recalculation for the same periods and calculation of the energetics for the special observing periods during the First Global Group Experiment (FGGE), e.g., January 1979. In the latter case, we intend to use Nimbus 7 Earth Radiation Budget Experiment (ERBE) data for comparison with calculated radiation budget components.

Radiative Transfer Characteristics of Clouds

In field experiments during the Joint Air-Sea Interaction project (1978 over the North-Atlantic Ocean), we measured radiation fields from aircraft and ships and also cloud structures (see, e.g., Schmetz and Raschke, 1980). Figure 2 shows a comparison between calculated and measured upward and downward solar radiation. Solid cloud decks, such as stratus, can satisfactorily be parameterized. Further work will be done for broken cloud fields. An experiment is planned for the fall of 1981.

Solar Radiation at Ground From Meteorological Data

A geostationary satellite, such as Meteosat, provides information on the cloud fields with a high spatial and temporal resolution. Thus, valuable information on the available solar energy can be derived for direct application.

Considering clouds as perturbations in the clear sky radiation field, we formulated the map of Germany shown in figure 3 (global radiation at 12:00 noon, average for June 1-15, 1979). Figure 4 shows a comparison with some simple pyranometer stations which is still not satisfactory.

Planetary Radiation Budget

The University of Cologne participates in preparations for the ERB satellite system, but we also intend to contribute actively to a European project. Therefore, a 10-channel radiometer is under study (breadboard model being built). Figure 5 shows a sketch.

The conical scan of this instrument (constant pixel size at all zenith angles of about 50-60 km) allows more accurate studies of the angular dependence of outgoing radiances and also stereo-analysis (with some limited accuracy) of cloud fields. The 10 channels are sensitive to the global radiation budget components, but also to variation of internal components, such as cloudiness, aerosols, water vapor, ozone, surface temperatures, and mean stratospheric temperatures. No spacecraft has yet been conceived as a platform.

REFERENCE

Schmetz, J.; and Raschke, E. 1980: Radiative Properties of Boundary Layer Clouds as Measured by an Aircraft. Univ. of Cologne paper presented at the International Radiation Symposium 1980 (Fort Collins, Colorado).

TABLE I.- RADIATION BUDGET GLOBAL AVERAGES

	ECMWF	Cologne	NOAA
Energy balance:			
Global, W/m^2	4.59	6.3	-5.56
Global mean of zonal variances, (W/m^2)^2	517.3	1827	493.9
Infrared emission:			
Global, W/m^2	240.45	239.6	241.6
Global mean of zonal variances, (W/m^2)^2	109.0	125.7	281.0
Planetary albedo:			
Global, percent	31.5	30.1	34.1
Global mean of zonal variances, (percent)^2	52.9	23.9	75.0
Infrared radiation balance:			
Global, surface, W/m^2	-55.84	-58.0	
Global mean of zonal variances, (W/m^2)^2	176.4	283.5	
Global radiation:			
Surface, W/m^2	174.24	179.6	173.7
Global mean of zonal variances, (W/m^2)^2	833.3	1630.3	5.70
Cloud cover:			
Global, percent	59.30	58.30	
Global mean of zonal variances, (percent)^2	320	370	

TABLE II.- COMPARISON OF VALUES OF GLOBAL RADIATION (W/m^2)

Period	Region	Ground measurements	ECMWF (a)	Cologne (a)	NOAA
August 25 to September 4, 1975	Africa I	161.1	218.9	132.5	205.3
	Africa II	239.2	218.5	174.6	227.7
	USA I	290.2	258.2	233.2	246.7
	USA II	229.2	220.8	192.5	217.0
	USA	259.7	239.5	212.9	231.9
	Western Europe	196.8	202.1	149.5	179.5
February 15 to 25, 1976	Africa I	238.5	202.6	148.0	220.7
	Africa II	273.8	179.8	162.5	227.8
	USA I	176.4	140.3	148.6	124.9
	USA II	158.8	132.0	131.8	108.7
	USA	167.6	136.2	140.2	116.8
	Western Europe	92.9	88.3	85.6	72.0

[a] Calculated in a circulation model.

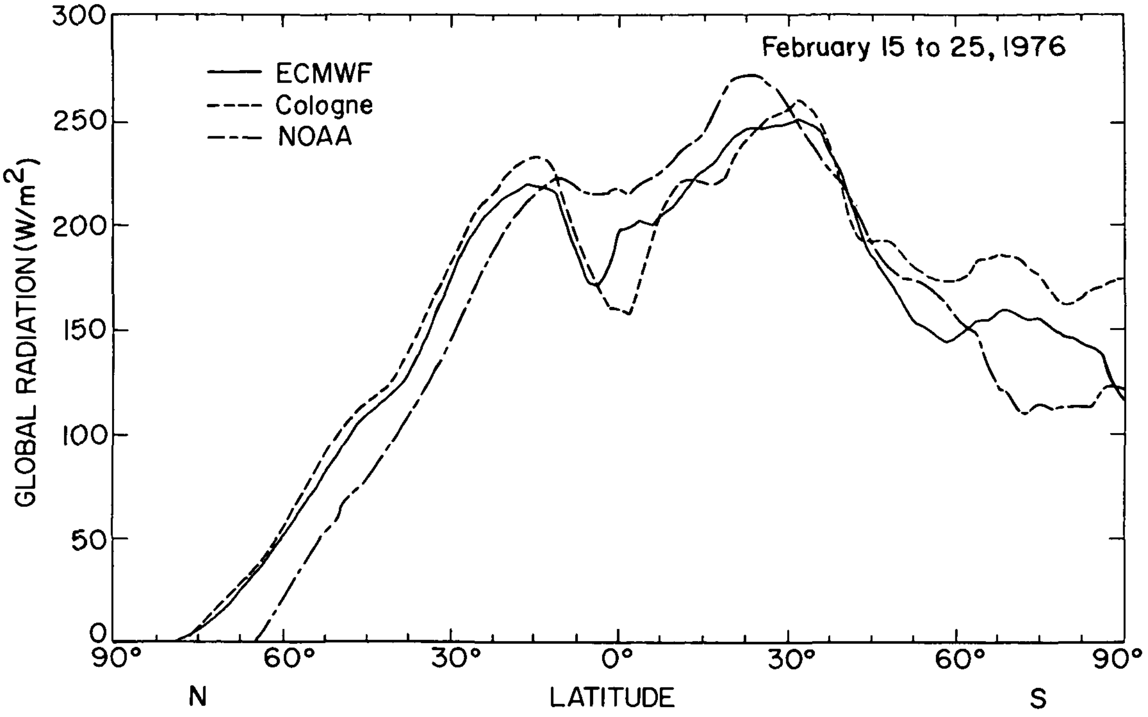

Figure 1.- Comparisons of global radiation calculated for the period of February 15-25, 1976.

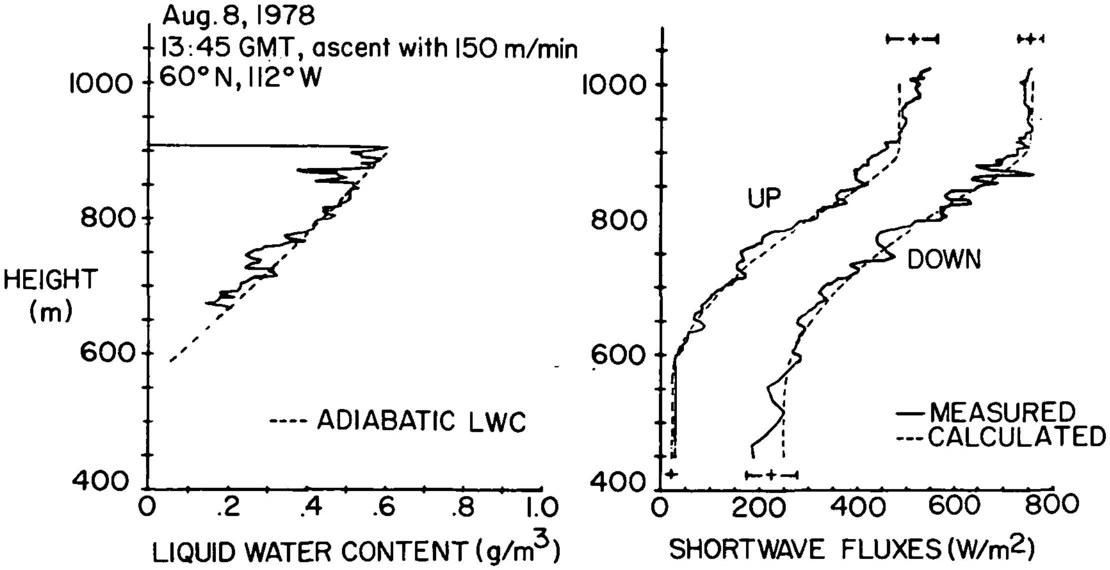

Figure 2.- Comparison of measured and calculated solar radiation components. (Schmetz and Raschke, 1980)

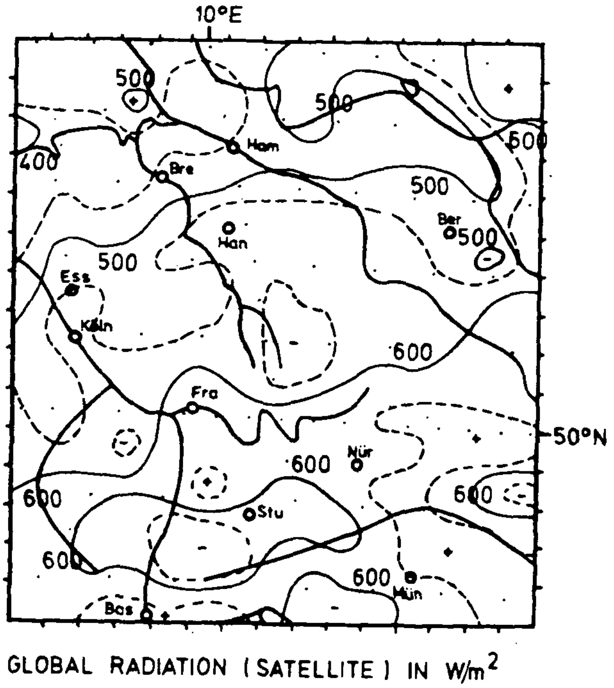

Figure 3.- Global radiation at 12:00 p.m. (average for June 1-15, 1979) over Germany as obtained from Meteosat.

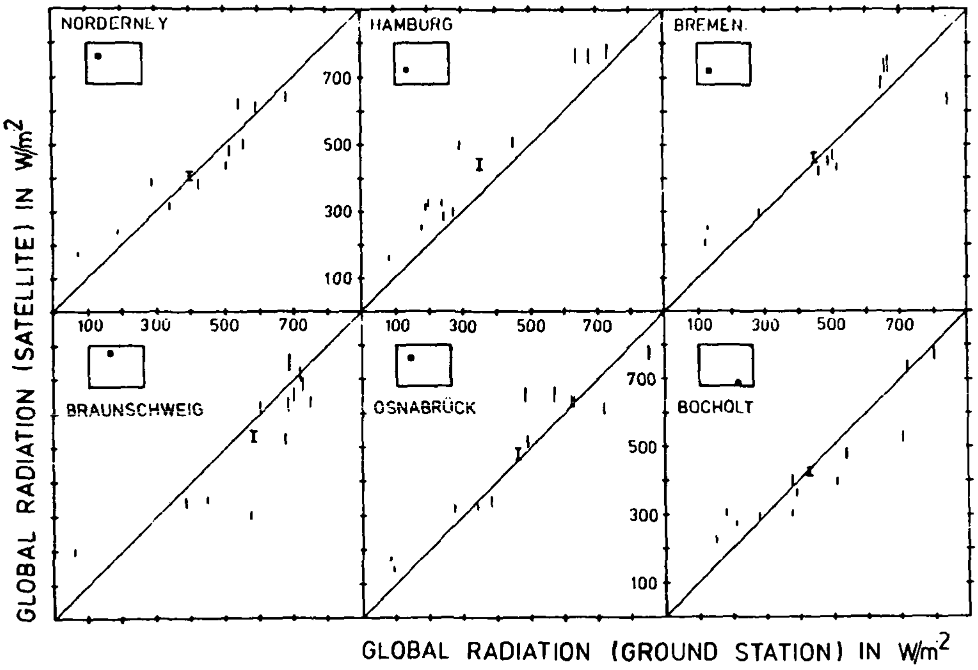

Figure 4.- Comparison between Meteosat and ground station global radiation at the ground. The inserted boxes show the location of each station relative to the grid center.

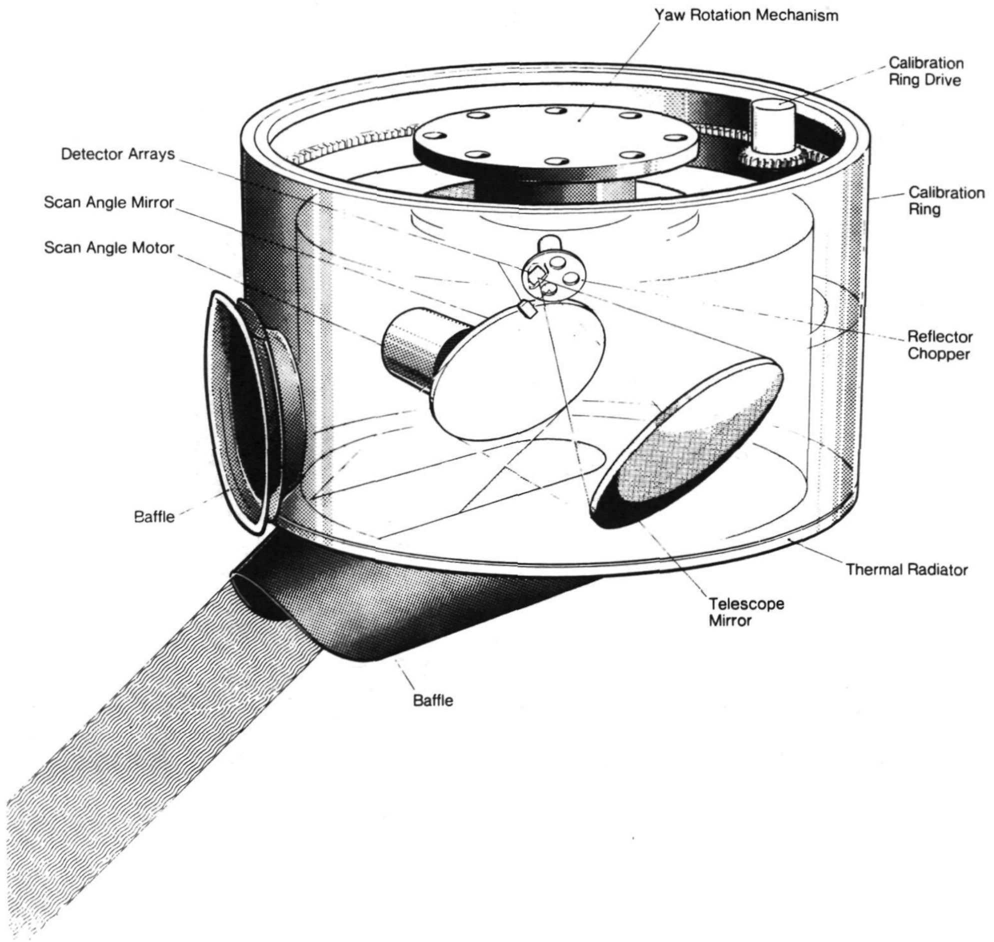

Channel no.	Spectral range, λ (μm)	Virtual target temperature, T (K)	Radiometric accuracy, (percent)	Objectives
A_1	0.25 - 4.0		1 - 2	Planetary and ground albedo
A_2	0.2 - 0.3		5	
A_3	0.35 - 0.7	Corresponding to 0.8 solar-constant	5	Aerosols, clouds
A_4	0.7 - 1.0		5	Vegetation
A_5	1.0 - 2.0		5	
B_1	4.0 - 70.0	200 - 300	1 - 2	Planetary emission
B_2	5.4 - 7.2	200 - 270	5	Water vapor
B_3	10.0 - 12.0	200 - 280	1 - 2	Surface temperature
B_4	9.3 - 9.8	200 - 280	5	Ozone
B_5	14.0 - 16.0	200 - 270	5	Stratospheric temperature

Figure 5.- Ten-channel conical scan radiometer.

N82 33326 D6

MEASUREMENT OF SOLAR RADIATION AT THE EARTH'S SURFACE

Fred L. Bartman
University of Michigan
Ann Arbor, Michigan

DEPARTMENT OF ENERGY SOLAR ENERGY METEOROLOGICAL RESEARCH AND TRAINING SITES (SEMRTS)

Eight universities have received grants from the U.S. Department of Energy (DOE) to establish Solar Energy Meteorological Research and Training Sites (SEMRTS). Under this SEMRTS program each of the universities selected will have the responsibility of carrying out a 5-year program of solar radiation measurements and establishing solar energy training courses in regular and special-educational programs at the university.

The eight universities selected are: University of Alaska, University of California at Davis, Georgia Institute of Technology, University of Hawaii, University of Michigan, State University of New York, Oregon State University, and Trinity University.

The regions of the United States for which each university has responsibility for a SEMRTS program are shown in figure 1. The University of Michigan has the responsibility for region 6, the Great Lakes States region, including the following states: North Dakota, South Dakota, Nebraska, Minnesota, Iowa, Wisconsin, Illinois, Indiana, Ohio, and Michigan. The measurement programs were begun October 1, 1977, and are expected to last through September 31, 1982.

The objective of this discussion is to provide a background of information regarding the characteristics of solar energy arriving at the Earth's surface. This will enable an understanding of the nature of the measurements being made. First we will look briefly at the history of the measurement of surface solar radiation in the United States. After this, characteristics of the SEMRTS measurement program will be described, and some of the interesting characteristics of solar energy measurements already made, as selected from the literature, will be presented.

DEFINITIONS: SOLAR RADIATION CHARACTERISTICS

The nature of solar radiation as it arrives at the top of the Earth's atmosphere and its modification through interaction with the Earth's atmosphere and clouds are discussed in many textbooks on meteorology and physical climatology. All aspects of this topic are discussed in the course notes for the University of Michigan College of Engineering Intensive Summer Conference Short Course, which was last held in Ann Arbor on July 9-10, 1979. (These notes

98 n

provided much of the background material for this presentation. In particular, the brief outline of the history of solar radiation measurements contained herein is based on material assembled by Associate Professor Dennis G. Baker.)

Solar Radiation Outside the Earth's Atmosphere

The amount of solar radiant energy arriving per unit time at a unit area of surface at the top of the Earth's atmosphere normal to the beam of radiation from the Sun, at the mean Earth-Sun distance, is called the solar constant. At this date it is thought to be 1367 W/m^2 (Hickey, 1978), or, in other commonly used units, 1.96 cal cm^{-2} min^{-1}. The spectral distribution of the solar radiation arriving at the top of the Earth's atmosphere in the UV, visible, and near-IR portions of the spectrum is shown in figure 2 compared with the amount of solar spectral flux density that would arrive at that point if the Sun radiated as a 5000-K, 5800-K, or 6000-K blackbody. The fraction of the solar constant which lies in three major wavelength bands is as follows:

Wavelength range, μm	0-0.38	0.38-0.78	0.78-∞
Fraction in range	0.0700	0.4729	0.4571

A much more detailed breakdown of the solar flux outside the Earth's atmosphere is given in table I.

The flux of solar radiation arriving at the Earth varies inversely as the square of the Earth-Sun distance. The annual variation of the solar flux during the course of a year as the Earth moves in its elliptical orbit is given in table II.

A quantity of interest for meteorological and climatological purposes is the total daily solar radiation arriving at a horizontal surface outside the Earth's atmosphere at an arbitrary latitude b. This quantity can be calculated from the equation

$$E_D = H_S R_{ES}^2 \int_{t_1}^{t_2} \frac{\cos\theta_o}{r_{ES}^2}\,dt \qquad (1)$$

where

E_D	total daily solar radiation on a horizontal plane
H_S	solar constant
R_{ES}^2	square of the mean Earth-Sun distance
r_{ES}^2	square of the Earth-Sun distance on the day of concern

θ_o zenith angle of the Sun

t_1, t_2 time of sunrise and sunset, respectively

The zenith angle of the Sun can be calculated from

$$\cos \theta = \sin b \sin \delta_s + \cos b \cos \delta_s \cos h_s \tag{2}$$

where

b latitude of the point on the surface of the Earth for which the calculation is made

δ_s declination angle of the Sun

h_s Sun's hour angle, which varies during the day

The results of the integration of equation (1) for each day of the year and all latitudes are shown in figure 3.

Effect of Earth's Atmosphere on Solar Radiation

The beam of direct radiation from the Sun is attenuated as it passes through the Earth's atmosphere by absorption by some of the minor gaseous constituents of the Earth's atmosphere, by Rayleigh scattering by the gaseous molecules of the Earth's atmosphere, and by Mie scattering and absorption by aerosols in the Earth's atmosphere. The atmospheric gases having the greatest effect in absorbing solar energy are ozone (O_3), carbon dioxide (CO_2), and water vapor (H_2O).

With suitable modeling, the effect of the above factors on the radiation in the direct beam of the Sun is as illustrated in figure 4, which shows the results of such a calculation by Gates (1966). This figure shows the spectral distribution of the radiation arriving at the Earth's surface in the direct beam of the Sun under clear sky conditions and with normal amounts of O_3 and CO_2 and rather small amounts of H_2O and aerosols in the atmosphere. Figure 5 shows the results of a similar calculation where the amounts of radiation absorbed and scattered out of the direct beam of the Sun by the various factors are identified (Paltridge and Platt, 1976).

The amount of H_2O and aerosols in the Earth's atmosphere is highly variable. The effect of this on the Earth's solar radiation is described by a quantity called the turbidity. This phenomenon has been studied with the aim of defining a parameter which can be evaluated by measurements of direct solar radiation. The Angstrom (1961) turbidity coefficient β is defined by the equation

$$\tau_\lambda = \beta\lambda^{-\alpha} \tag{3}$$

Measurements have shown that an average value of α is 1.3. For simplicity, then, one can use the equation

$$\tau_\lambda = \beta\lambda^{-1.3} \tag{4}$$

to provide a measurement of the amount of aerosol in the atmosphere. Using a filter at a wavelength of 0.5 μm, where water vapor has a negligible absorbing effect, the extinction τ_λ can be measured and β can be calculated. Volz (1969) has defined the turbidity coefficient in a somewhat similar fashion. His factor is 1.069 times that of Angstrom. Average values for July and December for the 13-year period from 1961 to 1974 are given in figures 6 and 7 (Flowers et al., 1969). The Volz turbidity coefficient is used in these figures. (Note that the average turbidity is significantly higher in the eastern part of the United States.)

The scattering of solar radiation by the air molecules and aerosols in the atmosphere results in the skylight which arrives at the Earth from all directions. Rayleigh scattering is greater in the forward and backward directions, but has a considerable amount of scattering in the sidewise direction. Aerosol scattering is mainly in the forward direction. The net result is that there is a large amount of scattering in the forward direction, as shown in figure 8. The scattering effects are wavelength dependent; however, the features shown in the figure appear in the skylight intensity to some extent at all wavelengths.

Solar Radiation Quantities Measured at Earth's Surface

The spatial distribution of the solar radiation arriving at the surface of the Earth and the instruments which are used to measure the several kinds of solar radiation are shown schematically in figure 9. The direct solar radiation (i.e., the almost-parallel beam of radiation) plus some of the circumsolar radiation (i.e., a portion of the quite intense forward-scattered radiation) is measured by a pyrheliometer, which tracks the Sun from sunrise until sunset. The global radiation (i.e., all of the radiation arriving on a horizontal surface from the hemispherical dome of the sky) is measured by an instrument called a pyranometer. The diffuse radiation from the sky, not including the direct plus circumsolar radiation, is measured by a pyranometer with a shadow band which is adjusted to keep the direct beam from arriving at the detector at all times as the Sun passes in its daily arc across the sky. A pyranometer with an occulting disk which tracks the Sun can also be used. When a shadow band is used, a portion of the diffuse radiation from the sky is also prevented from reaching the detector. A correction must be made for this effect. The occulting disk, if designed and operated properly, would normally not need a correction factor.

Each of these three measurements can be made with a spectral response which covers almost all of the spectral range of solar radiation arriving at the surface. In practice, the wavelength range measured is from 0.28 to 2.8 μm (clear glass) or from 0.29 to 4.5 μm (quartz). Additional measurements are made with filters. The details of the filter measurements will be noted subsequently in this report.

The global downcoming infrared radiation from the sky in the spectral range of 4 to 50 μm is also measured by a pyranometer-type instrument called a pyrgeometer. The ultraviolet radiation from the hemisphere of the sky in the spectral range 0.285 to 0.385 μm is measured with a UV radiometer (photometer). Another instrument used is a Campbell-Stokes sunshine recorder, which measures the duration instead of the intensity of the solar radiation. It consists of a spherical glass ball which focuses the Sun's rays onto the heat-sensitive surface of a card which is fastened into a spherical card holder. The focused Sun's rays burn a narrow track onto the card when the intensity of the direct beam of the Sun is greater than 0.1 to 0.2 of the solar constant. A time scale on the card enables the determination of the duration of sunshine in hours and tenths of hours.

Atmospheric turbidity is measured quite conveniently with a Volz sunphotometer, a compact instrument with appropriate filters, optics, and detector. It is hand held, and readings can usually be taken in less than a minute. The turbidity is then calculated. More details on the solar energy measurements at the University of Michigan are given subsequently in this report.

BRIEF HISTORY OF SOLAR ENERGY MEASUREMENTS IN THE U.S.

This historical outline of solar radiation measurements in the United States considers those data which have been archived at the National Climatic Center in Asheville, N.C. Other data, taken by individuals, private organizations, universities, and government laboratories, which have not been archived at the National Climatic Center are not discussed.

Direct solar radiation measurements were taken as far back as 1902 at Asheville, N.C. The network of normal-incidence measurements of direct solar radiation then slowly expanded, as shown in figure 10. Global solar radiation measurements were begun in 1906. The network of global solar radiation measurement stations developed slowly. The network locations as of 1939 are shown in figure 11. The network was cut back during World War II, but by 1950 it had increased to 83 stations (fig. 12), and by 1972 90 sites were regularly reporting data (fig. 13).

Problems with the global radiation measurements developed because of inadequate calibration procedures and also because of deterioration of a Parson's black paint used on the detectors of some pyranometers. The accuracy of the data in the network became questionable in the 1960's. Since 1972, data from only a limited number of 28 stations using the Eppley Precision Spectral Pyranometer (PSP) have been approved for publication. As a result of these problems, it was decided to start anew in building up a network with modern equipment. The new network is shown in figure 14. The locations of some of the DOE SEMRTS stations are also shown in this figure.

The data for the period of problem measurements have been rehabilitated and augmented. Rehabilitation was accomplished by the procedure of examining data for clear days under the assumption that there were no trends in the data. Three models were developed as follows: (1) standard year clear solar noon, (2) total horizontal solar radiation model, and (3) direct normal solar radiation model. The models were used to correct and fill in data gaps and to add direct normal values at the stations indicated in figure 15.

MEASUREMENTS AT UNIV. OF MICHIGAN AND OTHER SEMRTS SITES

The measurements being made at all SEMRTS sites are indicated in the specifications given in tables III, IV, and V. Radiation measurements are listed in table III, meteorological measurements appear in table IV, and calibration procedures are given in table V. These specifications may be changed slightly in some detail, but for the most part they are being adhered to at the SEMRTS stations.

Measurements at Univ. of Michigan Primary Site

Various radiation measurements are being made at the University of Michigan primary site on the roof of the Space Research Building. Global solar radiation on a horizontal plane is being measured by an Eppley Precision Spectral Pyranometer. A clear glass dome with a wavelength response of 0.285 to 2.8 µm is being used. Measurements are also made on occasion with the following filter domes: yellow (GG14), 0.5 to 2.8 µm; orange (OG1), 0.525 to 2.8 µm; red (RG2), 0.63 to 2.8 µm; and dark red (RG8), 0.71 to 2.7 µm. Diffuse measurements are made with an Eppley PSP with a clear glass dome and an occulting disk. Measurements are also made with an Eppley PSP tilted to the south at an angle from the zenith equal to the latitude of the station. A clear glass dome is used and the instrument is shielded so that it does not receive reflected radiation from the Earth.

Global ultraviolet radiation is measured with an Eppley UV Radiometer in the spectral range from 0.295 to 0.385 µm, and global infrared radiation is measured with an Eppley Infrared Radiometer (pyrgeometer) with a wavelength response of 4 to 50 µm. There are also plans to bring into operation a Funk total hemispherical radiometer, which will measure in the range from 0.2 to 60 µm. Measurements are also made with the Campbell-Stokes sunshine recorder (duration of sunlight) and with the Volz sunphotometer (turbidity). Photographs of the site and of some of the instruments used for the solar energy measurements are shown in figures 16 through 20. The recording station and mobile solar energy measurement facility are shown in figures 21 and 22, respectively.

Measurements With Mobile Univ. of Michigan Solar Energy Facility and at Other Locations in Great Lakes States Area

The mobile measurement facility shown in figure 22 contains two Eppley Precision Spectral Pyranometers, which measure direct plus diffuse solar radiation on a horizontal surface in the 0.28- to 2.8-μm spectral region and in four narrower spectral regions: 0.5 to 2.8 μm, 0.53 to 2.8 μm, 0.63 to 2.8 μm, and 0.7 to 2.8 μm. Another Eppley PSP measures direct plus diffuse solar radiation on a plane surface which can be inclined at various angles. An Eppley Normal Incidence Pyrheliometer (NIP) with a solar tracker measures the direct component of solar radiation. The facility has a collapsible meteorological tower for measurements of wind speed, wind direction, temperature, and dew point at heights up to 10 m. Measurements have been made with the mobile facility at Jordan College in Michigan, Iron Mountain, Mich., and Burlington, Vt.

Three secondary stations have been established at sites in the Great Lakes States area where long-term hourly data exist; i.e., Omaha, Neb.; Madison, Wis.; and the Argonne National Laboratory in Lemont, Ill. Each of these stations contains an Eppley PSP inclined at an angle equal to the station's latitude, along with an array of recording devices.

CHARACTERISTICS OF SOLAR RADIATION ARRIVING AT THE EARTH'S SURFACE

Figure 23 shows the annual variation of daily solar radiation arriving at the surface on cloudless days at Ann Arbor. These measurements were made at the University of Michigan primary site. The curves show direct radiation on a plane normal to the Sun's rays, global radiation on a horizontal plane, global radiation on a plane tilted by 42.3°, global radiation on a horizontal plane with a 0.63- to 2.8-μm filter, diffuse radiation on a horizontal plane, and ultraviolet radiation on a horizontal plane.

A typical curve of direct normal, total (global) horizontal, and diffuse horizontal radiation (fig. 24) shows the variation in these quantities from sunrise to sunset on a clear day. These measurements should satisfy the following equation at any time of the day:

$$\text{total (global)} = \text{direct} \cos \theta + \text{diffuse}$$

where θ is the solar zenith angle. The data shown in this figure are for Albuquerque, N.M.

Since not all days are clear, however, the direct solar radiation is often much less than that shown in figure 24. Direct normal solar radiation for Albuquerque is shown in figure 25 for the 31 days of January 1962. The daily totals of direct normal solar radiation for each day for a 4-year period at Albuquerque are shown in figure 26. The top curve shows the maximum available direct normal solar radiation. The curve of the average value shows that at Albuquerque the amount of direct normal solar radiation is, on the average, about 75 percent of the maximum possible. In contrast, the average amount of direct normal solar radiation at Maynard, Mass., is about 50 percent of the maximum possible (fig. 27).

Average measured global solar radiation on a horizontal surface is shown in figure 28 for the period of 1 year for four locations under three different sky conditions (clear skies, 50-percent cloud cover, and 100-percent cloud cover). In each case the solar radiation at the top of the atmosphere is shown for comparison. Note that the decrease in solar radiation in going from clear sky to 50-percent cloud cover is much less than the decrease in going from 50-percent to 100-percent cloud cover.

Figures 29 and 30 show the distribution over the United States, in May, of mean daily direct solar radiation and mean daily global solar radiation on a horizontal surface (Lester Machta, Air Resources Laboratory, NOAA, private communication, 1979). The superiority of the southwest part of the U.S. for solar energy applications is obvious.

The effects of turbidity on the direct and circumsolar radiation are shown in figure 31. On a clear day with low turbidity, with the circumsolar radiation equal to 1 percent of the direct normal measured value, the intensity toward the center of the Sun is great and the diameter of the Sun is well defined. When the turbidity is high, with the circumsolar radiation equal to 25.6 percent of the direct normal value, the intensity toward the center of the Sun is much lower, the diameter of the Sun is not as well defined, and it appears to be smaller than normal.

REFERENCES

Angstrom, A. 1961: Techniques of Determining the Turbidity of the Atmosphere. Tellus, vol. 13, no. 2, pp. 214-223.

Baker, Donald G.; and Klink, John C. 1975: Solar Radiation Reception: Probabilities and Areal Distribution in the North Central Region. North Central Regional Research Publication No. 225, Univ. of Minnesota Agricultural Experiment Station Tech. Bulletin No. 300.

Carter, E. A.; Christensen, D. L.; and Williams, B. B. 1978: Solar Radiation Data Sources: Applications and Network Design. Prepared by Kenneth E. Johnson Environmental and Energy Center, Univ. of Alabama, report no. HCP/T5362-01.

Flowers, E. G.; McCormick, R. A.; and Kurfis, K. R. 1969: Atmosphere Turbidity Over the United States, 1961-1966. J. App. Met., vol. 8, no. 6, pp. 955-962.

Gates, D. M. 1966: Spectral Distribution of Solar Radiation at the Earth's Surface. Science, vol. 151, no. 3710, pp. 523-529.

Gregher, D. F.; Evans, D.; Hunt, A.; and Whalig, M. 1979: Measurements and Analysis of Circumsolar Radiation. LBL Report No. 10243, Lawrence Berkeley Laboratory, Berkeley, Ca.

Hickey, J. R. 1978: Solar Radiation Measurements From Nimbus 6. Third Conference on Atmospheric Radiation, American Meteorological Society, Boston, pp. 91-94.

Jannuzi, John A. 1978: Solar Radiation. NOAA Tech. Memo. NWS WR-134.

Jessup, E. 1974: A Brief History of the Solar Radiation Program. Report and Recommendations of the Solar Energy Data Workshop, edited by C. Turner, NSF-RA-N-74-062, National Science Foundation, Washington, D.C., pp. 13-20.

Kano, M. 1964: The Effect of a Turbid Layer on Radiation Emerging From a Planetary Atmosphere. Ph.D. Dissertation, Univ. of California, Los Angeles.

Meinel, Aden B.; and Meinel, Marjorie P. 1977: Applied Solar Energy: An Introduction. Addison-Wesley Publ. Co., Reading, Mass.

National Oceanic and Atmospheric Administration 1972: Operations of the National Weather Service. National Weather Service, Silver Spring, Maryland.

Paltridge, G. W.; and Platt, G. M. R. 1976: Radiative Processes in Meteorology and Climatology. Elsevier Scientific Publishing Co., New York.

The Smithsonian Institution 1951: Smithsonian Meteorological Tables. Sixth Revised Edition, Washington, D.C.

Thekaekara, Matthew P. 1974: Data on Incident Solar Radiation. The Energy Crisis and Energy from the Sun, Supplement to Proceedings of 20th Annual Meeting, Institute of Environmental Sciences, Mt. Prospect, Ill., pp. 21-49.

U.S. Department of Energy 1978: On the Nature and Distribution of Solar Radiation. Prepared by Watt Engineering Ltd., report no. HCP/T2552-01.

Volz, F. 1959: Photometer mit Selen-Photoelement zur spektralen Messung der Sonnenstrahlung and zur Bestimmung der Wellenlängenabhängigkeit der Dunsttrübung. Arch. Meteor. Geophys. Bioklim, ser. B, vol. 10, no. 1, pp. 100-131.

TABLE I.- SOLAR FLUX ABOVE THE EARTH'S ATMOSPHERE

[From Thekaekara, 1974]

λ*	E_λ*	D_λ*	λ	E_λ	D_λ	λ	E_λ	D_λ
0.115	0.007	1×10^{-4}	0.43	1639	12.47	0.90	891	63.37
0.14	0.03	5×10^{-4}	0.44	1810	13.73	1.00	748	69.49
0.16	0.23	6×10^{-4}	0.45	2006	15.14	1.2	485	78.40
0.18	1.25	1.6×10^{-3}	0.46	2066	16.65	1.4	337	84.33
0.20	10.7	8.1×10^{-3}	0.47	2033	18.17	1.6	245	88.61
0.22	57.5	0.05	0.48	2074	19.68	1.8	159	91.59
0.23	66.7	0.10	0.49	1950	21.15	2.0	103	93.49
0.24	63.0	0.14	0.50	1942	22.60	2.2	79	94.83
0.25	70.9	0.19	0.51	1882	24.01	2.4	62	95.86
0.26	130	0.27	0.52	1833	25.38	2.6	48	96.67
0.27	232	0.41	0.53	1842	26.74	2.8	39	97.31
0.28	222	0.56	0.54	1783	28.08	3.0	31	97.83
0.29	482	0.81	0.55	1725	29.38	3.2	22.6	98.22
0.30	514	1.21	0.56	1695	30.65	3.4	16.6	98.50
0.31	689	1.66	0.57	1712	31.91	3.6	13.5	98.72
0.32	830	2.22	0.58	1715	33.18	3.8	11.1	98.91
0.33	1059	2.93	0.59	1700	34.44	4.0	9.5	99.06
0.34	1074	3.72	0.60	1666	35.68	4.5	5.9	99.34
0.35	1093	4.52	0.62	1602	38.10	5.0	3.8	99.51
0.36	1068	5.32	0.64	1544	40.42	6.0	1.8	99.72
0.37	1181	6.15	0.66	1486	42.66	7.0	1.0	99.82
0.38	1120	7.00	0.68	1427	44.81	8.0	0.59	99.88
0.39	1098	7.82	0.70	1369	46.88	10.0	0.24	99.94
0.40	1429	8.73	0.72	1314	48.86	15.0	4.8×10^{-2}	99.98
0.41	1751	9.92	0.75	1235	51.69	20.0	1.5×10^{-2}	99.99
0.42	1747	11.22	0.80	1109	56.02	50.0	3.9×10^{-4}	100.00

*λ wavelength, µm

E_λ solar spectral irradiance, $W/m^2\ \mu m^{-1}$, averaged over small bandwidth centered at λ

D_λ percentage of solar constant associated with wavelengths shorter than λ

TABLE II.- ANNUAL VARIATION OF SOLAR FLUX DUE TO ORBITAL ECCENTRICITY

[From Meinel and Meinel, 1977]

Date	Departure from mean	Solar flux, kW/m^2
Jan. 1	1.0342	1.438
Feb. 1	1.0296	1.431
Mar. 1	1.0181	1.415
Apr. 1	1.0016	1.392
May 1	0.9848	1.369
June 1	0.9721	1.351
July 1	0.9673	1.345
Aug. 1	0.9716	1.350
Sept. 1	0.9835	1.367
Oct. 1	1.0003	1.390
Nov. 1	1.0172	1.414
Dec. 1	1.0296	1.431

ORIGINAL PAGE IS
OF POOR QUALITY

TABLE III.- RADIATION MEASUREMENTS AT SOLAR ENERGY METEOROLOGICAL RESEARCH AND TRAINING SITES

Type of measurement	Instrument	Procedure	Sampling	Comments
Basic[a]:				
Global (WG7)	Eppley PSP	NOAA[b] + frost/dew prevention	1 minute + hourly (SOLMET)	SERI and NOAA coordinate purchase
Diffuse (WG7)	Eppley PSP - shadow band or tracking , disk	NOAA[b] + frost/dew prevention	1 minute + hourly (SOLMET)	SERI and NOAA check disk
Direct (WG7)	Eppley NIP + tracker	NOAA	1 minute + hourly (SOLMET)	SERI and NOAA coordinate purchase
Downward infrared (long & short)	CSIRO[c], Funk-type Sci. Associates Model 822	NOAA	1 minute + hourly (SOLMET)	SERI and NOAA coordinate purchase
Total (WG7) on surface tilted at latitude, pointed south	Eppley PSP	NOAA + document instrument view with fisheye photo; frost/dew prevention	1 minute + hourly (SOLMET)	SERI and NOAA coordinate purchase
Global (RG2)	Eppley PSP	NOAA + frost/dew prevention	1 minute + hourly (SOLMET)	SERI and NOAA coordinate purchase
Global (UV)	Eppley UV photometer	NOAA	1 minute + hourly (SOLMET)	SERI and NOAA coordinate purchase
Research[d]:				
Global, diffuse, direct (OG1, RG2, & RG8 filters)	Eppley PSP's + NIP	NOAA + IGY + WMO + frost/dew prevention	Interval determined by NIP filter wheel; hourly - SOLMET	SERI and NOAA coordinate purchase
Photovoltaic - horizontal lat., lat. + 10°, lat. - 10° (south)	Standard cells - JPL & NASA	JPL & NASA	1 minute + hourly (SOLMET)	SERI and NOAA to check with JPL and NASA Coordinate purchase
Total (WG7) on lat., lat. + 10°, lat. - 10°, vertical, at four cardinal points	Eppley PSP	NOAA + measure ground albedo + frost/dew prevention + document (photo) view	1 minute + hourly (SOLMET)	SERI and NOAA coordinate purchase
All of the above for spectral scans (bands), narrow fields of view	*Specified by PI*	*Specified by PI*	*Specified by PI*	*Includes circumsolar*

[a] Measurements will be archived at Solar Energy Research Institute (SERI), Golden, Colorado.
[b] NOAA network, plus annual photos of site (pyranometer FOV), using local standard time.
[c] Commonwealth Scientific Industrial and Research Organization.
[d] Data used by SEMRTS personnel.

TABLE IV.- METEOROLOGICAL MEASUREMENTS AT SOLAR ENERGY METEOROLOGICAL RESEARCH AND TRAINING SITES

Type of measurement	Instrument	Procedure	Sampling	Comments
Basic:				
Temperature Dew point Wind speed and direction Pressure Precipitation	Optional: PI's should coordinate with each other concerning their specific instrumentation and calibration	WMO and NWS	1 min + hourly (SOLMET)	Use best possible exposure
Cloud cover	NA	NWS	Hourly	Obtain from NWS
Percent sunshine	Campbell Stokes	WMO and IGY	Daily/hourly	
Present weather	NA	NWS	Hourly	
Research:				
Cloud cover	PI specified	PI specified	PI specified	May use satellite fisheye camera
Visibility	Observation (human) Nephelometer Contrast photometer, photograph	WHO and NWS	PI specified	
Turbidity	Volz photometer PI specified	WMO and IGY	PI specified	
Others:				
Total ozone, NO_x, CO, O_3, etc., particulates, precip. H_2O, cloud height, and altitude profiles of above	PI specified	PI specified	PI specified	PI's to report May 1978

ORIGINAL PAGE IS
OF POOR QUALITY

TABLE V.- CALIBRATION PROCEDURES AT SOLAR ENERGY METEOROLOGICAL RESEARCH AND TRAINING SITES[a]

Calibration of -	Instrument	Procedure	Sampling	Comments
Station log	NA	NOAA network		-
Pyrheliometers & pyranometers	Each PI maintain at least one reference	PI reference instrument traceable to NOAA (Boulder), traveling standard (NOAA) to be considered, calibration technique of NOAA	Annual	PI may want to purchase own instrument PACRAD[b] primary standard radiometer
Funk infrared radiometer	CSIRO	Conduct joint calibration/ comparison with all PI's; Trinity University to maintain traveling std.	Annual	SERI to maintain and establish standard and technique
UV photometer	Eppley photometer	Conduct joint calibration/ comparison with all PI's; Univ. of Cal. to maintain traveling std.	Annual	SERI and UC (Davis) will maintain standard and technique
Meteorological	-	WMO	As required	
Electronics	-	Common electrical standards and traceability to primary and secondary units	As required	Recommend back-up strip chart recorder(s) be used for quality control
Electromagnetic interference	-	PI to provide documentation and some measurement of electromagnetic interference environment and its impact on measurements	As required	

[a] PI's will deliver quality-controlled 1-minute data 30 working days after end of each month of data collected. Short-term data (less than 30 days) to be provided in publication form.

[b] Precision Active-Cavity Radiometer.

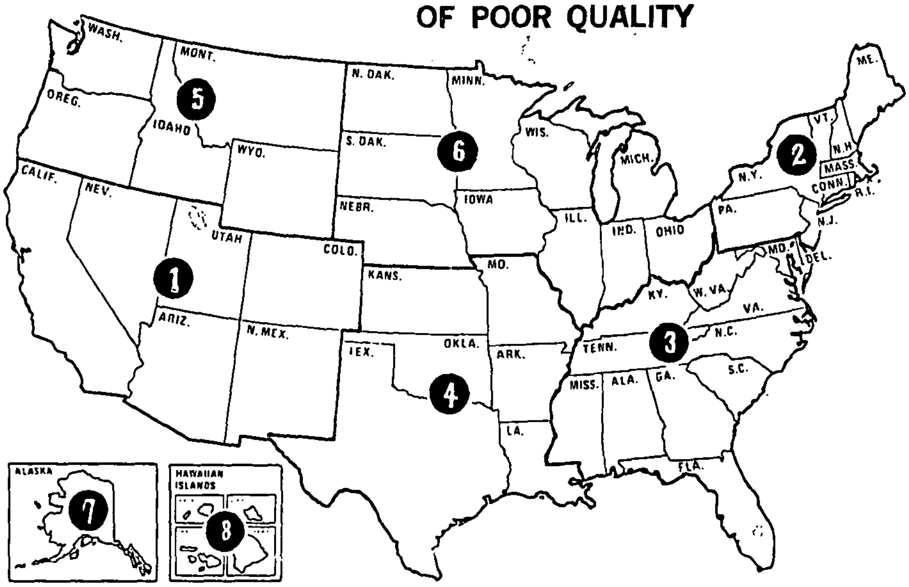

Figure 1.- Regions for Solar Energy Meteorological Research and Training Sites.

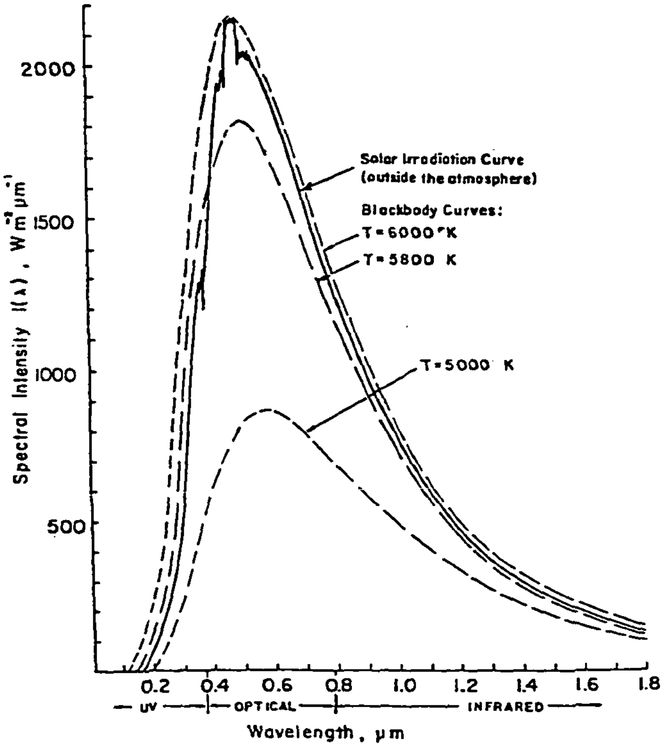

Figure 2.- Solar spectral irradiance at Earth's mean orbital distance compared to blackbody curves for 5000 K, 5800 K, and 6000 K.

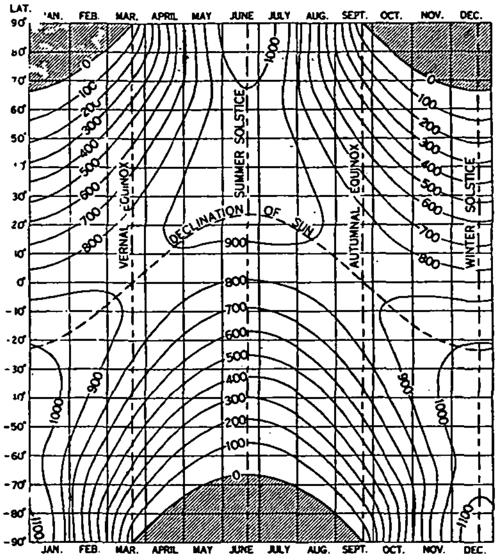

Figure 3.- Total daily solar radiation at top of atmosphere. Solar constant is assumed to be 1.94 cal cm^{-2} min^{-1}. Solid curves represent total daily solar radiation on a horizontal surface at top of atmosphere, measured in cal cm^{-2}. Shaded areas represent regions of continuous darkness. (From The Smithsonian Institution, 1951.)

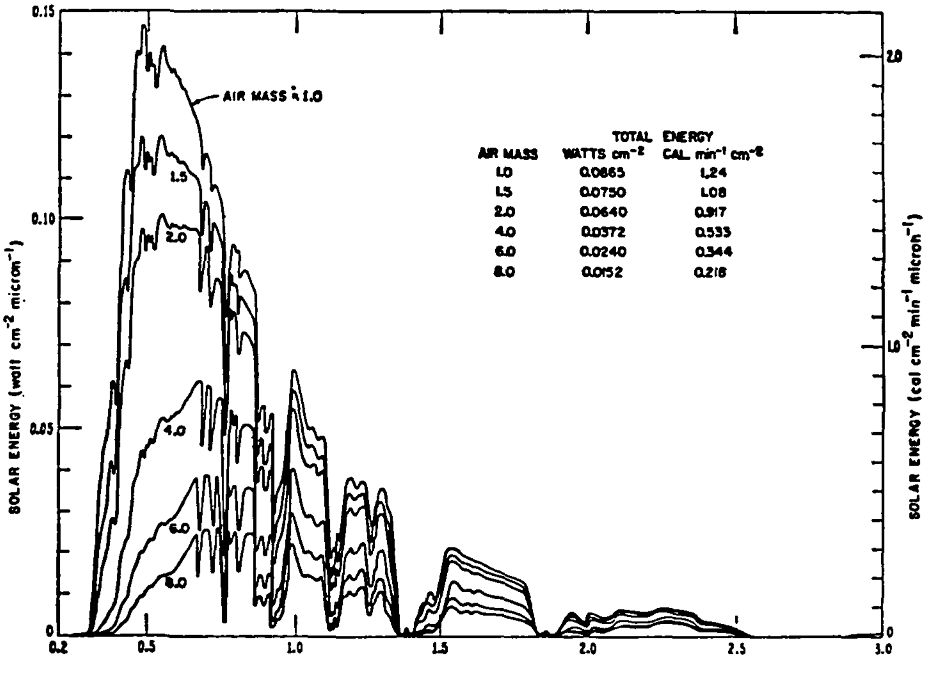

AIR MASS	TOTAL ENERGY WATTS cm^{-2}	TOTAL ENERGY CAL min^{-1} cm^{-2}
1.0	0.0865	1.24
1.5	0.0750	1.08
2.0	0.0640	0.917
4.0	0.0372	0.533
6.0	0.0240	0.344
8.0	0.0152	0.218

Figure 4.- Spectral distribution as a function of wavelength of direct solar radiation incident at sea level on a surface perpendicular to the Sun's rays for slant paths of air mass 1.0 to 8.0. Concentration of precipitable water = 10 mm, concentration of aerosol = 200 particles/cm^2, concentration of ozone = 0.35 cm. (From Gates, 1966.)

ORIGINAL PAGE IS OF POOR QUALITY

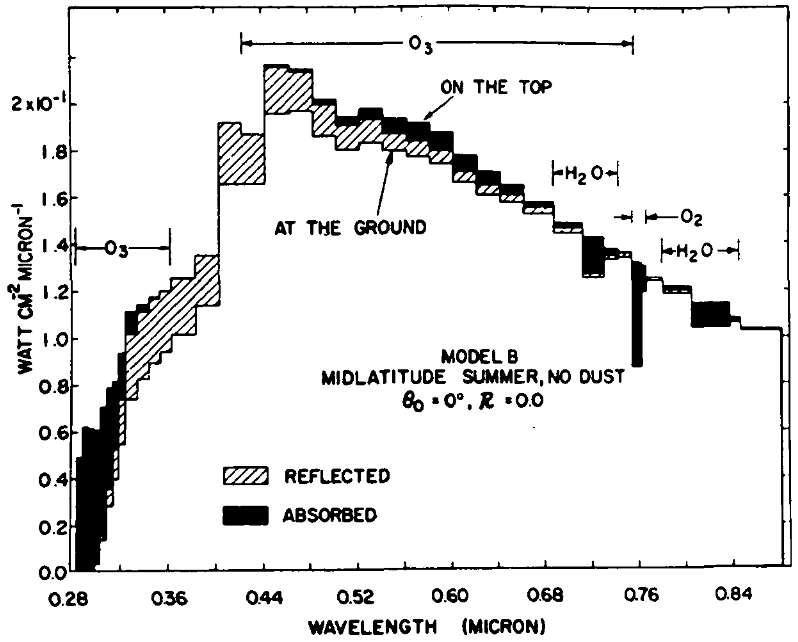

(a) 0.285- to 0.88-μm region.

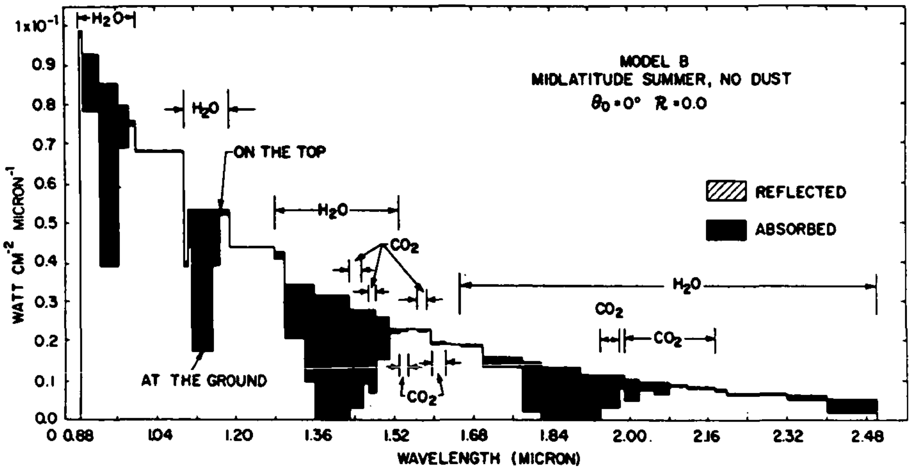

(b) 0.88- to 2.5-μm region.

Figure 5.- Computed spectral distribution of the 0.285- to 2.5-μm region of the solar flux absorbed within the atmosphere, reflected back to space, and transmitted to a perfectly absorbing ground by a dust-free standard atmosphere, with total ozone of 0.318 cm atm and total water vapor of 2.925 g cm^{-2} in the vertical column of the atmosphere. Sun at zenith. (From Paltridge and Platt, 1976.)

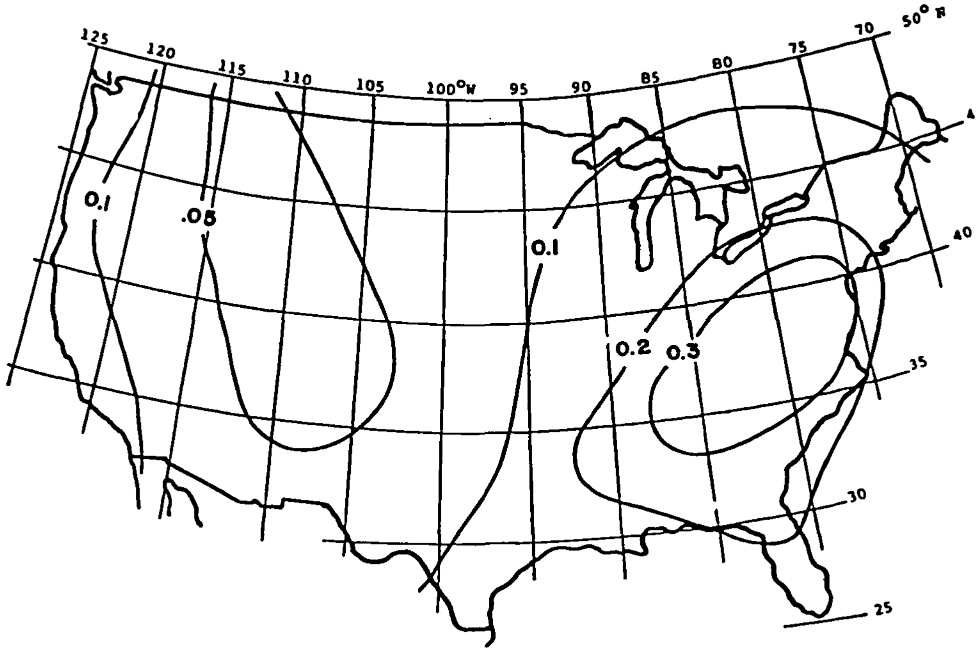

Figure 6.- Atmospheric turbidity over the U.S. in July at 0.5 μm, typical of years 1961 to 1974. (From Flowers et al., 1969.)

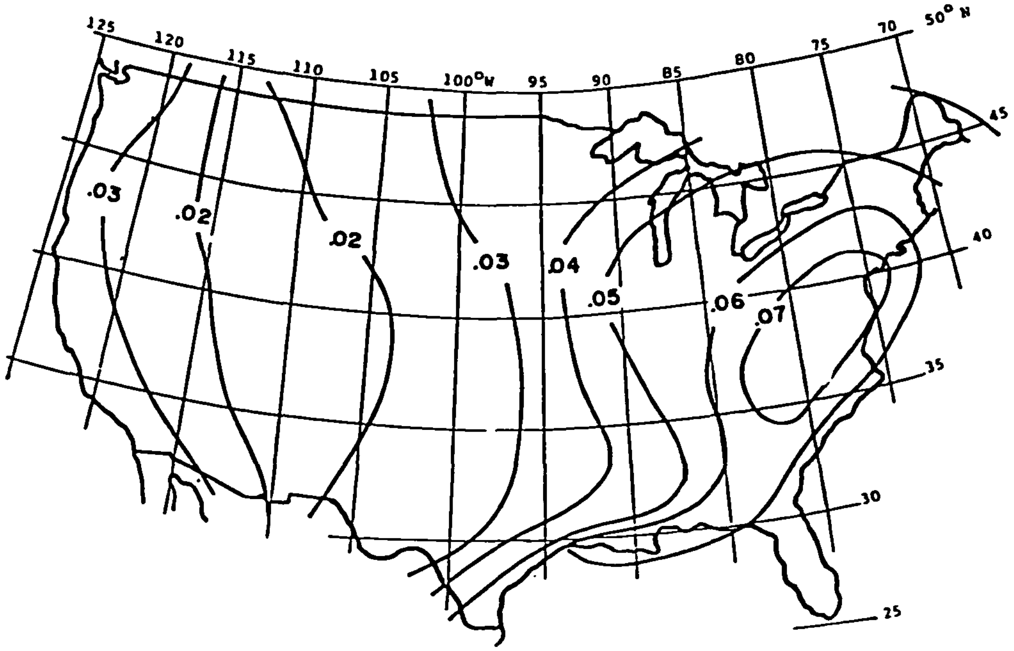

Figure 7.- Atmospheric turbidity over the U.S. in December at 0.5 μm, typical of years 1961 to 1974. (From Flowers et al., 1969.)

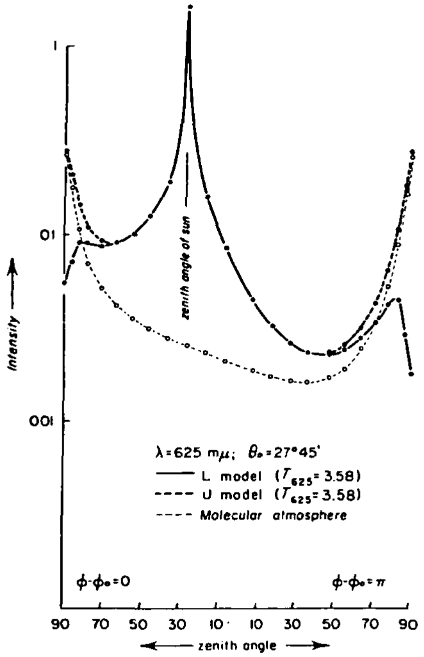

Figure 8.- Relative intensity of skylight in the principal plane for a molecular (Rayleigh) atmosphere and for a turbid layer below (L model) and above (U model) the molecular atmosphere. The Linke turbidity factor is expressed as T. (From Kano, 1964.)

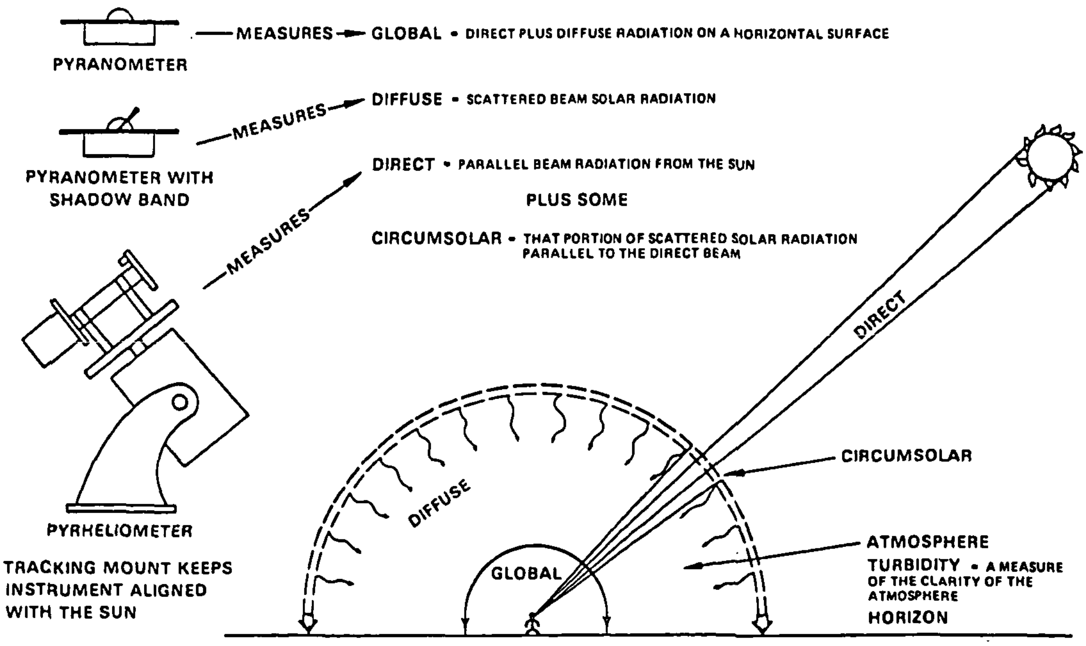

Figure 9.- Types of insolation and measuring instruments.

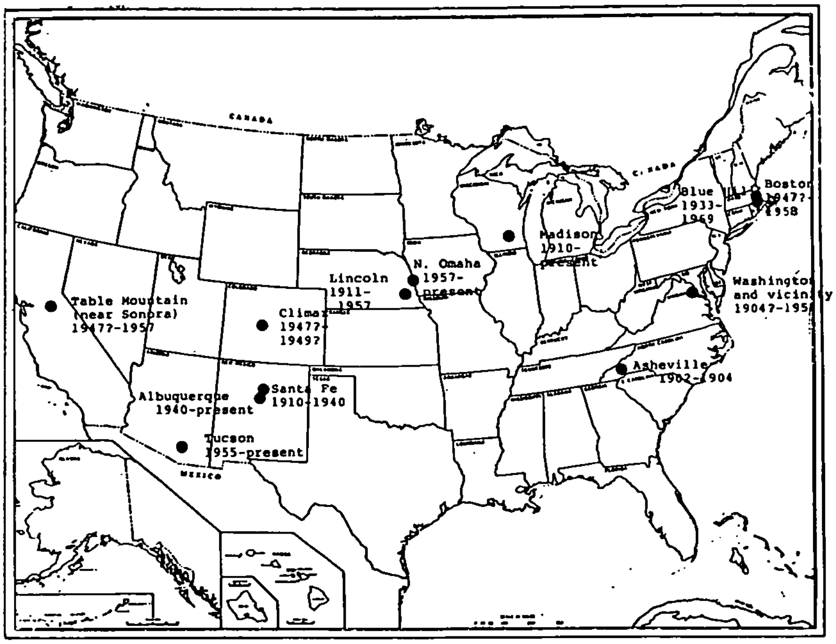

Figure 10.- Locations with normal incidence solar radiation data and period of observations. (After Jessup, 1974.)

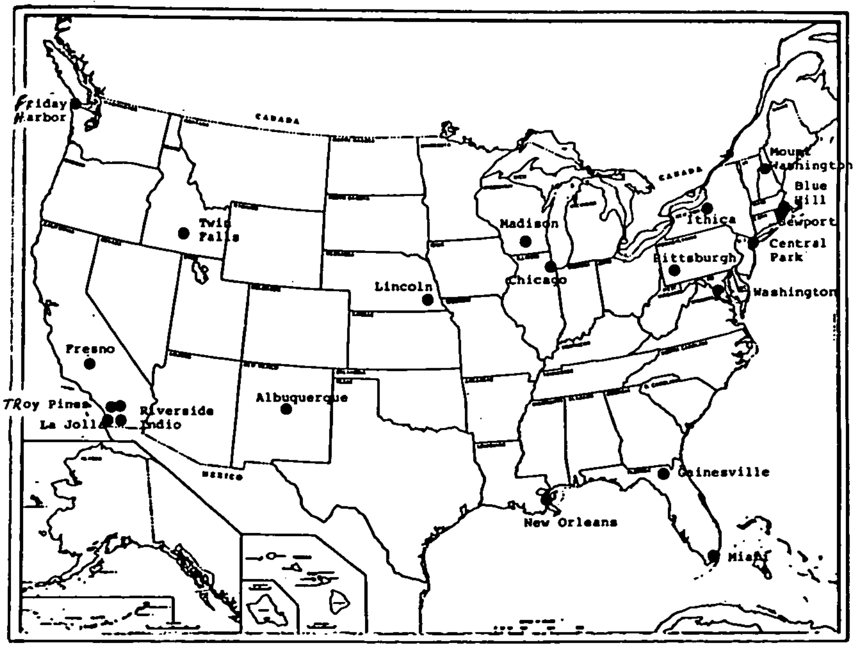

Figure 11.- Solar radiation network, 1939. (After Jessup, 1974.)

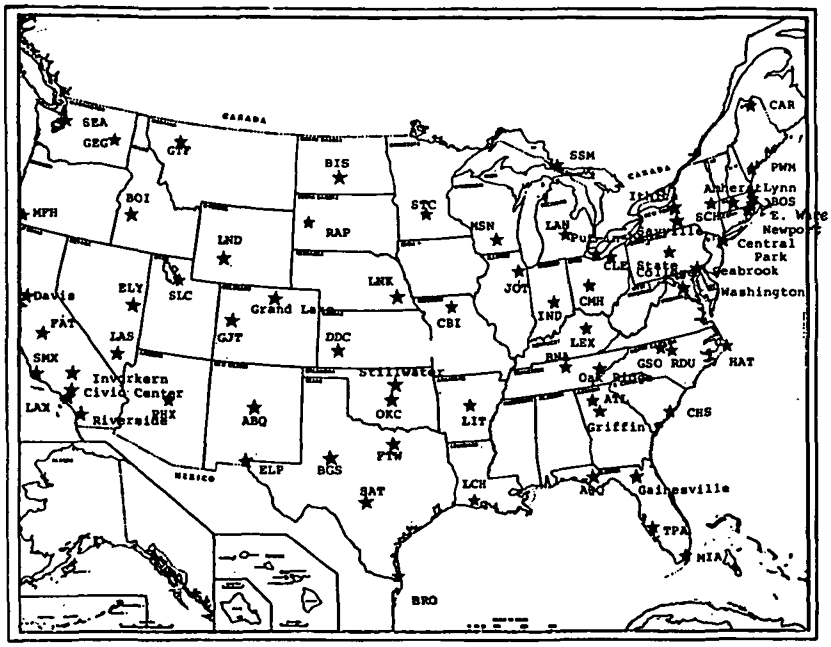

Figure 12.- Solar radiation network, 1951. (After Jessup, 1974.)

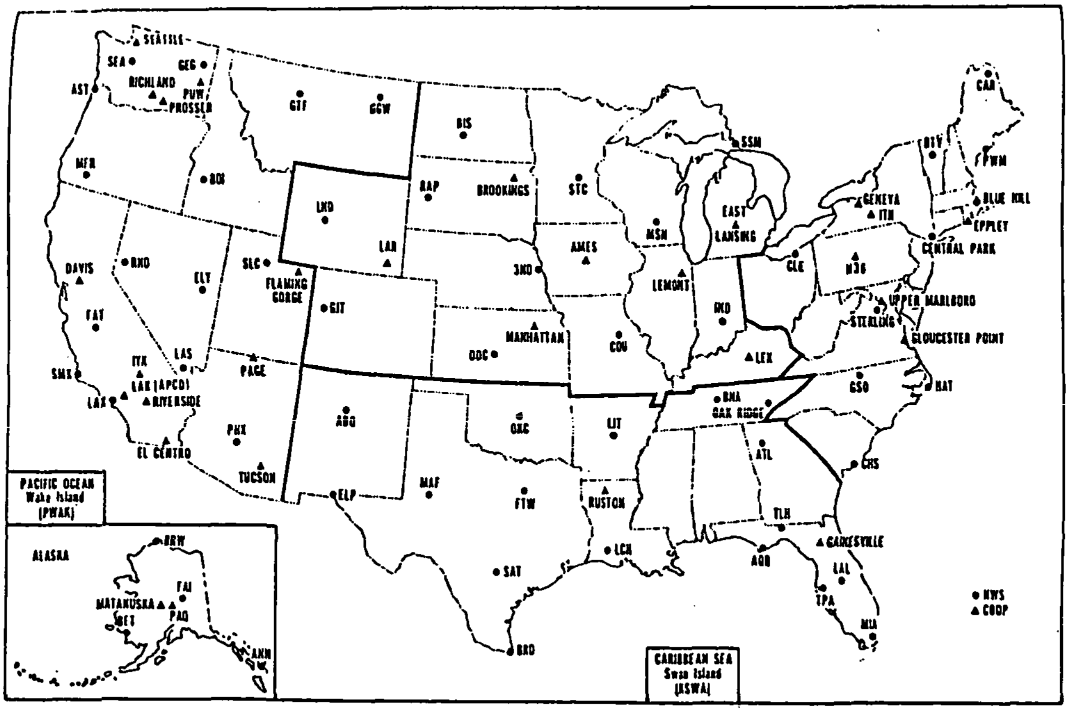

Figure 13.- Solar radiation stations, 1972. (From National Oceanic and Atmospheric Administration, 1972.)

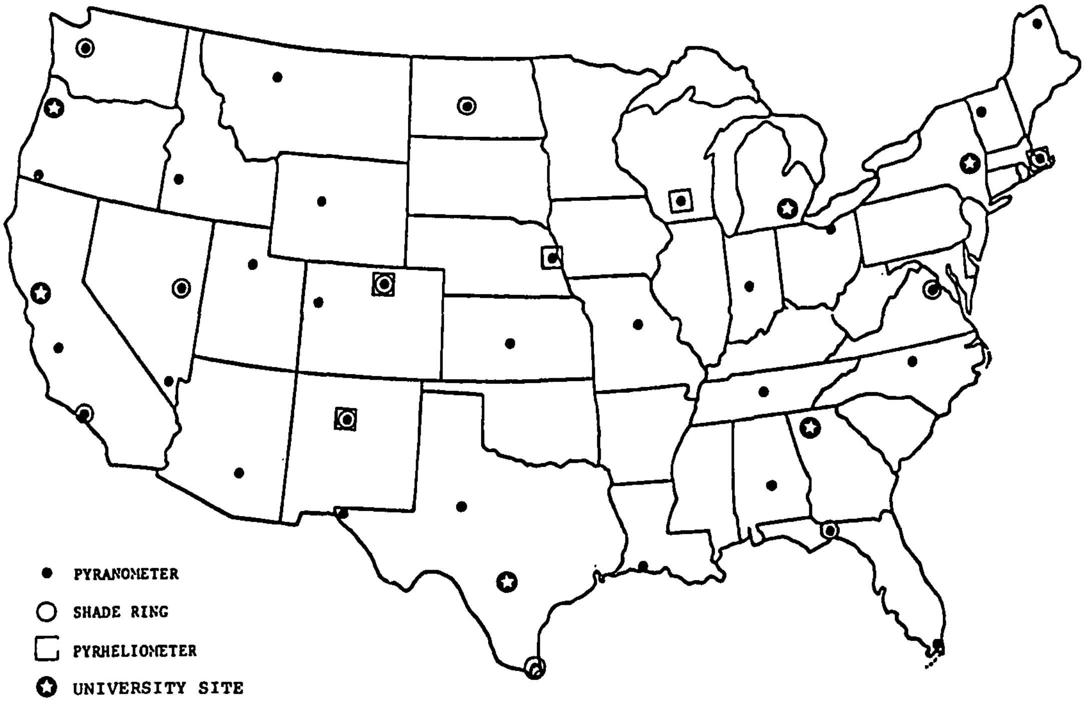

Figure 14.- New National Weather Service solar radiation station network. (Station at Fairbanks, Alaska not indicated.)

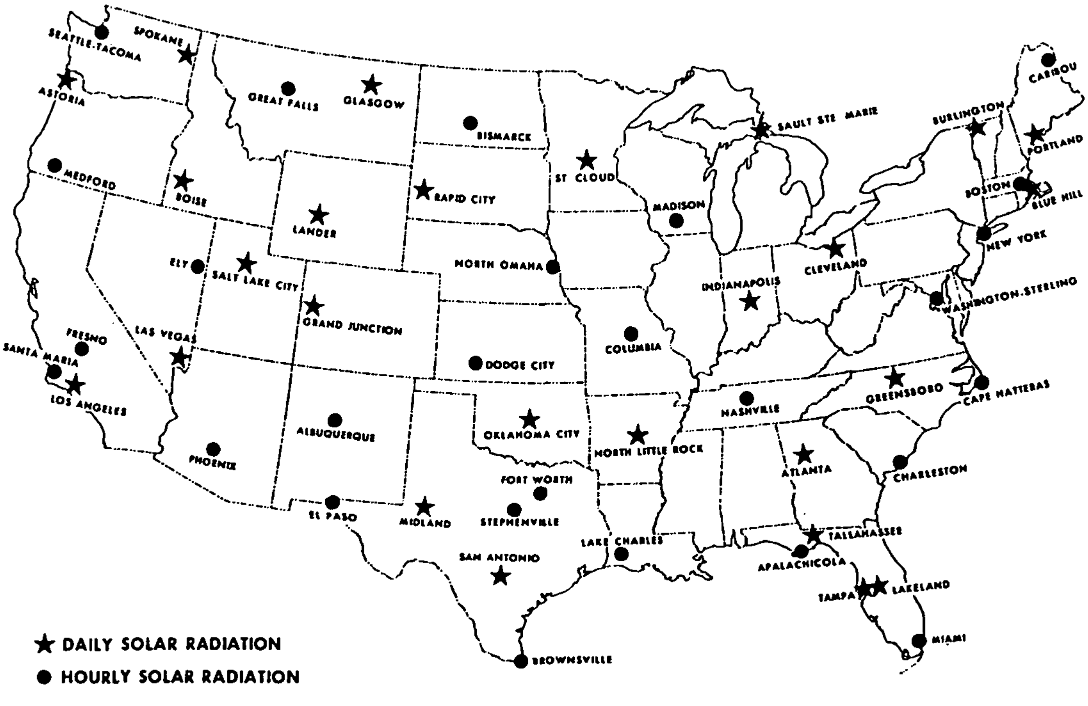

Figure 15.- Solar radiation data rehabilitation stations. (From Carter et al., 1978.)

ORIGINAL PAGE
BLACK AND WHITE PHOTOGRAPH

Figure 16.- Space Research Building on the University of Michigan North Campus, looking northeast. The table supporting the radiometers is just visible on the uppermost rooftop section.

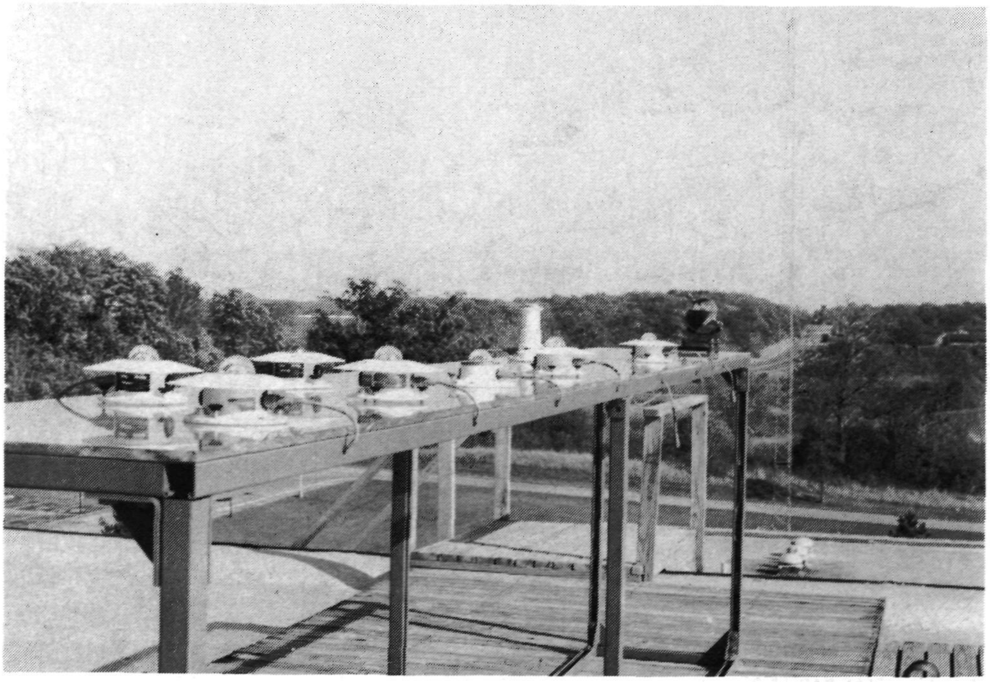

Figure 17.- Main instrument support table with radiometers, looking east-northeast. The 30-m meteorological tower is visible in the background.

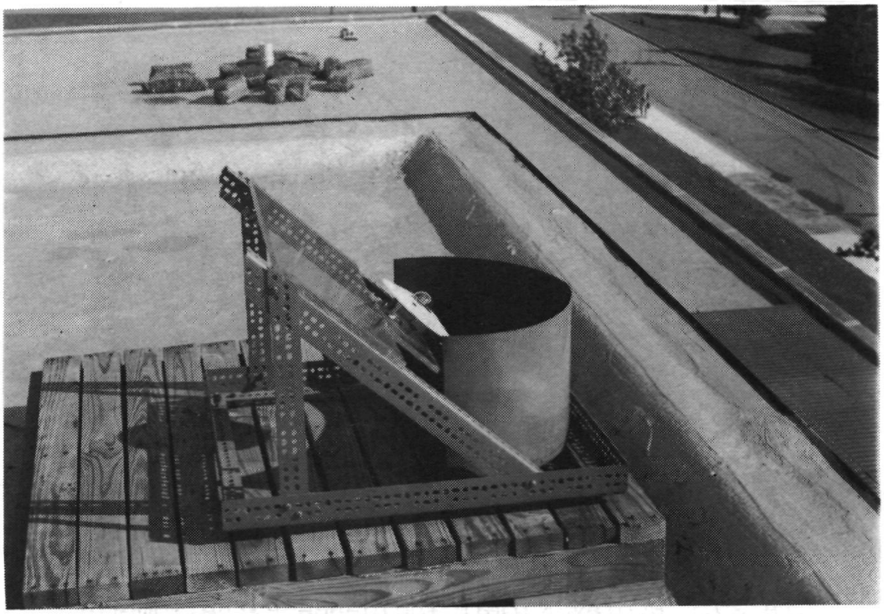

Figure 18.- Eppley PSP tilted at 42.3°-latitude angle and shielded from reflected solar irradiance.

Figure 19.- Eppley PSP shaded by occulting disk for measuring diffuse solar irradiance.

Figure 20.- Eppley Normal Incidence Pyrheliometer with filter wheel and solar tracker for measuring direct solar irradiance.

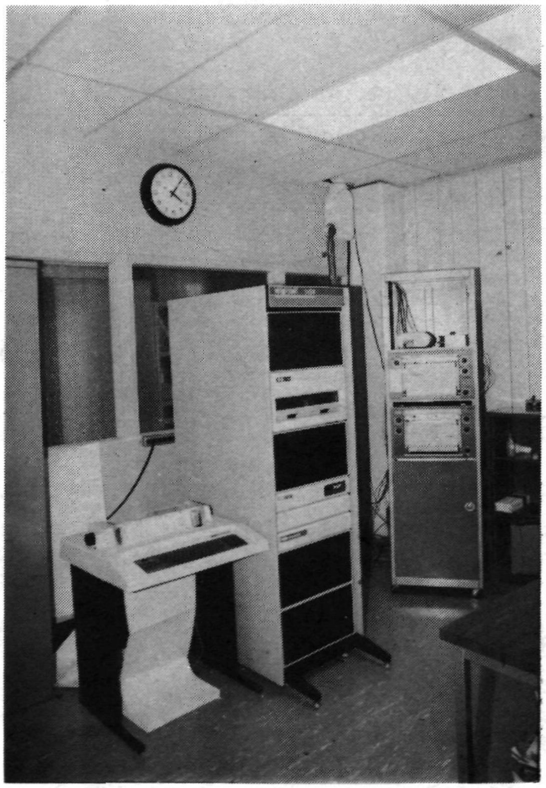

Figure 21.- Analog and digital recording systems - from left to right: typewriter-type terminal, data logging system, and 3- and 4-channel analog recorders.

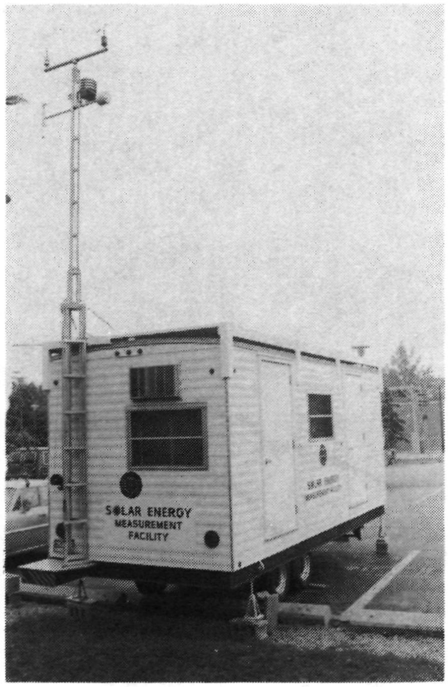

Figure 22.- Mobile measurement facility for solar and meteorological variables.

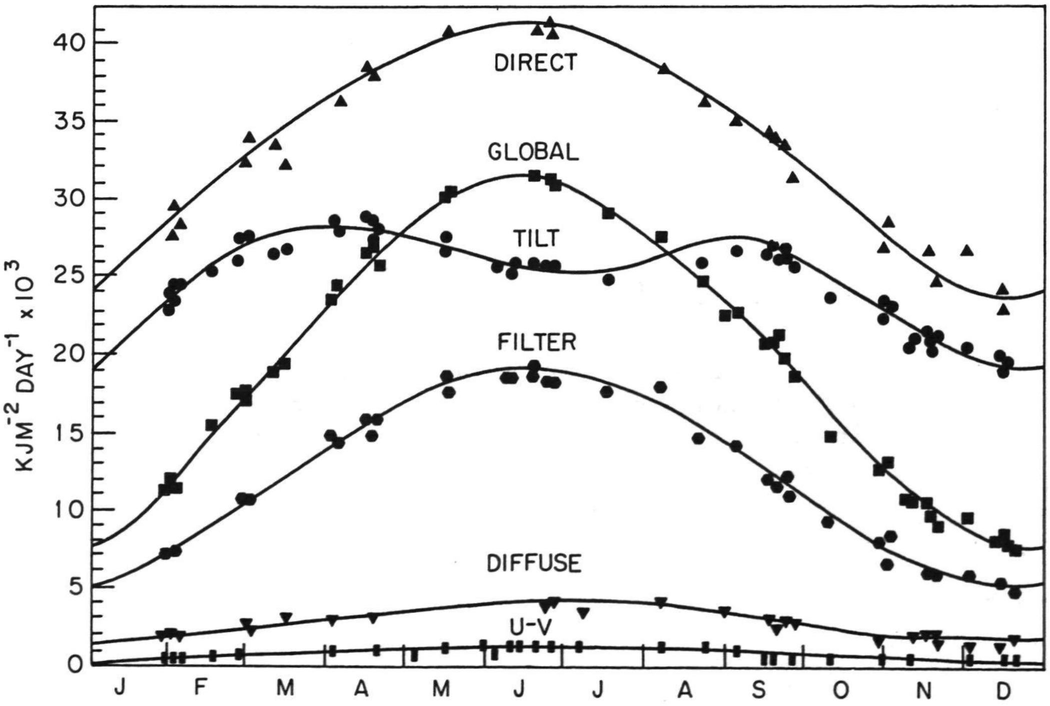

Figure 23.- Measurements of solar radiation taken at University of Michigan SEMRTS sites.

ORIGINAL PAGE IS
OF POOR QUALITY

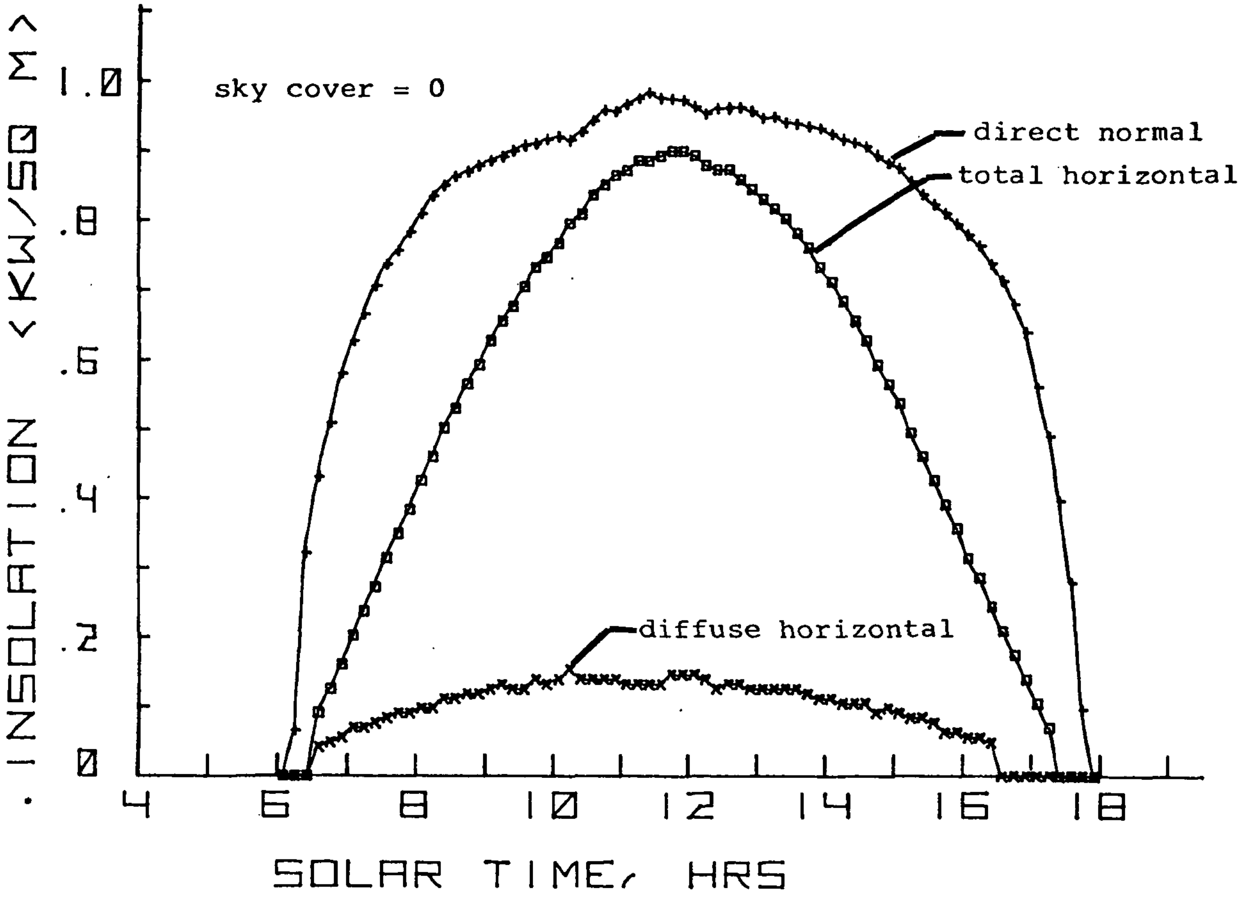

Figure 24.- Diurnal variation of direct normal, diffuse horizontal, and total horizontal insolation. (From U.S. Dept. of Energy, 1978.)

ORIGINAL PAGE IS
OF POOR QUALITY

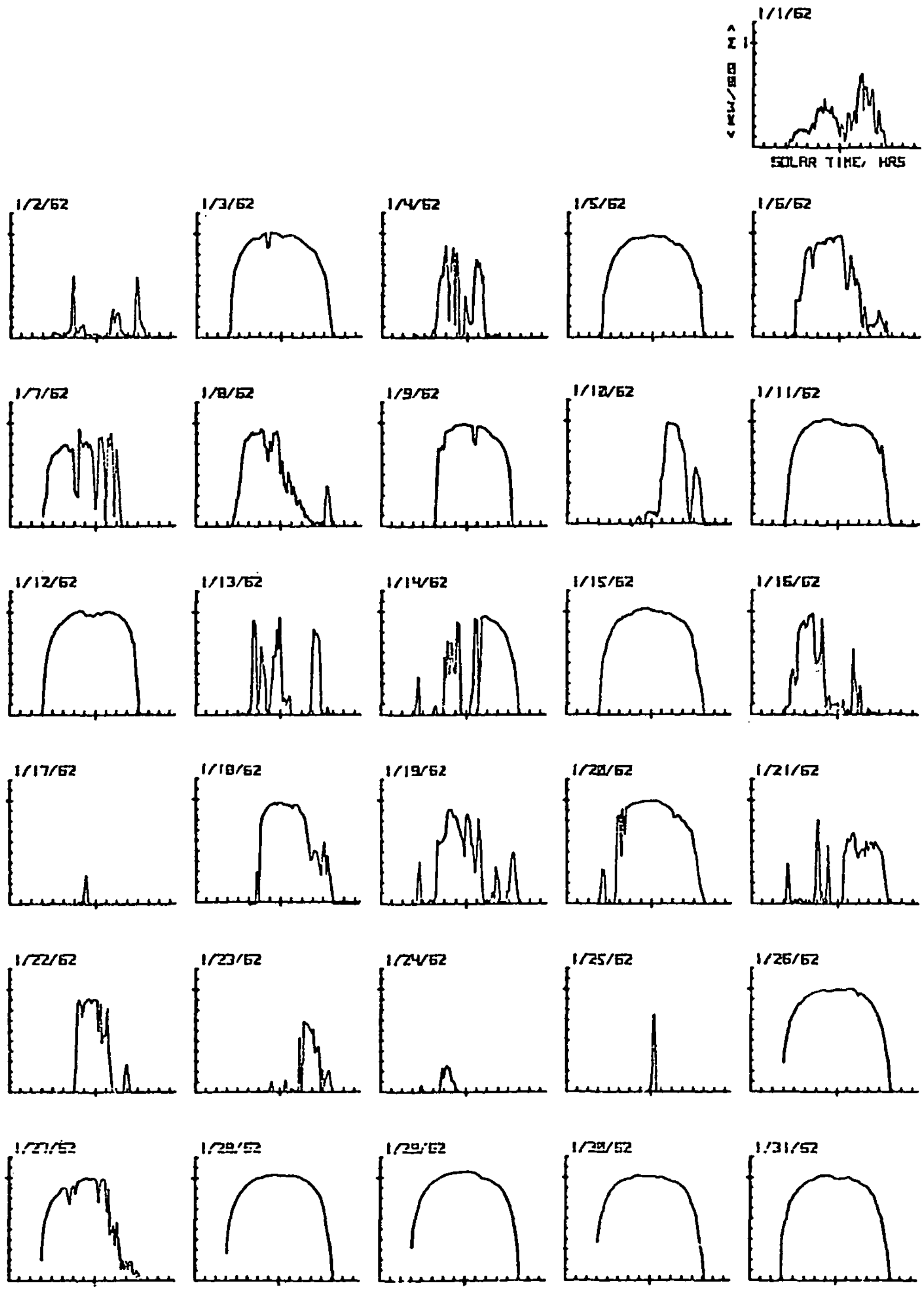

Figure 25.- Direct normal solar radiation for Albequerque, N.M., for January 1962. (From U.S. Dept. of Energy, 1978.)

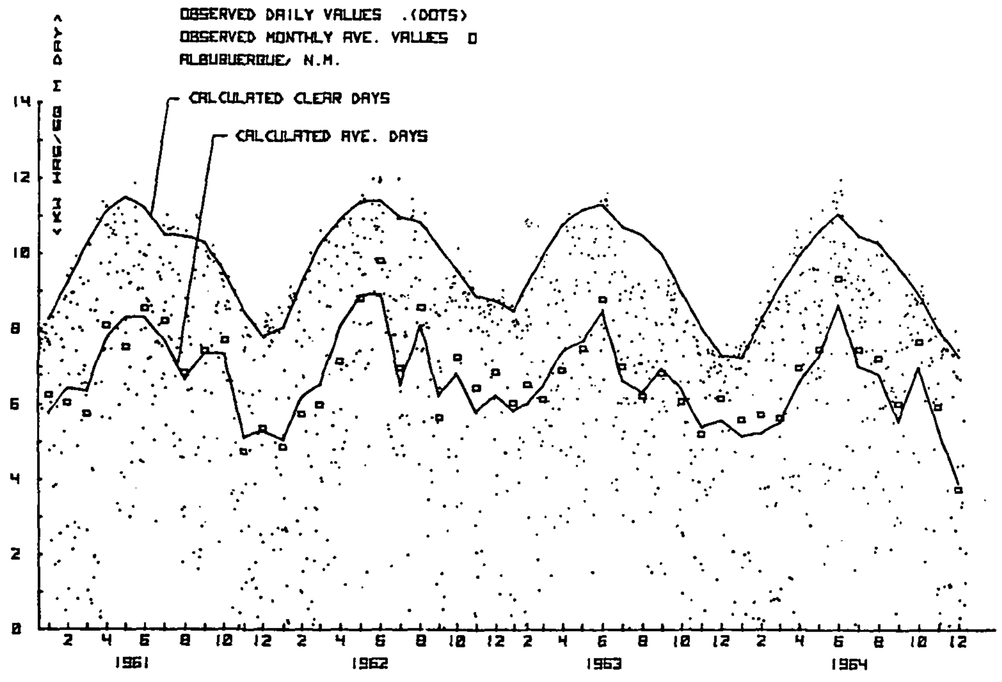

Figure 26.- Direct normal solar radiation for 4-year period at Albequerque, N.M. (From U.S. Dept. of Energy, 1978.)

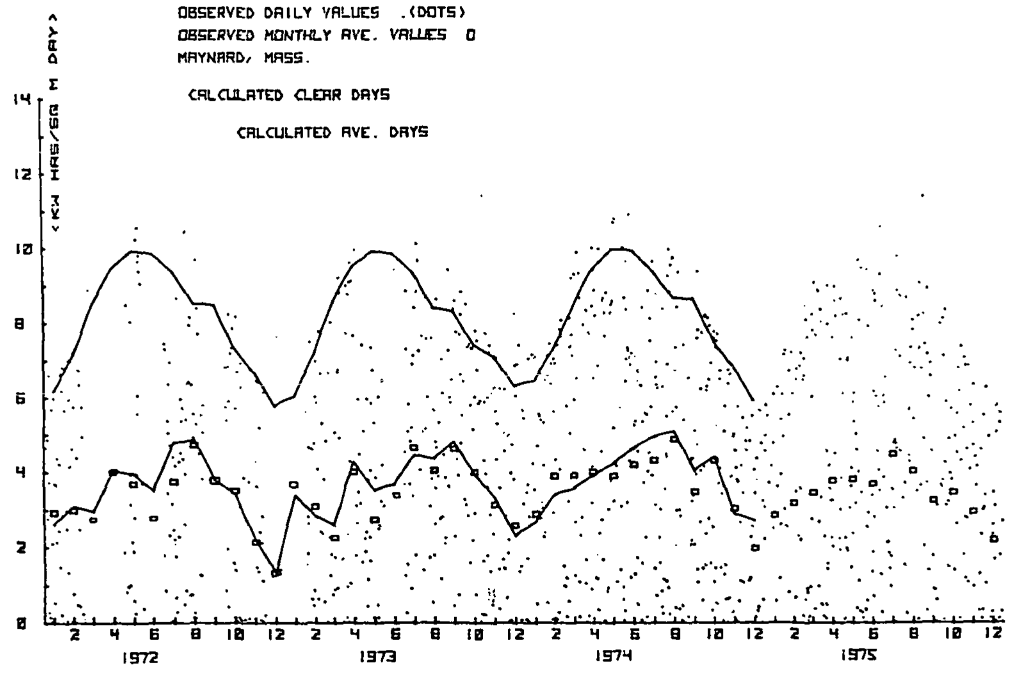

Figure 27.- Direct normal solar radiation for 4-year period at Maynard, Mass. (From U.S. Dept. of Energy, 1978.)

ORIGINAL PAGE IS
OF POOR QUALITY

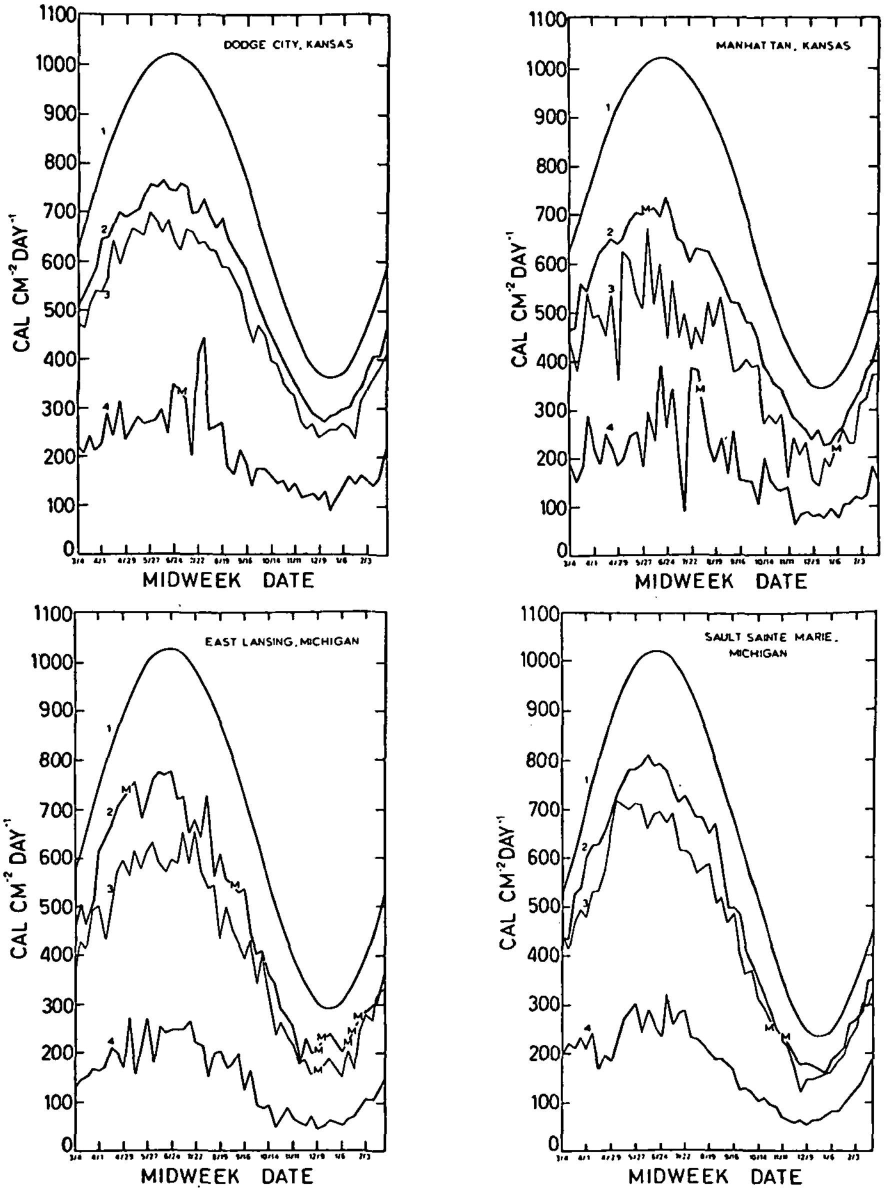

Figure 28.- Calculated total daily extraterrestrial radiation (curve 1) and average measured radiation under clear-sky conditions (curve 2), 50-percent cloud cover (curve 3), and 100-percent cloud cover (curve 4). The symbol M is used when the particular sky condition did not occur during the period of record. Values were plotted at the midweek date of each climatological week. Measured data for Manhattan are estimated to be low by 8.2 percent. (From Baker and Klink, 1975.)

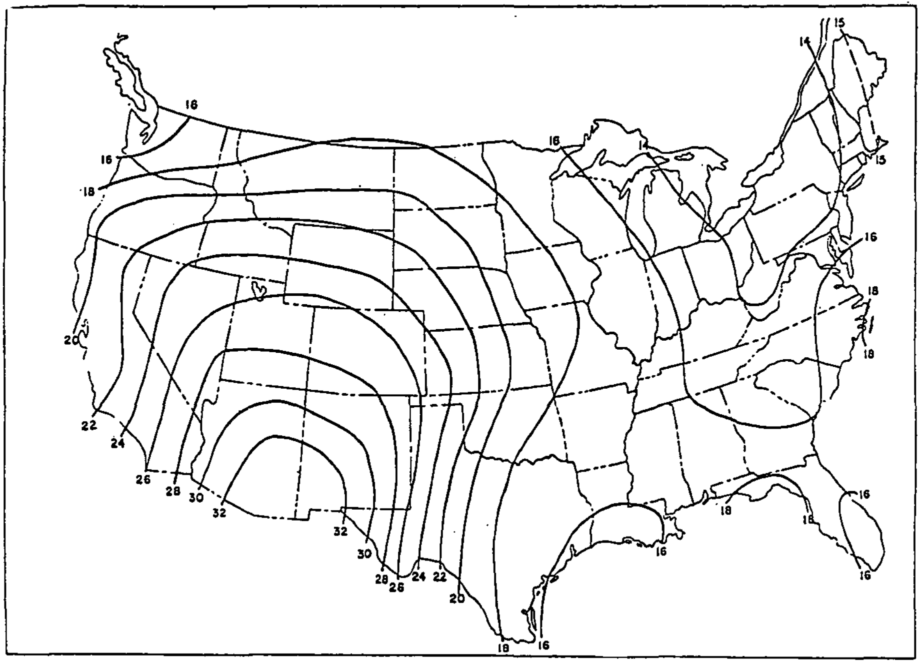

Figure 29.- Mean daily direct solar radiation, MJ/m^2, for May. (Lester Machta, personal communication, Jan. 1979.)

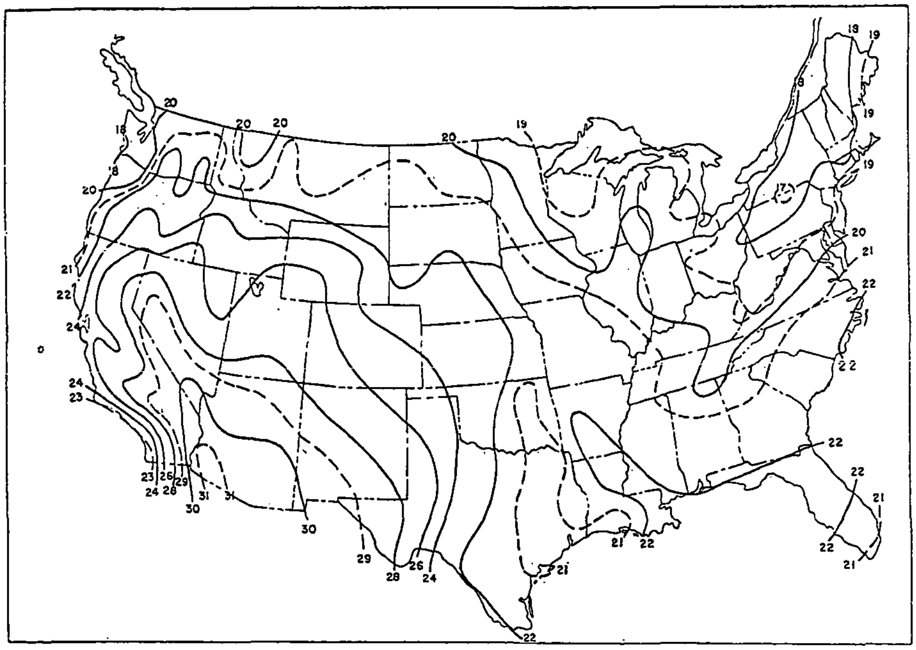

Figure 30.- Mean daily solar radiation on a horizontal surface, MJ/m^2, for May. (Lester Machta, personal communication, Jan. 1979.)

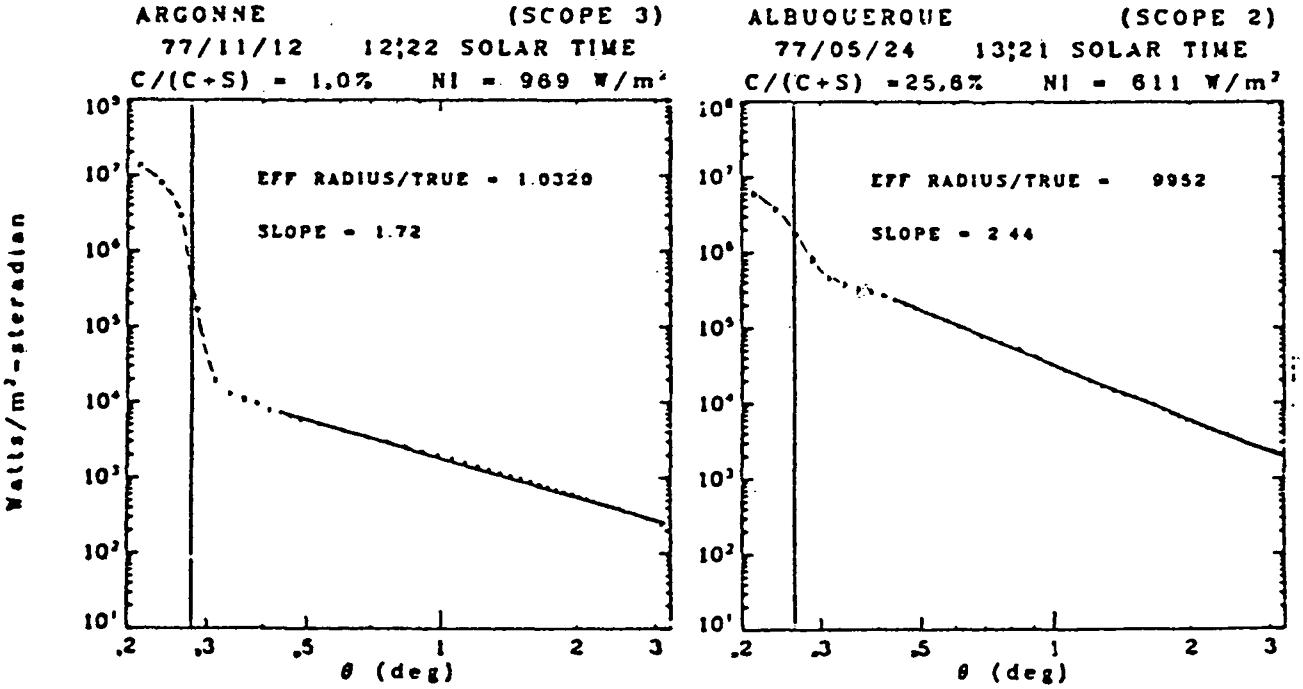

(a) Low turbidity.

(b) High turbidity.

Figure 31.- Effects of turbidity on direct and circumsolar radiation. (From Gregher et al., 1979.)

SOLAR RADIATION AT THE EARTH'S SURFACE: ITS CALCULATION AND INFERENCE FROM SATELLITE IMAGERY

Fred L. Bartman
University of Michigan
Ann Arbor, Michigan

INTRODUCTION: PHYSICAL AND EMPIRICAL MODELS

Solar radiation incident at the surface has not been measured at all locations on the Earth's surface. A valuable supplement to measured values are calculated values. This paper discusses a few methods for calculation of the insolation on a horizontal surface and refers to some of the many papers in the literature dealing with this topic.

A valuable reference for this paper has been the notes for the intensive short course entitled "Solar Energy Measurements and Instrumentation" which was presented as part of the University of Michigan Engineering Summer Conference Program on July 9-10, 1979. The notes were written by staff members in the Department of Atmospheric and Oceanic Science. Of particularly great help in the preparation of this paper is Chapter 8 of those notes, "Modelling of Received Solar Radiation," by W. R. Kuhn.

The various calculations can be broadly grouped into two categories, physical models and empirical models. Physical models use the basic physical principles of radiative transfer. They require the input of those quantities involved in the attenuation of the solar beam as it passes through the atmosphere. Data on these factors, i.e., the vertical distribution of water vapor and ozone, the aerosol vertical distribution, particle size distribution, and index of refraction, the physical characteristics of clouds, and the reflectivity of the Earth's surface, are not always available and are highly variable. In addition, the calculations are quite elaborate. Thus the other type of model, the empirical one, is often desirable. Empirical models are generally developed by using a known data set to calculate a set of regression coefficients for some set of parameters, such as the solar zenith angle, the duration of sunshine, or the amount of opaque cloud cover. Then the model can be used to predict the incident solar radiation for other values of the parameters. These models are easy to use but must be applied with care.

The advent of satellite remote sensing of clouds and the surface make the use of empirical models employing satellite images possible. Such a technique is also discussed.

In all the following sections, the surface receiving solar radiation is assumed to be horizontal. The case of solar radiation incident on an inclined plane is not discussed here.

PHYSICAL MODELS

Under clear sky conditions, we can write an equation for the flux (F) of radiation arriving at the surface as

$$F = I \cos \theta + D \tag{1}$$

where F is the global solar radiation (W/m^2), I is the direct beam of solar radiation, D is the diffuse component, and θ is the solar zenith angle.

Spectral Calculations

In terms of spectral components, I and D above can be written as

$$I = \int_0^\infty I_\lambda(0) \exp(-\tau_\lambda \sec \theta)\, d\lambda \tag{2a}$$

$$D = \int_0^\infty D_\lambda\, d\lambda \tag{2b}$$

where $I_\lambda(0)$ is the spectral solar irradiance at the top of the atmosphere, τ_λ is the spectral extinction optical depth, and λ is wavelength (µm).

The extinction is due primarily to absorption by ozone (O_3) and water vapor (H_2O), to scattering by air molecules, i.e., Rayleigh scattering (R), and to absorption and scattering by aerosols (A). Thus,

$$\tau_\lambda = \tau_\lambda(R) + \tau_\lambda(O_3) + \tau_\lambda(H_2O) + \tau_\lambda(A) \tag{3}$$

Leckner (1978) presented expressions for these extinction coefficients. The Rayleigh scattering extinction coefficient is given by

$$\tau_\lambda(R) = 0.008735\lambda^{-4.08} \frac{p}{p_o} \tag{4}$$

where p is the surface pressure (mbar) and p_o is 1013 mbar. For ozone,

$$\tau_\lambda(O_3) = -k(\lambda)\, \ell \tag{5}$$

where $k(\lambda)$ are spectral absorption coefficients (cm^{-1}) given in table I and ℓ is the total ozone amount in atm cm.

The optical depth for water vapor can be written as (see also McClatchey et al., 1971)

$$\tau_\lambda(H_2O) = \frac{0.3\ k_w(\lambda)\ X_w}{\left[1 + 25.35\ k_w(\lambda)\ X_w m\right]^{0.45}} \tag{6}$$

where $k_w(\lambda)$ are effective absorption coefficients of water vapor (cm^2-g^{-1}), X_w is the total precipitable water (g/cm^2), and $m = \sec\theta$, the optical air mass. The values of $k_w(\lambda)$ are given in table II.

The aerosol optical depth can be quite accurately written as

$$\tau_\lambda(A) = \int_0^\infty n(z)\ Q_\lambda(z)\ \pi[r(z)]^2\ dz \tag{7}$$

where $n(z)$ is the aerosol number density at height z, $Q_\lambda(z)$ is the mean spectral extinction efficiency for the aerosols at altitude z, and $r(z)$ is the mean aerosol radius at altitude z. Since the vertical variations of aerosol concentration, composition, size distribution, and index of refraction are difficult to know, it is best to use the simple power law expression for aerosol attenuation

$$\tau_\lambda(A) = -\beta\lambda^{-\alpha} \tag{8}$$

where β is the turbidity coefficient and α is the wavelength coefficient.

Measurements of α indicate a wide range of possible values. However, most values occur in the range from 0.8 to 2, with an average value of 1.3 being considered most reasonable. The turbidity coefficient can be measured with reasonable accuracy. Typical values are shown in table III.

The spectral diffuse component of solar radiation can be written as

$$D_\lambda = 0.5\left(I_\lambda(0)\ \exp\left\{-\left[\tau_\lambda(O_3) + \tau_\lambda(H_2O)\right] m\right\} - I_\lambda\right) \cos\theta \tag{9}$$

Leckner (1978) has made calculations of this kind and compared them with experimental measurements in a case where β was known to lie in the range from 0.05 to 0.1. The results are shown in figures 1 and 2.

Calculations for the Total Integrated Solar Radiation

The previous section indicates that the spectral calculation for solar radiation at the surface is fairly complex. Some simplification is achieved when the integrated values are calculated with wavelength-averaged values of the parameters involved and with aerosol effects neglected.

An effective mean value of Rayleigh optical depth $\bar{\tau}_\theta(R)$ is given in table IV as a function of zenith angle. The tabulated values refer to a vertical path only. Thus the direct solar radiation reaching the surface if the only extinction process were Rayleigh scattering would be

$$F(R) = I_0 \cos\theta \exp\left[-\bar{\tau}_\theta(R) \frac{p}{1013} \sec\theta\right] \tag{10}$$

where I_0 is the solar constant, θ is the zenith angle, and p is the surface pressure in mbar. The values of table IV can be calculated from

$$\bar{\tau}_\theta(R) = \frac{1}{\sec\theta} \ln\left\{\frac{\int_0^\infty I_\lambda(0)\, d\lambda}{\int_0^\infty I_\lambda(0) \exp\left[-\tau_\lambda(R) \sec\theta\right] d\lambda}\right\} \tag{11}$$

For ozone, the effective absorptance $\alpha(O_3)$ over the entire solar spectrum is given by Lacis and Hansen (1974) as

$$\alpha(O_3) = \frac{0.02118u}{1 + 0.042u + 3.23 \times 10^{-4} u^2} + \frac{1.082u}{(1 + 138.6u)^{0.805}} + \frac{0.0658u}{1 + (103.6u)^3} \tag{12}$$

where

$$u = \ell \sec\theta \tag{13}$$

The effective absorptance for water vapor according to Lacis and Hansen (1974) is

$$\alpha(H_2O) = \frac{2.9w}{(1 + 141.5w)^{0.635} + 5.925w} \tag{14}$$

where

$$w = X_w \cos\theta \tag{15}$$

Ozone absorption and Rayleigh scattering occur in the same region of the spectrum, but ozone absorption is at high altitudes where there is little Rayleigh scattering. Therefore the solar radiation reaching the surface if there were only attenuation by ozone and Rayleigh scattering would be

$$F(R,H_2O) = I_0 \cos\theta \exp\left[-\bar{\tau}_\theta(R) \frac{p}{1013} \sec\theta\right] [1 - \alpha(O_3)] \qquad (16)$$

Water vapor absorption occurs in the near-infrared region of the spectrum where ozone absorption and Rayleigh scattering are negligible. Thus the attenuation by water vapor can be subtracted directly from equation (16) to yield the direct solar beam of radiation at the surface as

$$I = I_0 \cos\theta \left\{\exp\left[-\bar{\tau}_\theta(R) \frac{p}{1013} \sec\theta\right] [1 - \alpha(O_3)] - \alpha(H_2O)\right\} \qquad (17)$$

The diffuse radiation arriving at the surface consists of the solar radiation scattered downward by the molecules and aerosols. With scattering by aerosols neglected, scattering downward to the surface can be approximated by the following equation (Paltridge and Platt, 1976):

$$\begin{aligned} D = & \left[(I_0 - I) \cos\theta - I_0 \cos\theta\, \alpha_R(\theta)\right] \left(1 + \alpha_g \bar{\alpha}_R^*\right) \\ & + I \cos\theta\, \alpha_g \alpha_R^* \end{aligned} \qquad (18)$$

In equation (18), $(I_0 - I)$ is the radiation removed from the direct beam by scattering, $I_0 \cos\theta\, \alpha_R(\theta)$ is the upward scattered radiation, and $\alpha_R(\theta)$ is an approximate coefficient for upward scattering (i.e. atmospheric reflection) given by Lacis and Hansen (1974) as

$$\alpha_R(\theta) = \frac{0.28}{1 + 6.43 \cos\theta} \qquad (19)$$

The term $\alpha_g \bar{\alpha}_R^*$ takes into account the downward scattering of the diffuse radiation reflected from the surface; α_g is the ground albedo, and $\bar{\alpha}_R^*$ the reflection coefficient for downward scattering, about 0.0685. The last term in equation (18) is the direct beam radiation which is reflected from the Earth and then scattered back downward.

EMPIRICAL MODELS

Clear Sky: Zenith Angle Variation

Under clear sky conditions, zenith angle is the main factor affecting the solar radiation arriving at the surface at a given location. In this case empirical relations can represent the long time average of direct, diffuse, and global solar radiation with good accuracy. For example, Paltridge and Platt (1976) derived empirical functions from data taken at Aspendale, Victoria, Australia, for the 5-year period from 1967 to 1972. The data and empirical curves are shown in figures 3 to 5. The empirical functions are as follows.

For global solar radiation on a horizontal surface, at Aspendale (latitude 38°02'S), the hourly total ($mW\text{-}hr/cm^2$) is

$$F = 1.0 + 141.1 \sin \gamma - 31.0 (\sin \gamma)^{1/2} \tag{20}$$

where γ is the solar elevation angle. The direct normal solar radiation is given by

$$I = 100.0[1 - \exp(-0.06\gamma)] \tag{21}$$

and the diffuse radiation on a horizontal plane by

$$D = 0.5 + 9.6[1 - \exp(-0.05\gamma)] \tag{22}$$

Cloudy Skies

It is difficult to treat clouds in solar energy calculations. Detailed studies require knowledge of cloud drop size distribution and cloud total water content. Although clouds generally diminish the solar radiation incident on the surface, the surface radiation may actually be increased under partially cloudy conditions if the solar disk is not occulted.

Table V indicates the percent decrease in flux of total surface radiation due to continuous cloud cover of various types as a function of the solar zenith angle (Kondrat'ev, 1973).

An empirical expression that yields reasonably accurate results for mean annual and mean monthly studies is (Berliand, 1961) for global radiation:

$$F = F_0(1 - an - bn^2) \tag{23}$$

where F_0 is the clear sky radiation, $b = 0.38$, a is a coefficient that varies with latitude as shown in table VI, and n is cloud cover in tenths. This relation should be used only for long time averages and not for calculations on a daily basis.

Models of the Air Resources Laboratory (NOAA)

The Air Resources Laboratory of NOAA has developed empirical models of global solar radiation on a horizontal plane. The models were developed for the rehabilitation of historical data archives for 26 stations in the NOAA solar radiation network (Solmet, 1978). The data tapes consisted of hourly records of observed weather data and

1. Integrated hourly global solar radiation
2. Duration of sunshine in minutes
3. Cloud opacity in tenths
4. Cloud cover in tenths
5. Sky condition observations

Five regression equations were developed and used for those stations with an appropriate data set for the regression analysis. The form of the equations for each model and examples of the parameters are as follows:

1. Clear Sky

$$SRC = A_0 + A_1 \cos(ZA) + A_2 \cos^2(ZA) + A_3 \cos^3(ZA) \tag{24}$$

where SRC is the clear sky hourly integral global solar radiation (kJ/m^2) and ZA is zenith angle. The coefficient A_0 is determined for mornings and afternoons for each month of the year; and A_1, A_2, and A_3 are estimated separately for mornings and afternoons, one set of each for the year.

2. Sunshine and Opaque Cloud (preferred estimating function)

$$SR = SRC\left[B_0 + B_1(SS) + B_2(OPQ) + B_3(OPQ)^2 + B_4(OPQ)^3 + B_5(RN)\right] \tag{25}$$

where SR is the hourly global solar radiation (kJ/m^2), SS is the number of minutes of sunshine divided by 60, OPQ is cloud opacity (0.1, 0.2, etc.), and RN is a precipitation variable which is 0 for no precipitation and 1 when precipitation is reported.

3. Opaque Cloud Only (same as 2 without sunshine term)

$$SR = SRC\left[C_0 + C_2(OPQ) + C_3(OPQ)^2 + C_4(OPQ)^3 + C_5(RN)\right] \tag{26}$$

4. Sunshine Only (converse of 3)

$$SR = SRC[D_0 + D_1(SS) + D_5(RN)] \tag{27}$$

5. Sky Condition

$$SR = SRC\left[E_0 + \sum_{j=1}^{7} E_i(SC_i) + E_8(RN)\right] \tag{28}$$

where each SC_i is 0 or 1 depending on whether the sky cover listed below is present at any one of up to four levels:

SC_1	thin scattered; 0.1-0.5 cover
SC_2	opaque scattered; 0.1-0.5 cover
SC_3	thin broken; 0.6-0.9 cover
SC_4	opaque broken; 0.6-0.9 cover
SC_5	thin overcast; 1.0 cover
SC_6	opaque overcast; 1.0 cover
SC_7	partial or total obscuration

The coefficients for the regression equations are available on punched cards; an example is listed below. The punched cards are arranged to provide a maximum of 12 fields of length 6 (including the decimal point). The last 8 columns of each card are identification. There are 7 cards for each station as follows:

Card order	Parameter	Number of coefficients	Number of punched fields on card	Description
1	A_0	12	12	Clear sky; Jan-Dec, morning
2	A_0	12	12	Clear sky; Jan-Dec, afternoon
3	A_1, A_2, A_3	6	6	Clear sky; first 3 are morning; last 3 are afternoon
*4	$C_0 - C_5$	5	6	Opaque cloud only: SS coef. = 0.0 ($C_1 = 0$)
*5	$B_0 - B_5$	6	6	Sunshine and opaque cloud coef.
*6	$D_0 - D_5$	3	6	Sunshine only: opaque cloud coefs. = 0.0 ($d_2 = d_3 = d_4 = 0$)
7	$E_0 - E_8$	9	9	Sky cond. coef.

*Cards 4, 5, and 6 have common ordered positions for the constant term, SS, OPQ, OPQ^2, OPQ^3, and RN. For example, on card 4 the sunshine coefficient (field 2) is always zero.

An example of a set of coefficients is

Washington, D.C.

```
-5.   12.   1.    -30.  -89.  -180. -219. -192. -128. -65.  -37.  -26.   WSH CLRM
9.    9.    20.   -30.  -87.  -172. -176. -195. -131. -67.  -59.  -15.   WSH CLRA
2350. 2810. -1540. 2100. 3570. -2060.                                    WSH CLRZ
1.000 0.000 -.474 0.920 1.070 -.214                                      WSH 0
0.000 0.000 0.000 0.000 0.000 0.000                                      WSH SS.0
0.000 0.000 0.000 0.000 0.000 0.000                                      WSH SS
0.932 0.048 -.005 -.007 -.141 -.055 -.471 -.131 -.251                    WSH SKYC
```

THE INFERENCE OF SOLAR RADIATION AT THE SURFACE FROM SATELLITE DATA

The technique involved in the application of satellite images to the prediction of solar radiation arriving at the Earth's surface has three steps:

1. Establish a set of equations which can be used to relate the data from the satellite images to the insolation. It may also be necessary to include some conventional meteorological parameters in the equations.

2. Use satellite data for a period of time plus surface solar energy measurements taken at the same time to determine unknown constants in these equations.

3. Then use satellite image data with the equations to predict the solar radiation incident upon the surface.

In the following, one of the more recent attempts, estimating hourly and daily global solar radiation from GOES geostationary satellite images, is discussed.

The Great Plains Experiment

The National Environmental Satellite Service and the Great Plains Agricultural Council have carried out an experiment to determine incoming solar radiation in the U.S. Great Plains area from geostationary satellite images (Tarpley, 1979).

The region selected for the experiment, shown in figure 6, was bounded by two latitude circles, 29° and 49° N, and two meridians of longitude, 95° and 105° W. Twenty-two sites were instrumented with pyranometers for measurement of incident global surface energy at the points shown in the figure.

The satellite data used were visible (0.55 to 0.75 μm) images from the GOES visible and infrared spin scan radiometer (VISSR), having 8 km resolution at Nadir. Relative brightness levels were digitized (0 to 63 counts). Hourly images were used for 7 to 10 hours per day distributed about local noon for the period from June 7, 1977, to August 15, 1977.

Surface meteorological data used were surface pressures and total precipitable water.

The grid used for analyses of the satellite images is shown in figure 7. The Great Plains area was divided into targets approximately 50 km on a side, each made up of 7 × 6 arrays of 8 km pixels.

Quantities used as variables for determination of surface insolation were

1. Surface pressure, a measure of total air mass, which therefore should be correlated with the depletion of solar radiation by molecular scattering

2. Precipitable water which provides information on absorption and scattering by water vapor

3. Mean target brightness which is a measure of reflected and scattered radiation due to all causes

4. Cloud amount and brightness which indicate the amount of radiation reflected by the clouds.

Determination of Cloud Free Brightness Levels

An initial task was to determine cloud free brightness in the images, by regression against functions of solar zenith angle χ and the azimuth angle ϕ between the Sun and the satellite. Cloud free brightness was calculated on a 2^{o} grid with interpolation to determine values at 0.5^{o} target intervals. For this purpose, 100 observations per target were used for 27 days in May 1977, just previous to the period of the test.

In order to obtain the regression coefficients, cloud contaminated observations were eliminated by an automatic cloud detection and elimination procedure, along with fitting the data to the cloud free regression equation of the form

$$B = A + b \cos \chi + c \sin \chi \cos \phi + d \sin \chi \cos^2 \phi \tag{29}$$

The cyclic procedure, shown in figure 8, produced cloud free data sets and regression coefficients after two iterations of the procedure, with the final standard error of the estimate for the regression equation of 0.5 to 0.9 counts.

Determination of Cloud Parameters and Target Brightness

The cloudiness of each pixel was established according to the following criteria: it was clear if the brightness was less than or equal to $B(\chi,\phi) + 3$, partly cloudy if the brightness was greater than $B(\chi,\phi) + 3$ but less than or equal to $B(\chi,\phi) + 5$, and cloudy if the brightness was greater than $B(\chi,\phi) + 5$.

The cloud fraction for the target was then calculated from

$$n = \frac{0.5N_2 + N_3}{N_1 + N_2 + N_3} \tag{30}$$

where N_1, N_2, and N_3 were the number of pixels in the clear, partly cloudy, and cloudy cases.

The mean cloud brightness I_{cld} was taken to be the mean of the brightness for the cloudy cases. The quantity

$$B_0 = B(45^{\circ}, 105^{\circ}) \tag{31}$$

was also calculated as the normalized clear brightness.

Estimation of Hourly Insolation

The form of the regression equations for hourly insolation was suggested by consideration of the equation of conservation of radiant energy

$$Q_0 = Q_R + Q_A + Q_G \tag{32}$$

where the subscripts indicate the following:

0	at the top of the atmosphere
R	reflected back into space
A	absorbed in the atmosphere
G	absorbed at the ground

But

$$Q_G = Q_S(1 - \alpha) \tag{33}$$

where Q_S is the insolation at the surface and α is the surface albedo. Substituting from equation (32) for Q_G results in

$$Q_S = \frac{1}{1 - \alpha}(Q_0 - Q_R - Q_A) \tag{34}$$

The regression equations used were determined by cloud amount; they were

$$\left.\begin{aligned}
Q_S &= a + b \cos \chi + c\psi + dn + e\left(\frac{I_m}{B}\right)^2 && (n < 0.4) \\
Q_S &= a + b \cos \chi + cn\left(\frac{I_{cld}}{B_0}\right)^2 && (0.4 \leq n < 1.0) \\
Q_S &= a + b \cos \chi + c\left(\frac{I_{cld}}{B_0}\right) && (n = 1.0)
\end{aligned}\right\} \tag{35}$$

where

Q_S	hourly surface insolation, ly (1 langley = 41.84 kJ/m^2)
χ	local solar zenith angle
ψ	transmittance of the clear atmosphere
n	fractional cloud amount
I_m	mean target brightness
I_{cld}	mean cloud brightness
B	predicted clear brightness
B_0	normalized clear brightness, $B(45^{\circ},105^{\circ})$
a,b,c,d,e	the regression coefficients

Precipitable water and surface altitude Z were used in the determination of the clear target transmission:

$$\psi = \psi_{ws}\psi_{wa}\psi_{r} \tag{36}$$

where the transmission due to water vapor scattering, water vapor absorption, and Rayleigh scattering, respectively, were taken to be:

$$\psi_{ws} = 1 - 0.00225wm \tag{37}$$

$$\psi_{wa} = 1 - 0.077(wm)^{0.3} \tag{38}$$

$$\psi_{r} = 0.972 - 0.0862m + 0.00933m^2 \tag{39}$$

where w is the precipitable water and m, the optical air mass, is given by

$$m = \sec\chi \exp\left(-\frac{Z}{8243}\right) \tag{40}$$

Results

To determine the technique for estimating surface insolation from cloud images, all of the data were included. This is referred to as the dependent development data set. In order to estimate how accurately insolation could be estimated under operational conditions, the data were divided into two parts, the dependent set with only 4 pyranometer sites and the independent set with 18 pyranometers to verify the regression equation.

The values of the regression coefficients and their standard errors are listed in table VII for the dependent developmental data set. For this set, satellite estimates from the regression equations are plotted versus actual measurements in figures 9(a), 9(b), and 9(c) for $n < 0.4$, $0.4 \leq n < 1.0$, and $n = 1.0$, respectively. Correlation coefficients and standard errors of the estimates are shown in the figures.

Daily cumulative insolation was also estimated, using the zenith angle to interpolate and fill in gaps in the data. These results are shown in figure 10.

Finally the statistics of estimated total insolation for four different cases are shown in table VIII. Cases considered are

1. Seven or more pictures per day, dependent data

2. Seven or more pictures per day, independent data

3. Two pictures per day, dependent data

4. One picture per day, dependent data

In each of the first three cases, the standard errors are less than 10 percent of the mean. In the last case, with only one picture per day, the standard error was about 20 percent of the mean. In this last case, sampling was insufficient.

The most significant problem with the technique is the overestimation of surface insolation under cloudy conditions (see fig. 9(c)).

REFERENCES

Berliand, T. G. 1961: Distribution of Solar Radiation Over the Continents. Gidrometdoiydat (Leningrad).

Kondrat'ev, K. Ya., ed. 1973: Radiation Characteristics of the Atmosphere and the Earth's Surface. NASA TT F-678, Amerind Pub. Co. Pvt. Ltd. (Available from NTIS.)

Lacis, Andrew A.; and Hansen, James E. 1974: A Parametrization for the Absorption of Solar Radiation in the Earth's Atmosphere. J. Atmos. Sci., vol. 31, no. 1, pp. 118-133.

Leckner, Bo 1978: The Spectral Distribution of Solar Radiation at the Earth's Surface - Elements of a Model. Sol. Energy, vol. 20, no. 2, pp. 143-150.

McClatchey, R. A.; Fenn, R. W.; Selby, J. E. A.; Volz, F. E.; and Garing, J. S. 1971: Optical Properties of the Atmosphere (Revised). AFCRL-71-0279, U.S. Air Force. (Available from DTIC as AD 726 116.)

Paltridge, G. W.; and Platt, G. M. R. 1976: Radiative Processes in Meteorology and Climatology. Elsevier Scientific Pub. Co.

Solmet, 1978: Solmet Manual - Volume 2. National Climatic Center.

Tarpley, J. D. 1979: Estimating Incident Solar Radiation at the Surface From Geostationary Satellite Data. J. Appl. Meteorol., vol. 18, no. 9, pp. 1172-1181.

TABLE I.- SPECTRAL ABSORPTION COEFFICIENTS OF OZONE (cm^{-1})

[From Leckner, 1978*]

λ	k	λ	k	λ	k	λ	k	λ	k
0.290	38.000	0.445	0.003	0.515	0.045	0.585	0.118	0.700	0.023
0.295	20.000	0.450	0.003	0.520	0.048	0.590	0.115	0.710	0.018
0.300	10.000	0.455	0.004	0.525	0.057	0.595	0.120	0.720	0.014
0.305	4.800	0.460	0.006	0.530	0.063	0.600	0.125	0.730	0.011
0.310	2.700	0.465	0.008	0.535	0.070	0.605	0.130	0.740	0.010
0.315	1.350	0.470	0.009	0.540	0.075	0.610	0.120	0.750	0.009
0.320	0.800	0.475	0.012	0.545	0.080	0.620	0.105	0.760	0.007
0.325	0.380	0.480	0.014	0.550	0.085	0.630	0.090	0.770	0.004
0.330	0.160	0.485	0.017	0.555	0.095	0.640	0.079	0.780	0.0
0.335	0.075	0.490	0.021	0.560	0.103	0.650	0.067	0.790	0.0
0.340	0.040	0.495	0.025	0.565	0.110	0.660	0.057	0.800	0.0
0.345	0.019	0.500	0.030	0.570	0.120	0.670	0.048	0.810	0.0
0.350	0.007	0.505	0.035	0.575	0.122	0.680	0.036	0.820	0.0
0.355	0.0	0.510	0.040	0.580	0.120	0.690	0.028	0.830	0.0

TABLE II.- EFFECTIVE ABSORPTION COEFFICIENTS OF WATER VAPOR (cm^2g^{-1})

[From Leckner, 1978*]

λ	k_w	λ	k_w	λ	k_w	λ	k_w	λ	k_w
0.69	0.160E-01	0.84	0.155E+00	0.99	0.125E+00	1.70	0.510E+00	2.90	0.650E+03
0.70	0.240E-01	0.85	0.300E-02	1.00	0.250E-02	1.75	0.400E+01	3.00	0.240E+03
0.71	0.125E-01	0.86	0.100E-04	1.05	0.100E-04	1.80	0.130E+03	3.10	0.230E+03
0.72	0.100E+01	0.87	0.100E-04	1.10	0.320E+01	1.85	0.220E+04	3.20	0.100E+03
0.73	0.870E+00	0.88	0.260E-02	1.15	0.230E+02	1.90	0.140E+04	3.30	0.120E+03
0.74	0.610E-01	0.89	0.630E-01	1.20	0.160E-01	1.95	0.160E+03	3.40	0.195E+02
0.75	0.100E-02	0.90	0.210E+01	1.25	0.180E-03	2.00	0.290E+01	3.50	0.360E+01
0.76	0.100E-04	0.91	0.160E+01	1.30	0.290E+01	2.10	0.220E+00	3.60	0.310E+01
0.77	0.100E-04	0.92	0.125E+01	1.35	0.200E+03	2.20	0.330E+00	3.70	0.250E+01
0.78	0.600E-03	0.93	0.270E+02	1.40	0.110E+04	2.30	0.590E+00	3.80	0.140E+01
0.79	0.175E-01	0.94	0.380E+02	1.45	0.150E+03	2.40	0.203E+02	3.90	0.170E+00
0.80	0.360E-01	0.95	0.410E+02	1.50	0.150E+02	2.50	0.310E+03	4.00	0.450E-02
0.81	0.330E+00	0.96	0.260E+02	1.55	0.170E-02	2.60	0.150E+05		
0.82	0.153E+01	0.97	0.310E+01	1.60	0.100E-04	2.70	0.220E+05		
0.83	0.660E+00	0.98	0.148E+01	1.65	0.100E-01	2.80	0.800E+04		

TABLE III.- TYPICAL ÅNGSTROM TURBIDITY COEFFICIENTS (β_0)

[The original data are converted from Schüepp's turbidity coefficient B through the relation $\beta_0 = 0.935B$. The three decimal digits in the table are a result of this conversion and do not indicate the accuracy; note that $\beta = \beta_0 0.5^{\alpha-1.3}$; from Leckner, 1978*]

Latitude	60°N	45°N	30°N	0°
Low limit	0.01	0.047	0.047	0.047
Medium	0.057	0.077	0.097	0.117
High limit	0.093	0.187	0.375	0.375

---

*Reprinted with permission from Sol. Energy, vol. 20, copyright 1978, Pergamon Press, Ltd.

TABLE IV.- MEAN OPTICAL DEPTH FOR RAYLEIGH SCATTERING

Zenith angle, deg	Mean optical depth	Zenith angle, deg	Mean optical depth
0	0.094	45	0.088
1	↓	46	.087
2	↓	47	.087
3	↓	48	.087
4	↓	49	.086
5	↓	50	.086
6	↓	51	.086
7	↓	52	.085
8	↓	53	.085
9	↓	54	.084
10	↓	55	.084
11	↓	56	.083
12	↓	57	.083
13	↓	58	.082
14	↓	59	.082
15	.093	60	.081
16	↓	61	.080
17	↓	62	.080
18	↓	63	.079
19	↓	64	.078
20	↓	65	.078
21	↓	66	.077
22	↓	67	.076
23	.092	68	.075
24	↓	69	.074
25	↓	70	.073
26	↓	71	.072
27	↓	72	.071
28	↓	73	.070
29	↓	74	.068
30	↓	75	.067
31	.091	76	.067
32	↓	77	.064
33	↓	78	.062
34	↓	79	.061
35	.090	80	.059
36	↓	81	.056
37	↓	82	.054
38	↓	83	.051
39	↓	84	.048
40	.089	85	.045
41	.089	86	.042
42	.089	87	.037
43	.088	88	.033
44	.088	89	.028

TABLE V.- RELATIVE DECREASE (IN PERCENT) OF THE FLUX OF TOTAL RADIATION FOR THE CASE OF A CONTINUOUS CLOUD COVER OF DIFFERENT TYPES AND DIFFERENT SOLAR ALTITUDES IN COMPARISON WITH THE CORRESPONDING VALUES FOR A CLOUDLESS SKY

[From Kondrat'ev, 1973]

Cloud type	Solar altitude, deg					
	5	10	20	30	40	50
Ci	44	50	34	22	10	2
Cs	33	39	51	35	20	10
Ac	33	39	46	55	46	38
As	44	50	59	64	63	63
St fr.	78	83	80	77	77	76
Sc	89	78	68	71	72	73
St	78	78	80	81	83	84

TABLE VI.- COEFFICIENT a IN EMPIRICAL EQUATION FOR MEAN MONTHLY AND MEAN ANNUAL GLOBAL RADIATION UNDER CLOUDY SKIES

Lat.	0°	5°	10°	15°	20°	25°	30°	35°	40°
a	0.38	0.40	0.40	0.39	0.37	0.35	0.36	0.38	0.38
Lat.	45°	50°	55°	60°	65°	70°	75°	80°	85°
a	0.38	0.40	0.41	0.36	0.25	0.18	0.16	0.15	0.14

TABLE VII.- REGRESSION COEFFICIENTS, THEIR STANDARD ERRORS, AND OTHER STATISTICS FOR HOURLY INSOLATION REGRESSIONS

[From Tarpley, 1979]

	Clear cases $(n < 0.4)$	Partly cloudy $(0.4 \le n < 1.0)$	Cloudy $(n = 1.0)$
a, ly	-19.33	-9.57	-6.56
b, ly	87.08	94.54	87.68
S_b, ly	0.71	1.78	3.16
c, ly	27.58	-7.62	-7.50
S_c, ly	2.33	0.28	0.35
d, ly	-10.48		
S_d, ly	1.33		
e, ly	-6.37		
S_e, ly	0.79		
Multiple-correlation coefficient	0.94	0.77	0.70
Standard error of the estimate	5.56	12.19	11.36
Number of cases	5736	2127	822

TABLE VIII.- STATISTICS OF ESTIMATED TOTAL DAILY INSOLATION

[From Tarpley, 1979]

	Seven or more pictures per day (dependent data)	Seven or more pictures per day (independent data)	Two pictures per day (dependent data)	One picture per day (dependent data)
Mean error, ly	10.7	17.5	12.4	7.0
Correlation coefficient	0.91	0.90	0.88	0.68
Standard error, ly	50.4	53.5	58.5	99.0
Mean daily insolation (pyranometer), ly	586.2	594.4	586.7	582.8
Number of cases	896	721	1036	1077

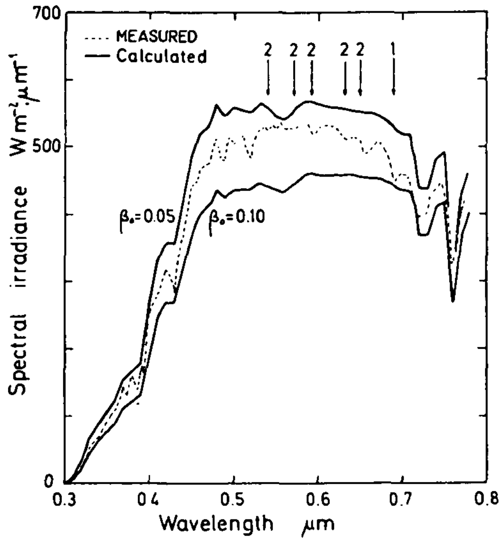

Figure 1.- Calculated direct irradiance on a horizontal surface at air mass 2 and two values of turbidity coefficient β, compared with measured values. The missing weak bands in the calculated curves are indicated with arrows. (From Leckner, 1978; reprinted with permission from Sol. Energy, vol. 20, copyright 1978, Pergamon Press, Ltd.)

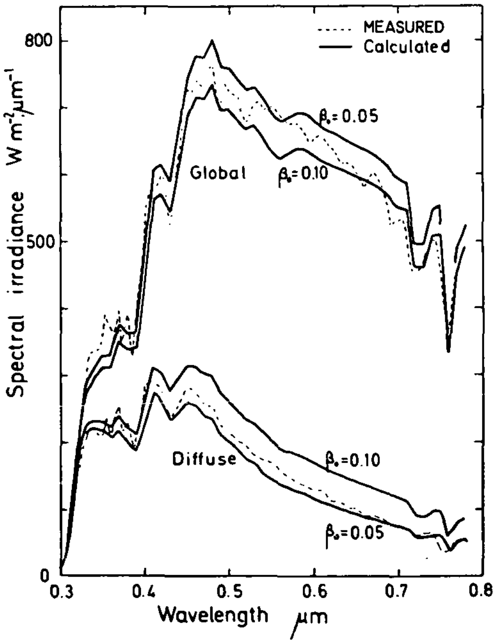

Figure 2.- Calculated global and diffuse irradiances on a horizontal surface at air mass 2 and two values of turbidity coefficient β, compared with measured values. (From Leckner, 1978; reprinted with permission from Sol. Energy, vol. 20, copyright 1978, Pergamon Press, Ltd.)

ORIGINAL PAGE IS
OF POOR QUALITY

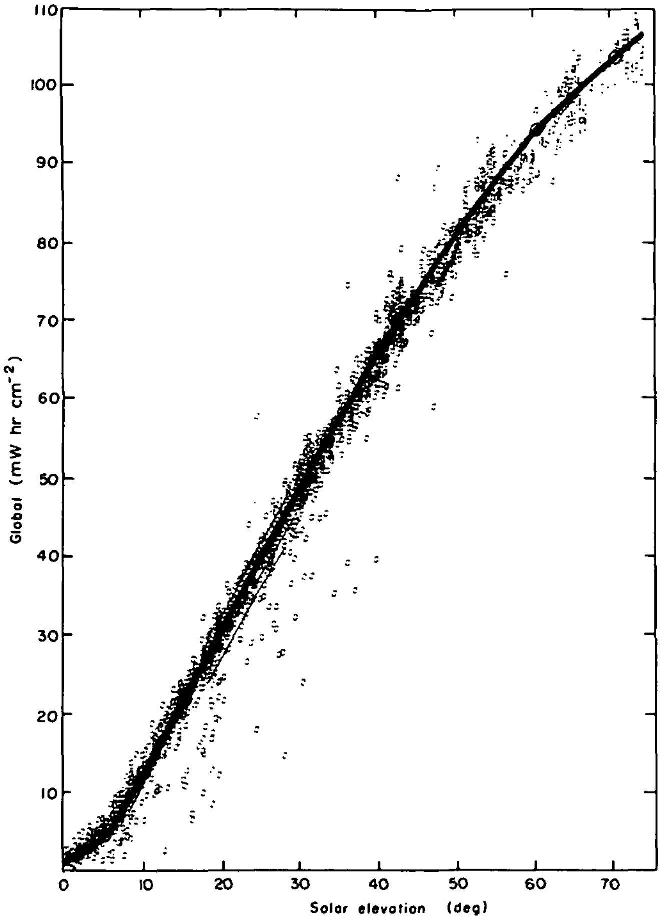

Figure 3.- Global solar radiation (hourly total) in clear skies as a function of solar elevation γ at Aspendale for the period from 1967 to 1972. (From Paltridge and Platt, 1976.)

ORIGINAL PAGE IS OF POOR QUALITY

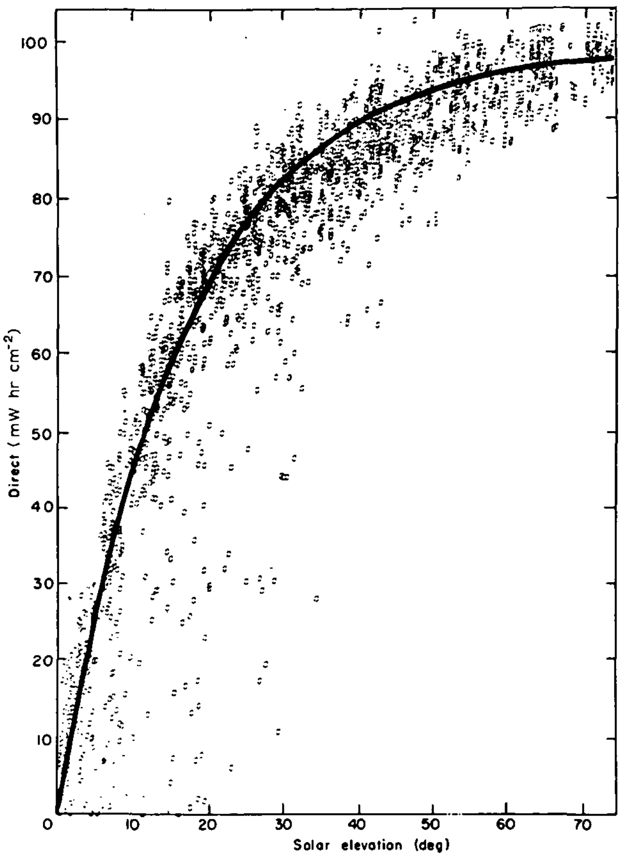

Figure 4.- Direct radiation (hourly total) in clear skies as a function of solar elevation γ at Aspendale for the period from 1967 to 1972. (From Paltridge and Platt, 1976.)

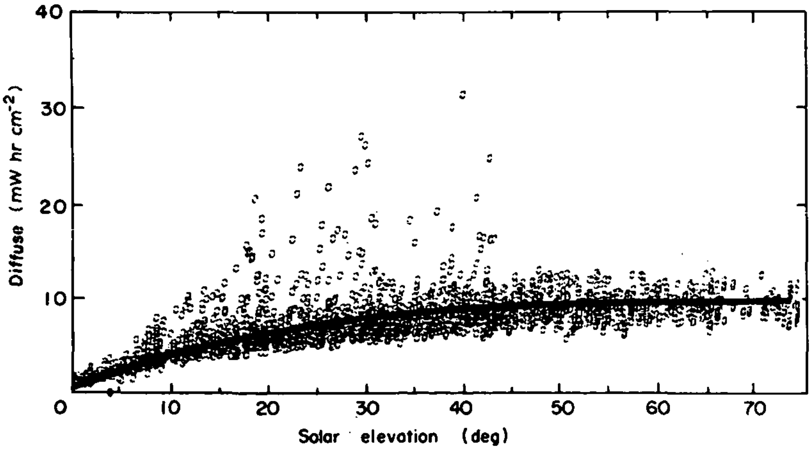

Figure 5.- Diffuse radiation (hourly total) in clear skies as a function of solar elevation angle γ at Aspendale for the period from 1967 to 1972. Note the definition of "clear sky" in the text. (From Paltridge and Platt, 1976.)

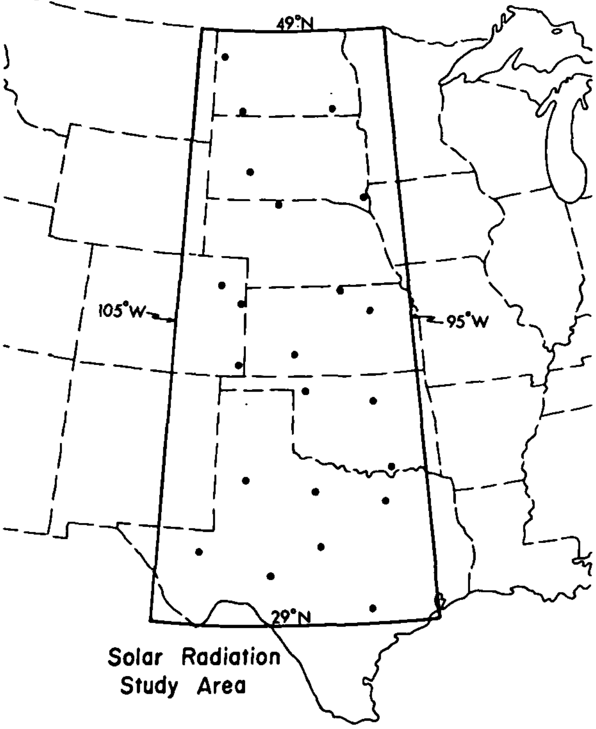

Figure 6.- The part of the Great Plains where satellite data were collected (dark line). The pyranometer sites used in this study are marked with dark circles. (From Tarpley, 1979.)

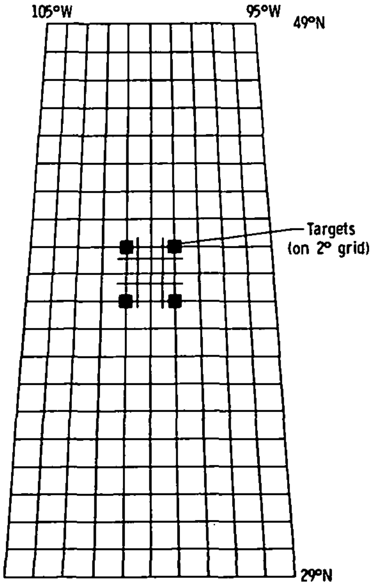

Figure 7.- Grid used for analysis of satellite images.

ORIGINAL PAGE IS
OF POOR QUALITY

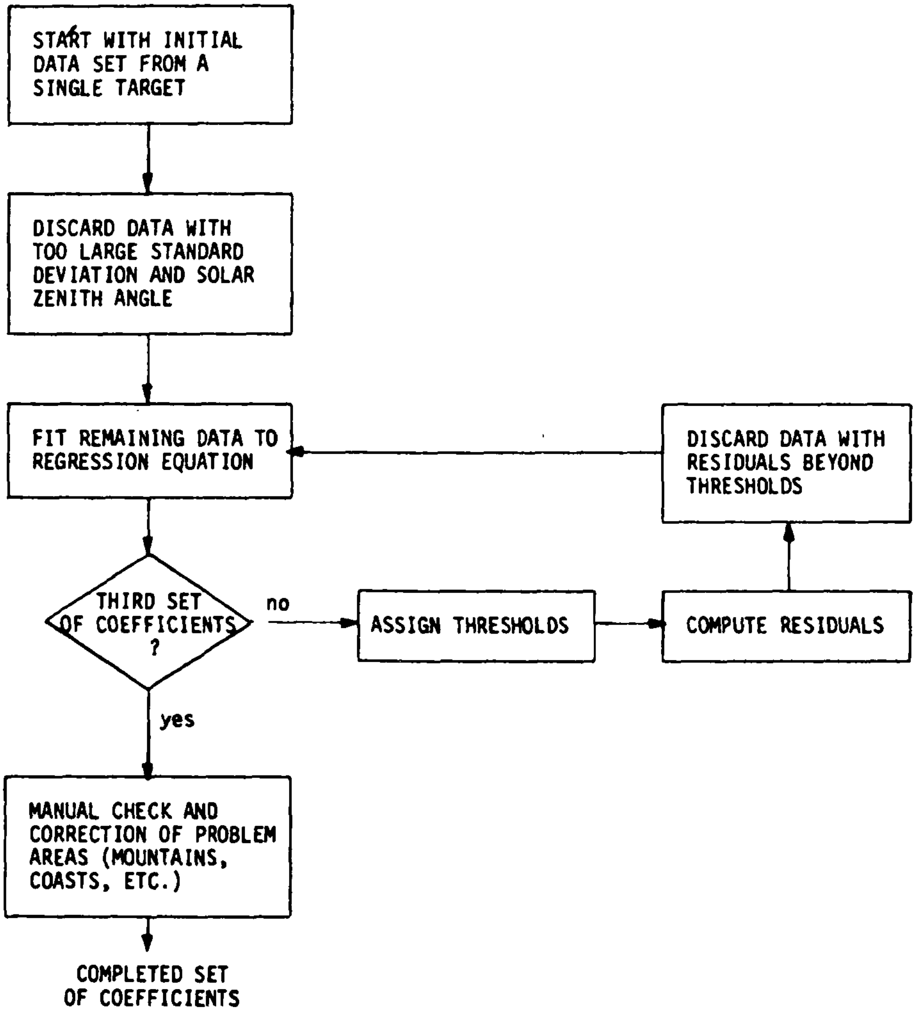

Figure 8.- Flow diagram for processing target brightness data into regression coefficients. (From Tarpley, 1979.)

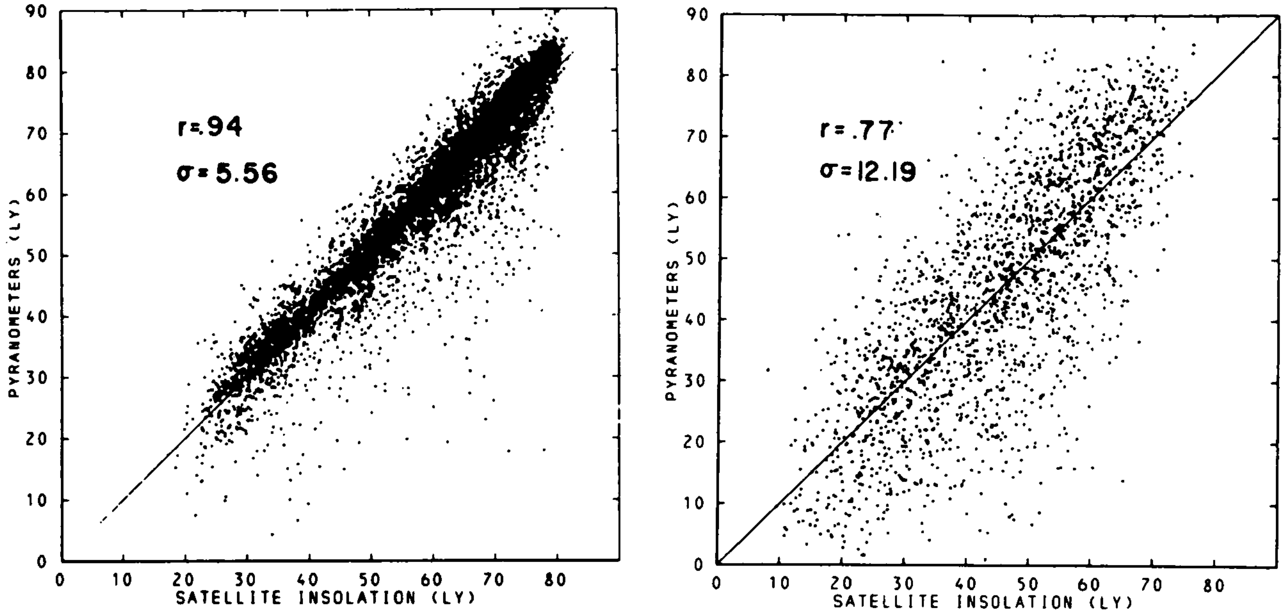

(a) 5736 clear cases (n < 0.4).

(b) 2217 partly cloudy cases (0.4 ≤ n < 1.0).

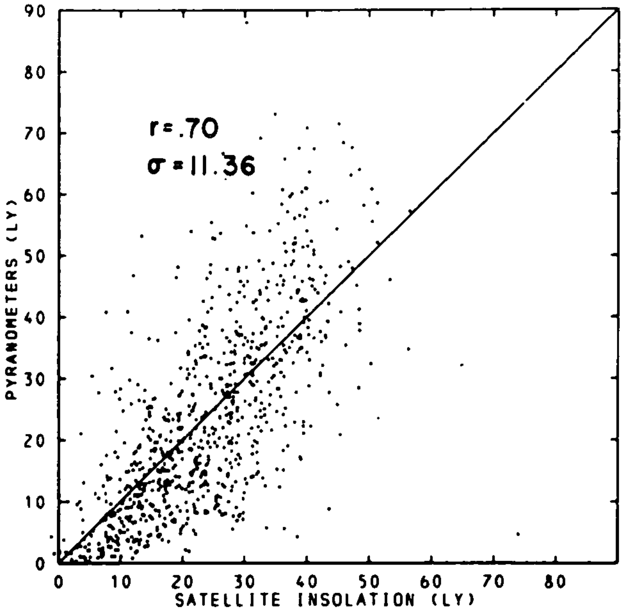

(c) 822 totally cloudy cases (n = 1.0).

Figure 9.- Hourly insolation measured by the 22 pyranometers plotted against satellite estimates (dependent data). If there were no errors, all points would lie on the diagonal line. Correlation coefficients r and standard errors σ are shown. (From Tarpley, 1979.)

ORIGINAL PAGE IS
OF POOR QUALITY

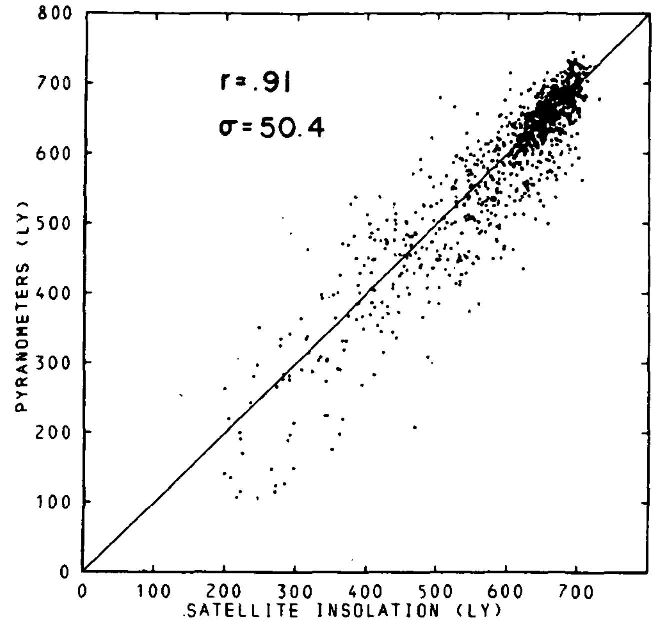

Figure 10.- Daily insolation measured by the 22 pyranometers (dependent data) plotted against satellite estimates ($\geq$7 pictures per day). Diagonal line shows perfect agreement between pyranometers and satellite estimates. (Correlation coefficient r and standard error σ are shown. (From Tarpley, 1979.)

N82 33328

METEOSAT STUDIES OF CLOUDS AND RADIATION BUDGET

R. W. Saunders*
University College London
London, England

INTRODUCTION

Three aspects of the work being carried out in the Laboratory for Planetary Atmospheres, University College London, are presented. Radiation budget studies of the atmosphere/surface system from Meteosat, cloud parameter determination from space, and sea surface temperature measurements from AVHRR data are all described. This work was carried out on the Interactive Planetary Image Processing System (IPIPS), which allows interactive manipulation of the image data in addition to the conventional computational tasks. The current hardware configuration of IPIPS is shown in figure 1. The I^2S is the principal interactive display allowing interaction via a trackball, four buttons under program control, or a touch tablet. Simple image processing operations such as contrast enhancing, pseudocoloring, histogram equalization, multispectral combinations, etc. can all be executed literally at the push of a button. For the studies described here, Meteosat and NOAA AVHRR data were analyzed to give the results presented.

RADIATION BUDGET STUDIES

Albedos and longwave fluxes are derived from the raw Meteosat images according to the scheme shown in figure 2. Having located the images so that each pixel can be assigned a latitude/longitude, the Meteosat visible images are converted into a map of broadband albedo using the calibration derived by Kriebel (1981). The calibration factor is a function of the underlying surface type because of the different frequency dependence of the reflected radiation (within the filter profile) from different surfaces. The calibration converts counts to radiances within the 0.4- to 1.1-μm region, and it is then assumed that the unfiltered albedo is the same as the filtered albedo within the above wavelength limits. The unfiltered albedo is given by:

$$a = \frac{\pi n_r}{sf \cos Z(t)} \qquad (1)$$

---

*Present affiliation: Rutherford Appleton Laboratory, Chilton, Didcot, Oxfordshire OX11 0QX, England.

where

n_r filtered reflected radiance

s filtered solar constant

f Earth-Sun distance correction factor from 1 AU

$Z(t)$ solar zenith angle at time t

The albedo derived is then corrected for anisotropic scattering effects by the following expression for each surface type m:

$$A_m = \frac{a_m(\theta,\phi,Z)}{X_m(\theta,\phi,Z)} \tag{2}$$

where X_m is the Nimbus 7 ERB anisotropic factor (Stowe et al., 1980) for model type m, viewing zenith angle θ, relative azimuth angle ϕ (between Sun and satellite), and solar zenith angle Z.

The 11-μm IR channel was calibrated, according to Morgan (1980), who computed calibration factors from radiosonde and ship data. The conversion from filtered to broadband radiance was first carried out using a regression relationship developed by Abel and Gruber (1979), and more recently using a relation developed by Gube (1980). Limb darkening effects (Rashke et al., 1973) were also included. Good agreement was found between the results obtained from both regression relationships.

The albedos and longwave fluxes were determined over Western Europe, averaged over 1° latitude/longitude squares for every hour of the day (21 August 1978). The instantaneous values at 1145 GMT are shown in figure 3, together with the original visible and infrared images from which these parameters were derived. The Meteosat data were obtained hourly so that the fluxes could be measured throughout 1 day. This allowed calculation of a true diurnal mean and the standard deviation of the values about the mean, as shown in figure 4. The regions of high visible standard deviations correspond to areas over which clouds formed and dissipated during the day. The diurnal heating of the cloud-free land surfaces also results in a higher standard deviation than that over the adjacent sea surfaces.

Diurnal variations are important when trying to infer an accurate daily mean from just one or two polar orbiter observations. Variations over different cloud and surface types have been measured (Saunders and Hunt, 1980) and are shown to be appreciable over cloud-free land (for outgoing flux) and over low stratocumulus clouds (for reflected flux). It is possible to model some of these variations for cloud-free scenes by looking at the Meteosat observations over many different surface types. These models can then be used to predict more accurate daily means from just one shortwave or two longwave polar orbiter observations.

Over cloud-free land or ocean the daily mean albedo $\bar{A}$ can be expressed as:

$$\bar{A} = \frac{1}{nSf} \frac{\sum_{i=1}^{n} Wr_i}{\sum_{i=1}^{n} \cos Z_i} \simeq \frac{Wr(\text{polar})}{Sf \cos Z(\text{polar})} \tag{3}$$

where

Wr_i	reflected irradiance for the i^{th} hour observed by Meteosat
n	number of Meteosat observations for the day
S	unfiltered solar constant
f	Earth-Sun distance correction factor
Z_i	the solar zenith angle for the i^{th} hour

Similarly, the mean outgoing flux $\bar{W}_E$ over cloud-free land can be expressed as:

$$\bar{W}_E = \frac{1}{n} \sum_{i=1}^{n} W_{Ei} \simeq \frac{W_{E,D}(\text{polar}) - W_{E,N}(\text{polar})}{\cos Z_D} \overline{\cos Z} + W_{E,N}(\text{polar}) \tag{4}$$

where

$W_{E,D}(\text{polar})$, $W_{E,N}(\text{polar})$	daytime and nighttime polar orbiter observations of outgoing flux
$\overline{\cos Z}$	mean solar zenith angle for daylight hours
Z_D	solar zenith angle an hour before daytime polar orbiter measurements

Over cloud-free ocean, equation (4) can be simplified to:

$$\bar{W}_E = \frac{1}{n} \sum_{i=1}^{n} W_{Ei} \simeq \frac{W_{E,D}(\text{polar}) + W_{E,N}(\text{polar})}{2} \tag{5}$$

Over clouds, both albedo and longwave flux are strongly dependent on cloud amount and height during the day. It is impossible to formulate a universal diurnal model for cloudiness, since different latitudes and seasons experience different cycles of cloudiness. Over the tropics there is a predictable diurnal cycle for the cumulonimbus clouds over the land, and recent work by Minnis and Harrison (1981) and Gube (1980) has shown that many other types of clouds also have diurnal cycles. The difficulties arise at midlatitudes, where synoptic features which are not linked to the diurnal cycle dominate the changes in cloudiness. In this case more than two observations per day are necessary in order to get an accurate daily mean from polar orbiters. This is an important point when considering the merits of a one- or two-polar-orbiter observation system.

A recent study by Saunders et al. (1982) has compared Nimbus 7, Meteosat, and TIROS-N (Gruber and Winston, 1978) radiation budget measurements. Twelve target areas were chosen over the Meteosat field of view, each with differing cloud/surface types and temporal variations. The daily means from the three different satellite systems were compared, and the best agreement was found between the Nimbus 7 ERB longwave flux values and the corresponding Meteosat values, as shown in figure 5. Differences between the values are due to insufficient diurnal sampling from just two ERB observations, inaccurate narrowband-to-broadband algorithms for the Meteosat filter profile, and differences between the scenes viewed in the Meteosat and ERB target areas. The latter uncertainty was reduced as much as possible by choosing uniform target areas over which the emitted and reflected fluxes were not varying rapidly. Doubts about the narrowband-to-broadband radiance conversions were investigated by comparing coincident Meteosat and Nimbus 7 ERB radiances for approximately the same viewing angles. The total reflected radiances inferred from the Meteosat VIS channel agreed to within 10 percent of the measured ERB radiances, and the total emitted radiances inferred from Meteosat were within 2.5 percent of the ERB values.

CLOUD STUDIES

Obtaining cloud parameters (amount and type) from satellite data is becoming increasingly important. The International Satellite Cloud Climatology Project (ISCCP) is now investigating the problems of obtaining a global cloud data set from the geostationary and polar orbiter data. Intercalibration of the satellites is one difficulty; this may be solved by using the polar orbiter, which underflies all of the geostationary satellites, to provide calibration data (Beriot et al., 1982). Gaps caused by missing geostationary satellites can also be filled at least once a day by the polar orbiter.

In order to obtain a global cloud climatology, the following parameters should be derived: total cloud amount over a predefined grid size (250 × 250 km for ISCCP), and amounts and heights of four well-defined classes, low, medium, convective, and cirrus clouds, measured once every 3 hours.

There are currently many different algorithms which can be used to extract cloud parameters from satellite radiance measurements. The threshold technique is the simplest, and with some refinements it can give accurate results. One problem with this method is that it assumes that the individual pixel either is completely filled with cloud or is cloud-free (Coakley and Bretherton, 1982). Also, gain changes in the radiometer must be accurately monitored in order to give consistent results. One extension of the threshold technique is to use two wavelengths (VIS and IR). The advantages of this bispectral approach are that low cloud is more easily detected during the day from the VIS channel, and cirrus cloud is easily detected using the IR channel. With many days of measurements over each region, a minimum (cloud-free) albedo and maximum (clear) IR radiance can be determined for every region, so that varying thresholds are used according to the properties of the underlying surface type. For instance, clouds are easier to detect over a dark ocean surface than over bright deserts.

Other methods for extracting cloud parameters from satellite measurements include using sounder data to give cloud top heights and cloud amounts (Wielicki and Coakley, 1981), using stereo techniques from two satellites with different viewpoints of the same cloud (Hasler, 1981), and using bidimensional histograms to discriminate between different cloud types. Results from the threshold method and the bidimensional histogram method are presented here.

Cloud amounts over Europe are shown in figure 6 for 1145 GMT on 21 August 1978. In this case there were three classes defined, separated according to the cloud top temperature. These cloud amounts were derived with a threshold technique using both the VIS and IR channel information. Comparison with the associated visible image (fig. 6(a)) gives an idea of accuracy. Problems in using the threshold method are:

1. Low cloud at night; to overcome this the last daylight visible observation can be used as a constraint on the derived cloud amount from the IR channel

2. Areas of sunglint; only the IR channel should be used over these areas over ocean

3. Clouds over snow or ice; the 3.7-μm channel on AVHRR has proved a useful tool for discriminating between clouds and snow or ice surfaces

4. Low clouds over desert areas at night; this can be avoided by modeling the variation of IR radiance under cloud-free conditions during the night

5. Thin cirrus detection; the 6.3-μm water vapor (WV) channels on Meteosat and 3.7-μm on AVHRR can both detect thin cirrus more easily than the conventional VIS and IR channels

Another approach we have studied uses bidimensional histograms. Figure 7 compares such histograms over low and high cloud using all three Meteosat channels. The different positions of the histogram peaks demonstrate how different cloud types can be separated. The importance of using the IR-WV combination is that observations can be made at night, whereas the VIS-IR combination can obviously only be used in daylight.

SEA SURFACE TEMPERATURE STUDIES

Methods have been developed for the analysis of sea surface temperatures (SST) from both TIROS-N and Meteosat images. In temperate latitudes, where the atmospheric water vapor absorption is relatively low, high-resolution (~1 km) sea surface temperature maps may be produced from cloud-free areas, as shown in figure 8(a) for the area around the UK on 12 July 1979. This map was obtained from TIROS-N AVHRR measurements, using data provided by ships to give a relative calibration (Saunders et al., 1982). The satellite-derived data provide considerably more structure in measurements of SST than can be derived from the corresponding ship measurements (fig. 8(b)).

An important feature in these data is the warm region of water to the north of the Netherlands. The center of this area was as much as 3.5°C warmer than the surrounding sea at 1500 GMT. The temporal variation of this feature was investigated using Mercator projected Meteosat images. To investigate the variation in a quantitative manner, a cross-calibration between the Meteosat and TIROS-N observations was developed.

From an analysis of the surface winds, it was found that the observed warm area appeared to be at the center of a ridge of high pressure where there was relatively low wind stress. Pingree and Griffiths (1978) have shown that this area is in a stratified regime during the summer months, which assists in inhibiting the mixing over a deep layer.

The energy balance of the ocean surface layer was modeled in order to simulate the temperature variation of the warm region (fig. 9). The best agreement with Meteosat data is obtained when a mixing layer of 0.6 m depth is assumed. This study eliminates the possible explanation that the anomaly was due to less atmospheric water vapor in this region. It was found that 8 mm of precipitable water would have to be removed from the atmospheric column through descent to achieve a temperature rise of 3.5 K. However, to achieve the observed heating rate, vertical velocities of 5 cm s^{-1} are required, which would cause the radiance to stabilize after 12 hours. This is incompatible with the TIROS-N observation of a temperature anomaly at noon on the previous day, which is strongly suggestive of a diurnal variation.

This study demonstrates the importance of combining both polar orbiter and geostationary data in order to obtain good spatial, radiometric, and temporal resolution. This applies to studies of radiation budget, clouds, and sea surface temperature.

REFERENCES

Abel, P. G.; and Gruber, A. 1979: An Improved Model for the Calculation of Longwave Flux at 11 μm. NOAA Tech. Memo. NESS 106.

Beriot, N.; Scott, N. A.; Chedin, A.; and Sitbon, P. 1982: Calibration of Geostationary Satellite Infrared Radiometers Using the TIROS-N Vertical Sounder. Application to Meteosat - 1. J. Appl. Met., vol. 21, no. 1, pp. 84-89.

Coakley, J. A., Jr.; and Bretherton, F. P. 1982: Cloud Cover From High Resolution Scanner Data: Detecting and Allowing for Partially Filled Fields of View. (Submitted to J. Geophys. Res.)

Gruber, A.; and Winston, J. S. 1978: Earth-Atmosphere Radiation Heating Based on NOAA Scanning Radiometer Measurements. Bull. Amer. Met. Soc., vol. 59, no. 12, pp. 1570-1573, Dec.

Gube, M. 1980: Outgoing Longwave Flux Computation From Meteosat Data. ESA Journal, vol. 4, no. 4, pp. 381-396.

Hasler, A. F. 1981: Stereographic Observations From Geosynchronous Satellites: An Important New Tool for the Atmospheric Sciences. Bull. Amer. Met. Soc., vol. 62, no. 2, pp. 194-212, Feb.

Kriebel, K. T. 1981: Calibration of the Meteosat VIS Channel by Airborne Measurements. Appl. Optics, vol. 20, no. 1, pp. 11-12, Jan.

Minnis, P.; and Harrison, E. F. 1981: Diurnal Variability of Regional Cloud Radiative Parameters From Geostationary Satellite Data. Paper presented at Fourth Conf. on Atmospheric Radiation, Toronto, June.

Morgan, J. 1980: Meteosat 1 Calibration Report, Issue 8, European Space Operational Center MDMD/MET.

Pingree, R. D.; and Griffiths, D. K. 1978: Tidal Fronts on the Shelf Seas Around the British Isles. J. Geophys. Res., vol. 83, no. C9, pp. 4615-4622, Sept. 20.

Rashke, E.; Vonder Haar, T. H.; Pasternak, M.; and Bandeen, W. R. 1973: The Radiation Balance of the Earth-Atmosphere System From Nimbus 3 Radiation Measurements. NASA TN-7249, p. 73.

Saunders, R. W.; and Hunt, G. E. 1980: Meteosat Observations of Diurnal Variation of Radiation Budget Parameters. Nature, vol. 283, no. 5748, pp. 645-647, Feb. 14.

Saunders, R. W.; Ward, N. R.; England, C. F.; and Hunt, G. E. 1982: Satellite Observations of Sea Surface Temperature Around the British Isles. Bull. Amer. Met. Soc. (To be published.)

Saunders, R. W.; Stowe, L. L.; and Hunt, G. E. 1982: An Intercomparison Between Radiation Budget Estimates From Meteosat 1, Nimbus 7, and TIROS-N Satellites. (Submitted to J. Appl. Met.)

Stowe, L. L.; Taylor, V. R.; Jacobowitz, H.; Ruff, I.; Chen, M.; Baldwin, E.; Van Cleef, F.; Hill, M.; and Coleman, D. 1980: A Unique Data Base for Studying Reflectance and Emittance Characteristics of Earth and Cloud Surfaces. Paper presented at International Radiation Symp., Fort Collins, Colorado, Aug.

Wielicki, B. A.; and Coakley, J. A., Jr. 1981: Cloud Retrieval Using Infrared Sounder Data: Error Analysis. J. Appl. Met., vol. 20, no. 2, pp. 157-169, Feb.

ORIGINAL PAGE IS
OF POOR QUALITY

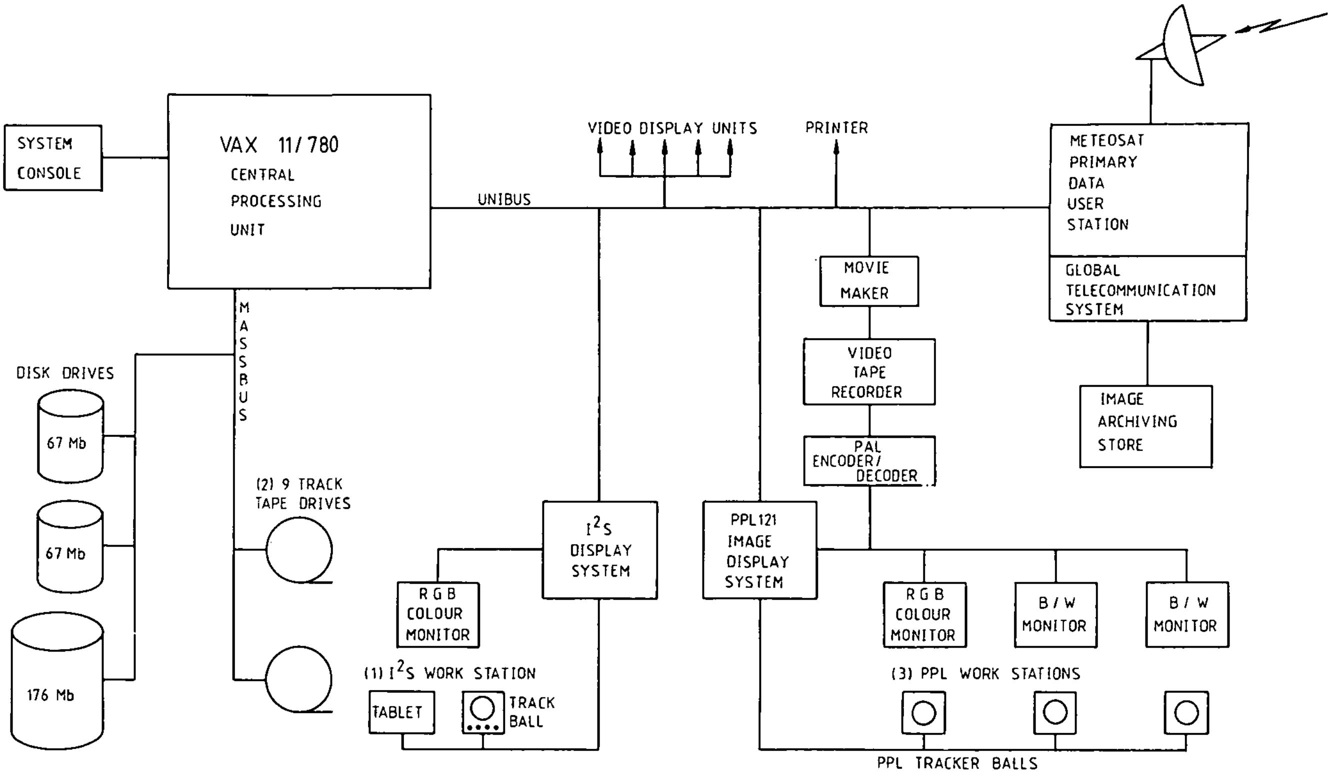

Figure 1.- Current hardware configuration of IPIPS.

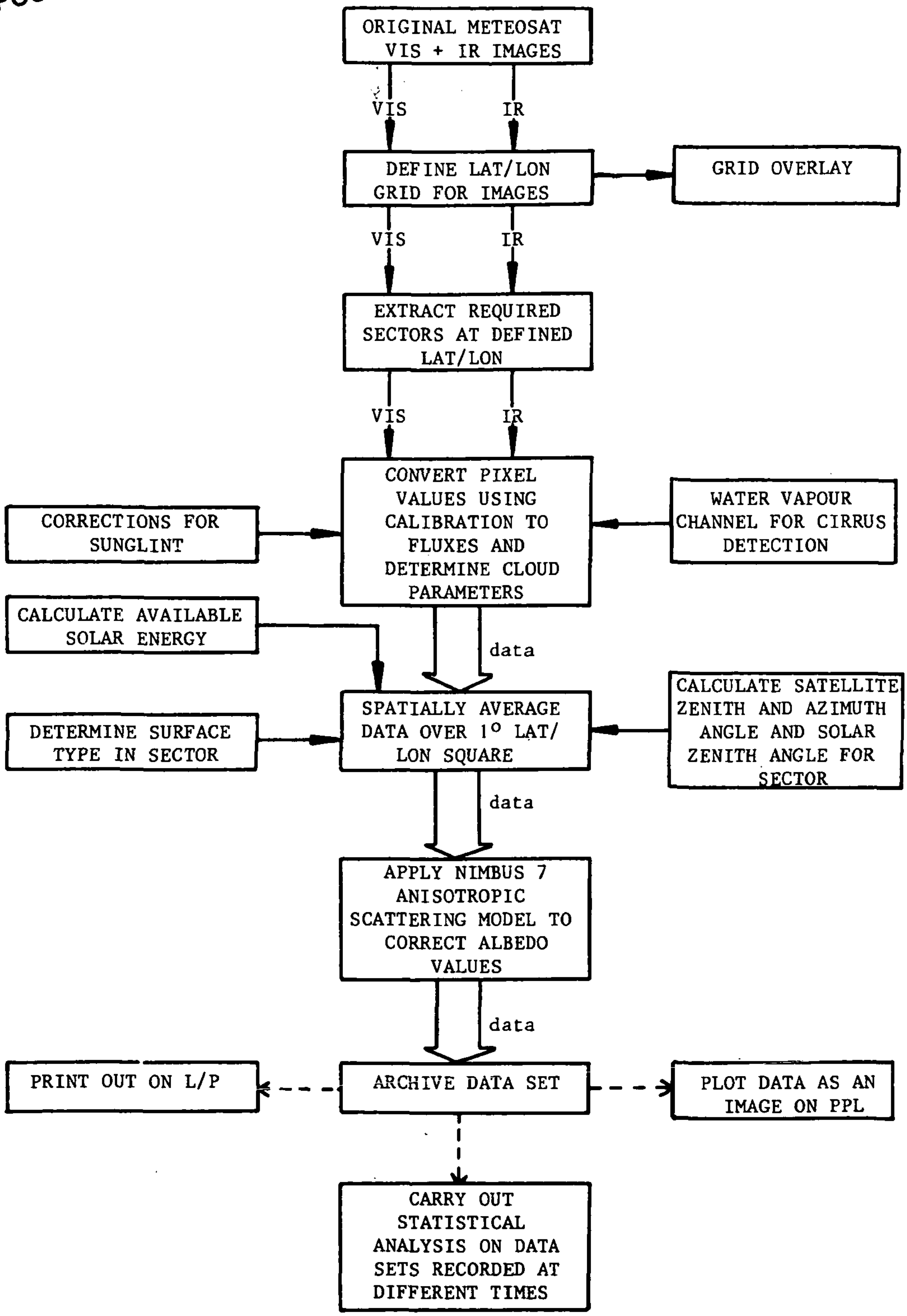

Figure 2.- Flow diagram for obtaining radiation budget parameters from raw image data.

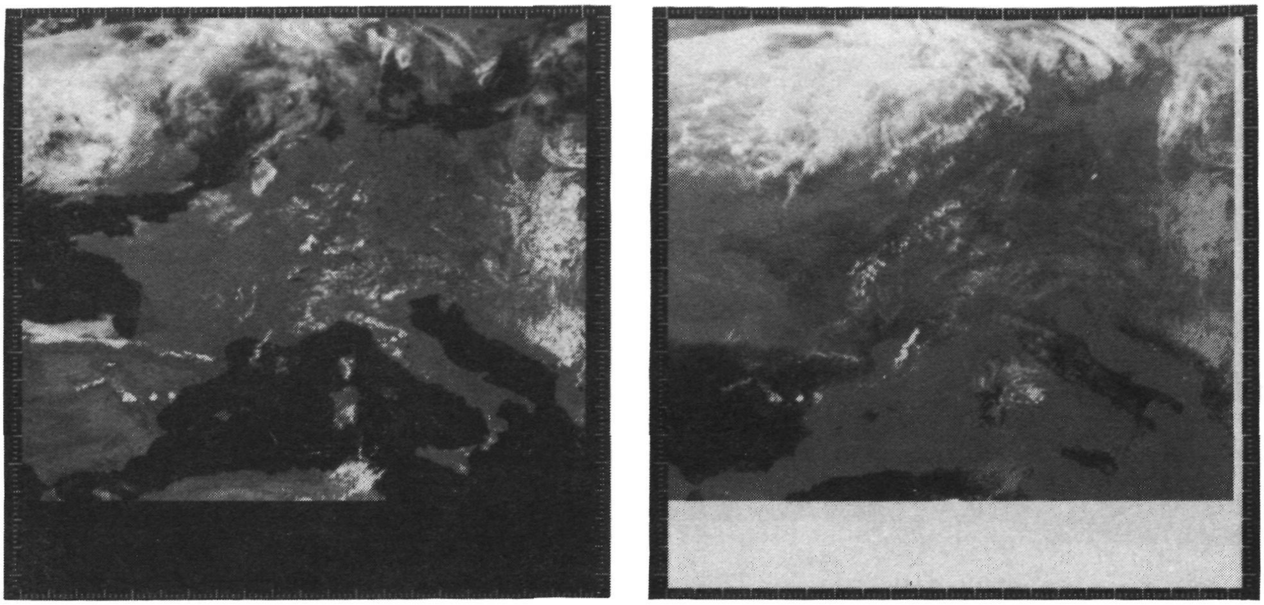

(a) Visible.

(b) Infrared.

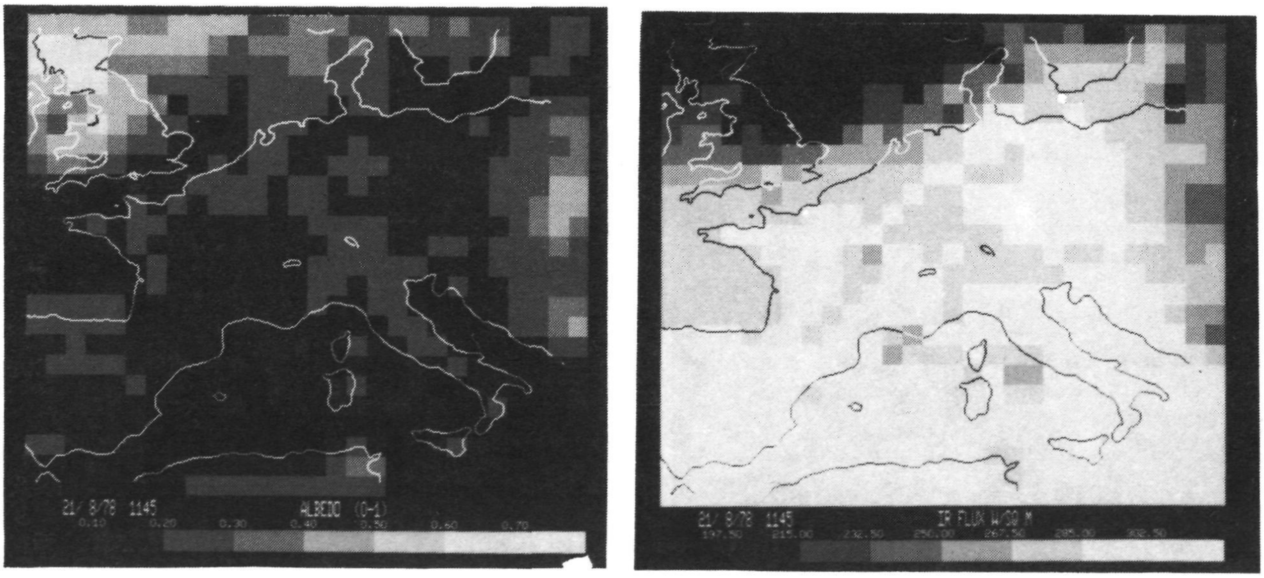

(c) Albedo.

(d) Outgoing flux.

Figure 3.- Visible and infrared square projections of Europe from Meteosat and the albedo and outgoing flux averaged over 1° latitude/longitude squares, derived from the VIS and IR satellite images for 1145 GMT on 21 August 1978. The parameter values are displayed according to the greyscale along the bottom.

ORIGINAL PAGE
BLACK AND WHITE PHOTOGRAPH

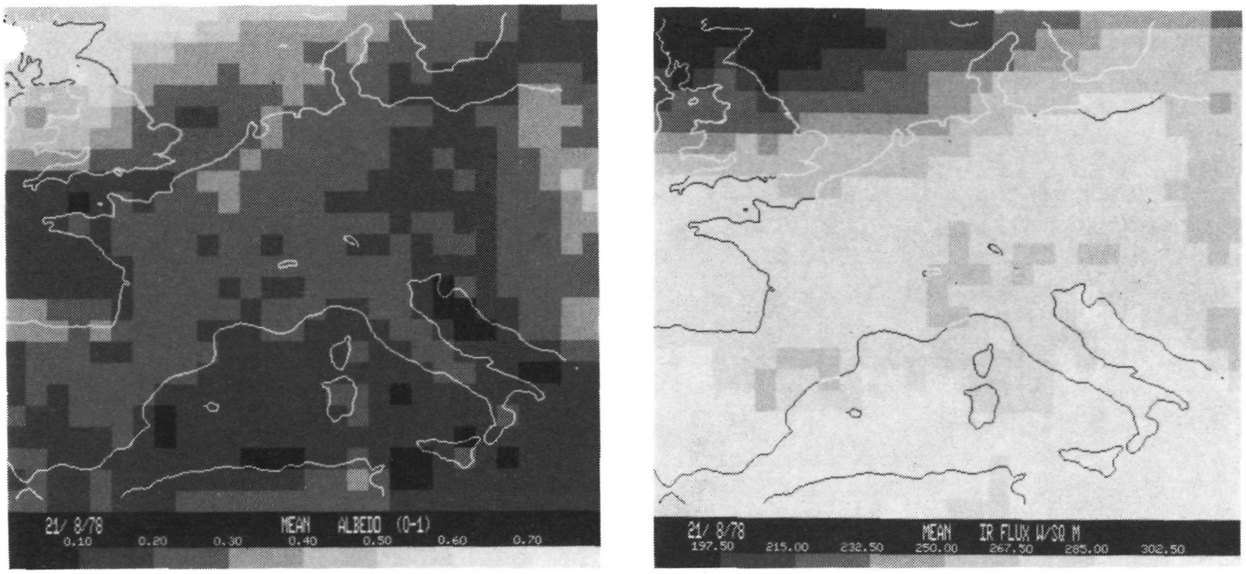

(a) Mean albebo.

(b) Mean longwave flux (W/m^2).

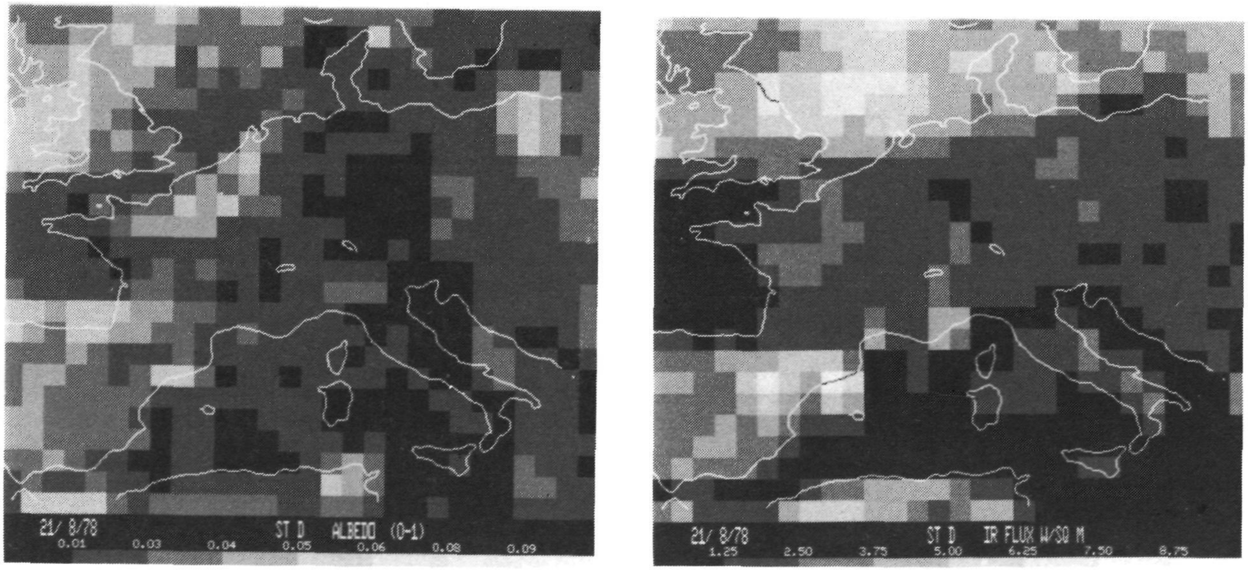

(c) Standard deviation of albedo.

(d) Standard deviation of longwave flux (W/m^2).

Figure 4.- Mean albedo, longwave flux, and their standard deviations for 21 August 1978 over Europe. The values are displayed according to the greyscale.

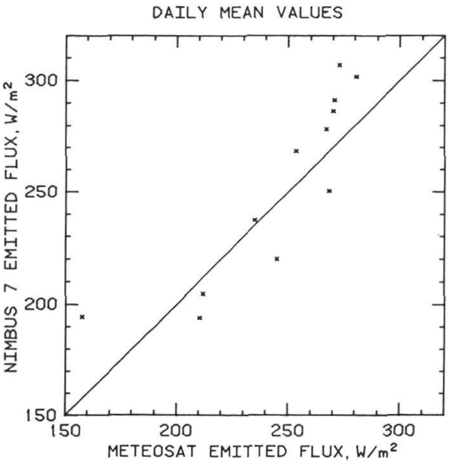

Figure 5.- Comparison of Nimbus 7 ERB and Meteosat daily mean emitted fluxes over 12 uniform target areas for 14 October 1979.

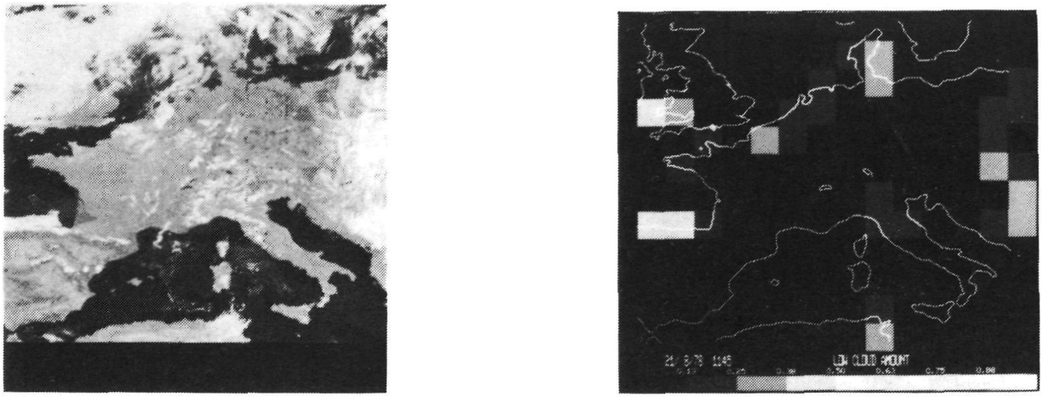

(a) Visible Meteosat square projection.

(b) Low-cloud amounts.

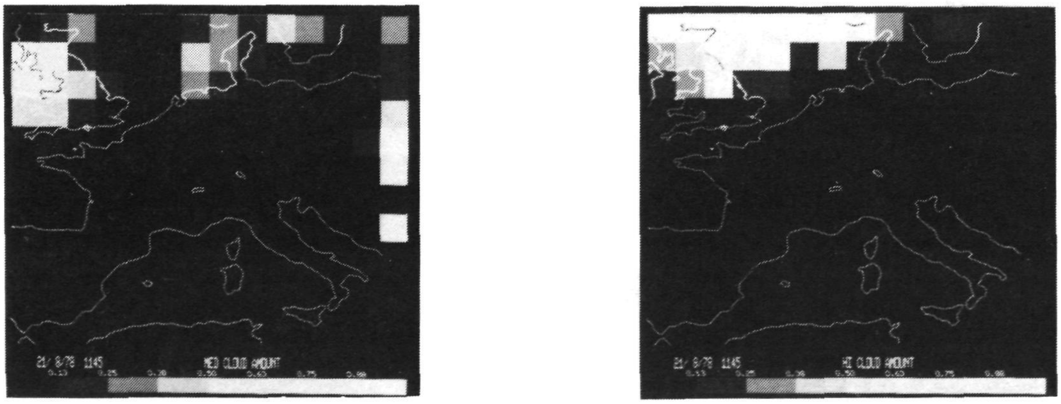

(c) Medium-cloud amounts.

(d) High-cloud amounts.

Figure 6.- Visible Meteosat square projection and low-cloud, medium-cloud, and high-cloud amounts averaged over 2° latitude/longitude squares derived from the VIS and IR satellite images for 1145 GMT on 21 August 1978. The minimum-cloud amount shown on this plot is 10 percent. The actual data record cloud amounts down to 1 percent.

ORIGINAL PAGE
BLACK AND WHITE PHOTOGRAPH

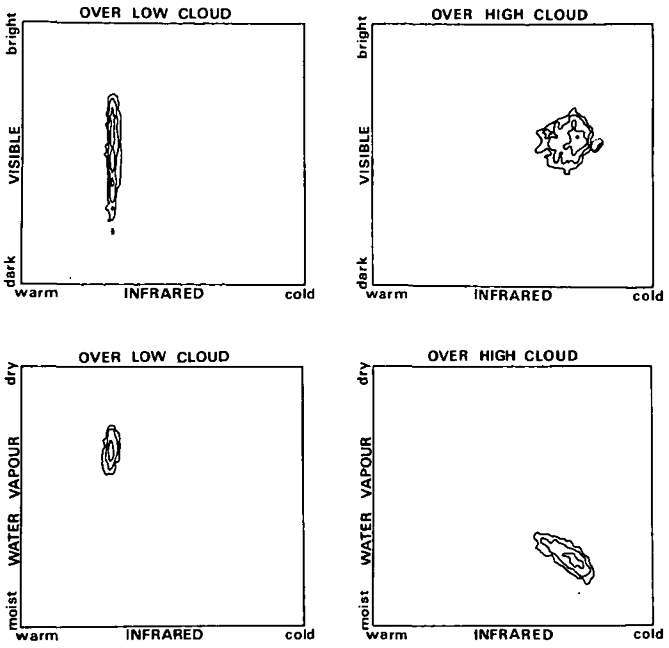

Figure 7.- Examples of bidimensional histograms over low and high clouds from Meteosat. Both VIS-IR and IR-WV combinations are shown.

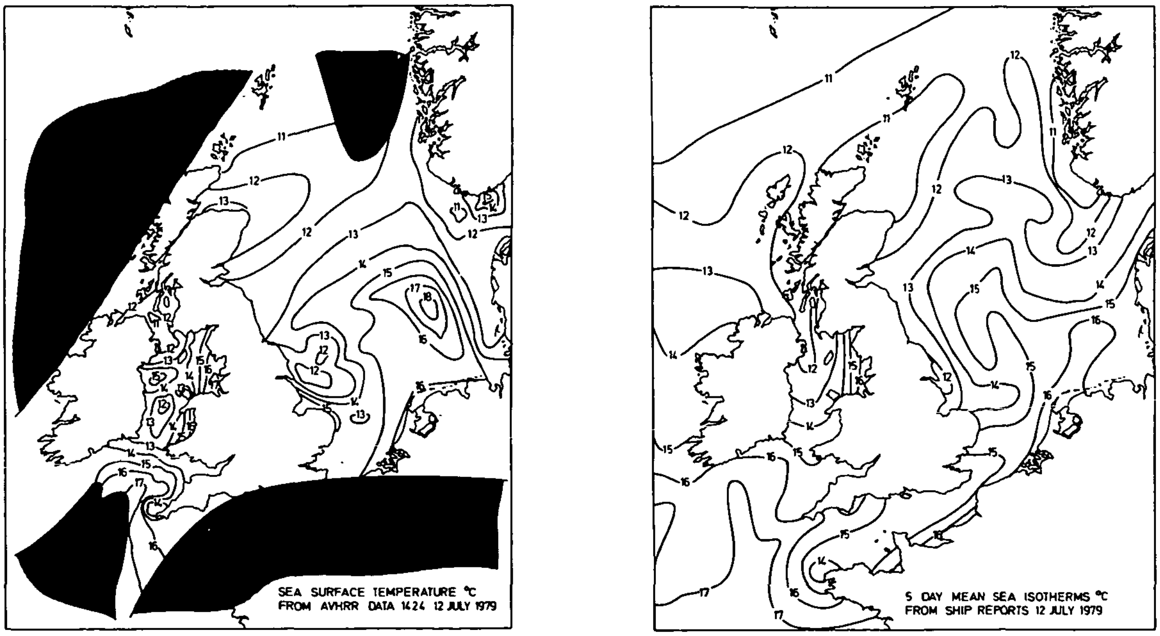

(a) (b)

Figure 8.- Isotherms of sea surface temperatures around the British Isles for 12 July 1979 from AVHRR 11-μm data, 1424 GMT (a), and ship reports, 1200 GMT (b).

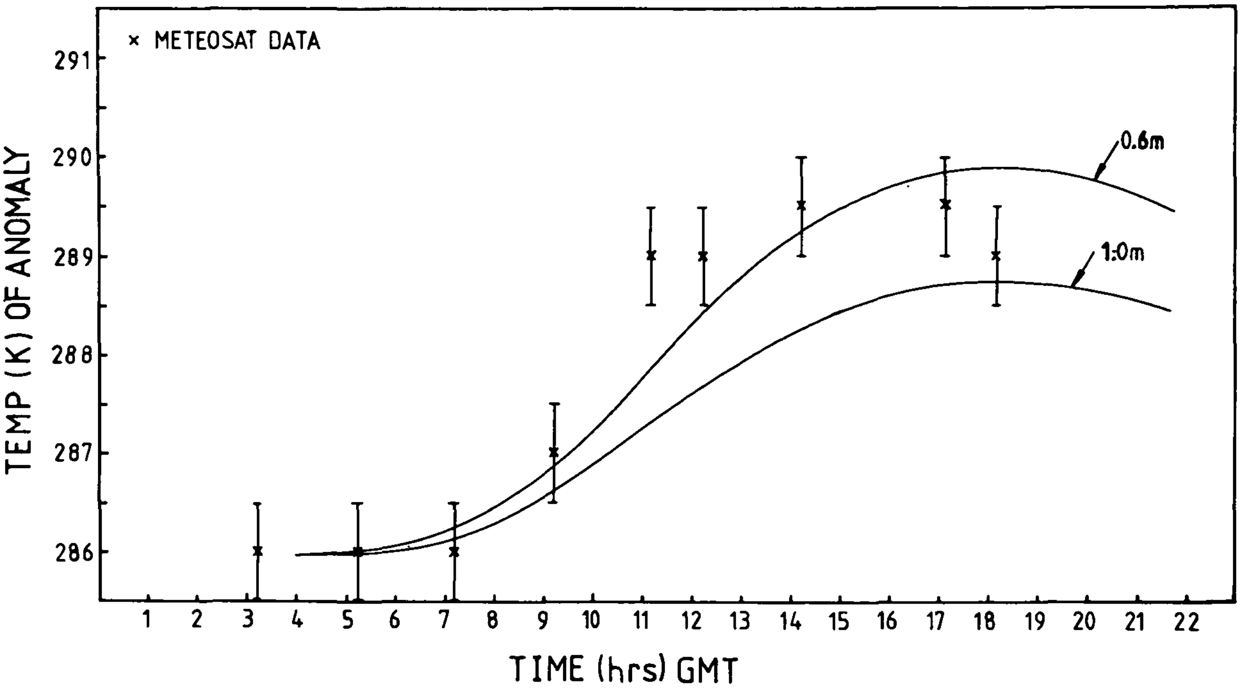

Figure 9.- Variation of sea surface temperature at the center of the anomaly as a function of time. The crosses denote Meteosat measurements. The solid lines represent predictions from a simple one-dimensional heat transfer model for different assumed mixing depths.

1. Report No. NASA CP-2239	2. Government Accession No.	3. Recipient's Catalog No.

4. Title and Subtitle
EARTH RADIATION SCIENCE SEMINARS

5. Report Date
August 1982

6. Performing Organization Code
146-10-06-05

7. Author(s)
John B. Hall, Jr., Compiler

8. Performing Organization Report No.
L-15483

9. Performing Organization Name and Address
NASA Langley Research Center
Hampton, VA 23665

10. Work Unit No.

11. Contract or Grant No.

12. Sponsoring Agency Name and Address
National Aeronautics and Space Administration
Washington, DC 20546

13. Type of Report and Period Covered
Conference Publication

14. Sponsoring Agency Code

15. Supplementary Notes

16. Abstract

This volume contains eight papers that resulted from a series of Earth Radiation Science Seminars held at NASA Langley Research Center, Hampton, Virginia, from June 1980 to October 1981. These papers cover a broad range of research activities pertinent to understanding the significance of the Earth radiation budget in influencing climate variability. Information presented includes radiation measurement fundamentals, radiation budget at the Earth's surface, parameters that significantly affect radiation measurements, and measurement history as obtained from Earth-orbiting satellites.

17. Key Words (Suggested by Author(s))
Earth radiation budget
Satellite measurements
Radiation modeling
Surface radiation budget
Radiation measurement fundamentals

18. Distribution Statement
Unclassified - Unlimited
Subject Category 93

19. Security Classif. (of this report) Unclassified	20. Security Classif. (of this page) Unclassified	21. No. of Pages 177	22. Price A09

For sale by the National Technical Information Service, Springfield, Virginia 22161

NASA-Langley, 1982

National Aeronautics and
Space Administration

Washington, D.C.
20546

Official Business
Penalty for Private Use, $300

SPECIAL FOURTH CLASS MAIL
BOOK

5 2 CP-LOW,D, 820728 S90569AU 850609
NASA
SCIEN & TECH INFO FACILITY
ATTN: ACCESSIONING DEPT
P O BOX 8757 BWI ARPRT
BALTIMORE MD 21240

NASA

POSTMASTER: If Undeliverable (Section 158
Postal Manual) Do Not Return